SOLIDIFICATION BEHAVIOUR AND HIPPING INDUCED SURFACE MODIFICATION IN Ti4522XD CASTINGS

CHAO YANG

A thesis submitted to
The UNIVERSITY OF BIRMINGHAM
For the degree of
DOCTOR OF PHILOSOPHY

School of Metallurgy and Materials
College of Engineering and Physical Sciences
The University of Birmingham
January 2012

Synopsis

The solidification behaviour of Ti45Al2Mn2Nb1B (at.%) has been studied together with its response to HIPing (Hot Isostatic Pressing) in order to understand the mechanism of grain refinement in castings and to understand the influence of surface changes occurring during HIPping on the properties of HIPped net shape cast turbine blades. Samples which had been rapidly cooled from near the melting point from a Bridgman furnace, where a thermal gradient was imposed, have been used to understand the grain refinement mechanism and the details of the solidification sequence. In addition the structure of powder samples, which have been gas-atomised and hence very rapidly cooled have also been used to further the understanding of solidification and of the role of borides. It has been shown that borides themselves play an important role in grain refinement. It has been shown that HIPping results in the formation of a surface which is caused by oxidation from the oxygen present in the argon used in the HIP. The details of the chemistry and microstructure of the surface layers have been shown to be influenced by oxygen partial pressure, by HIPping time and HIPping temperature. Conventional HIPping conditions lead to a surface which contains a γ-layer which does not appear to downgrade either the tensile properties or fatigue properties of the samples and may slightly improve the corrosion resistance. Further work is required to produce net shape castings, which have properties comparable with conventionally cast Ti4522XD, but the present work shows that these could then be HIPped without the γ-layer contained surface causing any downgrading in properties.

Acknowledgments

I am indebted to Dr. Dawei Hu, for his excellent supervision, invaluable assistance and continuous encouragement throughout the whole Ph. D years. Special thanks must go to Prof. M. H. Loretto for many useful discussions and comments on my projects. Prof. X. Wu, Dr. A. Huang and M. Dixon are gratefully acknowledged for their support and supervision of the Ph. D projects. Financial support from the School of Metallurgy and Materials, ORS Committee, and Rolls-Royce plc is also greatly acknowledged.

Many thanks go to Prof. P. Bowen and Dr. M. Attallah for their continuous support in my Ph.D study. Thanks are also expressed for the assistance of the secretarial and technical staff in the School of Metallurgy and Materials and the Interdisciplinary Research Centre. Special thanks are extended to M. Glynn and J. Shurvinton for their help with HIPping and heat treatment, Dr. T. Doel for helping the mechanical testing, and P. Stanley, T. Morris, and Dr. M. Chu for their training and help in SEM and TEM.

I am also obliged to the following people for many valuable discussions over the years: Prof. I. Jones, Prof. H. Dong, Dr. Y. Lung, Dr. H. Li, Dr. X. Li, Dr. Y. Tse, Dr. M. Strangwood and Dr. R. Ding. I would also like to express sincere thanks to all my friends and colleagues for their assistance and encouragement.

Finally, I wish to thank my families, i.e. grandma, parents and sister, for their precious understanding and constant support. I could never have completed my study without them.

Table of Contents

List of figures

partial dislocations. b_3 is perpendicular to the Burgers vector b = 1/6[$\bar{1}$ 10] for ordinary dislocations represent the Shockley partial dislocation for true twinning, where b_1 and b_2 represent pseudo-twinning.

Figure 2.17 The emission of dislocation loops from an interface (arrow 2) observed in Ti-48Al-2Cr alloy, which was compressed at 300 K to a strain of 3 %.

Figure 2.18 Tensile flow curves for TiAl alloys in two typical microstructural forms (duplex and fully lamellar) with various grain sizes.

Figure 2.19 Room temperature tensile properties with different surface conditions in (a) cast Ti-44Al-8Nb-1B alloy, and (b) PM Ti-47Al-2Cr-2Nb alloy. In (b), EP refers to electro-polishing and for each surface condition, two test pieces were tested.

Figure 2.20 shows variation of tensile ductility with temperature for different microstructures.

Figure 2.21 Curves 1: Crack growth resistance curves of investment cast Ti-48Al-2Cr (D-duplex) at 20 and 700 °C. □, ○: compact tension (CT)-50 specimens with fatigue precracks and displacement rates of 10 μm/h and 600 μm/h, respectively. Δ:CT-50 specimens with electron charging machining (ECM) slit notch (radius ~ 50 μm) and 600 μm/h. ♦: CT-2.6 specimen, 10 μm/h. Curve 2: K_R curve of fully lamellar (FL) Ti-47Al-2.6Nb-2(Cr+V) at 20 and 800 ℃; displacement rate 4.2×10^{-2} s^{-1}.

Figure 2.22 Dependence of fracture toughness on temperature for two phase TiAl alloys with different microstructures. FL: fully lamellar; NG: near gamma; D: duplex.

Figure 2.23 S-N curves for Alloy K5 (Ti-46.5Al-3Nb-2Cr-0.2W) with duplex and lamellar microstructures.

Figure 2.24 Influence of temperature on high cycle fatigue resistance.

Figure 2.25 Cyclic stress-strain behaviour of the cast Ti-48Al-2Cr-2Nb alloy at room temperature.

Figure 2.26 Influence of microstructure on fatigue crack growth behaviour at room temperature. XD, MD and PM stand for casting, forging and powder metallurgy process, respectively, and G7 stands for a reference material with coarse lamellar microstructure.

Figure 2.27 Schematic mode of the fatigue crack growth process.

Figure 2.28 Critical sizes for FCG and fracture as a function of maximum stress for two typical TiAl-based alloy microstructures as compared to a Ti6246 alloy.

Figure 2.29 Fatigue crack growth behaviour of a cast Ti-48Al-2Cr-2Nb in air and vacuum.

Figure 2.30 Influence of lamellar volume fraction on creep strain rate for Ti-48Al-1V with high C (0.3 %) and low C (0.07 %); 0 % lamellar (equiaxed microstructure), 20 % lamellar is duplex and 100 % lamellar is fully lamellar.

Figure 2.31 Creep characteristics of Ti-47Al-3.7(Nb, Mn, Cr, C)-0.5B, 1) investment casting, near-lamellar microstructure, lamellar spacing 0.1-1.5 mm, 2) investment casting +

Figure 4.2 SEM BSE images of enlarged microstructures quenched from (a) liquid, (b) β dendrites with liquid in the inderdendritic region and peritectic α in between, (c) (β+ α) region with Widmanstätten structure and (d) lamellar structure which is close to the unmelted area in unidirectionally solidified Ti4522.

Figure 4.3 SEM BSE microstructures of (a) mushy zone, (b) dendritic region, (c) enlarged image of dendrite in dendritic region, showing the long boride in the core, (d) enlarged image of interdendritic area in dendritic region, showing the very fine lamellar structure (e) (α + massive γ) region and (f) lamellar which is close to the unmelted region in unidirectionally solidified Ti4522XD. From the mushy zone to lamellar zone, the borides change from curvy bright to long bright.

Figure 4.4 The lamellar colony size distribution in the Ti4522 and Ti4522XD Bridgman samples.

Figure 4.5 (a) BSE microstructure of the liquid region in Ti4522 Bridgman sample with the corresponding α_2 grain map and grain size distribution graph in (b) and (c), the α_2 texture map in (d), and the misorientation map and the misorientation distribution graph in (e) and (f). It is shown in (d) that there are 8 α_2 texture components as labelled in the image.

Figure 4.6 Each texture component from the texture map in fig. 4.5 (b) with their variants and their corresponding (0001) pole figures.

Figure 4.7 Each texture component from the texture map in fig. 4.5 (b) with their variants and their corresponding $\{11\bar{2}0\}$ pole figures.

Figure 4.8 Results of orientation mapping of mushy zone in Ti4522, showing (a) the area of mapping, (b) phase map in which ■ and ■ stand for α_2 and γ phase, respectively, (c) and (d) the α_2 grain map and grain size distribution graph, (e) and (f) the γ grain map and grain size distribution graph, (g) and (h) the α_2 and γ texture map, (i) and (j) the α_2 grain misorientation map and its distribution graph, and (k) parts of the (0001) and $(11\bar{2}0)$ pole figure of α_2 and (110) and (111) pole figure of γ. The same colour circle marks in (k) indicate that the γ grains and α_2 grains follow Blackburn's OR, and twin structure among γ grains.

Figure 4.9 Enlarged orientation mapping of dendritic region in Ti4522, showing (a) the area of mapping, (b) phase map in which ■ and ■ stand for α_2 and γ phase, respectively, (c) and (d) the α_2 and γ texture map, (e) the (0001) and $\{11\bar{2}0\}$ pole figures of α_2, and {111} and {110} poles figures of γ. The circle marks in (e) indicate that the γ grains in the interdendritic regions and α_2 grains in the dendrites follow Blackburn's OR and the twin structure among γ grains.

Figure 4.10 Mushy zone in Ti4522XD Bridgman sample with (a) BSE image, (b) phase map in which ■ and ■ stand for α_2 and γ phase, respectively, (c) α_2 grain map with grain size distribution graph in (d), and (e) and (f) α_2 and γ normal direction orientation map with orientation colour key in (g) and (h), respectively.

Figure 4.11 Normal orientation maps of α_2 in (a) and γ in (b) from the selected area in fig. 4.10 (e) and (f), (c) part of the pole figures of α_2 grains in both (0001) and $\{11\bar{2}0\}$ poles and γ grains in both {111} and {110} pole figures.

Figure 4.26 (a) many beam TEM bright field (BF) image of matrix phase (dark grain) shown in fine Ti4522XD powders, and (b), (c) and (d) are the corresponding selected area diffraction (SAD) patterns which was identified to be α_2 phase with zone axis $[11\bar{2}\,0]$, $[14\bar{5}\,0]$ and $[11\bar{2}\,3]$, respectively. The tilting angles between (b) and (c), (b) and (d) and (c) and (d) are 20.4 °, 39.0 ° and 43.2 °, respectively.

Figure 4.27 (a) many beam TEM BF image of fine Ti4522XD powder, in which grain A is the second solid phase shown in fig. 4.25 and grain B the matrix α_2 phase. SAD patterns shown in (b), (c) and (d) were taken from grain A, which was identified as α_2 phase with zone axis $[01\bar{1}\,2]$, $[\bar{1}\,5\bar{4}\,6]$ and $[\bar{1}\,2\bar{1}\,6]$, respectively. The tilting angles between (b) and (c), (b) and (d) and (c) and (d) are 14.4 °, 23.7 ° and 29.9 °, respectively. When A is in zone axes $[11\bar{2}\,6]$ as shown in (e), B is in $[4\bar{5}\,16]$ and (f) was taken from their interface.

Figure 4.28 Superposed plane stereographic projections with $[11\bar{2}\,6]_A//[4\bar{5}\,16]_B$ and $(\bar{2}\,021)_A//(\bar{2}\,021)_B$. The angle between (0001) in each pole figure is calculated to be 60 °.

Figure 4.29 Superposed direction stereographic projections with $[11\bar{2}\,6]_A//[4\bar{5}\,16]_B$ and $(20\bar{2}\,\bar{1})_A//(20\bar{2}\,\bar{1})_B$. The angles between $<11\bar{2}\,0>$ planes in each stereographic projection are summarized in table 4.3.

Figure 4.30 SE SEM images showing corrosion resistance of γ-TiAl and α_2-Ti_3Al to 2% HF etchant, indicating γ phase is more resistant.

Figure 4.31 (a) many beam BF and (b) centered dark field (CDF) images of long curvy boride existing in Ti4522XD powders. The ***g*** vector used for CDF image in (b) is $1\bar{3}\,0$*. (c) and (d) are the corresponding SDA patterns from B_f [621] and [310] zone axis. The tilting angle between (c) and (d) is 9.4 °.

Figure 4.32 (a) BF and (b) DF images of short straight borides in Ti4522XD powder with CEBD in (c) showing the zone axis of [012] in B_f.

Figure 4.33 (a), (b) and (c) are BF image, DF image and SAD pattern of horizontal particles when it is in the B_f boride zone axis [012]; (d), (e) and (f) are BF image, DF image and SAD pattern of vertical particles when it is in the B_f boride zone axis [012], which was tilted 4.4 ° about 001* of B_f from (c); (g) and (h) show the BF image and the corresponding SAD pattern of the neighbouring α_2 phase in the zone axis of $[11\bar{2}\,0]$, which was tilted 15.7 ° about the other side 001* of B_f from (c).

Figure 4.34 TiB (B_f) (100) pole figure showing the angle between $(02\bar{1}\,)$ and $(01\bar{1}\,)$ is 15.9 °.

Figure 4.35 (a) BSE and (b) SE images of Ti4522XD powders at high magnifications, showing blocky particles, (c) many beam BF image of a blocky particle and their corresponding SAD patterns in (d)-(f), showing a TiB_2 particle. The zone axis in (d)-(f) are $[01\bar{1}\,1]$, $[14\bar{3}\,5]$ and $[01\bar{1}\,0]$, respectively. The tilting angles between (d) and (e), (d) and (f) and (e) and (f) are 14.6 °, 31.4 ° and 23.4 °, respectively.

Figure 4.36 BSE SEM images of (a) the overall and (b) the interdendritic BSE images of coarse Ti4522XD powder, SE SEM images of (c) the overall and (d) the enlarged SE images of coarse Ti4522XD powder with specimen surface etched.

Figure 4.37 (a) many beam BF image of Ti_3B_4 in coarse Ti4522XD powder and their corresponding SAD patterns in (b) with zone axis [311].

Figure 4.38 XRD result from fine Ti4522XD powders with diameter larger than 100 μm, showing a single α_2 phase.

Figure 4.39 (a) many beam BF image of γ grains in the interdendritic regions of coarse Ti4522XD powder and their corresponding SAD patterns in (b)-(d) with zone axis $[1\bar{1}2]$, [101] and $[1\bar{1}1]$, respectively. The tilting angles between (b) and (c), (b) and (d) and (c) and (d) are 30.5 °, 17.1 ° and 34.4 °, respectively.

Figure 4.40 BSE image of fine Ti4522XD powder in (a) and its corresponding α_2 orientation map in (b), (c) and (d) are the α_2 grain map and its corresponding grain size distribution graph; (e) and (f) are the α_2 grain misorientation map and its corresponding misorientation distribution graph; (g) shows that of all the 151 α_2 grains in this powder, only grains labelled 73 and 74, 100 and 110 are possible Burgers variants which are neighboured.

Figure 4.41 (a) SE image of etched fine Ti4522XD powder and (b) its corresponding α_2 normal orientation map.

Figure 4.42 Coarse Ti4522XD powder with BSE image in (a), phase map in (b), α_2 grain map and α_2 grain size distribution graph in (c) and (d), γ grain map and γ grain size distribution graph in (e) and (f), α_2 and γ normal orientation map in (g) and (h), respectively.

Figure 4.43 Enlarged α_2 and γ normal orientation maps in (a) and (b) from the selected dendritic region in fig. 4.21 (g) and (h); (c) and (d) are the corresponding α_2 misorientation map and its misorientation distribution graph.

Figure 4.44 Enlarged α_2 and γ normal orientation maps in (a) and (b) from a selected dendritic region in fig. 4.22; (c) shows the (0001) α_2 pole figures and {111} γ pole figures of the labelled α_2 and γ grains in (a) and (b), respectively.

Figure 4.45 BSE SEM images of (a), (b) and (c) in Ti4522XD button along the solidification direction; and (d), (e) and (f) in Ti48Al2Cr2Nb1B button along the solidification direction.

Figure 4.46 SE SEM images of the edge areas in etched samples (a) Ti4522XD button and (b) Ti48Al2Cr2Nb1B button, indicating the existence of equiaxed small borides particles.

Figure 4.47 Long curvy boride in Ti4522XD button, (a) many beam BF TEM image with SAD patterns in the Ti_3B_4 zone axes (b) [100], (c) [201] and (d) [10,1,0]. The tilting angles between (b) and (c), (b) and (d) and (c) and (d) are 25.2 °, 21.1 ° and 33.4 °, respectively.

Figure 4.48 Long curvy boride in Ti4522XD button, (a) many beam BF TEM image with SAD pattern in zone axes (b) $[001]B_f$ // [001]B2 and (c) $[102]B_f$ // [102]B2. The tilting angle between (b) and (c) is 29.6 °.

Figure 4.49 (a) BSE images of both bright and dark borides in Ti4522XD button, (b) the corresponding EBSD phase map, showing dark boride is TiB_2 with C32 structure and

bright boride TiB with B27 structure. The principle for the identification of the crystal structures of those borides is through the indexing of the Kikuchi patterns in (c) and (d) yielded from bright boride and dark boride, respectively. (e) and (f) are the (010) and (0001) pole figures from bright and dark boride, indicating the fastest growing directions of TiB with B27 structure and TiB_2 are along [010] and [0001], respectively.

Figure 4.50 (a) SE image of etched Ti48Al2Cr2Nb1B button containing long curvy borides; (b) marks the area sectioned for TEM sample preparation by FIB milling; and (c) shows the final morphology of TEM sample selected from the region marked in (b), indicating that those long curvy borides are two dimensional.

Figure 4.51 (a) Many beam BF TEM image of long curvy boride in Ti48Al2Cr2Nb1B button with (b) SAD pattern in $[11\bar{2}0]$ zone axes of TiB_2.

Figure 4.52 (a), (b) and (c) are many beam BF TEM images of one end of long curvy TiB_2 boride in Ti48Al2Cr2Nb1B button with their corresponding SAD patterns from zone axis $[1\bar{1}00]$ in (d), $[01\bar{1}1]$ in (e) and $[01\bar{1}2]$ in (f). The tilting angles between (d) and (e) and (d) and (f), are 27.1 ° and 47.7 °, respectively. It is noticed that the end of boride in image (a) is in edge-on condition.

Figure 4.53 (a) Many beam BF TEM images of one section of long curvy TiB_2 boride in Ti48Al2Cr2Nb1B button with its corresponding SAD patterns from zone axis $[11\bar{2}3]$ in (b), $[01\bar{1}2]$ in (c) and $[\bar{1}2\bar{1}3]$ in (d). The tilting angles between (b) and (c), and (b) and (d) are 19.6 ° and 39.9 °, respectively.

Figure 4.54 (a) BSE image of the centre of Ti45Al2Cr2Nb1B button containing blocky boride with dark contrast, (b) the corresponding EBSD phase map, showing this boride is TiB_2 with C32 structure, (c) the Kikuchi pattern from this boride and its corresponding indexing by TiB_2 structure, (d) the (0001) pole figures from this boride, indicating the fastest growing direction of TiB_2 is along [0001].

Figure 5.1 Backscattered SEM (BSE) images of (a) as-cast and (b) and (c) as-HIPped Ti4522XD from LP turbine blades.

Figure 5.2 (a) BSE image of as-cast Ti4522XD and (b) the corresponding EDS line scan in the micro-segregation region, indicating Mn and Nb are slightly enriched.

Figure 5.3 BSE SEM images of cross-sections of cast Ti4522XD (a) as-electropolished and (b) after HIPing at 1260 ℃/4 h/150 MPa and Ni-plating; Secondary electron (SE) SEM images of surface morphologies of cast Ti4522XD (c) as-electropolished and (d) after HIPping at 1260 ℃/4 h/150 MPa.

Figure 5.4 Analytical XRD results from the surface of 1260 ℃/4 h/150 MPa HIPped 4522XD castings.

Figure 5.5 (a) SE and (b) BSE SEM images of the cross-sections of 4522XD casting HIPped at 1260 ℃/4 h/150 MPa.

Figure 5.6 EDS line scans on the HIPped surface which was formed under standard HIPping conditions. (a) BSE image of cross-section microstructure of HIPped surface,

List of tables

CHAPTER 1 INTRODUCTION

TiAl-based alloys have been widely studied in the past 20 years or so years, in an effort to introduce these alloys into the market-place as engineering components, especially in the high temperature application environment such as turbine blades in gas-turbine engines. Their potential application is related to their low density and high specific strength from room temperature to as high as 750 ℃. However, limited low room temperature ductility has always been one of the obstacles for their practical application in industry. But great progress has been made to improve their ductility in terms of composition modification, improvement of processing technology, microstructural control etc.

Of all the developed TiAl alloys, Ti45Al2Mn2Nb1B (at.%), referred to as Ti4522XD, is one of the mature commercial alloys that are going to be used in low pressure turbine blades by Rolls-Royce in the near future which can endure at least 650 ℃ for a long time. To be cost-effective, near net shape casting is so far the preferred processing technology, since it can save both machining and raw materials. The addition of 1 at% boron can refine the as-cast lamellar microstructure which has been established to the best microstructure that can provide optimised mechanical properties. However, in the whole manufacturing process, the as-cast blades have to be hot isostatically pressed (HIPped) to get rid of internal porosity formed during solidification, otherwise, the existing pores may be detrimental to the material's mechanical properties, especially fatigue properties, since they could be crack nucleation sites. The optimised HIPping parameters for the as-cast Ti4522XD components have been established, which are called standard HIPping

conditions. Normally, the as-HIPped blades should be further heat treated at relatively low temperature to stabilise the microstructure to improve the creep properties.

To guarantee the mechanical properties in the application environment, control of as-cast microstructure and complete understanding of the effect of HIPping on the as-cast components are of great importance. Therefore, if the as-cast microstructure can be controlled through control of the casting parameters during solidification, the mechanical properties of the as-cast component can be guaranteed. However, control of as-cast microstructure of Ti4522XD is based on the understanding of its solidification behaviour and the factors which influence this, of which the cooling rate and the addition of boron are among the most important. Because net shape investment casting has limited the amount of machining required after HIPping the influence of the HIPping process on the nature of the surface and on the properties of HIPped samples needs to be understood and this is one area which has been studied in this thesis.

In Chapter 2, a comprehensive literature review starts with general introduction to intermetallics and TiAl alloys which include crystal structures, phase diagrams, solidification behaviours and alloy development history, followed by a summary of processing technologies, microstructures and mechanical properties. Since the solidification behaviour of boron-containing TiAl alloys is one of the main concerns in this thesis, the literature review on equilibrium and non-equilibrium solidification and the refinement mechanism by the addition of boron are presented in detail. Oxidation and corrosion properties are highlighted afterwards. Given that Ti4522XD is the main alloy

studied, a separate review on its processing, microstructure and properties is presented. Finally, the background and the main aims of the research project are summarised.

Chapter 3 describes the experimental methods used in this research, which includes the materials and analytical facilities. Ti4522XD is the main material that has been studied, but Ti4522 and Ti48Al2Cr2Nb1B buttons were also studied for comparison. Details on specimen preparation, microstructural characterisation, compositional analysis and crystal structure identification utilising electron beam techniques and other analysis techniques are given. Mechanical testing and fracture analysis methods are also presented.

Experimental results and discussion are divided into two chapters considering the different research interest in the solidification behaviour and the influence of HIPping on Ti4522XD castings. In Chapter 4, the solidification behaviours of Ti4522 and Ti4522XD unidirectionally solidified Bridgman samples, Ti4522XD powders with different particle sizes and Ti4522XD and Ti48Al2Cr2Nb1B buttons are analysed. The comparison between the solidification behaviours of Ti4522 and Ti4522XD Bridgman samples was designed to highlight the influence of the addition of boron. The study of the solidification behaviour of gas-atomised Ti4522XD powders was aimed at understanding the influence of a high cooling rate. Ti4522XD and Ti48Al2Cr2Nb1B buttons were used to understand the solidification behaviours of borides themselves in boron-containing TiAl alloys. In Chapter 5, the microstructural changes of both the bulk and the surface of Ti4522XD castings are presented after standard HIPping. The nature of the HIPped surface was analysed through scanning electron microscopy, transmission electron microscopy and X-Ray diffraction. The factors affecting the nature of the HIPped surface were also assessed by changing the

HIPping parameters. Mechanical tests of HIPped test pieces with and without HIPped surfaces were carried out to investigate the influence of HIPped surface on mechanical properties, including the test pieces after corrosion.

A general discussion is presented in Chapter 6 where the solidification behaviours of boron-containing TiAl alloys and the influence of HIPping on microstructures and properties of Ti4522XD castings are discussed separately. In terms of solidification behaviours, the basic solidification pathways and the influence of the addition of boron and cooling rate on solidification behaviour of Ti4522XD are discussed. The influences of cooling rate and alloy compositions on the solidification behaviours of borides themselves are also discussed. In terms of the influence of post HIPping on microstructures and properties, a mechanism for the formation of surface layers after standard HIPping is proposed and the influence of HIPped surfaces on properties are discussed.

Chapter 7 summarises the main conclusions in this study. Some future work is also proposed that should be carried out to obtain further understanding in this research area.

CHAPTER 2 LITERATURE RIVIEW

2 .1 Introduction

This thesis covers an experimental programme aimed at understanding the solidification behaviour of boron-containing TiAl alloys and the response to Hot Isostatic Pressing (HIPping) of net shaped cast turbine blades of a TiAl-based alloy. The literature review focuses on our current state of knowledge and understanding of the grain refinement mechanism and the microstructure-property relationships of boron-containing TiAl alloys, especially a particular alloy which has been studied, Ti45Al2Nb2Mn1B (at.%) (referred to as Ti4522XD), after covering some general aspects of intermetallics and TiAl alloys. The general areas covered include basic crystallography, phase diagrams, equilibrium and non-equilibrium solidification, solid phase transformations, processing methods, microstructures, crystal defects and mechanical properties, oxidation and corrosion. These topics are followed by a section on Ti4522XD in particular and a summary of the background and aims of the project.

2.1.1 Intermetallics

TiAl-based alloys are one member in the family of intermetallics. The first true observation of intermetallics or intermetallic compounds was that of the German chemist, Karl Karsten, in 1839, which is now the familiar beta brass, CuZn[1]. The definition of intermetallics was clearly stated by Schulze in 1967, who defined intermetallic compounds as solid phases containing two or more metallic elements, with optionally one or more non-metallic elements, whose crystal structure differs from that of the other constituents[2]. They are

formed when the bonding strength between unlike atoms (e.g. Ti-Al) is larger than that between like atoms (Ti-Ti, Al-Al). They possess crystal structures with an ordered atom distribution, and are known for high temperature properties including high melting points e.g. NiAl 1663 ℃, Nb_3Al 2060 ℃, high elastic modulus and typically they manifest high strength, creep and environmental resistance (e.g. oxidation, sulphidation) and low density. The main drawback to the use of intermetallics is their lack of toughness at room temperature and the high cost of processing. In terms of their properties they occupy an intermediate position between metals and ceramics. Intensive research of these materials started in the mid-1970s, or even earlier, in view of the expectation that they may become prime candidates for high temperature structural application, especially in jet engines in order to increase service temperature and reduce weight[3].

2.1.2 Titanium aluminide (TiAl)

There are three intermetallics based on the Ti-Al system, i.e. Ti_3Al, TiAl and $TiAl_3$. Normally, TiAl-based alloys refer to the alloys that contain one or two of those intermetallics, especially (Ti_3Al + TiAl) two phase alloys. They represent an important class of alloys providing a unique set of physical and mechanical properties that can lead to substantial payoffs in the automotive industry, power plant turbines and aircraft engines. It has taken more than 20 years of intensive research to introduce TiAl-based alloys into the market-place as engineering components[4]. The outstanding thermo-physical properties of these alloys mainly results from strongly ordered structures, which include: high melting point (>1440 ℃), low density of 3.9-4.2 g/cm^3, high elastic modulus (160-180 GPa)[5], low diffusion coefficient[6-8], good structural stability, good resistance against oxidation and corrosion and high ignition temperature when compared to traditional titanium alloys[9]. Fig. 2.1 illustrates the temperature-dependence of the specific strength of various groups of

alloys (i.e. properties divided by density)[10]. This figure shows that TiAl-based alloys have superior specific strength-temperature properties when compared with classical titanium alloys, steels and nickel-based superalloys in the temperature range from about 500 to 900 ℃. Fig. 2.2[11] indicates in detail that the specific 1000 hours rupture strength, specific modulus and specific strength are superior to the other titanium alloys and nickel-based superalloys in a certain temperature range. However, room temperature ductility is normally poor for all TiAl alloys no matter how they are processed. Low ductility is the biggest problem in the application of TiAl alloys as structural components because it makes them brittle and hard to be machined at room temperature. Another problem with TiAl-based alloys is the difficulty in processing them into components. Presently, wrought processing and near net shape casting are the most investigated methods with powder metallurgy being regarded as a very promising technology[9, 11-13].

2.2 Basic crystallography of TiAl alloys

As mentioned in 2.1.2, in the TiAl alloy system, there are three intermetallics depending on the Ti/Al ratio, namely Ti_3Al, TiAl and $TiAl_3$ which have their own crystal structure features[4, 14]. However, in general, Ti_3Al and TiAl are the main phases that are involved in TiAl-based alloys. Boron is a widely used grain refiner in TiAl-based alloys which gives rise to a range of borides. Therefore, both the crystallography of the main phases and borides in TiAl alloys are reviewed.

2.2.1 Intermetallics in Ti-Al system

The crystal structures of two main phases, Ti_3Al and TiAl, are shown in fig. 2.3[14]. Ti_3Al is normally referred to as α_2 in the TiAl alloy system. It has a hexagonal crystal structure

with Strukturbericht Designation $D0_{19}$ and has lattice parameters a_{ord} = 0.575~0.577 nm and c_{ord} = 0.462~0.468 nm. The lattice derives from the h.c.p type structure but presents long range order only in the direction perpendicular to the c axis.

TiAl is the γ phase and has an $L1_0$ type face-centred tetragonal structure consisting of alternate Ti and Al atomic layers along the c-axis. The lattice parameters for the γ phase are a = 0.3995~0.3997 nm and c = 0.4062~0.4079 nm. γ remains ordered up to its melting point.

The $[1\bar{1}0]$ direction and the other two $[10\bar{1}]$ and $[0\bar{1}1]$ directions on (111) in the γ phase are not equivalent to each other because of the tetragonal $L1_0$ structure of the γ phase while directions of the type $<11\bar{2}0>$ on the basal plane on the α_2 phase are all equivalent[14].

$TiAl_3$ phase orders according to the $D0_{22}$ structure. This structure is related to two $L1_2$ type unit cells stacked along the c-axis with an antiphase boundary of 1/2[110](001) type at every (001) plane.

In some TiAl alloy systems with high additions of β-stabilizing elements, β or B2 phase (ordered β phase) is found which has a cubic structure with a lattice parameter of approximately a = 0.316 nm[15], which of course is a function of alloy content.

2.2.2 Borides in TiAl alloys

For the boron-containing TiAl alloys, such as Ti4522XD, borides are present in addition to the γ and α_2 phases. In equilibrium, there are three types of borides, namely TiB, Ti_3B_4 and TiB_2 which exhibit B27, $D7_b$ and C32 structures, respectively. There is another equiatomic phase with the B_f structure, which does not appear in the binary system, but is a metastable phase in the Ti-Al-B ternary and a stable phase in quaternary and higher order Ti-Al-B-X alloys (where X = Nb, Ta and/or Zr)[16-20]. The crystallographic parameters are summarised

in table 2.1[21]. TiB_2 has a hexagonal structure, but the other three have orthorhombic structures.

For cast alloys, if the borides are formed directly from the liquid, they always have complex structures. De Graef et al.[21] and Cheng[17] studied the structure of plate-like borides in a Ti-41Al-1B alloy and in boron-containing Ti-44Al-8 (Nb,Zr,Ta) alloys respectively, for which β (Ti) is the first phase to solidify, and found they were composed of mixed B27 and B_f structures, which follow the orientation relationship (OR):

$[001]B_f$ // [010]B27; $(110)B_f$ // (100)B27

Both Inkson et al.[15] and Godfrey et al.[22] found the plate-like borides consisted of fine C32 plates interspersed with layers of an ordered B2 phase in Ti-45.5Al-1.6Fe-1.1V-0.7B (at.%) alloy and Ti-47Al-2Cr-2Nb-(0.1-1)B (at.%) alloy, respectively. The orientation relationships between C32 and B2 were observed to be:

$<0001>TiB_2$ (C32) // <010> B2; $\{10\text{-}10\}TiB_2$ (C32) // {001}B2

In their study on Ti-44Al-4Nb-4Zr-1B (at%) alloy, Kitkamthorn et al.[16] showed that the predominant phase in ribbon borides is TiB with B_f structure which was interspersed with layers of ordered B2 matrix. However, the boride with the B_f structure contained a high density of planar faults on (010), which corresponded to intergrowths of C32 and $D7_b$ structures. The B_f also contained thin embedded layers with B27 structure lying on {110} B_f. The orientation relationships between each of these plates were identified to be:

$[001]B_f$ // $[001]D7_b$ // [001]B2; $(010)B_f$ // $(010)D7_b$ // (010)B2

$[001]B_f$ // $[1\bar{2}10]$C32; $(010)B_f$ // $(01\bar{1}0)$C32

$[001]B_f$ // [010]B27; $(110)B_f$ // (100)B27

Even though there were well defined ORs between phases within borides, no clear ORs have been found with respect to the surrounding metals[16], since those ribbon borides formed as a eutectic mixture in the liquid ahead of the solidification front. However, if the borides were precipitated from the solid phases, the ORs between borides and the surrounding metals were recently determined[23, 24] to be:

$[0\bar{1}\,0]B27 // [1\bar{1}\,0]\gamma$; $(100)B27 // (11\bar{2})\gamma$[23]

$[010]B27 // [11\bar{2}\,0]\alpha_2$; $(001)B27 // (0001)\alpha_2$[24]

[100]B27 // [001]B2; (001)B27 // (010)B2[24]

2.3 Equilibrium phase diagrams

The first Ti-Al binary phase diagram that was used in a standard reference book was thoroughly assessed by Murray in 1987[25]. This was updated twice by Okamoto[26, 27]. So far the most acknowledged Ti-Al binary phase diagram was reassessed by Schuster in 2006 as shown in fig. 2.4[28]. One year earlier, Raghavan published a Ti-Al binary phase diagram pointing out the ordering of β phase in the high temperature in fig. 2.5[29]. It is clear that Ti_3Al and TiAl phases which are contained in the TiAl alloys exist over a wide range of Al content from around 20 to 55 at.%.

Since normally ternary and even quaternary alloying elements are added to TiAl alloys to enhance their mechanical or other properties, the influence of those alloying elements on the binary Ti-Al phase diagram has been modified as shown in fig. 2.6[11], which indicates that Zr, Nb and Ta can extend the high temperature β phase to lower Al-contents. In addition, interstitial elements, oxygen and carbon, were found to increase the α transus temperature[30].

The schematic liquidus projection of Ti-Al-B ternary system shown in fig. 2.7[20, 31, 32] has also been widely used. It shows that the crystal structure of borides changes from TiB to Ti_3B_4 and finally TiB_2 with increasing Al concentration, as with increasing boron concentration in the Ti-B system. Fig 2.7 also shows how the change of Al concentration in the TiAl-B system could affect the highest permitted boron concentration in the liquid front which is increased with decreasing Al concentration.

2.4 Solidification behaviour under equilibrium and non-equilibrium conditions

The solidification behaviour of TiAl-based alloys varies with alloy composition and solidification conditions, such as cooling rate, supercooling.

2.4.1 Solidification behaviour of binary Ti-Al alloys under equilibrium conditions

According to the equilibrium binary Ti-Al phase diagram shown in fig. 2.4, there are several solidification pathways for TiAl-based alloys depending on Al content.

When 39 < Al (at.%) < 45, the solidification path will follow:

$L \rightarrow L + \beta \rightarrow \beta \rightarrow \beta + \alpha \rightarrow \alpha \rightarrow \alpha + \gamma \rightarrow \alpha_2 + \gamma$

When 45 < Al (at.%) < 47, the solidification path will follow:

$L \rightarrow L + \beta \rightarrow L + \beta + \alpha \rightarrow \beta + \alpha \rightarrow \alpha \rightarrow \alpha + \gamma \rightarrow \alpha_2 + \gamma$

When 47 < Al (at.%) < 49, the solidification path will follow:

$L \rightarrow L + \beta \rightarrow L + \beta + \alpha \rightarrow L + \alpha \rightarrow \alpha \rightarrow \alpha + \gamma \rightarrow \alpha_2 + \gamma$

When 49 < Al (at.%) < 51, the solidification path will follow:

$L \rightarrow L + \alpha \rightarrow \alpha \rightarrow \alpha + \gamma \rightarrow \gamma$

When 51 < Al (at.%) < 55, the solidification path will follow:

$L \rightarrow L + \alpha \rightarrow L + \alpha + \gamma \rightarrow \alpha + \gamma \rightarrow \gamma$

When 55 < Al (at.%) < 59, the solidification path will follow:

$L \rightarrow L + \alpha \rightarrow L + \alpha + \gamma \rightarrow L + \gamma \rightarrow \gamma \rightarrow \gamma + TiAl_2$

As seen from the above solidification pathways, the Al content has a significant influence on the solidification behaviour of TiAl-based alloys. As the Al content increases, the first solidified solid phase changes from β to α and finally to γ. Accompanying these changes, there are two peritectic reactions:

$L + \beta \rightarrow \alpha$ and,

$L + \alpha \rightarrow \gamma$

In the subsequent cooling process, a series of solid-state phase transformations and ordering will occur. The β phase has a disordered body centred cubic (bcc) crystal structure and the α phase has a disordered hexagonal closed packed (hcp) crystal structure. The solid-state phase transformation from β to α follows Burgers orientation relationship (OR) [33, 34]:

$\{110\}\beta // (0001)\alpha; \langle 111\rangle\beta // \langle 2\bar{1}\,\bar{1}\,0\rangle\alpha$

Since the β phase has 12 variants, resulting from 6 {110} planes and 2 <111> directions in each {110} plane, there exist 12 possible variants for β to α transformation. As a result, there are 5 misorientation angles, 10.53°, 60°, 60.83°, 63.26° and 90° between α variants inherited from the same parent β grain[35, 36].

The solid phase transformation from α to γ follows Blackburn OR[37]:

$\{111\}\gamma$ // $(0001)\alpha$; $<110>\gamma$ // $<11\bar{2}0>\alpha$

Since there is only one (0001) variant in α, each α grain transforms to a lamellae composing α laths and γ laths which follow Blackburn OR in the slowly cooled as-cast condition. However, when γ precipitates from α parent phase, the $L1_0$ structure can be formed in six orientation variants according to the six possible orientations of the <110> direction along a reference $[11\bar{2}0]$ direction of the α phase. When a γ plate impinges on another γ plate, one γ plate can be rotated by θ, which can be 60° × n (n = 0~5), and/or translated by f, which can be 0, $1/2<10\bar{1}>$, $1/6<11\bar{2}>$ and $1/6<1\bar{2}1>$, with respect to the other γ plate[14]. Therefore, in each lamellar region, there are also lots of γ twins.

2.4.2 Solidification behaviour of TiAl-based alloys under non-equilibrium conditions

Increasing the cooling rate or supercooling could retain high temperature phases to room temperature and change the equilibrium solidification behaviour. Nishida et al.[38] studied the microstructures of gas-atomised Ti47Al (at.%) powders with average particle size of 250 μm and found 10 % of the powders had a martensitic structure which consisted of α_2 plates and 90 % of them had a dendritic structure with α_2 grains in the dendrites and γ grains in the interdendritic regions. It was also found that for the martensitic structure, the first solidified phase is β, while for the dendritic structure the first solidified phase is α. This showed that increasing the cooling rate during solidification could shift the primarily solidified phase from α to β in Al-rich TiAl alloys. This tendency was also observed by Valencia et al.[39] in a study on the effect of supercooling on the solidification behaviour of binary TiAl alloys. Gouma et al.[40] investigated the microstructures of Ti48Al2Mn2Nb (at.%) powders and observed similar dendritic microstructure, but further pointed out that

increasing cooling rate could reduce the volume fraction of interdendritic regions and that the microsegregation in the powders could cause inhomogeneity of HIPped products.

2.4.3 Solidification behaviour of boron-containing TiAl alloys

Since the addition of ternary or quaternary metal elements and interstitial elements can change the equilibrium Ti-Al phase diagram, they could also alter the solidification path accordingly. For the boron-containing TiAl alloys, their solidification behaviours are also associated with the formation of borides and the influence of boron on constitutional supercooling.

Hyman et al.[32, 41] studied the solidification behaviour of Ti-(49~52)Al-(0.95~4)B alloys extensively and concluded that it was related to the B and Al concentration which is summarised in a schematic liquidus projection of Ti-Al-B ternary system in fig. 2.7. According to those studies, whether the first solidified phase is boride or metallic phase depends on boron concentration and it is the Al content that decides which phase the first solidified metallic phase is.

In terms of morphologies of borides during solidification of TiAl alloys leaner in B, Hyman et al.[32] also found that they are related to supercooling and cooling rate. At the slowest solidification rate, borides tend to exhibit plate and needle morphologies. Increasing the cooling rate gradually changes the morphology to convoluted flakes and, finally, to very fine equiaxed particles. The authors proposed that all flake, plate and needle borides are secondary borides growing concurrently with the matrix by irregular eutectic-like solidification along the $L \rightarrow M + TiB_2$ monovariant line and constrained by the matrix. However, plates and needles are likely to have spent some time growing freely in the melt before they were trapped by the matrix. As regards to the blocky borides found

in the high B (> 1 at.%) containing TiAl alloys, they are assumed to be primary borides, nucleating and growing from the melt.

The introduction of boride or boron has been proven to be an effective method to refine the grain size in both wrought and cast materials[42, 43]. The mechanism for the grain size refinement of the cast TiAl alloys has been widely studied. All the proposed mechanisms for grain refinement are related to their influence on solidification behaviour due to the addition of borides or boron and also depend on the boron content. For the high boron-containing alloys, the first presumes that the boride particles added to the alloy act as inoculants because they do not dissolve entirely during melting[43]. This does not comply with many experimental observations, especially in lower boron-containing TiAl alloys in which the original borides, which were not Ti borides, were not found after casting[17]. The second is that the boride precipitation takes place first during solidification and that grain refinement occurs by nucleation at these precipitates[44]. The third suggested that the broken-off fragments of dendrites due to boron-weakened dendrite roots could be responsible for the grain refinement[45]. Neither the second nor the third mechanism could explain why when the boron concentration is increased over a critical level (0.5 at.% boron for most boron-containing alloys[11, 46]), the subcritical boron content has little or no impact on grain size. Cheng[17] proposed that boron would be built-up in the solidification front, leading to constitutional supercooling in the liquid ahead of the solidification front. In this situation, nuclei of both alloy and boride can form ahead of the growth front and enhance the formation of dendrite. Eventually, the microstructure is refined. For the β solidifying alloys with low boron content, Imayev et al.[47] and Hecht et al.[48] proposed that the origin of the grain refinement is through heterogeneous nucleation of α(Ti) on borides during the solid state phase transformation from β to α, facilitating many α variants (maximum 12

variants). However, this grain refinement failed if the peritectic reaction 'L + β(Ti) → α(Ti)' is part of the solidification path, for which the reason is not well understood.

2.4.4 Solidification of Bridgman samples

Bridgman samples refer to the samples that are subject to unidirectional solidification by Bridgman-Stockbarger technique. The Bridgman-Stockbarger technique is named after Harvard physicist Percy Williams Bridgman (1882 - 1961) and MIT physicist Donald C. Stockbarger (1895 - 1952). It is used for growing single crystal ingots, but which can be used for solidifying polycrystalline ingots as well.

This technique is performed in a Bridgman-Stockbarger furnace which can be in a horizontal or vertical geometry. For the vertical furnace, as shown in fig. 2.8, it consists of a heating zone on the top, a cooling device at the bottom and an isolation zone, baffle, in between[49]. During solidification, the furnace is moved upwards while the sample in crucible remains motionless and a temperature gradient is already in place. The technique involves heating polycrystalline material above its melting point and slowly cooling it from one end of its container, where a seed crystal is located. A single crystal of the same crystallographic orientation as the seed material is grown on the seed and is progressively formed along the length of the container. When seed crystals are not employed as described above, polycrystalline ingots can be produced from a feedstock consisting of rods, chunks, or any irregularly shaped pieces once they are melted and allowed to resolidify. The resultant microstructures of the ingots so obtained are characteristic of directionally solidified metals and alloys with their aligned grains.

Unidirectional solidification using Bridgman-Stockbarger technique is commonly applied to investigate microstructure formation during solidification, because it offers a good,

independent control of the solidification parameters, temperature gradient 'G' and solidification velocity 'V', and also the ability to effectively quench the sample at the end of a solidification experiment[48]. Quenching allows freezing in the high temperature phases and preserves the mushy zone for subsequent analyzing.

2.5 Alloy development and application

2.5.1 Alloy development

The TiAl-based alloys of the 1st generation are mainly binary Ti-Al alloys with various Al contents[9] and depending upon the Al-content, they may be single γ phase or two phase (γ + α_2). Subsequently, because of the lack of ductility and fracture toughness of single γ phase alloys, interest was focused on two phase alloys. Almost twenty years ago, Kim[50] summarised the compositions of two phase TiAl alloys to be Ti – (44-49)Al – (1-3)X1 – (1-4)X2 – (0.1-1)X3, where X1 stands for V, Mn, Cr; X2 for Nb, Ta, W, Mo and X3 for Si, C, B, N, P, Se, Te, Ni, Mo and Fe. It was said X1 elements increase ductility in two phase alloys, which was supported by both experimental[50-52], even though not very convincingly, and theoretical approaches. Most of the explanations of the improvement of ductility by the addition of these X1 elements existed in terms of reducing the axial ratio of the tetragonally distorted $L1_0$ unit cell[53], i.e. c/a approaching unity which is achieved by the changes in the electronic structures[54, 55], variation of unit cell volume[56] and site occupancy[57, 58]. It was suggested that this reduction of c/a could result in enhanced twin deformation and metallic character of TiAl alloys[52]. However, few of these studies made direct comparisons of chemical effects in constant microstructural conditions, which leaves many of the predictions awaiting verification. These elements were also reported to be solid solution strengtheners, with Cr appearing to be the most effective and Mn the least[50].

On the other hand, the group X1 elements are known to reduce the oxidation resistance of TiAl alloys and therefore, X2 elements are needed to overcome this problem[59]. Group X2 elements can also strengthen alloys by solid solution strengthening[60]. Small additions of group X3 elements have various effects wherein boron, silicon and carbon are known to refine the grain size[43, 61], carbon and nitrogen to improve creep resistance[62], silicon, boron, nickel and iron to decrease the melt viscosity[63], and silicon may yield some improvement in oxidation resistance and room temperature ductility[64]. Chen et al. found small additions of yttrium could also refine the microstructures[65].

Ten years ago, Appel et al.[66] updated the two phase alloy systems to be Ti – (45-49)Al – (0-2)(Cr, Mn, V) – (0.5-5)(Nb, W, Mo) – (0-1)(Si, B, C) with the role of the alloying elements unchanged from Kim's suggestions. Those alloy compositions are generally called 2nd generation TiAl-based alloys. Typical representatives of this group are Howmet, GE, ABB-2 and ABB-23 alloys with nominal chemical compositions of Ti-48Al-2Mn-2Nb, Ti-48Al-2Cr-2Nb, Ti-47Al-2W-0.5Si and Ti-45Al-2W-0.5Si-0.5B (at.%) respectively. Ti4522XD should be also classified as a 2nd generation alloy.

Five years ago, a new generation of TNB alloys, which contain high contents of Nb, was shown by Voice et al.[67] to have better mechanical performance than the traditional TiAl alloys. A base composition of Ti-(45-46)Al-(4-8)Nb (at%) with minor additions of C and B has been studied during this period and led to the development of the 3rd generation of TiAl-based alloys by GKSS[12].

The latest 4th generation of cast TiAl-based alloys with the chemical composition of Ti-46Al-8Ta (at.%) was developed for the IMPRESS project[9, 13]. The design of these alloys is based on the addition of alloying elements which reduce significantly diffusion during

cooling so that the massive transformation occurs even during air cooling[68, 69], which can be used for microstructural refinement in cast components and will be discussed later.

2.5.2 Application

Despite many problems, like room temperature ductility, fracture toughness, TiAl-based products are currently used in automotive applications. By the end of 2003, more than 20,000 turbochargers were successfully fitted to top of the range Lancia cars[11]. Importantly the alloy is melted using a cold wall furnace and the turbochargers are cast using counter gravity casting. This will allow experience in casting technology to be built up so that eventually safety-critical components can be manufactured using this route. Thermo-mechanically processed valves have been used for many years in formula one cars (where cost is not the main issue) but formula one regulations no longer allow their use[11]. Attempts to develop cast TiAl-based valves have been successful in term of performance[11, 70, 71] but are still far too expensive because the amount of scrap is too large and the cost of raw materials is an increasing cause of concern.

The application referred to most frequently in the literature for TiAl-based alloys is in aircraft engines. Improved performance of aircraft engines can be obtained by higher thrust-to-weight ratios, fewer compressor and turbine stages (with higher pressure ratios across each) and increased turbine entry temperature[4]. In civil engines, the prospect of weight savings through displacement of nickel alloys and steels and a consequent improvement in specific fuel consumption would be particularly attractive. Ti_3Al and TiAl-based alloys offer interesting potential in rotating components of turbines because of their low density and good resistance to temperature. When the density of the material is considered, their exceptional specific mechanical properties are the major driving force

leading to the development and maturation of these materials. The materials currently used in aero-engines are shown in fig. 2.9[13], although it should be noted that GE have recently used TiAl-based alloys in their latest engines. Titanium alloys are used as the compressor blades, but they oxidise rapidly above 600 ℃. As a consequence they can only be used in cooler engine parts. Nickel-based alloys are the main materials used in turbine parts, but they have a high density impeding the improvement of efficiency. To overcome these strong thermal and mechanical loads, it would be possible in some components, like low pressure turbine blades, high pressure compressor stators, transition duct supports to substitute the nickel-based superalloys with intermetallic compounds based on TiAl alloys. They also have potential applications in aircraft engines in locations where clearance is crucial, such as frames, seal supports and cases due to their excellent specific stiffness[72]. The Ti4522XD alloy studied in this thesis is expected to be used as low pressure (LP) turbine blades in the next generation of engines by Rolls-Royce.

2.6 Processing methods of TiAl-based components

At present, there are mainly three processing methods used to produce TiAl-based components, such as LP turbine blades, and these are discussed in turn below.

2.6.1 Wrought processing (ingot production + hot working)

One of the processing approaches is wrought processing including ingot production which is carried out by vacuum arc remelting (VAR) or by induction skull melting followed by extruding, rolling or forging. Wrought processing allows a broad range of tailored microstructures to be developed and, in particular, offers the possibility of obtaining lamellar microstructure with both refined colony size and lamellar spacing[12]. Therefore,

the production of TiAl-based alloys through wrought processing appears promising with respect to the mechanical properties and also from a technical point of view. However, for the production of large size ingot, it is difficult to guarantee the homogeneity of microstructures and even impossible to avoid the macro- and micro- segregation of Al. Furthermore, the processing costs are very high[9, 11, 73].

2.6.2 Near net shape casting (investment casting + HIPping)

Near net shape casting using investment casting followed by hot isostatic pressing (HIPping) or/and heat treatment is a second method for component production. In principle casting offers the most cost-effective route for the production of complex shapes since investment casting is a well established process and if components can be produced to net shape the need for machining is eliminated or very significantly reduced.

2.6.2.1 Investment casting

At present, centrifugal, tilt and counter-gravity casting processes are the most studied and developed techniques for the manufacture of γ-TiAl turbine blades[13]. Fig. 2.10 schematically shows the basic principles of those casting techniques. Centrifugal casting typically provides complete mould filling but with significant turbulence, while the other two techniques offer more quiescent filling.

However, there are several problems in this process that mean the cast component still cannot meet aerospace requirements of reliability and cost[74]. One of the big problems is the high reactivity of molten TiAl-based alloys. To overcome this problem, the majority of titanium alloys including TiAl-based alloys are melted in a water-cooled copper crucible or hearth, therefore the first metal to melt immediately resolidifies on the inside of the copper container and acts as a protective layer for the remainder of the melt. When the molten

metal is eventually cast into a mould, a skin of metal remains in the crucible and is referred to as a 'skull'. Unfortunately, all skull-melting processes result in metal with low superheat since much of the energy is lost to the water-cooled crucible. As a result, it is difficult to fill thin casting moulds and the section thickness often has to be increased and the additional material subsequently removed by machining[74]. Furthermore, when the molten alloy is poured rapidly into a mould the resulting surface turbulence always generates bubbles, which are entrained into the castings where they are readily trapped by the rapidly solidifying metals. As a consequence, the cost of near net shape casting of TiAl alloys would be higher than expected.

2.6.2.2 Hot isostatic pressing (HIPping)

Since it is very difficult to avoid defects such as pores in investment castings, HIPping is required. During HIPping, the components are subject to both elevated temperature and isostatic gas pressure in a high pressure containment vessel[75]. A pressurizing gas is used and the pressure is applied to the material from all directions. The HIPping process can eliminate internal voids and microporosity through a combination of plastic deformation, creep and diffusion bonding[76].

HIP equipment is basically an electric furnace which is contained in a pressure vessel. The most important elements of the HIP equipment include a pressure vessel, furnace, heating elements, pressure system and thermocouples[77]. Fig. 2.11 shows the basic concept of a HIP furnace.

However, HIPping adds a significant cost penalty and furthermore leads to surface sinks because of the collapse of internal porosity, as shown in fig. 2.12(b)[11]. One way to reduce the surface sink problem is by pre-heating the mould in order to improve filling but this leads to slow cooling and to the production of components with large alpha grain sizes and

thus large lamellar length as shown in fig. 2.12 (c). It is well known that large fully lamellar grains give rise to low ductility and to a large scatter in properties and lead to an increased tendency to pre-yield cracking which will be discussed in 2.7. Therefore, it is of great interest to refine the microstructures. Fortunately, a great deal of work has been done to refine the microstructure of cast products. Currently, the most popular way is by addition of boron and there is no doubt that this is an effective technique which was discussed in section 2.4.3. On the other hand, great caution must be taken in the addition of boron and the cooling rate during solidification of castings, because it has been proven that large boride precipitates formed by large amount of boron or by slow cooling are detrimental to the ductility of cast products[46]. Alternative approaches to microstructure refinement in cast products are realised by heat treatments based on the fact that cooling at an appropriate rate from the alpha phase field gives rise to massively transformed gamma. Subsequent aging in the two phase region leads to alpha precipitation on all four {111} in the gamma and very fine microstructure can be formed[78-81]. The aging can be carried out during HIPping.

2.6.3 Powder metallurgy (PM)

Even though near net shape casting can reduce processing cost compared with the wrought route, it still has lots of problems as discussed above, in particular, micro- and macro-segregation and scatter in properties[82, 83]. Powder metallurgy (PM) provides a serious alternative to avoid those problems since the inherently high cooling rate of gas atomisation suppresses segregation and results in uniform compositions of prealloyed powders and also refined microstructures[82, 84-86]. Furthermore, increase of the scale of powder production and improvements in the yield have resulted in substantial manufacturing cost reduction[84], however, compared with near net shape casting tool

systems are needed to manufacture PM components which increase the manufacturing cost significantly.

Generally, powder metallurgy contains two major processing stages, i. e. the production of pre-alloyed powders and the consolidation of those powders. For each stage, there have been many different approaches developed.

2.6.3.1 Production of prealloyed powders

Gas atomisation is the most frequently used technique in producing alloy powders. Since molten TiAl alloys are very aggressive and react with nearly any crucible material and, in addition, the melt, the atomised droplets and the hot powder particles are susceptible to oxygen, nitrogen and carbon pickup, only special techniques such as crucible-free or cold crucible techniques can be employed[82]. An example for a crucible-free technique is the EIGA-technique (Electrode Induction Melting Gas Atomisation), which is schematically illustrated in fig. 2.13 (a). For this technique, pre-alloyed rod is required. The lower end of the rod is dipped into a conical induction coil. The tip of the rod is heated up and the melt drops into the centre of a gas nozzle, where the melt is atomised by Ar gas. At the same time, the rod is rotated at different speeds. When high rotation speed is used, the powder produced in this way is called REP (Rotating Electrode Process) powders. Another example for the powders production is called PIGA-technique (Plasma Melting Induction Guiding Gas Atomisation) which is a cold crucible technique and especially developed in titanium and titanium alloys as shown schematically in fig. 2.13 (b). In this technique the use of ceramic materials could be completely avoided. The properties of TiAl-based alloy powders, for instance the particle size distribution, the impurity level and the closed pores which are filled with atomisation gas which normally is Ar, and the cooling rate are affected by those techniques apart from the intrinsic physical properties of the melt, e.g.

density and temperature which influence the viscosity and surface tension, and the gas flow field which depends e.g. on the geometry of the gas nozzle, the type of atomisation gas and the gas pressure[82]. In addition, the high cooling rate in the atomisation process is one of the advantages of PM, since a high cooling rate promotes high microstructural and chemical homogeneity. However, to guarantee the homogeneity in the powders, the segregation of pre-alloyed rod or liquid should be minimised. Segregation in the pre-alloyed rod can be minimised by using thermomechanically processed feedstock, but some segregation during melting - which will be influenced by the liquidus-solidus gap - is inevitable.

To avoid increase in oxygen and nitrogen prior to compaction, normally the γ-TiAl alloy powders are handled exclusively under inert gas[82]. But inert gas atomised powders usually contain closed pores, which are filled to a certain extent by the gas used for atomisation. Such gas entrapment can be completely avoided by a powder production under vacuum, but the cooling rate is much smaller and the surface will be depleted of Al because of evaporation under such conditions[82].

2.6.3.2 Consolidation of prealloyed powders

For the consolidation of prealloyed γ-TiAl powders, HIPping is one of the main techniques. The alloy powders are filled under inert gas into steel or titanium alloys cans, which subsequently are degassed and sealed gas-tight. The HIPping procedure usually is conducted at temperatures between 1000 to 1300 ℃, pressures between 150 to 200 MPa and holding times ranging from 2 to 4 hours[82].

The facility used for powder HIPping is the same as described in section 2.6.2. The above method is used when a simple shape is required. When a near net shaped complex component is required, there are normally two traditional ways to consolidate the powders.

The first approach is achieved by encasing the powders in a gas-tight container (typically welded sheet metal). Another one is by performing some other consolidation process, such as cold press, to get the powders to a preformed state having a density greater than ~ 92-95 % of theoretical density. This part can then be HIPped without a can (mould) as the part itself can transmit the force to any internal porosity (provided that they are not connected to the surface) and the final densification can be achieved to the theoretical limit[87]. However, during HIPping of powders, the inert gas trapped in the pores of prealloyed powders cannot be removed, and during subsequent heat treatment at high temperatures, thermally induced porosity can develop.

For the near net shape HIPping of a component it is now possible to model the shape change which will occur during densification and the tooling which will define the final shape of the component is designed accordingly. The sacrificial tooling is removed by machining and acid pickling and the fully dense final component produced. With current modelling it is usual to have to use a second iteration and to modify the geometry of the tooling to accommodate any inaccuracies in the component. Any final inaccuracies are designed to be in areas where subsequent machining is straightforward[88-91].

Pre-alloyed powders can also be consolidated by direct hot extrusion[82, 86, 92]. Powder extrusion differs from conventional extrusion only in the need to have a canned perform prior to the extrusion and removing the canning material after extrusion[93]. For the powders of TiAl alloys, normally, the canning material is Ti[86, 94, 95]. During extrusion, the canned powders are pushed or drawn through a die of the desired cross-section. Hot extrusion has the advantages that it can create very complex cross-sections from materials that are brittle, because the materials encounters only compressive and shear stresses.

However, the maximum component size produced in this way is limited by frictional forces, which develop between the powders and die wall during compaction[87].

Sometimes for near net shaped PM components, post heat treatment might be needed to optimize the microstructure and therefore improve the mechanical properties[84]. Moreover, HIPped or extruded powders can be further thermomechanically processed by extruding, forging, sheet rolling etc, to required components[82] and PM samples would exhibit a better hot workability compared with ingot metallurgy (IM) based samples. The reason is in the more uniform and refined microstructure of PM materials[86]. However, the cost of processing is certainly increased in this way.

2.7 Microstructures of TiAl-based alloys

As will be reviewed later, the mechanical properties of TiAl alloys are related to their microstructural characteristics. Therefore, the understanding and controlling of all possible microstructures are of great importance. Traditionally in γ-based two phase TiAl alloys, there are four distinctive final microstructures, near-gamma, duplex, near lamellar and fully lamellar microstructures, as shown in fig. 2.14[50]. These structures are formed when wrought products, near net shape cast parts and other products such as sheet and foil are heat treated under appropriate conditions. Alternatively, TiAl-based alloys can be classified into three groups, i.e. near gamma, duplex and lamellar[82]. However, the following literature review is based on traditional view of four distinctive groups. The factors which influence the microstructures are also summarised.

2.7.1 Microstructural characteristics

2.7.1.1 Near gamma microstructure

A near γ microstructure which is dominated by γ grains, is obtained by annealing at temperatures just above the eutectoid temperature which is around 1200 ℃ according to the Ti-Al binary phase diagram[28]. As-HIPped TiAl powders, which are HIPped below the α transus (T_α), in most cases form near gamma microstructure with equiaxed gamma grains[82, 94, 96].

2.7.1.2 Duplex microstructure

The duplex microstructure is a combination of lamellar and equiaxed grains of different proportions according to the treatment temperature and time and alloy composition, which is typically produced after annealing at temperatures where γ and α phases are approximately equal by volume.

2.7.1.3 Near lamellar microstructure

The near lamellar microstructure is produced by heat treatment at temperatures near the α transus (T_α) for about one hour or slowly cooling after solution treatment in the α phase field[11]. This microstructure consists of plates of α_2 and γ together with some equiaxed γ grains, the volume fraction and size of which depend on the composition and cooling rate. The orientation relationship of the lamellar structure between α_2 and γ phases follows Blackburn OR.

2.7.1.4 Fully lamellar microstructure

The fully lamellar microstructure only contains α_2 and γ plates which have the same orientation relationship as in the near lamellar microstructure and is obtained by heat treatment above T_α for a short time (to limit grain growth)[11] and slowly cooling. It is now established that the formation of the lamellar structure does not occur through a eutectoid

reaction but results from the precipitation of γ lamellae in either a disordered α or ordered α_2 matrix, following one of the two reactions[97, 98]:

(1) $\alpha \rightarrow \alpha_2 \rightarrow \alpha_2 + \gamma$;

(2) $\alpha \rightarrow \alpha + \gamma \rightarrow \alpha_2 + \gamma$

Denquin et al.[99] studied the phase transformation mechanism in two phase TiAl alloys and also found that the formation of the lamellar structure resulted from precipitation of γ lamellae in the α or α_2 matrix. This reaction is achieved through a pre-nucleation stage corresponding to the formation of a local f.c.c type stacking sequence by the movement of Shockley partials and nucleation and growth stages involving both ordering and ledge movement.

The authors further pointed out that longer heat treatment in the (α + γ) or (α_2 + γ) phase field would cause coarsening of the lamellar structures[100]. At first the growth of γ lamellae is through a ledge mechanism. The driving force for the growth is provided by the solute supersaturation, and such a thickening gradually slows down and becomes more and more difficult because of a decrease in ledge mobility associated with the decrease of solute supersaturation. If the supersaturation can be exhausted in spite of such a difficulty, the growth of γ lamellae is brought to completion and further coarsening of lamellar requires a competitive diffusion-assisted growth between two lamellae, maintaining their volume fraction. The driving force for such a coarsening may be provided by a reduction of total interface energy.

2.7.2 Factors influencing the microstructure

2.7.2.1 The effect of cooling rate on the microstructure

The lamellar microstructure can form only when the cooling rate is low enough to allow the γ plates to nucleate and grow. The cooling rate in most castings is rather low, so that most cast TiAl alloys have the typical fully lamellar microstructure. However, when heat treatments in the α phase field are carried out, the resulting microstructure depends on the cooling rate and massive, feathery, Widmanstätten lamellar, lamellar or granular gamma can be produced, as shown in fig. 2.15[68], with decrease of the cooling rate, like oil quenching, air quenching to furnace cooling[68, 98, 101]. Furthermore, at very high cooling rates, the massive transformation can be suppressed by the competing α to α_2 transformation. Even for the lamellar microstructure, fast cooling can produce finer lamellar spacing and smaller grain size.

2.7.2.2 The effect of alloying elements and impurities on the microstructures

- β-stabilisers

Nb, Ta, W, Zr, Mo are β-stabilisers. A large addition of those alloying elements would introduce a third phase, β or B2, in the as-cast lamellar microstructure[102-105]. However, different element has different β stabilisering strength.

- Boron

Since the solubility of boron in both γ phase and α_2 is very small, 0.011±0.006 at.% and <0.003 at. % respectively[106], boride precipitates such as TiB_2[15, 20, 22, 32], Ti_3B_4[16, 21] and TiB with both B_f[17, 21] and B27[17, 18, 20, 21] crystal structures commonly exist in boron-containing TiAl alloys. It has been widely accepted that the addition of a certain amount of

boron can effectively refine the microstructure. The refinement mechanism has been discussed in 2.4.3.

The addition of boron was also reported to suppress the formation of massive gamma[107, 108], which refines the grain size in post heat treatment. Therefore, grain refinement through heat treatment is not favoured by the addition of boron.

- Oxygen, nitrogen and carbon

Oxygen, nitrogen and carbon have higher solubility in the α_2 phase than in the γ phase[109, 110], for example, the oxygen solubility in α_2 and γ phase is (10 - 15) % and (0.025 ± 0.05) %, respectively. Since oxygen is an α and α_2 phase stabilizer[106, 109], for the same alloy system the higher oxygen content always leads to higher α_2 volume fraction[111]. It is also reported that because of the increased stability of α phase, oxygen could suppress the massive transformation[111-113].

2.8 Crystal defects and mechanical properties

2.8.1 Crystal defects and micro-deformation behaviour

TiAl alloys are typical brittle materials, exhibiting little plasticity at ambient temperature. At elevated temperature, TiAl alloys suffer from insufficient creep resistance and structural changes[12]. Such deformation behaviours are associated with dislocation characteristics at ambient and elevated temperature. Thus, the factors governing the multiplication and mobility of the dislocations will be considered.

2.8.1.1 Generation of dislocations and twins

The investigations on the deformation behaviour of TiAl alloys cover a wide range of parameters such as alloy composition, microstructure and deformation temperature. The

deformation behaviour of two phase alloys is mainly confined to the γ-TiAl phase[12]. Deformation of γ-TiAl is closely related to its $L1_0$ structure and occurs exclusively on {111} planes along close-packed directions by ordinary dislocations 1/2<110> and superdislocations 1/2<11$\bar{2}$> and <011>. The γ phase may also deform by twinning along 1/6<11$\bar{2}$>{111}. The potential slip and twinning systems in the γ phase are illustrated in fig. 2.16.

Ordinary 1/2 <110> dislocations have compact core structures[114], which suggests that cross slip and climb are relatively easy. At room temperature multiplication has been found to be associated with jogs in screw dislocations, which were probably generated by cross slip[12, 115]. Since the jogs are immobile in the direction of the motion of screw dislocations, dislocation dipoles are trailed at the jogs and the anchored segments bow out under the applied stress in a fashion similar to a Frank – Read source.

For two phase TiAl alloys with lamellar microstructure, a mechanism common to both low and elevated temperatures is the emission of dislocations from the lamellar interfaces[116]. The process is closely related to mismatch structures and coherency stresses present at semicoherent interfaces. In the case of the α_2/γ interface, the mismatch occurs due to the differences in crystal structure and lattice parameters. Similarly, misfit strains are present across 60° and 120° interfaces of γ variants due to their tetragonality. The coherency stresses are comparable with the yield stress of material and give rise to the formation of loop structures adjacent to the interfaces, as shown in fig. 2.17[12, 117].

Likewise, the lamellar interfaces in lamellar microstructure and grain boundaries of equiaxed materials were found to be prevalent sites for twin nucleation[12, 118]. In addition, several other heterogeneous nucleation mechanisms were also proposed, which basically are related to dissociation of superdislocations[119, 120]. Twins can also nucleate

homogeneously in the defect-free region of the crystal when the interfacial energy is low and very high stresses are present[118].

The observed interface-related twin nucleation and generation of perfect dislocations are beneficial for the material ductility. The mechanisms are, on the other hand, a serious limitation to the structural stability and strength properties at elevated temperature.

TEM observation of the deformation structure of polycrystalline two phase alloys has confirmed that at room temperature glide of ordinary 1/2<110> dislocation is the primary deformation mode, followed by twinning and by glide of <011> superdislocations[115]. This is consistent with their relatively low Peierls stress when compared with superdislocations, but glide along 1/2<110> often occurs simultaneously with true twinning[115]. At sufficiently large strains, all three deformations are thought to operate[121].

2.8.1.2 Mobility of dislocations and the growth of twins

The stress experienced by individual dislocation results from the superposition of the applied stress σ and the stress from internal sources[12]. The coherency stresses existing at the lamellar interfaces of two phases TiAl alloys represent a typical example of internal stress. An effective stress σ* is therefore defined as

$$\sigma^* = \sigma \pm \sigma_\mu \quad (1)$$

Where σ_μ is the internal stress.

For a certain strain rate during deformation, the effective stress σ* is temperature-dependent. Apparently, there are three temperature-related domains in which the micro-mechanisms controlling the dislocation's velocity changes significantly[12, 117, 124, 125]. A detailed analysis[115, 122] has established that in domain I (<500 ℃), the dislocation velocity is controlled by a combined operation of localised pinning, jog dragging and lattice friction.

The dislocation mobility in domain II (500-700 ℃) is speculated to arise from the dynamic interaction of diffusion defects such as impurity atoms with dislocations, but not yet clearly identified. Deformation at elevated temperature (>700 ℃, domain III) is characterized by a diffusion-assisted dislocation climb process.

The lateral growth of twins is also temperature-dependent. At room temperature the twins' structure shows the fully coherent and high perfect nature of shear planes and also plane ledges in the interfaces. These suggest the twins grow through the propagation of Shockley partials[118, 123]. Twins generated at elevated temperatures are often fragmented and exhibit rough interfaces[124, 125]. It is speculated that these structural feature arise from the complex reactions between Shockley partial dislocations and matrix dislocations which have been incorporated into matrix/twin interfaces and the twins appeared to grow by successive formation and bowing out of twinning dislocations from grain boundaries on adjacent {111} planes.

2.8.2 Processing- microstructure- property relationships

2.8.2.1 Tensile properties

- General microstructure-property relationships

It is known that the yield strength of TiAl alloys at room temperature varies from about 350 MPa to 650 MPa, ultimate strength from 400 MPa to 720 MPa, and tensile plastic elongation from 0.2% to 3.5%[50, 126-128].

For a given alloy composition, the tensile properties are strongly dependent on microstructure, grain size and orientation. Generally, duplex microstructure and near lamellar microstructure showed higher yield and ultimate tensile strengths and ductility, which is associated with small grain size[115, 126], as is shown in fig. 2.18. However, with a

similar grain size, the yield strength of duplex TiAl alloys increases with the increase of lamellar volume fraction, but the ductility changes in a contrary way[127].

In wrought lamellar TiAl alloys, decreases in lamellar grain size and lamellar spacing increase both strength and ductility. Kim[129] found the relationship between yield strength and grain size obeyed the Hall-Petch relation, and Cao et al.[130] further pointed out yield strength and lamellar spacing followed the same law.

- Specific characteristics in cast alloys

The ductility-lamellar colony size relationship described above was not always followed in cast TiAl alloys with a lamellar microstructure. Hu et al. found that in the boron-containing cast TiAl alloys, there are two other important factors. The first, in highly-alloyed TiAl alloys, large sized titanium boride precipitates cause premature failure through promoting crack propagation via debonding between boride-matrix interfaces and via cracking through borides precipitates themselves, giving rise to a typical tensile ductility of 0.3%[46]. The second is attributed to those parallel lamellar colonies which may originate from the Burgers alpha grains (obeying Burgers orientation relationship with beta phase) formed during solid phase transformation from β to α. It was suggested that cleavage would occur in those lamellar colonies with parallel lamellar interface simultaneously under certain stress condition to form a cluster of small parallel cracks and the collective effect of the cracks would give rise to low ductility[131].

- Specific characteristics in powder metallurgy (PM) alloys

PM processed samples are reported to have higher strength and ductility than wrought and cast samples, because they possess fine grain size and homogeneous microstructures[85, 95, 96, 132, 133]. Those superior properties were found mainly in samples with a lamellar structure,

especially those that were hot extruded[85, 96]. With the choice of HIP-parameters and a subsequent heat treatment, a variety of different microstructures designated as 'near gamma', 'duplex' and 'near lamellar' can be established[82, 134, 135]. For the as-HIPped powder alloys, microstructure played the most important role in the tensile properties, with lamellar microstructure superior to the others[84, 85, 135]. Table 2.2 illustrates the influence of microstructures on tensile properties of the as-HIPped Ti-46Al-2Cr-2Nb powders[84]. The authors further observed that when microstructural differences were largely eliminated, the influence of HIPping temperature on mechanical properties was small. Heat treatment after HIPping could change both the strength and ductility, but this was attributed to their influence on the microstructure by changing fractions of lamellar colonies, lamellar spacing and grain size, which depend on heat treatment temperature and cooling rate.

The influence of the size distribution of the starting pre-alloyed powders was also studied and it was found that their influence on the properties was very small and it was predominantly the HIPping temperature and heat treatment temperature which governed the grain size of the compact[82, 85, 135].

- The other factors affecting the tensile properties

Orientation: The study of tensile properties on polysynthetically twinned (PST) crystals revealed that the tensile properties strongly depend on the angle θ between lamellar plane {111} and loading axis. PST crystals exhibited the highest strength at $\theta = 90^{\circ}$, however, the ductility at $\theta = 90^{\circ}$ is almost zero. A good balance of strength and ductility is obtained at $\theta = 0^{\circ}$, where strength is not as high as that at $\theta = 90^{\circ}$, but tensile ductility is as large as 5 - 10 % at room temperature. When θ is in the range of 30-60°, the yield stress is much lower and elongation is much higher than $\theta = 0°$ and 90 °[136]. The θ dependence of yield stress and ductility of PST crystals results from the fact that shear occurs parallel to the lamellar

boundaries (deformation termed soft mode) for θ = 30-60 °but it occurs mostly on {111} planes intersecting the lamellar boundaries (deformation termed hard mode) when θ is close to 0 °and 90 °[14], so that slip within α_2 is required for significant ductility.

Alloying elements: The role of alloying elements on the tensile properties is significant. It has been reported that the addition to the same microstructure of Nb[137, 138], V, Mo[50], Ta, Zr, Hf[137] and W[133] could significantly increase the tensile strength by solid-solution strengthening[138]. As stated in section 2.5, Cr, Mn and V have been reported to increase the ductility of TiAl alloys, but the role of other factors, such as grain size was not always clear.

Surface finish: Botten[139] and Thomas et al.[140] studied the influence of machining conditions on the surface of tensile test pieces in cast and powder metallurgy (PM) TiAl alloys respectively, by machining, hand polishing and electropolishing, and found that surface roughness and the residual stress from surface deformation did not make a great contribution to the tensile properties, as shown in fig. 2.19 (a) and (b). Botten found one of the electropolished test pieces had better tensile properties, however, it was not repeatable and conclusive.

Temperature: The tensile ductility of two phase TiAl alloys is characterized by a sharp brittle to ductile transition (T_{bd}) at a temperature range from 620 ℃ to 800 ℃ depending on microstructure as illustrated in fig. 2.20[115]. T_{bd} is lowest for near gamma and duplex microstructure and highest for lamellar microstructure[115, 141]. Below T_{bd}, the ductility remains almost constant and increases steeply with increasing temperature above T_{bd}. The ductility of fine grained duplex, near gamma and fully lamellar microstructure commonly exceeds 30 % at 800, 900 ℃, respectively, when tested at low strain rate ($\leq 10^{-4}$/s). This result already points towards the creep strength being a problem.

2.8.2.2 Fracture toughness

The fracture behaviour of TiAl alloys is known to be very sensitive to microstructure and has been frequently analysed in terms of fracture resistance (K_R) curves. Fig. 2.21 shows the K_R curves reflecting the fracture behaviour of TiAl alloys with different microstructures and at different temperatures[115, 142]. The initiation value which is under plain strain conditions corresponds to the fracture toughness K_{IC}. When tested at room temperature, K_R values of duplex and near gamma microstructures material run almost flat indicating brittle behaviour with little resistance to crack growth or tearing, while the K_R curve behaviour of the polycrystalline fully lamellar alloys suggests crack initiation to be followed by stable crack growth. Fine grained duplex microstructure has K_{IC} values ranging from 10 MPa$\sqrt{m}$ to 16 MPa$\sqrt{m}$, depending on the volume ratio between γ and lamellar grain. Fully lamellar microstructure with randomised colony orientation exhibited remarkably increased fracture toughness values ranging from 20 MPa$\sqrt{m}$ to 40 MPa$\sqrt{m}$[50]. With increasing temperature, the fracture toughness is found to increase continuously for all microstructures and alloys (fig. 2.22[115]), however, fully lamellar microstructure still exhibit better fracture toughness than duplex and near gamma alloys even though its dependence of K_{IC} on temperature is less pronounced.

Obviously, the fully lamellar alloys have a better fracture toughness and more stable crack growth behaviour. Furthermore, the study in both cast and PM lamellar TiAl alloys found that, in general, the fracture toughness increases with decreasing lamellar spacing and with increasing lamellar colony size[129, 133, 143, 144].

However, the dependence on lamellar colony size is more complex. Chan and Kim found when the colony size exceeded around 600 μm the fracture toughness became independent of colony size and appeared to be controlled by lamellar spacing and the colony

orientation[133]. Many researchers also found that coarse grained lamellar materials suffer from a large variability of toughness[115, 145, 146]. The large variability is seen to be caused by the anisotropy of the crack resistance within the lamellar morphology. This has been evidenced from studies on crack propagation parallel and perpendicular to the lamellar boundaries in PST crystals and in the as-cast materials with a preferred orientation of the lamellar colonies. For cracks propagating parallel to the lamellar interfaces, the K_{IC} is low (~12.5 MPa$\sqrt{m}$) and shows a large scatter when compared with cracks propagating perpendicular to the lamellar interfaces, the K_{IC} of which is rather higher (~20-25 MPa$\sqrt{m}$) and the variability small.

For duplex microstructures, intergranular fracture and cleavage are the dominant fracture mechanisms while interfacial delamination, translamellar fracture and decohesion of lamellar colonies are the most important processes in lamellar alloys. The intrinsic brittleness under T_{bd} temperature has been attributed to a combined effect of low cohesion strength, insufficient deformation modes, which can simultaneously operate at a given stress, and low dislocation mobility[12].

Both Campbell[147] and Chan[116] suggested improvement of the fracture toughness in the lamellar microstructure is provided by the presence of uncracked ligaments bridging in the crack wake, which acts to shield the crack tip from the far field loading.

Addition of a certain amount of β-stabilizers, such as Cr or Nb, results in three-phase microstructure and the presence of ductile β/B2 phase may also contribute to the fracture toughness[148].

2.8.2.3 Fatigue properties

2.8.2.3.1 High cycle fatigue (HCF) life

- The influence of microstructure

The S-N curves determined for a K5 alloy (Ti-46.5Al-3Nb-2Cr-0.2W) with duplex and lamellar microstructure are shown in fig. 2.23[149]. In this figure, the duplex microstructure showed a higher fatigue life than the lamellar material in the temperature range 600-870 ℃ because of finer grain size and higher yield and ultimate fracture strength. This is also true for room temperature HCF life[150]. When the applied stress is normalized by ultimate tensile strength (UTS), the duplex and lamellar materials exhibit essentially identical fatigue lives at a given value of the normalized stress. Furthermore, in any case, the fatigue limit at 10^7 cycles is higher than 75 % of the ultimate tensile strength[150].

- The influence of temperature

TiAl alloys have a good retention of fatigue resistance to high temperature as is shown in fig. 2.24, where the ratio between the fatigue strength determined at 10^6 cycles and the ultimate tensile strength is plotted as a function of temperature[150, 151]. This ratio, equal to 0.8 at room temperature, remains higher than 0.7 for temperatures under 700 ℃, which nearly corresponds to the temperature range for planned application.

- The influence of surface finish, notches and defects

The influence of surface finish on the fatigue resistance of TiAl alloys has been widely studied and was shown to be related to surface roughness and residual stress[152-155]. It has been proven that the beneficial effect of compressive residual stress induced by machining can counterbalance the deleterious effect of surface roughness and defects. However, Wu et al.[156], by using acoustic emission, studied the onset of preyield cracking in a Ti-44Al-8Nb-1B alloy prepared with various surface conditions, corresponding to different levels of

residual stress and found that microstructure plays a more important role than surface conditions in determining the onset of surface cracks.

More general investigations on the influence of surface defects, like surface defects induced by electrical discharging machining (EDM), holes of various size produced by EDM and casting defects such as inclusions and surface shrinkage, show that, in the presence of such defects, the fatigue limit value is always higher than 70 % of the baseline value[150, 157]. Thus, the defect-sensitivity of these alloys is not an issue.

2.8.2.3.2 Low cycle fatigue (LCF) life

Hénaff et al. showed that the LCF behaviour of TiAl alloys is influenced by composition and microstructure[150]. According to a series of LCF tests carried out by Recina et al.[158-161], Ti4522XD with near lamellar microstructure presented the highest resistance compared with Ti4722XD (Ti-47Al-2Mn-2Nb + 0.8 vol.% TiB_2) with a duplex microstructure, ABB alloy (Ti-48Al-2W-0.5Si) with a duplex and lamellar microstructure and GE (Ti-48Al-2Cr-2Nb) alloy with a duplex microstructure. Those researches also revealed that samples with a duplex microstructure have a higher LCF resistance than fully lamellar samples below 850 ℃. However, this difference may be due to the difference in grain sizes. It is also concluded that LCF resistance is primarily governed by yield strength, but is also influenced to some extent by ductility[150]. So far the highest resistance is observed for the low aluminium material in samples that have the finest lamellae[150].

2.8.2.3.3 Cyclic deformation behaviour

Deformation behaviour under cyclical condition, first of all, has the same characteristics as discussed in the normal deformation. The plastic deformation depends on the nucleation and multiplication of normal dislocation, twinning and superdislocations[162-165] and the

deformation behaviours are also influenced by microstructure[162, 164], temperature[163], alloying elements[163] and orientation[163-165].

However, apart from those common deformation behaviours, cyclic deformation has its own features. A study on both cast and PM Ti-48Al-2Cr-2Nb alloy with fully lamellar microstructure indicated the room temperature cyclic stress-strain (CSS) behaviour (fig. 2.25) is dependent on the applied total strain amplitude $\Delta\varepsilon_t$[162]. At high $\Delta\varepsilon_t$ value, cyclic strain hardening was observed and the main deformation mode was twinning. At intermediate strain amplitude, where the cyclic strain hardening is moderate, the deformation structure is characterised by a vein-like structure, which consists of walls containing a high density of tangled dislocations and separating channels of low dislocation density where ordinary dislocations can easily glide. For lowest $\Delta\varepsilon_t$, the cyclic stress-strain behaviour is characterised by a hardly noticeable initial hardening followed by a stabilisation of the stress-amplitude. The main deformation substructure in this case is mainly 1/2<110> ordinary dislocations without any particular structure. In stress-controlled fatigue testing, it was found the deformation behaviour was also affected by applied stress amplitude $\Delta\sigma$ with plastic strain energy monotonically increasing as $\Delta\sigma$ rose[165].

Another feature under cyclic deformation was reported that dislocation climb assisted by vacancy diffusion could occur in substructures at temperatures as low as 400 ℃[166].

2.8.2.3.4 Fatigue crack nucleation

Chan[149] suggested that fatigue cracks nucleate at forging defects and casting pores. In the absence of these defects, fatigue cracks initiate at slipbands and grain boundaries. Large boride particles formed by the addition of boron in cast TiAl alloys might be nucleation

sites[46], but they are not the site in a forged alloy[167] or sheet alloy[116] since they are broken down to smaller particles during working.

Like conventional alloys, fatigue crack nucleation in TiAl alloys is sensitive to surface roughness and to the acuteness of notches. Rough surfaces tend to promote crack initiation and lead to reduced fatigue life when compared with specimens with polished surfaces[149].

2.8.2.3.5 Fatigue crack propagation

- Influence of microstructure

Generally speaking, for materials with large cracks (> 5 mm) coarse lamellar microstructures exhibited superior fatigue crack growth (FCG) resistance to samples with a duplex microstructure, which in turn is superior to the equiaxed microstructure[147, 148, 168-170], especially at low load rate. As shown in fig. 2.26[169], the fully lamellar microstructure exhibits a higher growth threshold and a less steep slope. The higher FCG resistance in the lamellar microstructure under cyclic loading is consistent with its superior R – curve behaviour under monotonic loading, as shown in fig. 2.21. However, the refinement in lamellar dimensions, like lamellar colonies and lamellar spacing, did not introduce further improvement in fatigue performance[147]. Furthermore, in the presence of small cracks (<300 μm), the distinction in the fatigue growth resistance of the lamellar and duplex microstructures becomes far less significant[147, 168].

It has been suggested[147, 148] that the enhancement of crack growth resistance of the fully lamellar microstructure is mainly attributed to the extrinsic effects such as crack-tip shielding by crack closure and uncracked ligament bridging. The intrinsic crack growth resistance like lamellar interface sliding may make a small contribution. Due to variations in lamellar colony size and orientation, the variations in the degree of crack-tip shielding

are largely responsible for the differences in fatigue crack growth resistance between the various lamellar microstructures[147]. As regard to the anomalous behaviour of small cracks, it was attributed primarily to a limited role of crack-tip shielding, specifically from closure and uncracked ligament bridging, in cracks with limited wake[147, 168].

Experimental observations have been made[148] which showed that fatigue crack growth occurred by microcrack nucleation, growth and coalescence at the crack tip and the resultant bridge formation in the crack wake, as shown schematically in fig. 2.27. The author further pointed out that the nature of microcracks, their orientation and shape depend on the microstructure. In the case of materials with lamellar colonies, the microcracks may nucleate at an interface or at the lamellar colony boundaries. In samples with an equiaxed microstructure, the microcracks may nucleate at grain boundaries.

Fig. 2.28[150] presents critical defects size for FCG and fracture determined for two typical microstructures (duplex for PM alloy and lamellar for cast alloys) as a function of the maximum stress in the case of a surface defect in a round bar at R=0.1, compared with the same type of data from Ti-6246[171]. It is shown that once a crack starts to grow in the PM alloy, the final failure occurs within a short propagation distance (0.3-1 mm for σ_{max}=200 MPa). In the case of cast lamellar material, the propagation distance between the onset of propagation and final fracture is large, which would make possible the detection of the defect during service before catastrophic failure of the component. The difference is related to their fracture toughness.

- Influence of environment and temperature

It has been widely acknowledged that FCG resistance of TiAl alloys is severely lessened in air compared to vacuum over a wide range of temperature[150, 172-174]. The intrinsic FCG

behaviour (i.e. corrected for crack closure shielding) of a cast Ti-48Al-2Cr-2Nb alloy with lamellar microstructure at different temperatures and environment is shown in fig. 2.29. Indeed, the threshold value in air is lower than that observed in vacuum and above this threshold FCG resistance increases much more rapidly. Furthermore, it can be seen that the near-threshold FCG behaviour in air and in vacuum is almost unaffected when the temperature is raised. This suggests that the fatigue crack growth mechanism in TiAl alloys at elevated temperature is basically the same as in the near-threshold region at low temperature, but the atmospheric environment could strongly enhance crack propagation, even though this effect decreases as the temperature is increased above the brittle to ductile transition[175].

The influence of water vapour and oxygen on the FCG behaviour was also studied at different temperatures[176]. It was found that the near-threshold behaviour in air at elevated temperature in TiAl alloys is controlled by water vapour, not by oxygen, and this effect of water vapour has a nearly constant magnitude in the range of 25-850 ℃. The water vapour effect is reported to be caused by hydrogen embrittlement at the crack tip[177].

2.8.2.4 Creep properties

Design concepts for advanced energy conversion systems and aeroengines require low creep deformation of the components in order to ensure that the clearance between rotating parts and their casings can be kept small[12]. Fully lamellar microstructure in wrought and cast TiAl alloys showed dramatic advantage in creep deformation resistance compared with other microstructures[115, 178-180] and reducing the lamellar spacing reduces the creep rate[12, 72, 181-183], as shown in fig. 2.30 and 2.31 respectively. This was also true for the PM TiAl alloys[96]. The enhancement of creep resistance with lamellar microstructure is related to the lamellar interfaces which can inhibit dislocation glide by reducing gliding

distance[180, 184] and limiting the climb of dislocation segments causing bowing of segments between interfaces[180, 185].

However, as fig. 2.31 shows, fully lamellar TiAl alloys exhibited high primary creep rates. Appel et al. attributed this phenomenon to the relaxation of mismatch structures and coherency stresses present at the interfaces[186]. Creep behaviour studies on many different TiAl alloys with lamellar microstructure also found that the creep curves showed no steady state creep rate, which is mainly associated with microstructural instabilities such as recrystallisation and spheroidisation of α_2 laths[183, 186-188]. The stress exponent in the power-law creep equation ranges from 2.4[182] to 7.6[180, 181]. Observation of the geometry of the 1/2<110> dislocations in the γ lamellae suggested the creep deformation was controlled by dislocation climb at minimum creep rate and high temperature [72, 183]. During the tertiary stage, at lower applied stress, the creep specimen failed by the growth and coalescence of cavities and small cracks formed along α_2/γ interfaces. At highest applied stresses, the specimens failed by nucleation and propagation of cracks.

Additions of niobium[187, 189], tungsten[190], and carbon[187] were reported to improve the creep resistance. The role of Nb addition was attributed to increase the shear stress required to initiate dislocation glide and twinning. Furthermore, the dislocation climb rate may also be reduced due to the low diffusivity of Nb solute[191]. For alloys with tungsten and carbon additions, W-rich β_0 and fine titanium carbides precipitates would block the dislocation emission and motion, therefore reducing the primary creep rate. A serrated grain boundary morphology was also found to contribute strongly to the creep resistance of fully lamellar microstructure[50].

2.9 Oxidation and corrosion resistance

2.9.1 Oxidation and its influence on mechanical properties

2.9.1.1 Oxidation mechanism

Maurice et al.[192] studied the initial stages of oxidation of TiAl alloys at 650℃ at low oxygen pressure and pointed out that the oxidation occurred through three stages. The first stage is a pre-oxidation stage characterised by the absorption of oxygen species. When the subsurface is saturated with dissolved oxygen, the second stage starts leading to the nucleation and growth of an ultrathin alumina layer. The growth of alumina layer leads to Al-depletion in the metallic phase underneath the oxide. When a critical concentration is reached, titanium oxidation occurs. This is the third stage.

Kim et al.[193] studied the long time oxidation behaviour of TiAl alloys at 1100˚C using Pt-marker test and suggested that the growth of oxides scale was by simultaneous outward diffusion of Ti-ions and inward diffusion of oxygen, especially the inward diffusion of oxygen. It is further assumed transport processes occur through TiO_2 and grain boundaries. Transport in α-Al_2O_3 is very small compared with that in TiO_2, and can be neglected[194]. However, in general it is concluded the transport process is dominated by interstitial Ti ions at low oxygen pressure and high temperature and oxygen ion vacancies at high oxygen pressure and low temperature[194, 195]. The dominant point defects in TiO_2 as a function of temperature and oxygen pressure were confirmed by Kofstad[196] and He et al.[197] by thermodynamic calculation, as shown in fig. 2.32.

Dissolution of Al_2O_3 and oxides of other alloying elements can change the transport properties of TiO_2. It is widely recognised that the solubility of Al_2O_3 in TiO_2 decreases

with increasing oxygen pressure, which can only be explained by an interstitial solution of Al ions[198, 199].

- The influence of oxidation temperature and time

Ignoring the effect of ternary and quaternary elements, generally for the Nb-containing TiAl alloys when the oxidation temperature is less than 900 ℃, the weight gain as a function of time was parabolic[193, 200]. A complex oxide layer formed composed of a TiO_2 layer, Al_2O_3 layer, mixed TiO_2 and Al_2O_3 layer, Nb-rich layer and Al-depleted layer successively from the outer surface. However, once the temperature was higher than 1000 ℃, the weight gain as a function of time was linear. In this case, the oxide scale could no longer protect the matrix from further oxidation, because lots of pores and voids formed at the boundaries between the randomly oriented rod-like grains of Ti oxides.

- The influence of alloy composition

Thermodynamic calculations on the oxidation of TiAl alloys in the temperature range 700 ℃ to 1100 ℃ established that the equilibrium oxide products depend on the Al content[201]. Fig. 2.33 is a schematic graph showing the stable oxide products and also the corresponding equilibrium oxygen partial pressure as a function of Al content. In single phase Ti_3Al and Ti-rich two phase TiAl + $TiAl_3$ composition range, the partial pressure for the formation of Al_2O_3 is higher than that required for the formation of TiO, thus stabilising TiO over Al_2O_3; however, in Al-rich TiAl + $TiAl_3$ composition range, the partial pressure for the formation of TiO is 3-4 orders of magnitude greater than that required for the formation of Al_2O_3, resulting in the termination of oxidation of Ti and initiation of Al_2O_3 formation.

Alloying elements in TiAl alloys also have a significant influence on oxidation resistance. Nb is one of the most frequently used elements to improve TiAl alloys' oxidation property. The mechanism will be discussed later.

- The influence of oxygen partial pressure and environmental atmosphere

At any temperature each metal-oxide system has its own equilibrium oxygen partial pressure, below which oxidation will not occur and above which oxidation occurs so that oxides will form. Fig. 2.35 shows the possible oxidation products and their own equilibrium oxygen partial pressures against Al content at 900 ℃[201]. Fig. 2.36 is the Ellingham diagram showing the equilibrium oxygen partial pressure for the oxidation of pure Ti and pure Al as a function of temperature[202].

Overall, the equilibrium oxygen partial pressure for the oxidation of TiAl alloys is very low, below 1×10^{-24} atm. This means that oxidation of TiAl alloys is almost unavoidable when exposed to the air no matter what the temperature is. However, the stability of various oxides is different. The lower equilibrium oxygen partial pressure the oxides have, the more stable they are. As discussed above, the stability of Ti oxides and Al_2O_3 depends on the alloy compositions, but for the Ti oxides their stability increases from TiO to TiO_2 with increase in oxygen partial pressure.

Many authors observed a higher oxidation rate of TiAl alloys in air compared with that in oxygen, therefore, nitrogen is suspected to be involved in the oxidation process and to have a negative effect[203, 204], however, the opposite effect was also found in Nb-containing TiAl alloys[198, 199]. The role of nitrogen in the oxidation process is not clear, but both negative and positive effects were assumed to be related to the formation of nitride layer which might prevent or favour the formation of protective Al_2O_3 layer.

- The influence of surface preparation

It has been found[204] that when TiAl alloys are exposed in oxygen the abraded surface has a better oxidation resistance than the fine polished surface has at 900 ℃. It was suggested that the improvement in oxidation resistance is because recrystallisation can promote the formation of an alumina film in oxygen by enhancing diffusion via short circuits within the deformed alloy surface. At temperatures higher than 1000 ℃, the effect of surface finish is masked by overall rapid oxidation due to nodule growth. Therefore, in terms of oxidation, the surface preparation should not be a problem when the oxidation temperature is higher than 1000 ℃. When TiAl alloys are exposed to air, no surface-finish effect exists. The reason was attributed to the nitrogen-effect discussed above, precluding the formation of an alumina layer.

- The influence of microstructure

Gil et al.[205] studied several TiAl alloys with different microstructures and found the oxidation behaviour is significantly affected by the composition and the distribution of the phases in the alloy, as well as by the overall alloy composition. A fine lamellar distribution of α_2 and γ has a favourable effect on the alloy's oxidation behaviour. It is suggested that if the α_2, which has a low-Al content, is finely dispersed within the gamma matrix, the oxidation behaviour is governed by alumina formation on the γ phase.

A physical model of the oxidation process in two phase TiAl alloys proposed by Kekare et al. is illustrated in fig. 2.34[206]. In the early stages of oxidation, isolated islands of oxides are formed. Since the kinetics of Ti oxides formation are typically greater than that of Al_2O_3 formation, the metal surface is rapidly covered with a thin layer of Ti oxides. As a continuous outer oxide scale of Ti oxide is formed, its exposure to air in the absence of Al

will convert all the transient Ti oxides, such as TiO, Ti_2O_3 and Ti_3O_5, to pure TiO_2. But as the TiO_2 layer is formed, Al is enriched underneath this layer initiating the oxidation of Al and finally forming an Al_2O_3-rich layer underneath the outer TiO_2 layer. Once the outer layer of TiO_2 and the inner layer of Al_2O_3 are sufficiently thick, the oxidation proceeds by diffusion of oxygen into the scale and outward diffusion of Ti ions. This leads to two possibilities. The first is the formation of alternate channels of TiO_2 and a mixture of Al_2O_3 and TiO_2 oxides. The other possibility is the formation of a mixture of TiO_2 and Al_2O_3 in the interior. Simultaneously it can be seen that an Al-depletion layer is formed at the oxide-metal interfaces. The formation of this Al-depleted layer is due to the oxidation of Al from the alloy to the intermediate layers and the dissolution of oxygen in $\alpha(\alpha_2)$ grains. However, there is no direct proof that the Al is always preferentially oxidised in the metal/oxides interface, and even it is so, no mechanism can be found to explain it. Actually, the subsurface between oxides scale and metal phases was not always Al-depleted. Al-rich subsurface was also discovered after oxidation which will be reviewed in section 2.9.2.

2.9.1.2 The influence of oxidation on properties

A study by Kelly et al.[207] on cast Ti-48Al-2Cr-2Nb alloy showed a reduction of both strength and ductility below 200 ℃ after exposure at 649 ℃ in air for 16 hours. However, no reduction was found when the tensile testing was carried out in Ar. As a result, the authors suggested that the reduction was due to the formation of a brittle surface layer, which produces small cracks during tensile testing in the presence of atmospheric moisture.

Pather et al.[208] investigated cast Ti-46Al-2W alloy and extruded Ti-46Al-5Nb-1W alloy and found that over 70 % of the ambient temperature ductility was lost after exposure at 700 ℃ for even 2 hours in both air and vacuum. For the room temperature property

reductions, several possibilities were proposed, including changes in the surface residual stress state, oxygen or hydrogen embrittlement, etc.

A similar ductility reduction was reported by Thomas et al.[140] in a study of PM Ti-47Al-2Cr-2Nb alloy with near gamma microstructure when the tensile test pieces were exposed in air at 700 ℃ up to 400 hours and the authors also found that tensile properties were not really affected by the surface machining conditions.

Draper et al.[209] investigated the influence of the environment during thermal exposure on the tensile properties of extruded Ti-45Al-5Nb-B-C alloy and found that exposure at 700-800 ℃ up to 200 hours either in Ar, in air, or in high-purity oxygen resulted in a loss of room temperature ductility with the extent of the reduction in ductility increasing with oxygen content in the environment. No difference in tensile ductility was found between samples tested in Ar and those tested in air for these exposed samples. Furthermore, the fracture toughness was also reduced at temperatures up to 650 ℃, but the fatigue strength was unaffected after the same exposure. The embrittlement was suggested to be due to the diffusion of oxygen into the alloy, but how the diffusion of oxygen affects the brittleness was not explained, although oxygen is known to reduce ductility.

Wu et al.[210] also found oxidation-induced embrittlement of TiAl alloys after thermal exposure at 700 ℃. An example of tensile properties between the test pieces with and without thermal exposure is listed in table 2.3. The authors proposed that the embrittlement may be caused by: (i) the tensile stress induced by the oxygen-rich region and (ii) the corresponding ease of crack nucleation in this region.

A significant drop in mechanical properties, especially the ductility, at both room temperature and high temperature was also reported by others[140, 211]. In several of these

papers it was shown that the bulk microstructure was stable, and the ductility can be restored after the oxygen-influenced layer was removed, therefore, it is clear that the tensile ductility degradation after exposure is directly related to the formation of surface layers. Unfortunately, there is no general agreement of the mechanism of embrittlement.

2.9.2 Near-surface microstructure change during thermal exposure

As discussed in 2.9.1, the near-surface microstructure can be changed during thermal exposure either in air or in other gases such as argon. Ramanujan et al.[212] studied the near-surface microstructures of Ti-47Al-X alloys vacuum aged from 800 ℃ to 1200 ℃ for 168 hours, in which the bulk material had lamellar microstructure. They found that annealing at 800 ºC resulted in fine recrystallised grains and at 1200 ºC, primarily α grains. After aging at 1000 ℃, the edge of samples formed a layer of α grains, and deeper beneath this surface layer, a thick layer of equiaxed γ grains was found. However, the near-surface microstructure was affected by alloying elements with W stabilizing the matrix lamellar microstructure. The formation of an α layer was attributed to the loss of Al during aging in vacuum and the formation of equiaxed γ grains to recrystallisation because of surface deformation during cutting.

A similar Al-depleted surface layer was found after tensile testing Ti-47.3Al-1.9Nb-1.6Cr-0.5Si-0.4Mn at 1280 ℃[213], in vacuum and argon. Annealing of Ti-45Al-2Mn-2Nb at 1200 ℃ in argon was also reported to result in an Al-depleted surface layer, as shown in fig. 2.38[214]. The authors proposed that this kind of surface layer was due to vapourisation of Al during testing or annealing. It is known that Al has a relatively high vapour pressure compared with Ti[215].

Xia et al.[216, 217] and Yang et al.[200] studied the oxidation behaviour of Ti-48Al-2Nb-2Cr-1B at 800-850 ℃ and Ti-47Al-5Nb at 900 ℃, respectively. Both of them found that an Al-rich layer was formed in the near-surface underneath the surface oxide scale. However, no details were reported either on the crystal structures of these layers or how they were formed.

Draper[209] studied the microstructural changes in detail in the near-surface after thermal exposure of Ti-45Al-5Nb-B-C and pointed out that after exposure at 800 ℃ for 200 hours in air and argon, a nearly pure γ-grain layer formed in the near-surface beneath the surface oxide layers. However, if the sample was exposed at 800 ℃ for 200 hours in pure oxygen, an α_2-rich layer formed in the near surface, instead of a γ-grain layer. The surface microstructures of those cases are illustrated in fig. 2.39. Unfortunately, no explanations were given for the formation of those surface layers.

Many investigators have reported that a Z-$Ti_5Al_3O_2$ phase[218-223] is formed during studies of various Al-depleted sub-surface layers formed after thermal exposure of TiAl alloys, This phase has been confirmed by the studies on the Ti-Al-O ternary phase diagram[218, 224, 225]; it has a cubic structure with a lattice parameter of 0.69 nm and is based on the space group P432. It is proposed that the Z-phase derives from the reaction between γ-TiAl and the dissolved oxygen[219].

2.9.3 Corrosion properties

2.9.3.1 Corrosion properties of single α_2 and γ phase at room temperature

Several researchers have reported the corrosion behaviour of single α_2 and γ phase in aqueous solution, of NaCl, HCl, H_2SO_4, HNO_3 and NaOH[225-228]. Those researchers showed that the corrosion behaviour of titanium aluminides is related closely to the bulk

compositions and corrosion solutions. For instance, Saffarion et al. showed that α_2 and γ can passivate in sodium sulphate (Na_2SO_4). In NaCl solutions, however, both phases are susceptible to pitting. The pitting potential (E_{pit}) decreased with increasing Al-content (i.e., α_2-Ti_3Al has higher E_{pit} and, therefore, a greater resistance to pitting than γ-TiAl).

Lee, et al.[225] investigated the corrosion behaviour of single α_2 for 3 weeks at 35 ℃ in salt fog which is 5 % NaCl solution and suggested the corrosion mechanism of α_2 in this case is the dissolution of Al and oxidation of Ti.

2.9.3.2 Corrosion properties of two phase TiAl alloys at high temperature

The corrosion behaviour of two phase TiAl alloys at high temperature seems to be very different from that of the single phase at room temperature. Du, et al.[229] investigated the corrosion behaviour of several TiAl alloys with different Al and Nb contents in $H_2/H_2S/H_2O$ environments which yielded high sulphur ($Ps_2 \sim 6.8\times10^{-1}$ Pa) and low oxygen ($P_{O2} \sim 1.2\times10^{-15}$ Pa) potential at 850 ℃. They found that the corrosion-resistance was increased with increase of Al and Nb content. After corrosion, a multilayered scale formed on all materials. The outer oxide layers were composed of alternate TiO_2 and Al_2O_3 with the Al_2O_3 layer underneath the TiO_2 layer. Both thermodynamic and kinetic calculations demonstrate that TiO_2 would be the expected product when these alloys are exposed to $H_2/H_2S/H_2O$ environment at 850 ℃. Just as for the oxidation mechanism discussed before, the development of TiO_2 led to the depletion of Ti and increase in Al activity beneath the TiO_2 layer, which promoted the formation of an Al_2O_3 layer by the ingress of oxygen through the TiO_2 layer. As the corrosion time increased, $NbAl_3$ and TiS layer develop with the accumulation of Nb and S between the oxides and metal interface and the alternate change in the Al and Ti activities.

Tang et al.[230] found that when Ti-50Al was corroded in (K, Na)SO_4 melts at 900 ℃ for 100 hours, a continuous Al_2O_3 scale was formed which was suggested to be due to the low oxygen pressure environment, high Al content and the absence of the detrimental effect of nitrogen. However, in some regions complex corrosion products formed which was due to non-uniformity of microstructure since α_2 may exist in some regions in this alloy. In addition, TiS and an Al-rich layer of $TiAl_3$ formed near the surface. However, neither continuous Al_2O_3 scale nor sulphide was observed on the scale on Ti-48Al-2Cr-2Nb, which was attributed to its higher α_2 content and more dense oxide scale which could prevent salt penetrating through the scale. Ti-50Al-10Cr formed adherent Al_2O_3 scale with no TiO_2 nodules and exhibited excellent hot corrosion resistance in the same corrosion condition. In addition, many investigations[211, 230, 231] found the addition of NaCl could significantly accelerate the corrosion of TiAl alloys, since Al_2O_3 and TiO_2 can react with NaCl as follows:

$$4NaCl + 2Al_2O_3 + O_2 \rightarrow 4NaAlO_2 + 2Cl_2$$

$$2NaCl + 2TiO_2 + 2O_2 \rightarrow 2NaTiO_4 + Cl_2$$

The Cl_2 is able to penetrate through oxide scales quickly through cracks or pores and react with Ti and Al directly on the alloy surface to form volatile chlorides:

$$Ti + Cl_2 \rightarrow TiCl_2$$

$$2Al + 3Cl_2 \rightarrow 2AlCl_3$$

The volatile chlorides may diffuse outward through cracks and pores to the outer surface. At the surface of scales, where the oxygen pressure is high, the chlorides may re-oxidize:

$$TiCl_2 + O_2 \rightarrow TiO_2 + Cl_2$$

$$4AlCl_3 + 3O_2 \rightarrow 2Al_2O_3 + 6Cl_2$$

Cl_2 is then regenerated and is able to diffuse into the alloy surface. Based on this mechanism, the corrosion process is self-sustaining and chlorides just act as catalysts. At the scale-alloy interface, the Ti and Al are consumed in the process and, in the meantime, pits may initiate on the alloy surface.

According to the surface structures after hot corrosion, apparently, oxidation occurs during hot corrosion, but the corrosion products are affected by the alloy composition and corrosion solutions.

2.9.3.3 The influence of hot corrosion on properties

The influence of hot corrosion on mechanical properties has not been widely reported in the literature. The research carried out by Bacos et al.[211] shows that hot corrosion could degrade the high temperature (700 and 800 ℃) tensile properties, especially the ductility, of Ti-46.5Al-4(Cr, Nb, Ta, B) and Ti-45Al-X(Nb, B,C) when those alloys were exposed to Na_2SO_4 + NaCl or pure NaCl at 750 ℃ for 1000 hours. One example of the results is shown in fig. 2.37. It was suggested that the origin of the brittleness after hot corrosion might be either an oxide layer which could generate cracks from the surface or an excessive solid solution hardening due to oxygen diffusion.

2.10 Ti4522XD alloy

Ti4522XD is the main alloy used in the research in this thesis and is an established commercially available TiAl alloy, with a nominal composition of Ti-45Al-2Mn-2Nb-1B (at.%) composed of (α_2 + γ) two phases. XD is a term that is used to refer to an exothermic process where ceramic particles such as borides, carbides, nitrides and silicides may be formed in situ in a molten metal, but now it is only a trade mark of Martin Matietta

Corporation, Bethesda, MD[147, 232]. High specific tensile and fatigue strength, fire resistance as well as inherent castability and consistent properties due to its XD grain refinement make Ti4522XD alloy very attractive for a number of different aero-engine components[233-235].

2.10.1 Alloy composition and effect of alloying elements

The addition of alloying elements like Mn and Nb, and the minor element B play an important role in the alloy's properties. The impurity level of oxygen is also important in terms of its influence on properties.

2.10.1.1 Niobium

- Increase of strength

The addition of Nb was found to enhance the tensile strength of TiAl alloys up to 900 ℃[138]. These high strengths were suggested to arise from the solid solution hardening of Nb. The hardening effect of Nb was found to be dependent on the Al content of the γ phase, being less significant in the γ phase containing higher aluminium.

- Increase of oxidation resistance

The addition of Nb to TiAl alloys is widely acknowledged to improve the oxidation resistance[236-238]. However, the improvement is decreased when the oxidation temperature is higher than 900 ℃. In addition, if the Nb content is too high in TiAl alloys, the oxidation resistance could be decreased by the formation of $TiNb_2O_7$ or $AlNbO_4$[239]. The possible mechanism for the improvement of oxidation resistance by the addition of Nb can be summarized as:

(a) Nb has a valency of 5 and therefore, can potentially annihilate doubly ionized oxygen vacancies and hence reduce the kinetics of oxidation by reducing the kinetics of oxygen diffusion.

(b) The addition of Nb is reported to reduce the difference of the coefficient of the thermal expansion (CTE) between the oxide scale and the alloy.

(c) Nb addition promotes the formation of TiN in the oxide scales and Nb-enriched diffusion layer between oxide scales and the substrate, impeding the diffusion of oxygen and titanium.

- Increase of corrosion resistance

Nb has also been established to increase the corrosion and pitting resistance in some acid and neutral chloride solutions at both room temperature[225] and high temperature[229].

The benefits of Nb are attributed to:

(a) Nb ions replace Ti ions in TiO_2 leading to a decrease in oxygen vacancies, which slows the diffusion of oxygen;

(b) Nb increases the thermodynamic activity of Al relative to that of Ti, which promotes the formation of a stable alumina scale;

(c) Nb reduces the solubility of oxygen in the alloy, thus retarding the internal oxidation of the alloys.

To some extent, the proposed mechanisms for the corrosion resistance of TiAl alloys by the addition of Nb are similar to those proposed for the improved oxidation resistance, particularly in the oxygen diffusion-controlled mechanism. However, the presence of an excess of Nb was reported to increase the corrosion rate, since the formation of acid oxide

Nb_2O_5 increases local acidity and then induces the acidic dissolution of Al_2O_3, and Cr_2O_3 if it exists[230].

2.10.1.2 Manganese

Manganese is reported to increase the ductility of TiAl alloys with lamellar microstructure[52]. It is speculated that the addition of Mn to binary, two phase alloys may reduce the aluminium content in the γ phase, thus increasing the metallic bonding in γ-TiAl, which may be responsible for the increased ductility[240]. Experimental observations carried out by Tokuzou et al.[52] found that addition of Mn to the binary Ti-Al alloys decreased the c value in the γ crystal lattice which suggests that the covalent-like bonding can be weakened. The authors also found that the addition of Mn promoted the generation of deformation twins. Calculations of the change of electronic structure[54, 55] and site occupancy[57] supported the idea that a small addition of Mn could increase the metallic bonding in γ-TiAl and thus, enhance the ductility of two phase TiAl alloys. However, larger additions of Mn did not further improve properties[52].

2.10.1.3 Boron

Boron has a beneficial effect on tensile strength and ductility[137, 241], and reduces hydrogen-induced embrittlement[241], but most importantly refines the grain size as discussed in section 2.4.3. In terms of grain refinement of Ti4522XD alloy, since it contains 1 at.% boron and 45 at.% Al, the refinement mechanism is best fitted to the mechanism proposed by Cheng[17] which is related to constitutional supercooling, however, a new mechanism for the grain refinement of Ti4522XD will be proposed in the thesis. The refinement of grain size would improve the mechanical properties as discussed in section 2.8.2.

2.10.1.4 Oxygen

Apart from the influence of oxygen on the microstructures as described in section 2.7.2, Morris[242] observed that two phase TiAl alloys with low oxygen content had a better tensile ductility and lower strength, which was due to better mobility of ordinary 1/2<110> dislocation in the γ phase at all temperatures. By contrast, alloys with high oxygen content deformed by superdislocations and were brittle at room temperature, but they became more ductile at temperatures at which ordinary dislocation became active. Therefore, the author concluded that increasing the oxygen content would reduce two phase TiAl alloys' ductility by inhibiting the activity of ordinary 1/2<110> dislocation in γ phase at room temperature, and further suggested that the pinning of dislocations by oxygen atoms in solution was the controlling mechanism responsible for the deformation process. Excess oxygen concentration could give rise to oxide precipitates which could increase the strength if dislocations bypass them by an Orowan mechanism, however, the ductility could be harmed. In addition, for two phase TiAl alloys with overall low oxygen content, a lower oxygen content in γ phase may be due to the internal gettering of the interstitial oxygen by the α_2 phase[243]. Given the detrimental effect on the room temperature ductility, it is important to keep oxygen content at a low level.

2.10.2 Processing-microstructure-properties relationship

In terms of making a component from Ti4522XD alloy, either by investment casting or by production of powder particles, the original ingot is made through the XD process. The XD (sometimes it is called XD^{TM}) process utilizes an Al-TiB_2 master alloy material, which, added to the base alloy melt, produces a fine dispersion of TiB_2 particles[234, 244]. However, acicular TiB particles were also identified in cast Ti4522XD alloy[244, 245].

For investment cast of Ti4522XD, HIPping and post HIP heat treatment are normally used to close the internal porosity and stabilise the microstructure. The typical HIPping conditions for this alloy were 1185-1260 ℃ at 170-175 MPa for 4 hours[154, 234, 244, 246-249]. However, the as-HIPped products exhibited equiaxed γ grains in the regions where the pores existed in the as-cast conditions because extensive plastic deformation occurred there leading to recrystallisation. These transformed equiaxed γ grains have a detrimental effect on fatigue crack initiation[234, 246]. Heat treatment after HIPping has a significant effect on the stability of the lamellar microstructure. Seo et al.[246] measured the α transus of Ti-45Al-2Mn-2Nb-0.8 vol.% TiB_2 to be 1310 ℃ and found that a fully lamellar microstructure could be obtained as long as the heat treatment temperature was above the α transus. However, equiaxed γ grains began to appear in specimens heat treated below 1310 ℃ and the volume fraction of equiaxed γ grains increased as the heat treatment temperature decreased. Heat treatment time had little influence on the microstructure except for treatments longer than 24 hours. Increasing the cooling rate by oil quenching decreased the lamellar spacing and grain size, whilst depressing the formation of Widmanstätten, but most of the lamellar colony boundaries were planar after oil quenching, while slower cooling such as air cooling and furnace cooling resulted in many interlocked lamellar colony boundaries. The author attributed this to higher α → lamellar transformation temperature. For the lamellar microstructure formed during air cooling, aging at 800-900 ℃ for more than 24 hours resulted in little change in γ thickness, while the α_2 thickness slightly decreased after aging. However, it was observed[244] that for the lamellar microstructure which was obtained by oil quenching, both the α_2 volume fraction and the thickness of α_2 lamellar were reduced significantly after aging in the same conditions. On the other hand, aging had the opposite effect on γ lamellae. TEM investigation on the

microstructures of those 800 ℃ and multiple step aged specimens found the dissolution of α_2 lamellar and coarsening of γ lamellar is due to movements of the ledges in α_2 and γ phases along the α_2/γ interfaces, but increasing aging temperature to 900 ℃ resulted in the dissolution of α_2 lamellar perpendicular to the α_2/γ interfaces, and therefore the break-up of α_2 lamellar and formation of discontinuous α_2/γ interfaces, which is detrimental to creep properties.

For the stabilized and randomly orientated lamellar microstructure, Ti4522XD exhibited good mechanical properties. Voice et al.[235] investigated cast and HIPped bars and showed that the 0.2 % proof stress, the UTS and the elongation could reach 550 MPa, 680 MPa and 1.4 %, respectively, at room temperature for samples with a near lamellar microstructure. Those properties at 650 ℃ were 440 MPa, 610 MPa and 2.0 %, respectively. The equiaxed γ grains formed during HIPping showed little influence on the room temperature tensile properties, but reduced UTS and elongation at 650 ℃, and particularly creep resistance.

As discussed earlier, aging could stabilise the microstructure by converting an unstable α_2 to γ phase. The aging experiment carried out by Voice et al.[235] demonstrated that aging at 1010 ℃ could aid the creep resistance and increase 0.2 % proof stress between 25 to 750 ℃. Given the application temperature, cost and mechanical performance, the author recommended the optimised aging time is 8 hours at 1010 ℃.

Thermal exposure experiments between 650 to750 ℃ found that surface oxidation caused little reduction in proof stress, but could reduce creep resistance and fatigue performance. For instance, after thermal exposure at 650 ℃ and 750 ℃ for 1000 hours, HCF fatigue strength was reduced from 485 MPa to 455 MPa at ambient temperature and was reduced from 475 MPa to about 400 MPa at 650 ℃. Therefore, it was also recommended that for

application as compressor blades and turbine blades, for which fatigue life is critical, the operation temperatures are restricted to <650 ℃[235].

Lee et al. [250] studied the oxidation behaviour Ti4522XD from 800 to 1000 ℃ in air for 50 hours and found that the oxide scale consisted primarily of an outer TiO_2 layer, an intermediate Al_2O_3-rich layer, and an inner (TiO_2 + Al_2O_3) mixed layer. Mn and Nb tended to segregate at the outer TiO_2 layer and inner (TiO_2 + Al_2O_3) mixed layer, respectively. The outer layer grew primarily by outward diffusion of Ti and Mn, and the inner mixed layer by the inward transport of oxygen. Dispersoids of TiB_2 oxidised to semiprotective TiO_2 and highly volatile B_2O_3 which evaporated.

In summary, despite the attractive properties of Ti4522XD alloy, before near net shaped cast Ti4522XD can be produced on an industrial scale for application in a gas turbine engine, several problems have to be addressed[235]:

1. The casting techniques need to be modified to ensure that porosity is either minimised or contained within a non critical part of the component.
2. The microstructure should be stabilized before the high temperature application
3. Oxidation resistance at the applied temperature needs to be improved.

2.11 Background and aims of the project

As discussed above, near net shaped casting of Ti4522XD is very promising from the industrial point of view in terms of properties. Moreover, near net shape casting is cost-efficient, and Ti4522XD is a commercially mature alloy. Therefore, Roll-Royce is going to apply this alloy in the low pressure (LP) turbine blades in jet engines in the near future. However, the universal problem of porosity of as-cast products also exists in the near net

shape cast Ti4522XD turbine blades. As a consequence, HIPping has to be used to remove these internal porosities. But before this material and this processing technology are put into practical industrial application, it is of great importance to control the as-cast microstructure and to have a complete understanding of the influence of HIPping on the microstructures and properties of Ti4522XD castings.

The as-cast microstructures are directly related to the casting conditions, however, in order to control and to optimise the as-cast microstructure it is necessary to understand the solidification behaviour of the alloy. In terms of solidification behaviour of Ti4522XD alloy, it is important to know about its solidification route, the influence of the addition of boron and the influence of cooling rate. Therefore, these aspects are widely studied in this thesis. In addition, since the addition of boron plays such an important role in the solidification of Ti4522XD alloy, the solidification behaviour of borides themselves are also studied.

The microstructure and properties of cast plus HIPped Ti4522XD casting have been well investigated[233], but in all previous work test-pieces have been machined from the HIPped samples and thus no data has been obtained concerning the influence of the as-HIPped surface on properties. If investment casting is to be a cost-effective process-route it is essential that only very limited machining will be required and thus that the as-HIPped surface (or near-surface) of components will be retained in the final component. The data reviewed above has shown that exposure to virtually all atmospheres to temperatures as low as 700 ℃ can result in significant degradation of the properties of TiAl-based alloys and it is therefore vital that the influence of the HIPping process is investigated and the nature of any changes in the surface of the HIPped samples understood. Recent work has in fact shown that Ti4522XD castings form complex surface microstructures after HIPping as

would be expected in view of the fact that heat treating in argon, the gas used in HIPping, leads to embrittlement associated with changes on the surface[209]. Unfortunately, as has been noted above, although there is a significant amount of data concerning the changes in properties associated with changes induced by high temperature exposure to different atmospheres, there is no understanding of the mechanisms causing these changes. It is therefore important to carry out an in-depth investigation of the near-surface microstructural changes caused by HIPping and the associated changes in properties of Ti4522XD so that net shape cast blades can be HIPped which have acceptable properties and that the nature and significance of any surface layers are understood.

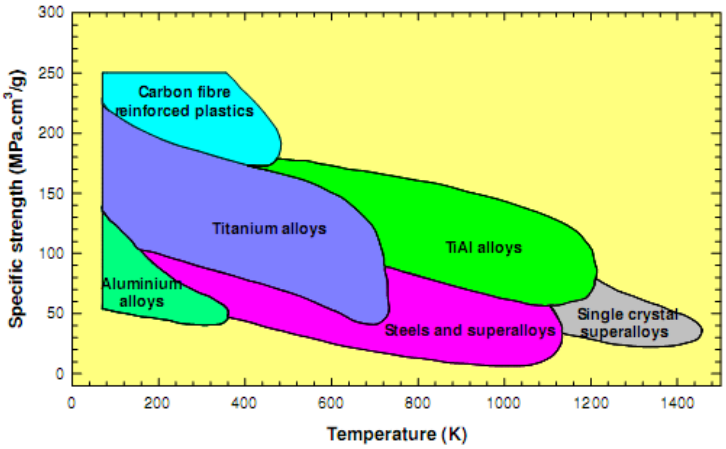

Figure 2.1 Temperature dependence of specific strength of various groups of alloys[9].

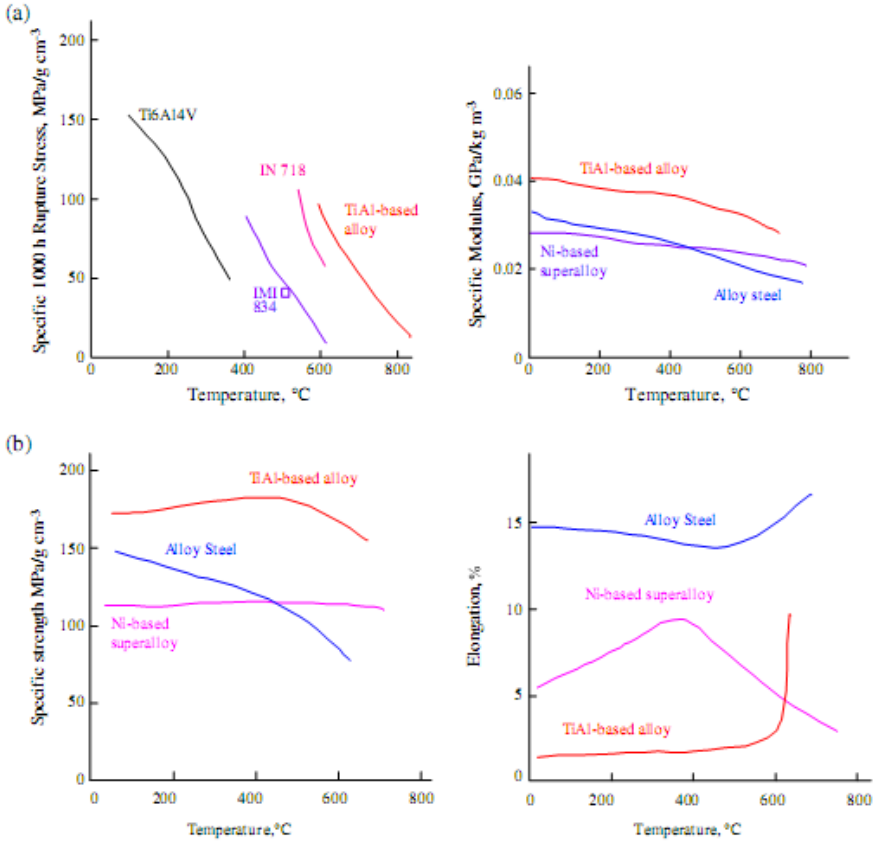

Figure 2.2 (a) 1000h rupture strength and specific modulus as a function of temperature for a TiAl-based alloy, Ti834, IN 718 and Ti6Al4V and (b) specific strength and ductility as function of temperature for an alloy steel, a Ni-based alloy and TiAl-based alloy[11].

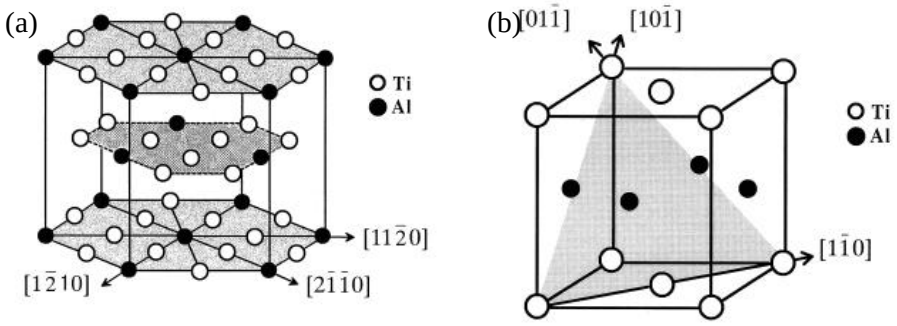

Figure 2.3 Crystal structure of (a) Ti_3Al; (b)TiAl[14].

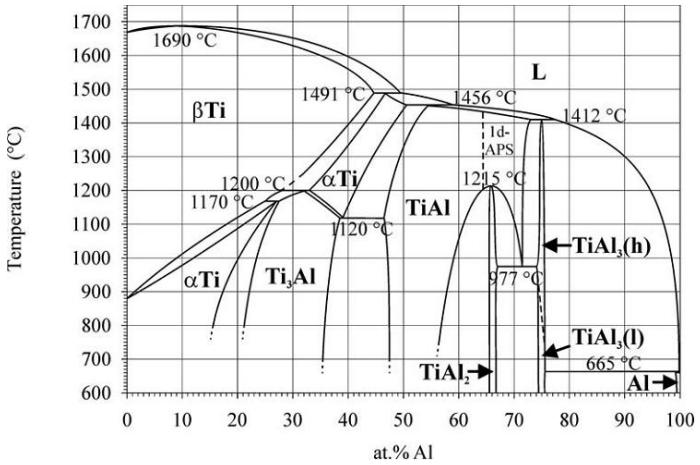

Figure 2.4 Ti-Al binary phase diagram published by Schuster in 2006[28].

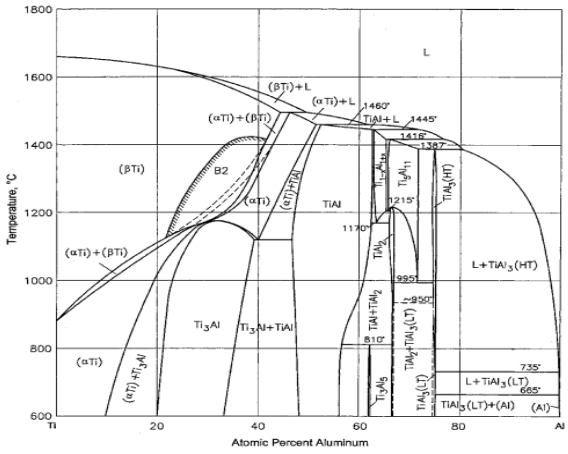

Figure 2.5 Ti-Al binary phase diagram published by Raghavan in 2005[29].

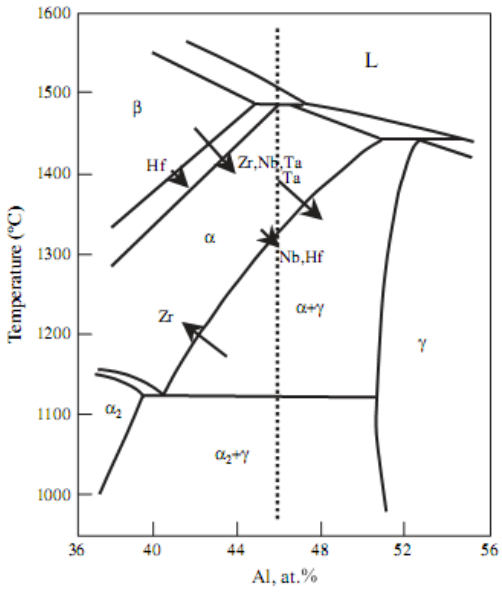

Figure 2.6 Section of the Ti-Al phase diagram. The arrows indicate the sense of movement of the phase boundaries for ternary alloying additions[11].

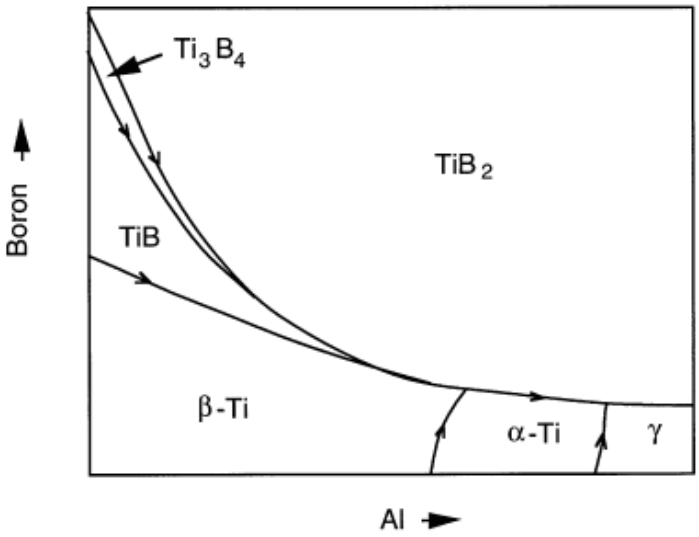

Figure 2.7 Schematic illustration of liquidus projection of the ternary Ti-Al-B system[20]. (based on Refs.[31] and[32])

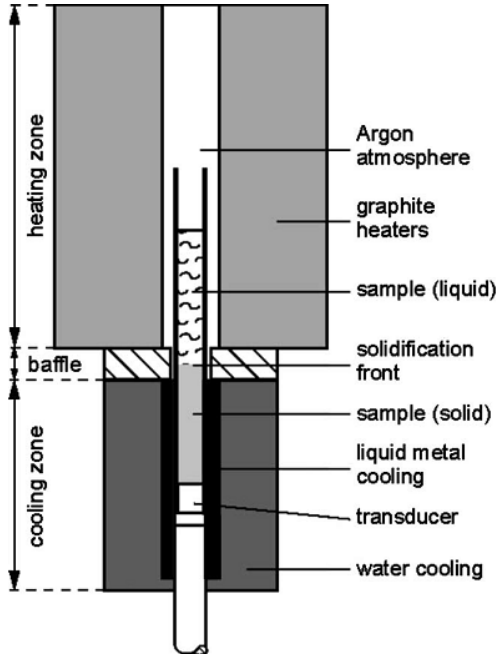

Figure 2.8 Schematic of a Bridgman-type furnace. The isolating zone (baffle) between heating and cooling zone provides for an exclusively vertical thermal gradient[49].

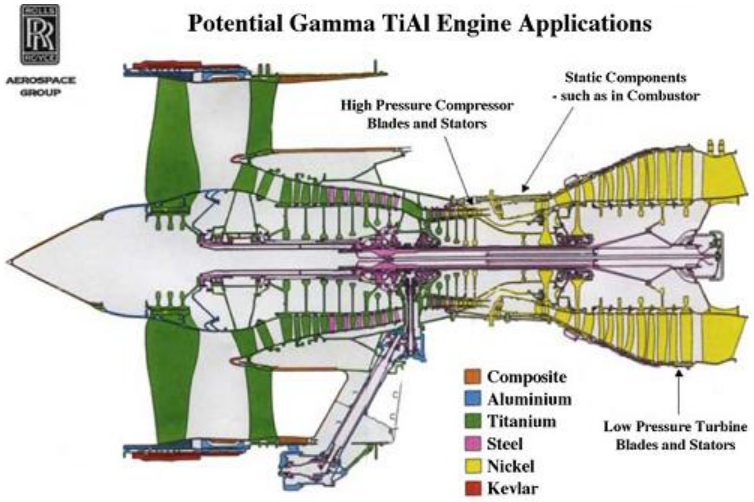

Figure 2.9 The present application of materials in aircraft engines. The low pressure turbine blades and stators are expected to be replaced by TiAl-based alloys[13].

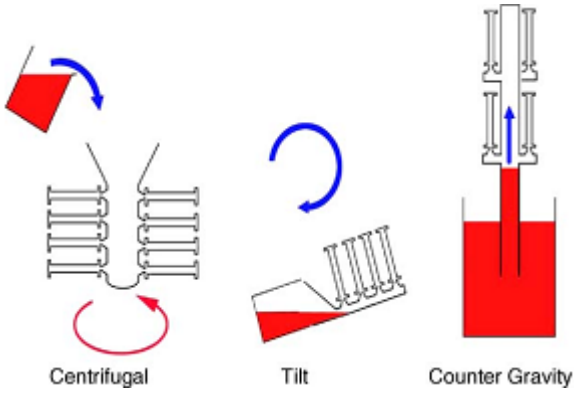

Figure 2.10 Three investment casting processes under development for the manufacturing of γ-TiAl turbine blades[13].

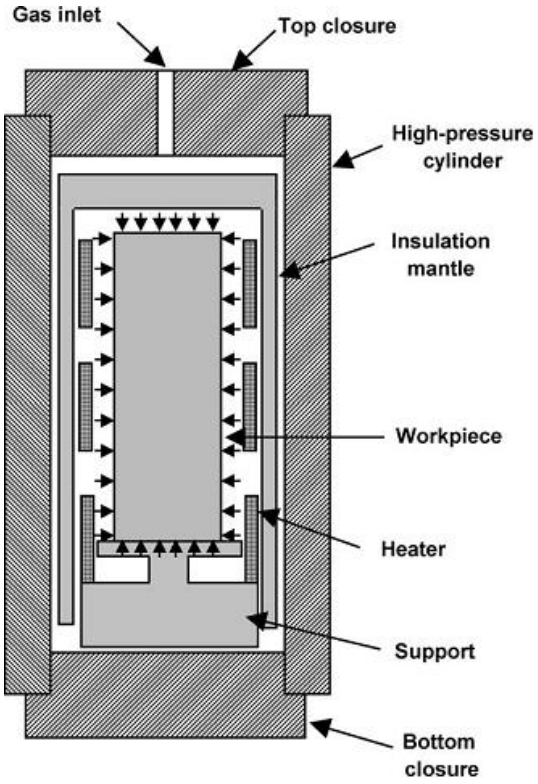

Figure 2.11 Schematic drawing of HIP unit[77].

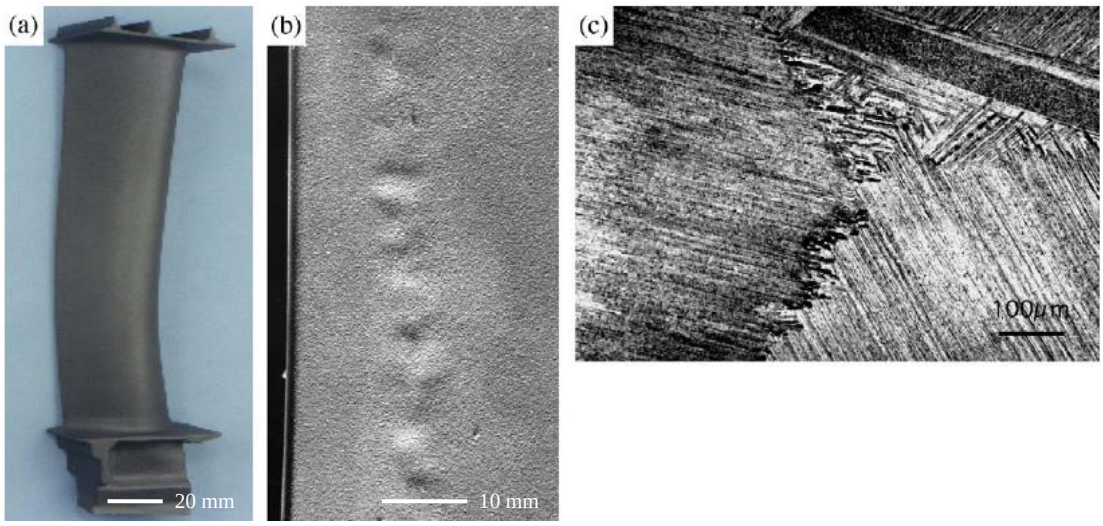

Figure 2.12 (a) cast LP turbine blades with (b) the dimples caused by collapse of porosity on HIPping such a blade and (c) the coarse grained lamellar microstructure of the casting[11].

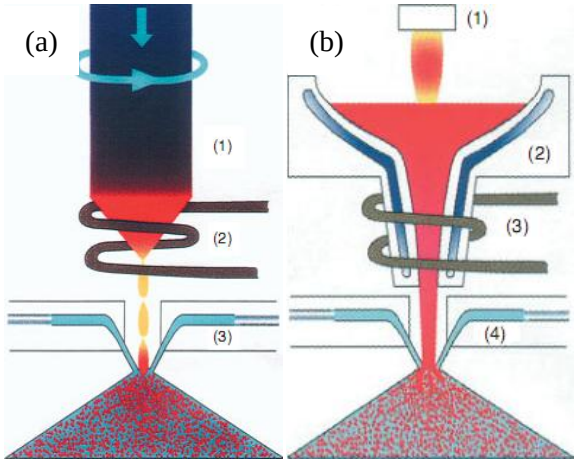

Figure 2.13 Schematic drawing of (a) the Electrode Induction Melting Gas Atomisation (EIMGA) technique, (1) Electrode, (2) Induction coil, (3) Gas Nozzle; (b) the Plasma Melting Induction Guiding Gas Atomisation (PIGA) technique, (1) Plasma Torch, (2) Cold Copper Crucible, (3) Induction Heated Cold Copper Funnel, (4) Gas nozzle[82].

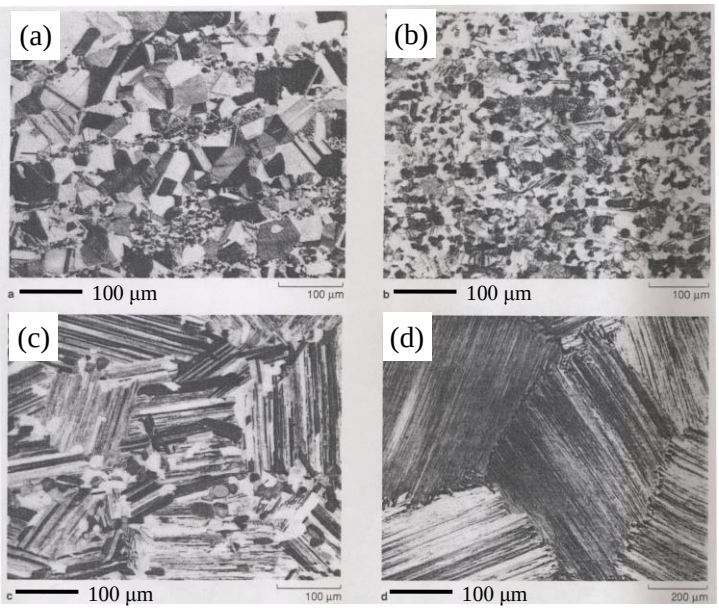

Figure 2.14 Four typical optical microstructures of TiAl alloys obtainable after post-hot work heat treatment. (a) Near gamma; (b) Duplex; (c) Nearly lamellar; (d) Fully lamellar[50].

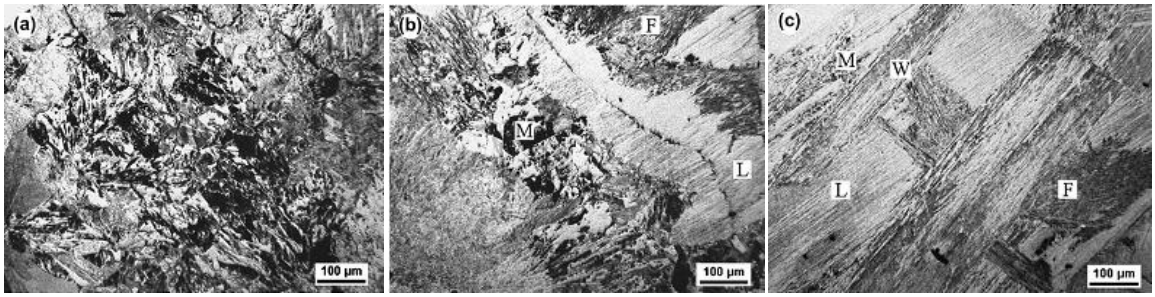

Figure 2.15 Typical optical microstructure of continuously cooled Ti-46Al-8Nb from 1360 °C (alpha phase field). (a) Fully massive γ obtained at a cooling rate of 180 $^{\circ}Cs^{-1}$; (b) a mixture of massive γ + feathery + lamellar microstructure obtained at a cooling rate of 25 $^{\circ}Cs^{-1}$; (c) a mixture of massive γ + Widmanstätten + lamellar microstructure obtained at a cooling rate of 10 $^{\circ}Cs^{-1}$. Letters M, F, W and L stand for massive, feathery, Widmanstätten and lamellar microstructure, respectively[68].

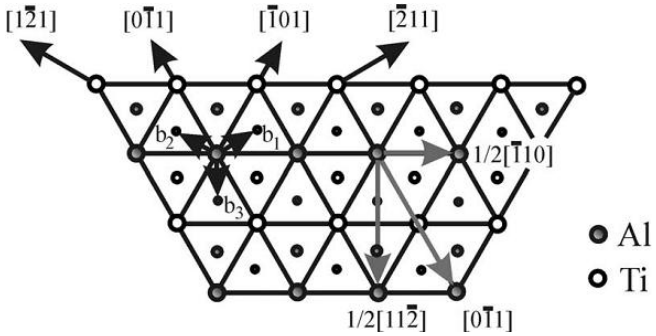

Figure 2.16 Potential slip and twinning system of the $L1_0$ structure, schematic drawing of three-layer sequence of atom stacking on the (111) plane shown by small, medium and larger circles. b_1 = 1/6[$\bar{2}$11], b_2 = 1/6[1$\bar{2}$1] and b_3 = 1/6[11$\bar{2}$] are the Burgers vectors of partial dislocations. b_3 is perpendicular to the Burgers vector b = 1/6[$\bar{1}$10] for ordinary dislocations represent the Shockley partial dislocation for true twinning, where b_1 and b_2 represent pseudo-twinning[115].

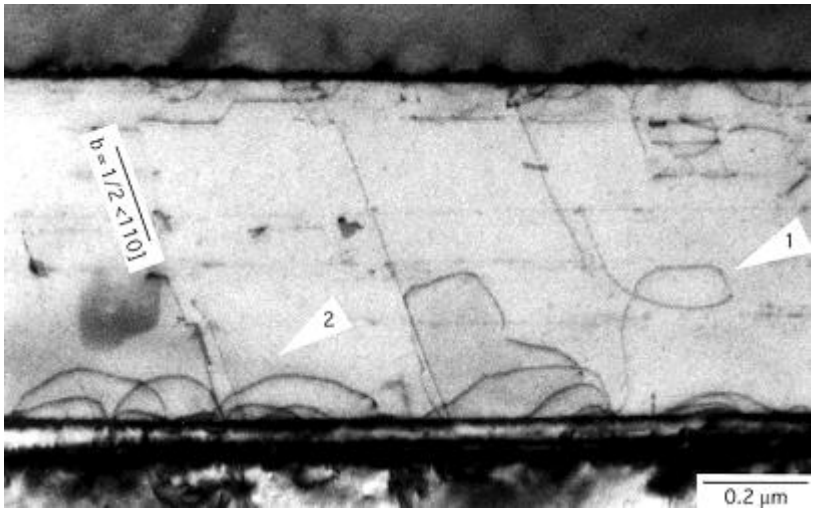

Figure 2.17 The emission of dislocation loops from an interface (arrow 2) observed in Ti-48Al-2Cr alloy, which was compressed at 300 K to a strain of 3 %[12].

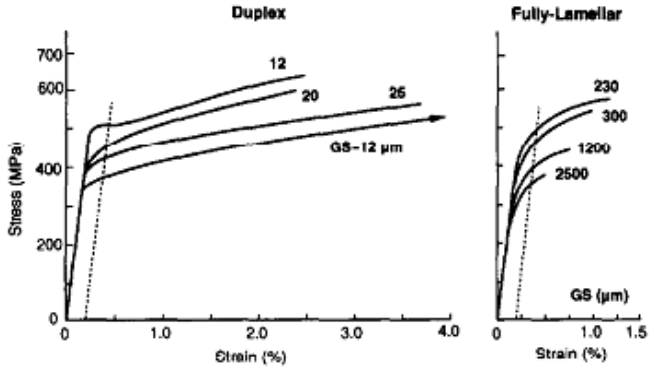

Figure 2.18 Tensile flow curves for TiAl alloys in two typical microstructural forms (duplex and fully lamellar) with various grain sizes[143].

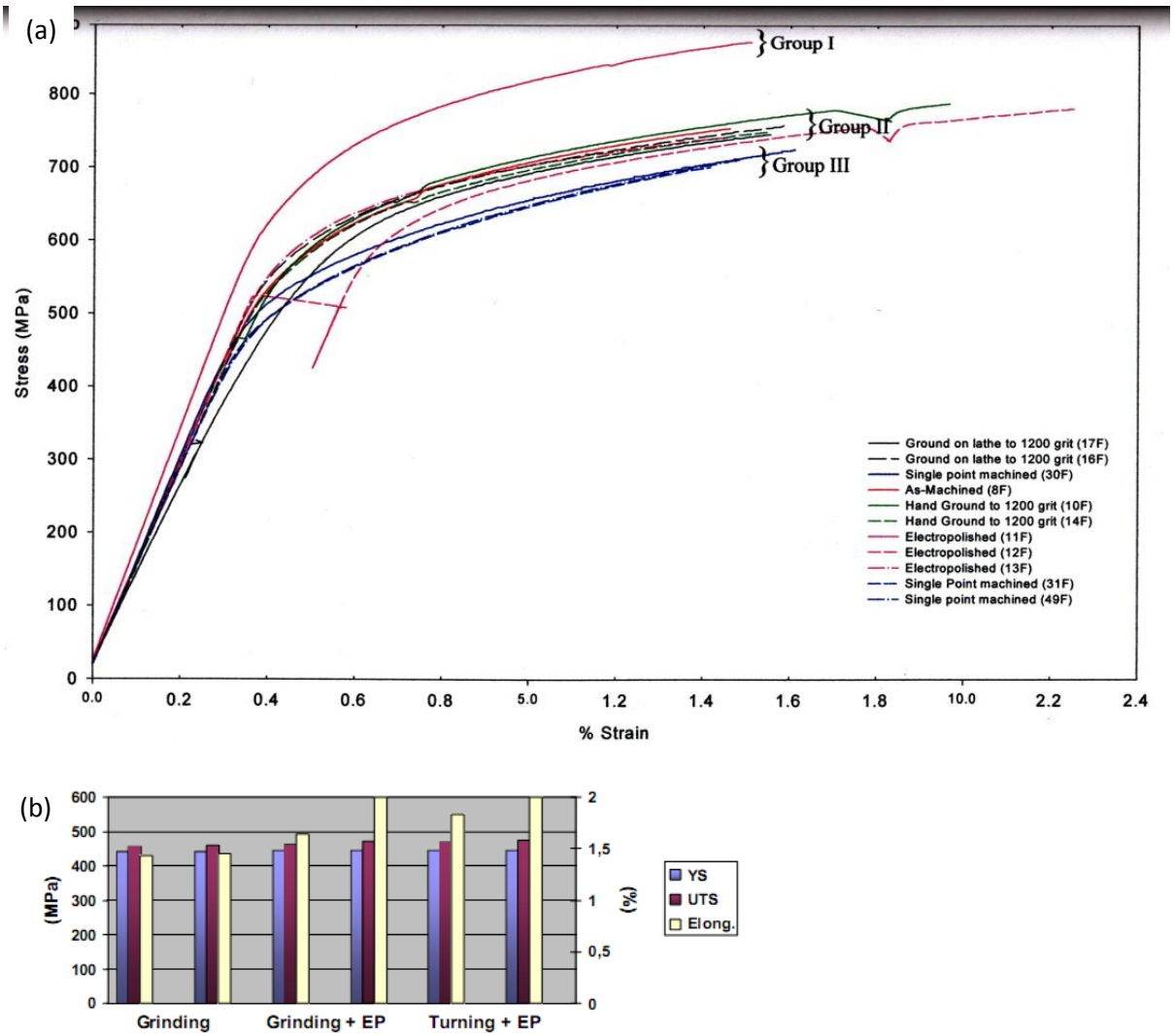

Figure 2.19 Room temperature tensile properties with different surface conditions in (a) cast Ti-44Al-8Nb-1B alloy[139], and (b) PM Ti-47Al-2Cr-2Nb alloy[140]. In (b), EP refers to electro-polishing and for each surface condition, two test pieces were tested.

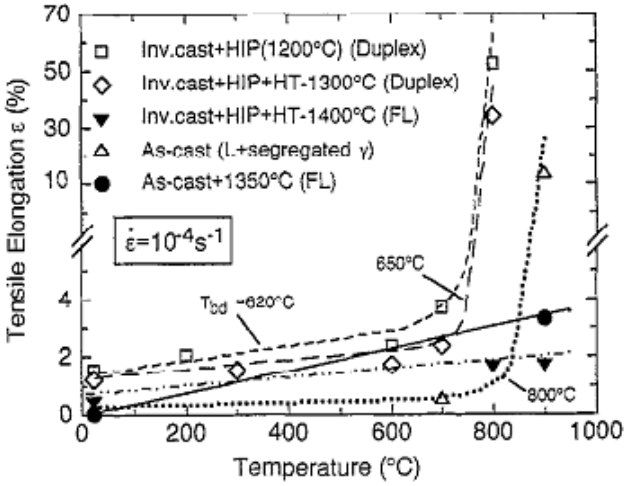

Figure 2.20 shows variation of tensile ductility with temperature for different microstructures[115].

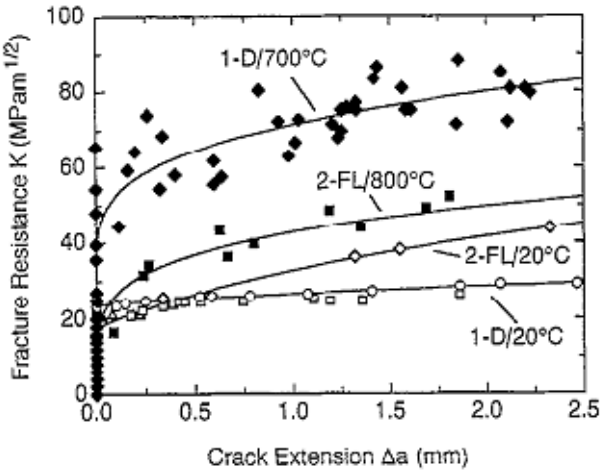

Figure 2.21 Curves 1: Crack growth resistance curves of investment cast Ti-48Al-2Cr (D-duplex) at 20 and 700 ℃. □, ○: compact tension (CT)-50 specimens with fatigue precracks and displacement rates of 10 μm/h and 600 μm/h, respectively. Δ:CT-50 specimens with electron charging machining (ECM) slit notch (radius ~ 50 μm) and 600 μm/h. ♦: CT-2.6 specimen, 10 μm/h. Curve 2: K_R curve of fully lamellar (FL) Ti-47Al-2.6Nb-2(Cr+V) at 20 and 800 ℃; displacement rate 4.2×10^{-2} s^{-1}[115, 142].

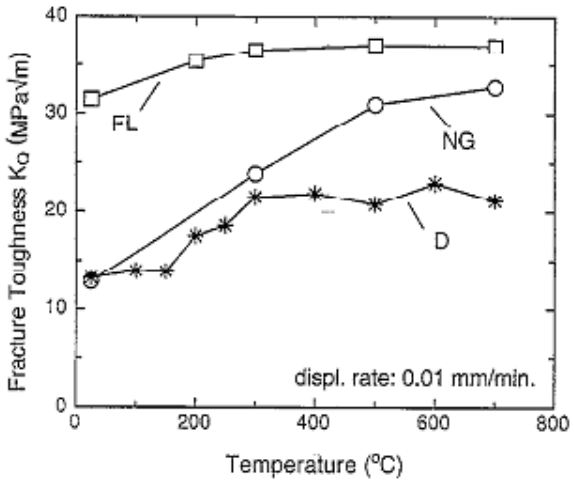

Figure 2.22 Dependence of fracture toughness on temperature for two phase TiAl alloys with different microstructures. FL: fully lamellar; NG: near gamma; D: duplex[115]

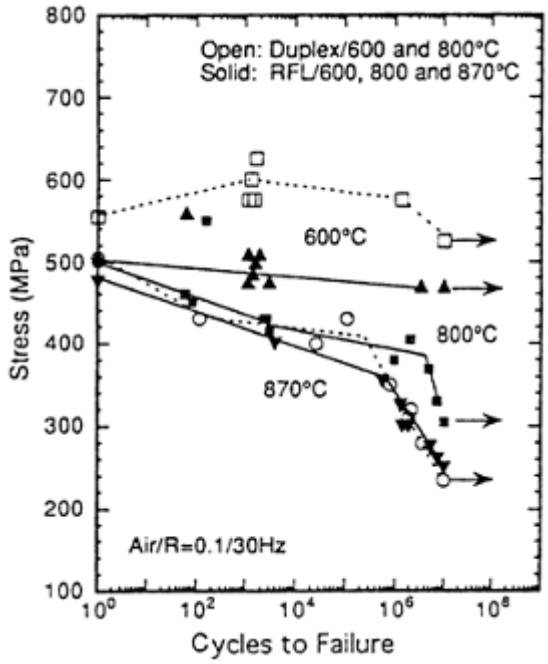

Figure 2.23 S-N curves for Alloy K5 (Ti-46.5Al-3Nb-2Cr-0.2W) with duplex and lamellar microstructures[149].

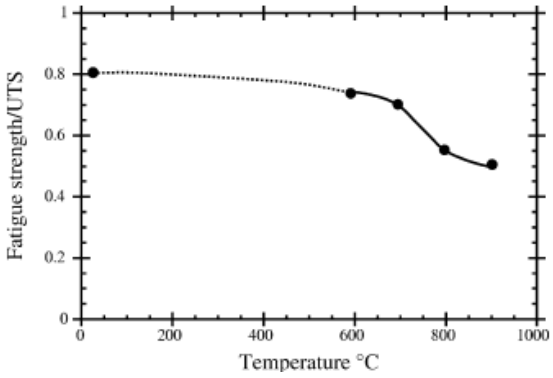

Figure 2.24 Influence of temperature on high cycle fatigue resistance[150, 151].

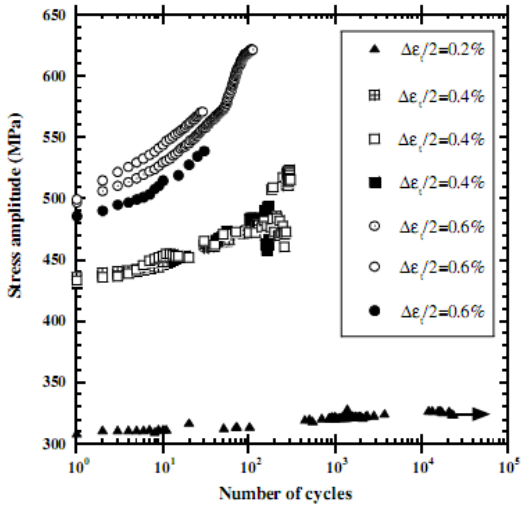

Figure 2.25 Cyclic stress-strain behaviour of the cast Ti-48Al-2Cr-2Nb alloy at room temperature[162].

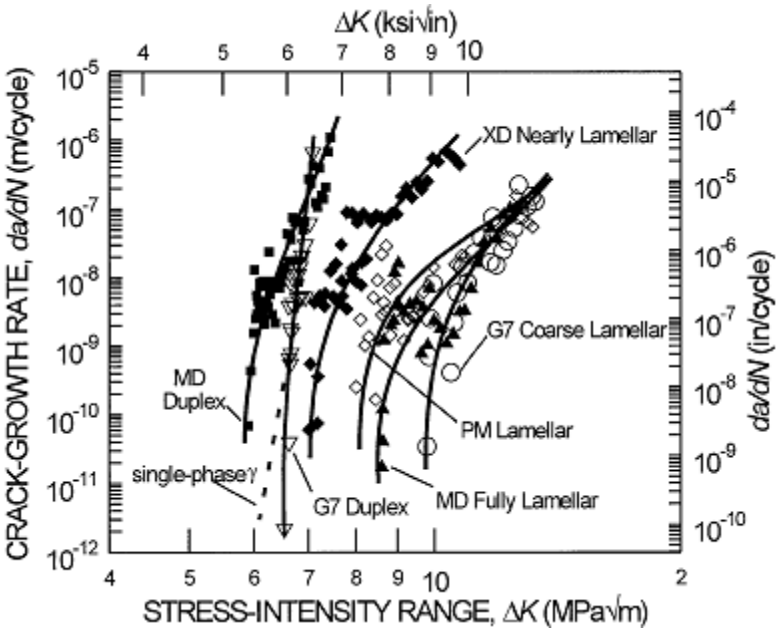

Figure 2.26 Influence of microstructure on fatigue crack growth behaviour at room temperature[147]. XD, MD and PM stand for casting, forging and powder metallurgy process, respectively, and G7 stands for a reference material with coarse lamellar microstructure.

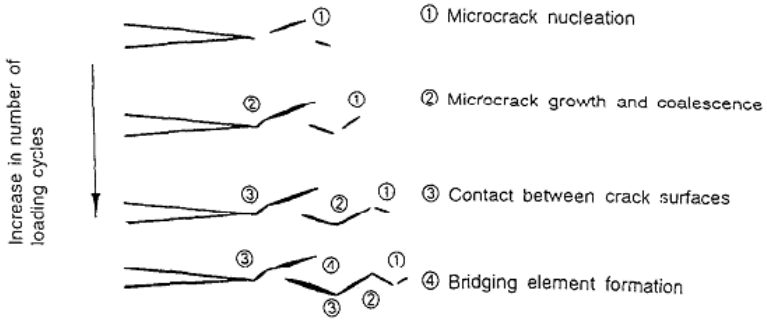

Figure 2.27 Schematic mode of the fatigue crack growth process[148].

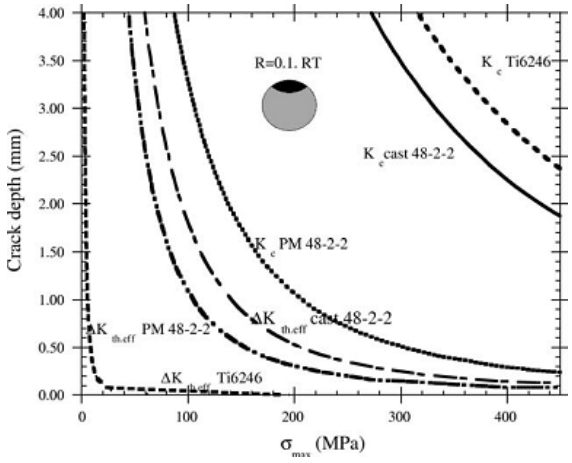

Figure 2.28 Critical sizes for FCG and fracture as a function of maximum stress for two typical TiAl-based alloy microstructures as compared to a Ti6246 alloy[150, 171].

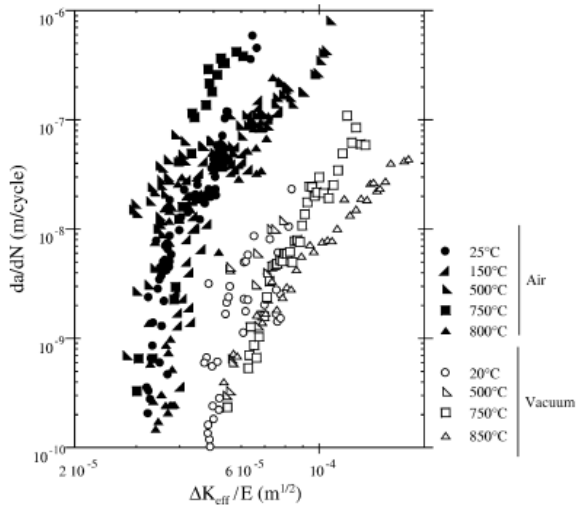

Figure 2.29 Fatigue crack growth behaviour of a cast Ti-48Al-2Cr-2Nb in air and vacuum[173].

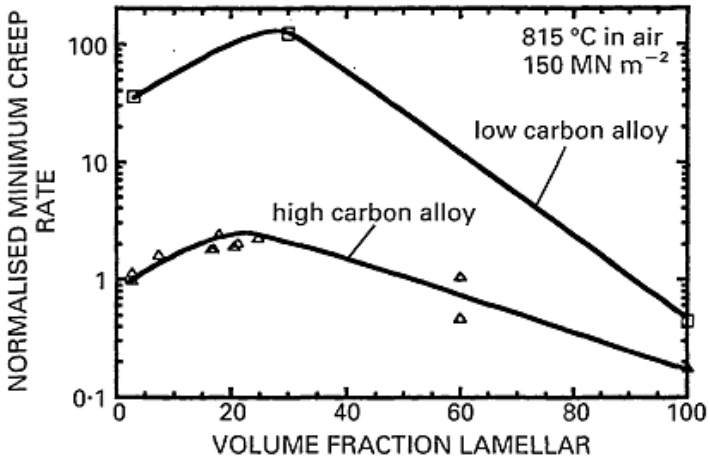

Figure 2.30 Influence of lamellar volume fraction on creep strain rate for Ti-48Al-1V with high C (0.3 %) and low C (0.07 %); 0 % lamellar (equiaxed microstructure), 20 % lamellar is duplex and 100 % lamellar is fully lamellar[178].

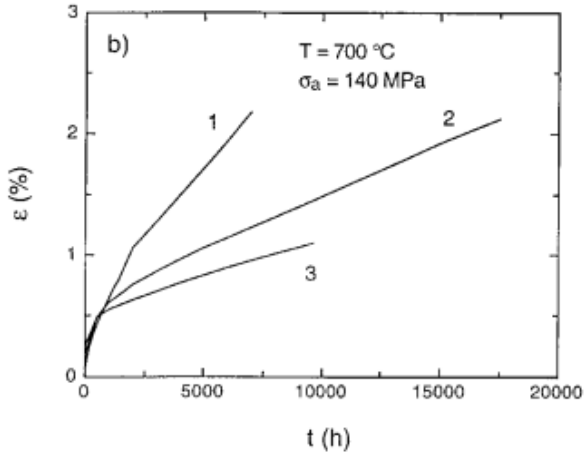

Figure 2.31 Creep characteristics of Ti-47Al-3.7(Nb, Mn, Cr, C)-0.5B, 1) investment casting, near-lamellar microstructure, lamellar spacing 0.1-1.5 mm, 2) investment casting + HIP, duplex microstructure, 3) investment casting + HIP + heat treatment at T_α (α transus) + ΔT = 1380 ℃, near-lamellar microstructure, lamellar spacing 10 nm to 0.5 μm[12].

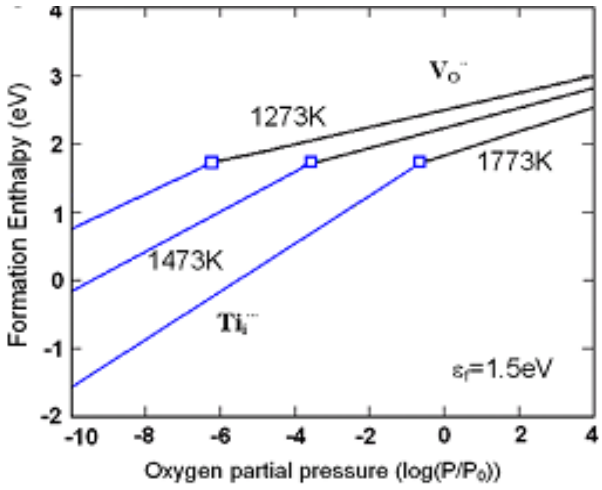

Figure 2.32 shows the transition of dominant point defect in undoped TiO_2 (ε_F = 1.5 eV) from titanium interstitial ($Ti_i^{\cdot\cdot\cdot\cdot}$) to oxygen vacancy ($V_O^{\cdot\cdot}$) at different high temperatures [197].

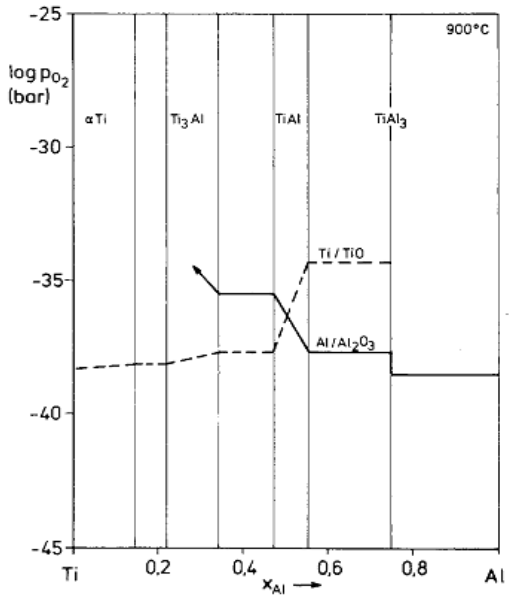

Figure 2.33 Variation of metal/oxides equilibrium pressures in Ti-Al-O system at 900 ℃[201].

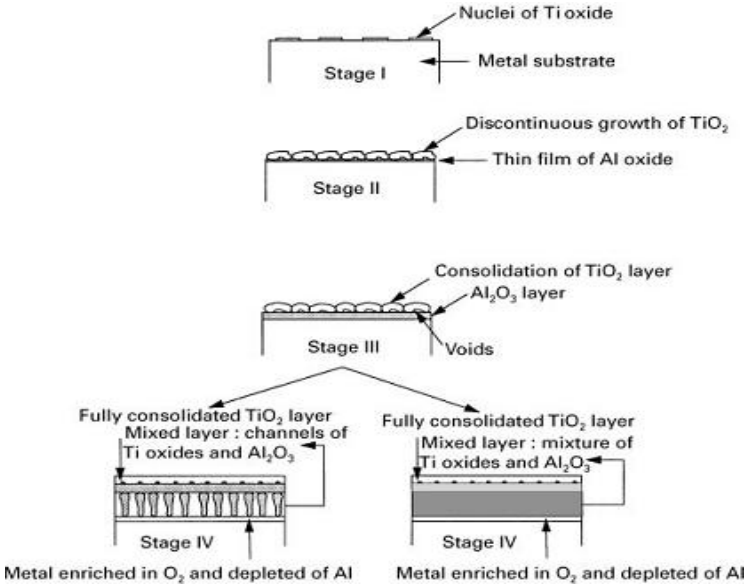

Figure 2.34 A physical model detailing the different stages of oxidation in binary and ternary TiAl-based intermetallic alloys[206].

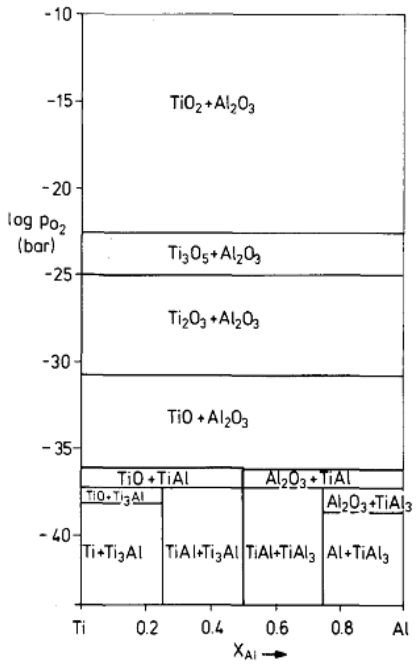

Figure 2.35 Simplified Ti-Al-O phase diagram. Isothermal section at 900 ℃. (All phases are treated as line compounds.)[201]

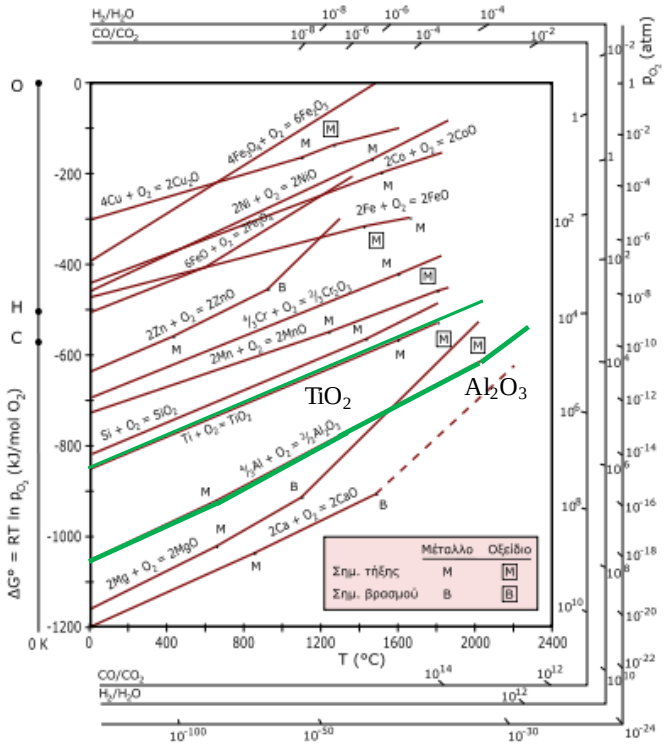

Figure 2.36 Ellingham diagram[202].

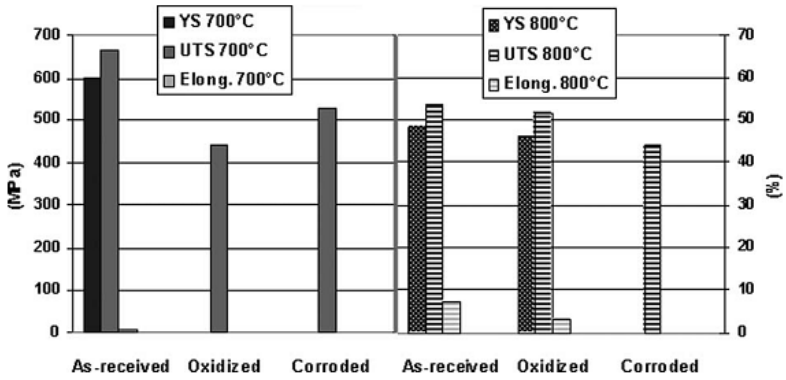

Figure 2.37 Effect of long term exposure (1000 1-h cycles) in oxidation and corroding atmospheres on the 700 and 800 °C tensile properties of the γ-Ti-45Al-X(Nb, B, C) alloy[211].

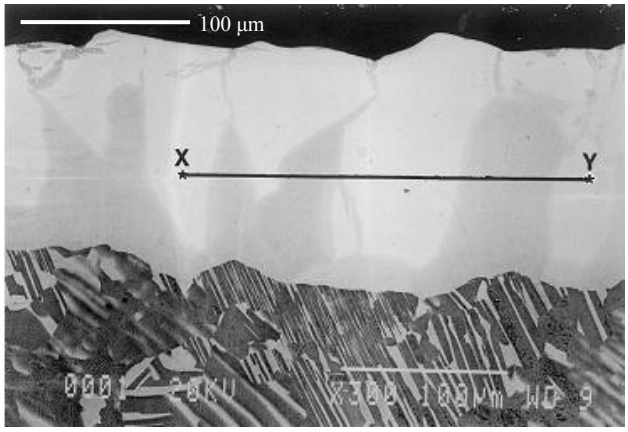

Figure 2.38 Back scattered electron (BSE) images of the cross-section of the specimen heat treated at 1200 ℃ for 50 h in argon[214]. The line XY is the trace line used for EDS measurement.

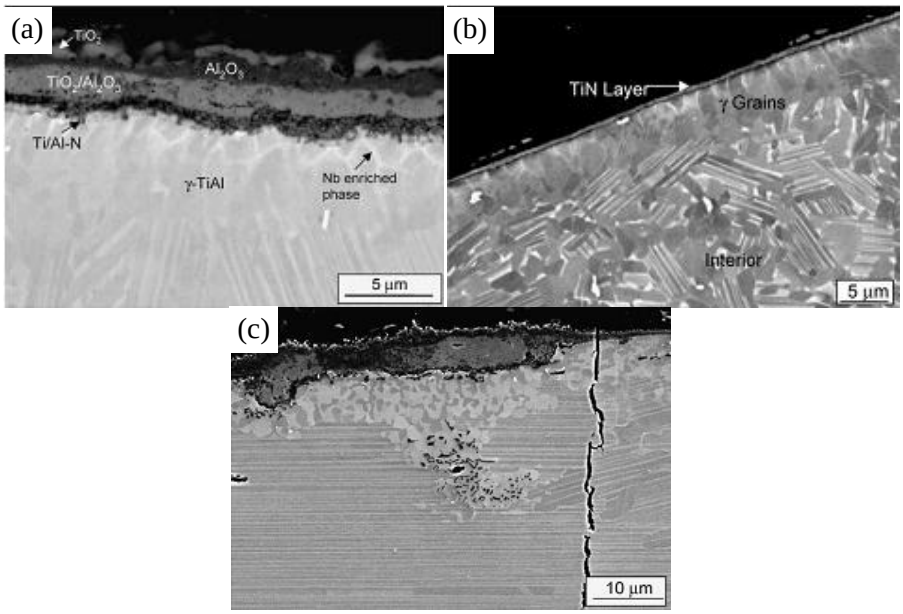

Figure 2.39 Near surface microstructures of an as-extruded sample exposed to 800 ℃ for 200 h in (a) air, (b) Ar, and (c) dry, ultra-high purity oxygen[209].

Structure	Space group	Unit cell (nm)	Atom	Fractional coordinates		
TiB	Pnma	$a = 0.611$	Ti (4c)	0.177	0.250	0.123
B27	(no. 62)	$b = 0.305$	B (4c)	0.029	0.250	0.603
		$c = 0.456$				
TiB	Cmcm	$a = 0.323$	Ti (4c)	0.000	0.146	0.250
B_f	(no. 63)	$b = 0.856$	B (4c)	0.000	0.440	0.250
		$c = 0.305$				
Ti_3B_4	Immm	$a = 0.326$	Ti (2c)	0.500	0.500	0.000
$D7_b$	(no. 71)	$b = 1.373$	Ti (4g)	0.000	0.180	0.000
		$c = 0.304$	B (4g)	0.000	0.375	0.000
			B (4h)	0.000	0.444	0.500
TiB_2	P6/mmm	$a = 0.303$	Ti (1a)	0.000	0.000	0.000
C32	(no. 191)	$c = 0.323$	B (2d)	0.333	0.666	0.500

Table 2.1 Structure type, space groups, lattice parameters, Wyckoff positions and fractional atom coordinates for the borides[21].

HIPping Temperature (℃)	Microstructure	0.2% YS (MPa)	UTS (MPa)	Tensile Elongation (%)
1200	Near Gamma	715	715	0.2
1240	Duplex	610	665	1.0
1270	Duplex (with higher lamellar volume fraction)	525	660	1.6
1300	Near lamellar	445	590	1.7

Table 2.2 As-HIPped tensile properties of PM Ti-46Al-2Cr-2Nb[84].

Alloys	Condition	YS (MPa)	UTS (MPa)	Elongation (%)
Ti-44Al-8Nb-1B near-fully lamellar	As-polished	650/629	760/673	1.1/0.4[a]
	Polished + 700 °C/2 h, AC	655/690	723/760	0.6/0.6
	Polished + 700 °C/2 h, AC, hand polished to remove surface	617/635	713/727	0.8/0.9
Ti-46Al-8Nb-1B duplex	As-polished	627/626	675/680	1.1/1.2
	Polished + 700 °C/2 h, AC	625/656	627/665	0.2/0.2
	Polished + 700 °C/2 h, AC, hand polished to remove surface	608	627	0.6

[a] Broken at knife edge.

Table 2.3 Room temperature tensile properties of alloys with different microstructures before and after exposure and of samples lightly polished after exposure[210].

CHAPTER 3 EXPERIMENTAL METHODS

In this chapter, the raw materials used for the study and the processing methods used are described together with specimen preparation and equipment used. The analysis techniques used for microstructural analysis, crystal structural analysis and mechanical tests are described in order to define the methods used for the microstructural characterisation and measurements of properties.

3.1 Materials and their processing

3.1.1 Ti4522(XD) Bridgman samples

Ti4522(XD) Bridgman samples were produced in a vertical Bridgman-Stockbarger furnace in ACESS Materials and Processes in Germany, which operated under 1000 mbar argon. The difference between Ti4522 and Ti4522XD is in 1 at.% boron. This method involves remelting cylindrical feedstock which was contained in densely sintered yttria crucible tubes prior to withdrawal from a heat sink at constant velocity of 5.0 mm/min through a temperature gradient of 20 ± 2 ℃/mm into a water bath. These conditions correspond to a cooling rate of about 2 ℃/s. the Ti4522XD feedstock was machined from a 200 mm diameter ingot and the Ti4522 feedstock was prepared from a plasma arc melted button ingot. The oxygen content in two alloys was about 500 wtppm. Heating and cooling temperatures were adjusted to 1750 ℃ and 25 ℃, respectively. Within this temperature field the samples were solidified in direction opposite to gravity over a length of 60 mm, followed by quenching at a rate of about 100 ℃/s.

3.1.2 Gas atomised Ti4522XD powders

Gas atomised Ti4522XD powders were produced in the Institute of Metal Research (IMR), Chinese Academy of Sciences, China using the electrode induction melting technique as discussed in section 2.3.3 in Chapter 2. As a precondition, the prealloyed electrode was prepared by cold hearth induction melting. The facility and the electrode used for gas atomisation are illustrated in fig. 3.1. During gas atomisation, the cooling rate was measured to be above 10^3 ℃/s. Fig. 3.2 shows the particle size distribution from which it is clear that the sizes of the majority of gas atomised powders were less 200 μm with median particle size D_{50} = 76 μm, which means that 50% particles have the size less than that and the rest larger than that. The oxygen content of those powders was measured in INCO TEST, which showed an oxygen concentration of 570 wtppm. For further analysis, those starting powders were sieved into three categories: <50 μm, 50-100 μm and >100 μm.

3.1.3 Ti4522XD and Ti48Al2Cr2Nb1B buttons

Two boron-containing TiAl alloys, Ti4522XD and Ti48Al2Cr2Nb1B (at%), were prepared by arc remelting blocks cut from plasma melted ingots in an argon environment which was purified with Ti sponge. A schematic diagram of the arc melting furnace is shown in fig. 3.3. The small alloy buttons, which were semi-ellipsoidal and weighed about 20 g, were melted 3 times in order to improve their homogeneity. The bottom view of each button is shown in fig. 3.4, from which it is noticed that there is an unmelted part in the centre of the button bottom during each melting process which is due to the contact with the water-cooled copper wall. Therefore, the cross-sections of these buttons were cut close to the tip of buttons to avoid those unmelted parts for microstructural investigation, as indicated in fig. 3.4.

3.1.4 As-cast Ti4522XD blades and ingots

Both the near net shape cast LP turbine blades as shown in fig. 3.5 and gravity cast Ti4522XD ingots were made IMR, and used in the study of HIPping effect on the change of surface microstructures and the corresponding influence on properties. The ingots were cut by electro-discharging machine (EDM) to 35×35×24 mm blocks. Some of the blocks had one face ground in a milling machine and 10×35×3 mm plates with those machine-ground surfaces were cut from those blocks using EDM. Blocks without surface ground surfaces were cut into 10×10×24 mm small blocks again by EDM and those small blocks had all surfaces manually ground to 1200 SiC grinding paper and finally electropolished. Some of the 10×10×24 mm blocks which had surfaces electropolished had all the surfaces sand-blasted with Al_2O_3 particles at 3 bar pressure. All those samples with ground surfaces, sand-blasted or electropolished surfaces were used for the subsequent HIPping processes.

3.1.5 Hot isostatic pressing

All hot isostatic pressing (HIPping) processes were done using the EPSI Lab HIP facility in the IRC in materials, The University of Birmingham, UK as shown in fig. 3.6 (a). In the study, the HIPping temperature and time may be varied according to experimental requirement, but the HIPping pressure was always kept at 150 MPa, and both the heating rate and cooling rate were controlled at 5 ℃/min above 200 ℃. When the temperature was less than 200 ℃, the heating and cooling rates were 10 ℃/min. If the HIPping temperature and time are 1260 ℃ and 4 hours, respectively, the above HIPping conditions are standard HIPping conditions. During heating and cooling, the HIPping temperature and pressure were increased and decreased simultaneously. Argon, with a purity of 99.9995 % and oxygen concentration of 1 vpm provided by BOC UK, was used as the protective and

pressure transmitting medium. The furnace within this HIP unit has two zones, i.e. the top and the bottom hot zones with thermocouples positioned in two zones separately and both are heated by molybdenum heating elements, which are shown in fig. 3.6 (b). A computer system is used to monitor the temperature and pressure continuously inside the HIP furnace. Temperature control is within ±3 ℃ throughout the working zone. No special treatments are needed before HIPping near net shape cast or gravity cast Ti4522XD alloy, since they are already solid.

3.1.6 Hot sea water corrosion

The cast Ti4522XD samples and mechanical test pieces before and after HIPping were classified into two groups. Each group contained specimens with and without a γ surface layer which was formed during standard HIPping. Samples in the first group were immersed in $NaCl/SO_x/H_2O$ solution with salt deposition rate of 0.75 μg/cm^2/h and sulphide concentration 100 ppm at 650 ℃ for 200 h and the second one in a more severe $NaCl/SO_x/H_2O$ solution with salt deposition rate of 0.75 μg/cm^2/h but sulphide concentration 300 ppm and at 700 ℃ for 200 h.

3.2 Microstructural characterisation

3.2.1 Specimen preparation

The as-supplied materials were cut into small pieces for microstructural observation, using either the Struers Accutom cutting machine fixed with a silicon carbide cutting wheel or electro-discharge machine (EDM) depending on the original sizes of the to be cut materials. Those small pieces were hot mounted in conductive Bakelite in a mounting machine. Then they were manually ground from 240× to 1200× silicon carbide grinding paper step by step

before final polishing. The suspension used for the final polishing is OP-S colloidal silica activated with about 5 % hydrogen peroxide and the polishing disc is the Struers produced MD-Chem. All the polishing was carried out in a Struers DAP-7 polishing unit fitted with a pedemin-s automatic polishing head. Normally, the final polish needed around 10 mins. After that, the polished surfaces were cleaned using wash detergent, water and ethanol and finally dried with a hair drier.

In most cases, the as-polished samples were good enough for microstructural investigation by scanning electron microscopy (SEM) in the back scattered electron mode. In order to better observe the tiny borides in Ti4522XD alloy and very small microstructural features in Ti4522XD powders, some samples were chemically etched with Kroll's reagent of 2 vol.% hydrogen fluoride (HF), 10 vol.% nitric acid (HNO_3) and balance water for ~10 s and observed with optical microscopy and secondary electrons in an SEM.

To investigate the surface morphologies of the starting Ti4522XD powders they were directly scattered evenly onto the surface of carbon tab, whereas to observe the microstructure in cross-section individual powder particles were hot mounted in edge protective and conductive Bakelite, then ground directly on 1200× silicon carbide grinding paper in order to avoid the removal of the powder particles and finally polished in the normal way. Some polished powders were also lightly etched in Kroll's reagent for ~5 s.

To identify the crystal structures of the starting Ti4522XD powders, borides and the surface layers formed during HIPping of Ti4522XD castings, cross sections of samples for transmission electron microscopy (TEM) observation were prepared by a Quanta 3D FEG focused ion beam (FIB) miller. Compared with traditional twin jet electro-polishing or ion milling, FIB milling has the advantages of precisely controlling the areas of interest, like thin surface layer and small particles. Traditional dimpling and ion beam milling processes

were also used to prepare TEM discs. In this way, the samples of interest were firstly cut into 0.1 mm slices by EDM. Those slices were cut into 3 mm discs again using another EDM machine fitted with a copper tube with an internal diameter of 3 mm and then hand-polished with grinding paper to less than 100 μm before dimpling. Those polished discs were dimpled from both sides with the brass dimpling wheel and mixed diamond abrasive paste with a small amount of water. The finished disc with highly polished dimpled surfaces on both sides should ideally be approximately 100 μm in thickness on the edge and less than 10 μm in thickness in the dimpled centre. Fig. 3.7 is a rough sketch of the completely dimpled disc in cross-section. The final step after dimpling is ion beam milling for which PIPS (precise ion polishing system) was used. Before a small hole was detected by checking the transmitted light a higher energy of 5 V and higher angle of 10 °from both sides were used. Once the transmitted light was detected, PIPS parameters were changed to a lower energy 4 V and lower angle of 5 °for the purposes of increasing the thin areas and cleaning.

3.2.2 Microstructural characterisation

The facilities used for microstructural observation were a Philips XL-30 and JEOL 7000. The Philips XL-30 was only used for the investigation of fracture surfaces from broken tensile and high cycle fatigue (HCF) samples, since it has larger sample chamber but lower resolution than the JEOL 7000.

The JEOL 7000 is a field emission scanning electron microscope (SEM), which can be used for secondary electron (SE), backscattered electron (BSE) and electron backscattered diffraction (EBSD) SEM observation. It also incorporates an energy dispersive x-ray spectrometer (EDS) and wavelength dispersive x-ray spectrometer (WDS), which can be

used for compositional analysis. For the observation of microstructures, only 20 KV was used in both SE and BSE imaging.

SE imaging technique uses the secondary electrons which result from the interaction between the incident electrons and the top layers of the sample surface and the signal intensity depends strongly on surface tilt and weakly on atomic number and crystal orientation. This imaging mode, which has a large depth of field, is therefore used for examination of etched and fracture surfaces. BSE imaging collects the electrons which are back scattered by the sample without loss of energy. The yield of BSEs mainly depends on atomic number and weakly on crystal orientation. The heavier the elements are, the higher the BSE yield. For the microstructural observation of Ti4522XD alloy, in most cases, BSE imaging was used since the α_2 and γ phases in the alloy have a big difference in composition which results in a big difference in the intensity of back scattered electron, therefore giving rise to good contrast in the images.

EBSD is a very useful technique and was frequently used in this study, because it provides clear phase maps with crystal structure information over a large area, orientation maps which can be used to analyse crystal orientation, texture, orientation relationships between different grains, misorientation angles between grains and grain size distribution. For the operation of EBSD, the sample must be tilted 70 ° and the working distance should be kept within the range 15-20 mm.

One of the commonly used functions from EBSD in this study is grain size and grain size distribution measurement. When the grain size is measured by EBSD grain mapping, the misorientation limit for the neighbouring grains is set to 5 ° which means if the misorientation of neighbouring grains is less than 5 ° they are regarded as one grain, and the method used for measuring grain size is by the equivalent circle diameter (ECD) which

means each grain is treated as a round circle of equivalent area and the diameter of this grain is equal to the diameter of this circle. This is same for other EBSD grain mappings in this thesis. However, the traditional linear interception method was also used for the measurement of lamellar colony size in Ti4522(XD) Bridgman samples.

In terms of orientation relationship (OR) analysis by EBSD technique in TiAl alloys, an orientation or a texture map of a certain phase is needed, which can be chosen from the data base or can be created by Oxford Instruments INCA software. In these orientation or texture maps, the crystal orientation of each grain or texture component can be obtained. Texture component means a component in which all the grains have a very close crystal orientation with a very small grain boundary angle which can be chosen manually. In most cases, one texture component contains only one grain. Normally, the orientation of a grain in an orientation map includes the normal orientation which is normal to the sample surface and a RD orientation which is the direction parallel to the surface and defined by the INCA software itself. Transforming the crystal information from the orientation or texture maps to the corresponding pole figures, the OR and the angles of some particular crystal directions or planes between adjacent grains can be calculated. The calculation method for the angles between two different directions or planes in the pole figure is attached in Appendix 2.

It is established that if hcp α is precipitated from bcc β, the OR between α and β should follow Burger's OR:

$(0001)\alpha // \{110\}\beta$; and $<11\bar{2}0>\alpha // <111>\beta$

If α grains come from the same parent β, those α grains are called Burger's variants. To check if those α grains are Burgers variants, a new mathematical method has been

developed based on EBSD results, which in turn are based on the special OR between Burgers variants. First of all, the angles between (0001) planes of Burgers variants can only be 0 °, 60 ° and 90 °. Furthermore, for each angle between the (0001) planes of Burgers variants, the angles between their corresponding <11$\bar{2}$0> directions are fixed. For 0 ° and 90 ° angles, there is only one fixed angle matrix for each, but for 60 ° there are three groups of fixed angle matrix. These fixed angle matrixes are called standard angle matrixes for Burgers variants which are analysed and presented in detail in Appendix 3. For OR analysis among α_2 grains in the next Chapter, the angles between their (0001) planes and <11$\bar{2}$0> directions are measured and calculated and are compared to the standard angle matrixes in Appendix 3 to check if they are Burgers variants. This newly developed method for the analysis of Burgers OR is time-consuming, especially when there are too many grains to be analysed, however, it is so far the most accurate and effective way. There are two others methods that can be used for the same purpose. The first one is TEM which is also based on the standard angle matrixes. But this method is limited to a few grains due to the small size of a TEM sample and moreover, it also time-consuming. Another one is through the misorientation analysis based on the EBSD results. As discussed in literature review, there are only five misorientation angles between Burgers variants, namely, 10.53 °, 60 °, 60.83 °, 63.26 ° and 90 °. If all the misorientation angles are close to those five angles, the corresponding α grains might be Burgers variants. However, even though the misorientation of the neighbouring α grains is close to those five angles, it is not convincing that they are Burgers variants, since any α grains can make misorientation angles close to those five angles. This problem will be met in the late OR analysis.

3.2.3 Compositional analysis

The most commonly used method for the composition analysis is energy dispersive x-ray spectrometry (EDS). The main virtues of EDS are that it is convenient and time-efficient, allowing simultaneous quantification of all elements present in the sample[251]. During the measurement of compositions by EDS, the accelerating voltage was 20 KV, working distance 10 mm, acquiring time > 60 s, dead-time in the range 20-40 % and zero sample tilt. Since the acquisition rate is less than the input rate during EDS measurement, there is always a dead-time which means the percentage time for which the pulse processor is unavailable for further counting. For all the quantified results the collected counts were always greater than 2×10^6 to minimise the statistical error.

Wavelength dispersive x-ray spectrometry has higher energy resolution (1-5 eV) and lower limit of detection (< 0.01 %) than EDS (133 eV measured at Mn Kα and typically 0.1-0.5 %) and in this research work, WDS was used to analyse oxygen content in the samples. A beam voltage of 5 kV and scan current larger than 10 nA were used. In the examination of oxygen concentration by WDS, an MgO standard was used and a working distance of 10 mm was guaranteed. However, the exact quantification of oxygen concentration was not attempted, instead, the oxygen counts collected from each point were used for semi-quantitative analysis.

The operation and analysis of EDS and WDS results are also controlled by Oxford Instruments INCA software, which is interfaced to the JEOL 7000.

Apart from EDS and WDS, a wet chemical method was employed to measure the oxygen content in the Ti4522XD powders in IncoTest company before and after HIPping. Glow

discharge optical emission spectroscopy (GDS) was used to measure the oxygen content in depth profile from the HIPped surface to the subsurface.

3.2.4 Crystal structure identification

3.2.4.1 Transmission electron microscopy

For the phase identification of borides, the starting Ti4522XD powders and of the HIPped surface of Ti4522XD castings, transmission electron microscopy (TEM) was carried out on a JEOL 2100 and Philips Tecnai F20, operating at 200 KV. The JEOL 2100 uses a LaB_6 filament as the electron emission source and incorporates a charge-coupled device (CCD) to capture the digital images, however, traditional films are also used. EDS analysis is available and also controlled by INCA software. Before the measurement of compositions of a particular area which can be focused to a few nanometres, the TEM samples were tilted +15 °towards the detector.

To interpret crystal structure information, at least three selected area diffraction (SAD) patterns with different zone axis with low index were taken from the same area. The tilt angles between those different zone axes were recorded and calculated to make sure that the indexing of each SAD pattern was correct. During the tilting of the TEM samples, Kikuchi lines were used to help follow the tilting directions.

3.2.4.2 X-ray diffraction

The phase constitutions of the samples in the study were also analyzed by X-Ray diffraction (XRD) technique on a Philips X'PERT X-Ray diffractometer, using Cu Kα radiation at 40KV and 40mA.

3.2.4.3 EBSD phase mapping

As long as the grain is big enough, normally bigger than 500 nm in thickness, the Kikuchi patterns yielded from EBSD phase mapping could be used to identify the crystal structures of phases of interest, in conjunction with the data base stored in INCA software or edited manually.

3.3 Mechanical testing

3.3.1 Tensile testing

To assess the influence of surface layers formed during HIPping of Ti4522XD castings on tensile properties, round tensile test pieces were prepared for tensile testing. First of all, 9 mm (diameter) × 60 mm (length) cylinders were cut out from the original blocks using EDM, then they were sent to GTG company for finish-machining to the final shape shown in fig. 3.8. In reality, two batches of tensile test pieces were prepared from two batches of original blocks. One group of the tensile test pieces were HIPped under standard conditions to form the HIPped surface layers. Another group of the HIPped tensile test pieces were additionally hand polished with SiC grinding paper from 400× to 1200× to remove the HIPped surface to the required thickness. Tensile tests were carried out in a Zwick at a strain rate of 10^{-4} s^{-1} in air at room temperature. During testing, an extensometer with a gauge length of 20 mm was used to record the displacement. The load/displacement curves obtained were converted into nominal stress/nominal strain curves from which tensile strength, yield strength and plastic elongation were measured and calculated.

3.3.2 High cycle fatigue testing

Cylinders with diameter 15 mm and length 125 mm were cut out from cast Ti4522XD alloy and then machined by GTG company into round high cycle fatigue (HCF) test pieces with dimensions shown in fig. 3.9. HCF testing was carried out under tensile to tensile mode with a stress ratio R=0.1 at room temperature. Like the situation in tensile tests, some HCF test pieces were HIPped to form surface layers in order to compare the fatigue properties of samples with and without HIPped surfaces.

For each condition, six samples were prepared to obtain an S-N curve and to define the fatigue strength of HIPped castings with and without surface layers. During HCF testing of each test piece, the initial stress was set to a low level and if the sample did not fail after 10^7 cycles, the stress was increased in steps of 25 MPa.

3.3.3 Hardness testing

Micro hardness was measured by a Mitutoyo MVK-H1 micro-hardness tester with Vickers or Knoop indenters. The load could be varied from 10 g to 1 kg and a standard sample (EP9716400 with 757.3 HMV0.3) was used as calibration to conduct the hardness tests. For the hardness testing in this project, a Knoop indenter with 10 g load was used; this is the smallest indenter and it can provide data at the spatial resolution required in the experiment. The hardness values are the average of at least six measurements and standards BS EN ISO 4545, 6507 were taken as reference for the Knoop hardness tests.

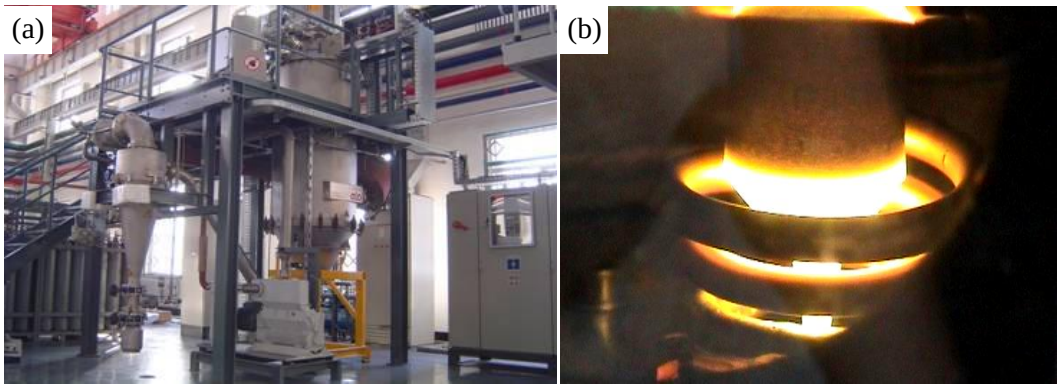

Figure 3.1 (a) Electrode induction melting gas atomisation machine in IMR, China; (b) the tip of electrode in the process of melting.

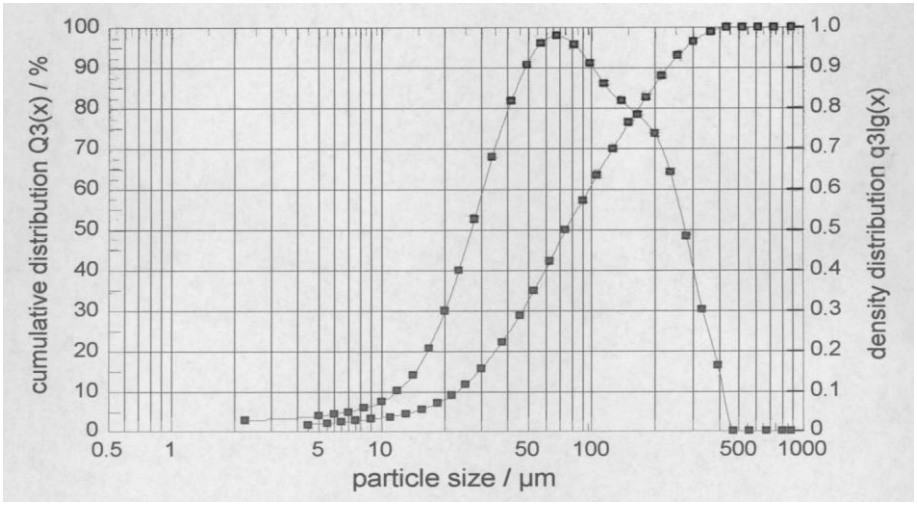

Figure 3.2 Particle size distribution of starting Ti4522XD powders.

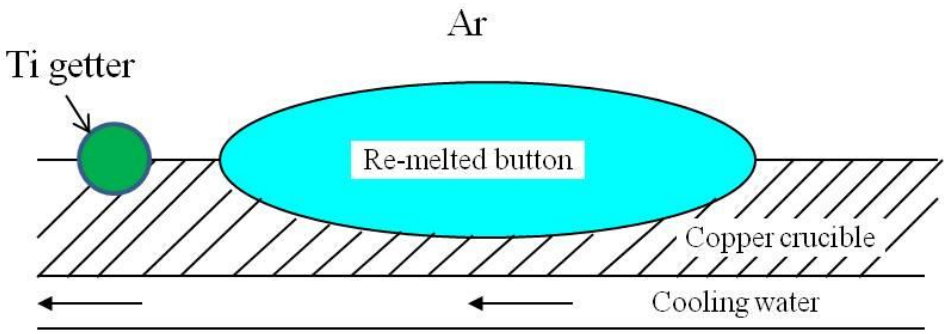

Figure 3.3 Schematic diagram for the remelting of small button.

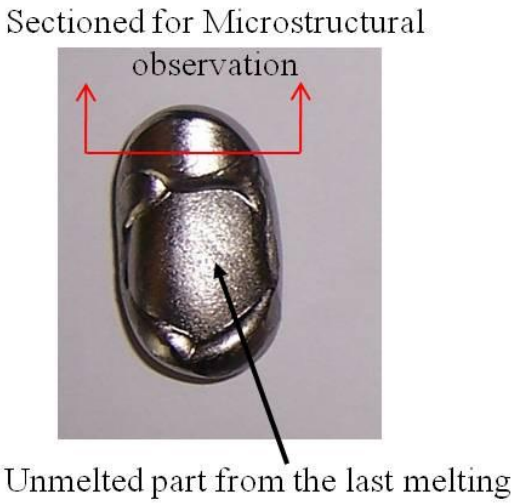

Figure 3.4 Bottom view of remelted TiAl button.

Figure 3.5 Low pressure turbine blade made by IMR

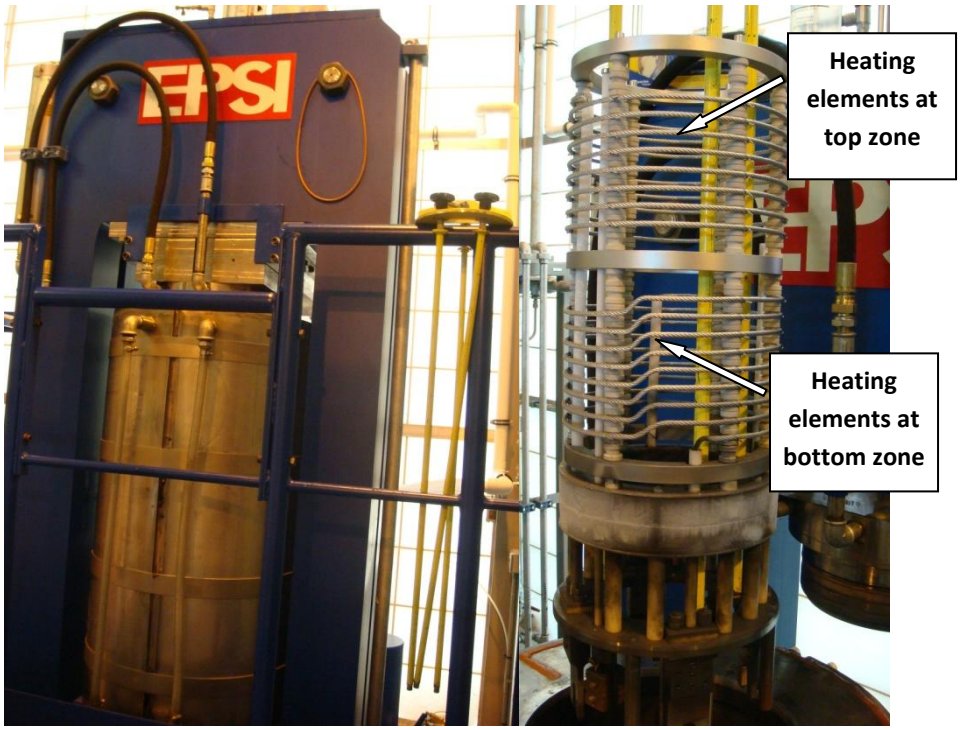

Figure 3.6 (a) EPSI Lab HIP facility, (b) the two zone molybdenum furnace used for (a).

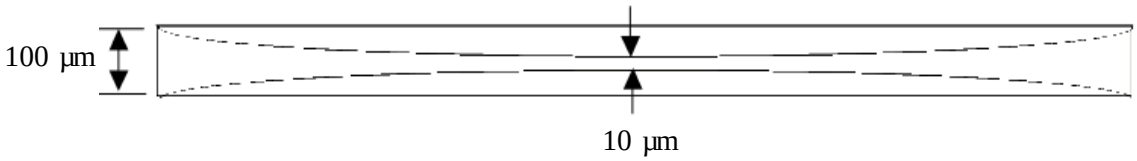

Figure 3.7 Schematic cross-section of completely dimpled TEM disc.

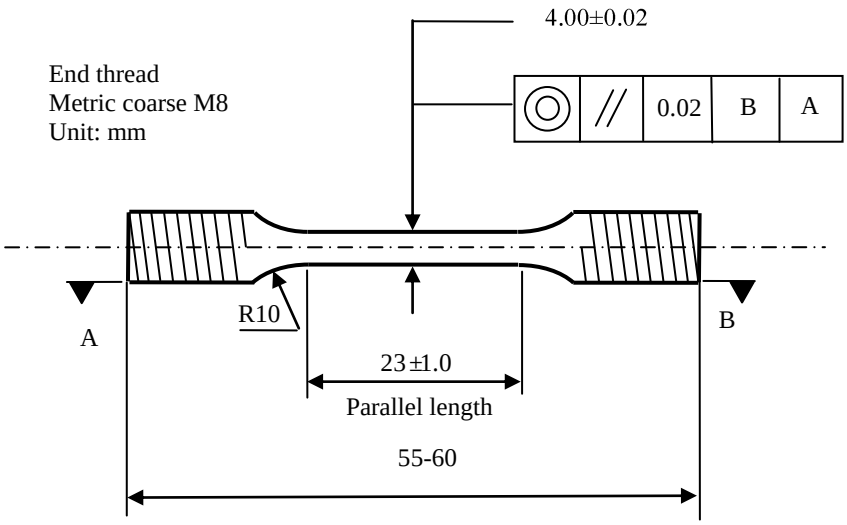

Note: Roughness value for machined surfaces to be 1.6 micrometers unless otherwise stated; all dimensions and tolerances are in mm

Figure 3.8 Schematic dimensions and machining requirement of round room temperature tensile test piece.

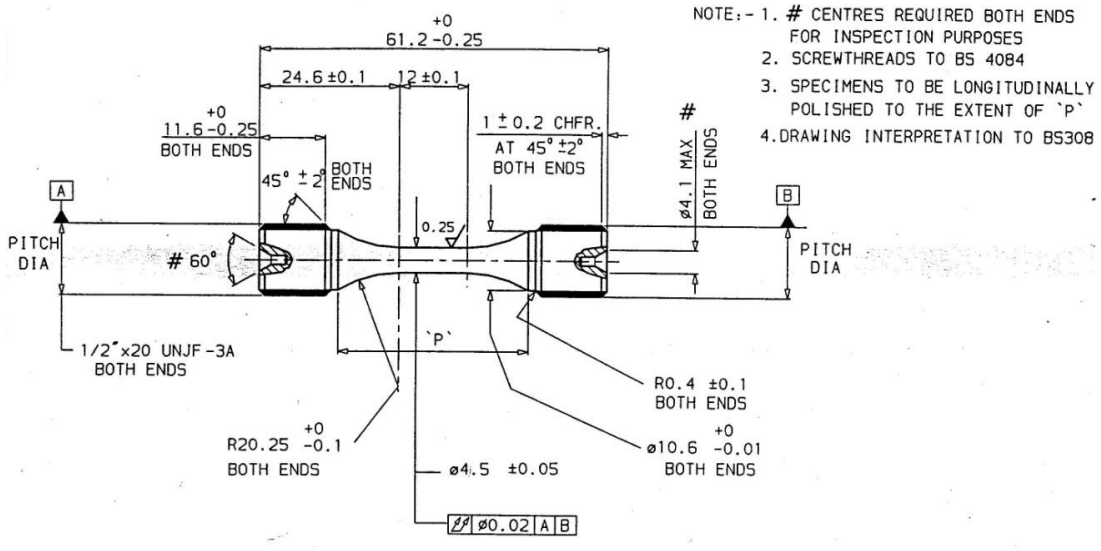

Figure 3.9 Schematic dimensions and machining requirement of round room temperature HCF figure test piece.

CHAPTER 4 SOLIDIFICATION BEHAVIOUR OF TI4522XD CASTINGS

4.1 Solidification behaviour of Ti4522(XD) Bridgman samples

As described in the experimental section the Bridgman method is a technique whereby a sample which is held in a furnace with an imposed temperature gradient can be quenched so that the different microstructures existing at different temperatures can be retained or traced back through known phase transformation. The solidification behaviour of a Ti45Al2Mn2Nb Bridgman sample, referred to as Ti4522, was also analysed as a reference to Ti45Al2Mn2Nb1B Bridgman sample, referred to as Ti4522XD.

4.1.1 Microstructural characteristics of Ti4522(XD) Bridgman samples

The high temperature microstructures cannot be seen directly, because some phase transformations occur during quenching and it is necessary to infer what the microstructures were before quenching from those seen in the quenched samples.

The overview of the microstructures along the longitudinal section of the unidirectionally solidified Ti4522 and Ti4522XD is shown in fig. 4.1 (a) and (b). The solidification direction is from left to right. Because of the space limitation, the regions close to the unmelted end are not shown in those figures. In both alloys, the white particles in fig. 4.1 are yttria which is formed due to dissolution of yttria from crucible walls and precipitation from the melt during solidification.

For Ti4522, the frozen-in microstructure in fig. 4.1 (a) can be classified into three regions of which the phase constitution before quenching are labelled at the bottom of this figure. The enlarged images of those microstructures for each region are shown in fig. 4.2. The first one is from the zone frozen-in directly from the liquid which is characterised by α_2 grains. The next region was quenched from β dendrites with liquid in the interdendritic region and a small volume fraction of peritectic α between β dendrites and the liquid, as illustrated in fig. 4.2 (b). However, during quenching the β dendrites transformed to α_2 grains, the peritectic α grains and the interdendritic liquid transformed to γ grains, some of which transformed to very fine lamellae. For α_2 grains transformed from β dendrites, white traces are always observed in the back scattered electron images. This is due to micro-segregation of β stabiliser, here the Nb, during β to α solid phase transformation during quenching. No such micro-segregation can be observed in peritectic α grains. When the liquid completely solidifies into solid, a Widmanstätten microstructure is formed which can be clearly seen from fig. 4.2 (c). It is formed by the precipitation of α grains from β during slow withdrawing. In the region close to the unmelted side which has a lower temperature before quenching, a fully lamellar structure is observed, as shown in fig. 4.2 (d), indicating that β had fully transformed to α before quenching.

For Ti4522XD, the overall microstructure in fig. 4.1 (b) can also be classified into three regions which were obtained from the quenched liquid, the mushy zone which includes both solid and liquid, and the complete solid region. In the region which was quenched from liquid, as shown in fig. 4.3 (a), there are lots of fine curvy borides which can be as long as 10 μm and as thick as 100 nm. Given those fine curvy borides mainly existed in the Al-enriched areas, it is more possible that most of them were formed during quenching after the β solidified. As indicated in fig. 4.1 (b), the mushy zone in Ti4522XD sample can

be further subclassified into three regions, namely a fine dendritic region, a coarse dendritic region and a very coarse dendritic region. For each dendritic region, the dendrites are characterised by α_2 grains and the interdendritic regions by γ grains. However, the α_2 grains in the dendrites were transformed from original β dendrites and the γ grains in the interdendritic regions were transformed from the liquid and the peritectic α grains during quenching, as indicated by the fine lamellae shown in fig. 4.3 (d). For those coarse and very coarse dendrites, fig. 4.3 (b) reveals that in the interdendritic regions there are also a lot of fine curvy borides of a similar size to those found in the liquid. In the cores of the dendrites long and relatively straight borides are observed which can be 50 μm long and 3 μm thick, as shown in the enlarged image in fig. 4.3 (c). The long bright borides in the cores of β dendrites might form slightly after the β solidification and the fine curvy borides in the interdendritic regions must form after the β solidification. After the liquid completely solidified, a long region composed of massive γ grains and retained α_2 grains appears which is shown in fig. 4.3 (e). The massive γ microstructure is formed by solid phase transformation from α grains during quenching as discussed in the literature review. The volume fraction of massive γ grains increases as the distance away from the mushy zone increases. In the region very close to unmelted end, the alloy has been transformed to fully lamellar, as shown in fig. 4.3 (f). It is worth noting that when the microstructure turns from dendritic to fully lamellar, the morphologies of the borides and the contrast of the borides in BSE images also change from curvy bright to long bright. These curvy and bright borides have been identified either as TiB with a B_f structure or Ti_3B_4 by TEM. The long bright borides have been identified as TiB with B_{27} structure by TEM and by EBSD. The detailed discussion of morphologies and crystal structures of borides and their relationships with cooling rate and alloy compositions will be addressed later. In addition,

traces of microsegregation of Nb and Mn are also observed in Ti4522XD in the α_2 grains as long as they were formed by solid phase transformation and in the fully lamellar microstructure.

Comparing the microstructures of Ti4522 and Ti4522XD Bridgman samples, it is evident that the Ti4522XD sample has the more refined microstructure. The lamellar colony size and the size distribution of these lamellar colonies for each sample are presented in fig. 4.4, from which it is seen that the microstructure is more homogeneous and the lamellar colony size is smaller in Ti4522XD than in Ti4522. It is specially noticed that in Ti4522, there are some colonies larger than 1000 μm. The average lamellar colony size for Ti4522 is 169 μm, while that in Ti4522XD is 91 μm. The grain size in the regions quenched from the liquid and mushy zone is also smaller in the Ti4522XD sample which will be discussed in the following section. The length of the dendritic region in Ti4522 is about 4170 μm, while that in Ti4522XD is about 2120 μm. Even though it is seen that the dendrites in the mushy zone in both Ti4522 and Ti4522XD are not parallel and not homogeneous, the primary dendrite arm spacing (PDAS) and secondary dendrite arm spacing (SDAS) in Ti4522XD are much smaller than those in Ti4522. Furthermore, it is clearly shown the length of secondary dendrite arms is also much shorter in Ti4522XD than that in Ti4522.

4.1.2 Orientation relationship analysis of Ti4522 Bridgman sample

The orientation relationship (OR) analysis between the grains in the quenched samples is aimed to trace back the solidification behaviours of those Bridgman samples before quenching, which is based on a newly developed method which needs combined EBSD experiment results and calculation that has been described in the experimental section.

4.1.2.1 Orientation relationships of α_2 grains in the liquid region

In the frozen-in liquid region of Ti4522, the observed grains are α_2 grains which are the ordered form of α grains. Fig. 4.5 shows the microstructure of the liquid region in (a) and the corresponding grain map and grain size distribution graph in (b) and (c). The average grain size was measured to be 38 μm.

Fig. 4.5 (d) shows the α_2 texture map where a group of α_2 grains that are from one texture family are marked in the same colour. Compared with the grain map in fig. 4.5 (b), it is seen that a few α_2 grains are not recognised and shown in black in the texture map. This is because there are no other α_2 grains in the same texture family as those grains. The misorientation between each α_2 grain is shown in fig. 4.5 (e) and (f), which show that the majority of the misorientation angles are close to 10°, 60° and 90°. According to the traditional method as mentioned in section 3.2.2, those α_2 grains may be Burgers variants which were formed by solid phase transformation from one parent β grain. However, this method cannot give a definite answer and the new method was used to check if the OR between each texture component comply with Burgers OR. There are 8 α_2 texture components in total which have been labelled in the image. To analyze the OR, the first step is identifying the (0001) plane of each component in an (0001) α_2 pole figure as shown in fig. 4.6, and then calculate the angles between (0001) planes from each component. The results are summarised in table 4.1. From the table, all the angles that are within 4° of 0°, 60° and 90° are underscored, as shown in table 4.1, and their corresponding texture components are further analysed. The second step is to identify the $<11\bar{2}0>$ directions of each marked component in their own $\{11\bar{2}0\}$ α_2 pole figure as shown in fig. 4.7, and then calculate the angles between $<11\bar{2}0>$ directions from those α_2 texture components in which their (0001) planes make angles close 0°, 60° and 90°. Some examples of the results are shown in table 4.2. Comparing with the calculated angle matrix

with the standard angle matrix in Appendix 3, it is revealed that there are 7 α_2 texture components that are from one Burgers family, confirming that most of the α_2 grains in these texture components were formed by solid phase transformation from one parent β grain. The α_2_8 texture component also follows Burgers relation with α_2_2, α_2_3 and α_2_7, but since it does not follow the same relation with the rest, their Burgers relation might be a coincidence.

4.1.2.2 Orientation relationships between α_2 grains in dendritic regions and between dendritic α_2 grains and interdendritic γ grains

Fig. 4.8 (a) shows the microstructure of frozen-in mushy zone in Ti4522 and the corresponding phase map is shown in fig. 4.8 (b) which indicates the dendrites are composed of α_2 phase and the interdendritic regions are composed of γ phase. The α_2 and γ grain maps and their grain size distribution graphs are shown from fig. 4.8 (c) to (f). The average grain sizes of α_2 and γ in this region are 101 and 22 μm, respectively. It is noticed that there are only a few α_2 grains and some of them are very big. Therefore, the α_2 grain size value in this area is not accurate. In addition, the actual γ grain size is smaller than the measured value, which will be discussed later. Before quenching the mushy zone was composed of β dendrites and the liquid in the interdendritic regions, therefore, the α_2 grains in the dendrites and the γ grains in the interdendritic regions were formed during quenching.

However, it is noticed that there is a higher γ volume fraction in the phase map in fig. 4.8 (b) than the volume fraction of the interdendritic areas in the BSE image in fig. 4.8 (a), which was interdendritic liquid before quenching. The difference between the volume fraction of γ phase in phase map and the volume fraction of interdendritic areas in BSE image indicates that there is a solid area before quenching between the β dendrites and the

liquid in the interdendritic regions that transformed into γ during quenching. This solid area includes peritectic α and parts of β dendrites, as indicated in fig. 4.2 (b) and fig. 4.8 (a) and will be illustrated again in fig. 4.9. Peritectic α grains are very different from the β dendrites in the terms of microstructures, since as discussed before, peritectic α grains have no white microsegregation traces and always locate in between the β dendrites and interdendritic liquid in BSE images. In addition, peritectic α contains higher Al level than β dendrites but less Al level than the interdendritic liquid, as indicated by BSE images. Whether the β dendrites that are close to the peritectic α and interdendritic liquid can transform into γ during quenching depends on the local Al concentration. Obviously, the structural and compositional features in the interface between β dendrites and interdendritic regions merits further investigation by TEM.

The OR between α_2 grains in the dendrites and between α_2 grains and interdendritic γ grains were analysed by the same method as described in section 4.1.2.1. First of all, each individual α_2 and γ texture component was isolated and labelled from texture maps in fig. 4.8 (g) and (h). It is seen that there are 3 α_2 texture components and 4 γ texture components. However, there are 4 small α_2 grains labelled in fig. 4.8 (c) not shown in the texture map in fig. 4.8 (g) since there are no other grains in the same texture as those. The (0001) and $\{11\bar{2}0\}$ pole figures of each α_2 texture component and each α_2 grain and the {110} and {111} pole figures of each γ texture component were analysed to measure the angles between each component. It is found that the α_2 texture components α_2_1 and α_2_2, along with a small α_2 grain α_2_4, are from one Burgers family. The misorientation map in fig. 4.8 (i) and its corresponding misorientation distribution graph in fig. 4.8 (j) further indicate the possibility of Burgers OR between α_2_1, α_2_2 and α_2_4. One dendrite was one parent β dendrite, but some small α_2 grains in the dendrites may not belong to Burgers variants like

α_2_3, α_2_5, α_2_6 and α_2_7, which may be attributed to the disturbance of yttria during solidification. It is also noticed that the α_2 grains separated by the same interdendritic region have the same orientation. Probably they were formed from parallel dendrites. It is also found that γ texture components γ_A and γ_B follow the Blackburn's OR with α_2_1 and so are γ_C and γ_D with α_2_2. In addition, the γ texture components γ_A and γ_B, and γ_C and γ_D are twins. However, normally there should be 6 γ variants when they precipitate from α, but because these 6 variants are very close to each other in crystallographic features and EBSD map is not sensitive, there are always only two variants distinguishable. Therefore, the γ grain size measured by EBSD mapping is actually bigger than their real grain size, and will not be considered in the following discussion. Since most of the γ grains were formed from peritectic α and liquid during quenching, this is an indication that the peritectic α nucleated on the existing β grains and during quenching the γ grains that formed directly from the liquid nucleated either on the peritiectic α or the β. Otherwise, the Blackburn's OR could not be followed. Parts of the pole figures are shown in fig. 4.8 (k).

It is worth noting that in the fct structure of γ and in the hcp structure of α, [110] is normal to (110) and $[11\bar{2}\,0]$ is normal to $(11\bar{2}\,0)$, respectively. Therefore, the OR between {110} in γ and $\{11\bar{2}\,0\}$ in α_2 is also applicable to the OR between <110> in γ and $<11\bar{2}\,0>$ in α_2.

To obtain a deeper insight into interdendritic regions, EBSD mapping with high magnification was carried out and the results are shown in fig. 4.9. The BSE image in fig. 4.9 (a) and the γ texture map in fig. 4.9 (d) clearly show that the interdendritic region has a very fine lamellar structure and the γ volume fraction in fig. 4.9 (d) is larger than the volume fraction of the interdendritic area in fig. 4.9 (a). Combined with BSE image analysis, this indicates that the peritectic α grains already existed between the β dendrite

and the interdendritic liquid before quenching, since γ grains formed directly from the liquid could not form lamellae structure. However, the liquid which contained higher Al level than peritectic α nucleated on those peritectic α grains during quenching, causing the coarsening of those peritectic α grains. When the liquid completely solidified, the coarsened peritectic α grains transformed into lamellar structure on subsequent cooling. It is noticed again that some area in β dendrites might also transformed into γ during quenching, which is attributed to the local enriched Al concentration. OR analysis from the α_2 texture map in fig. 4.9 (c) and γ texture map in fig. 4.9 (d) confirms that the interdendritic γ grains and dendritic α_2 grains follow Blackburn's OR, as shown from the pole figure sin fig. 4.9 (e).

In addition, pole figures also show that γ texture components γ_A and γ_B are twins and γ_C and γ_D are also twins, confirming that they were formed from α grains. The γ_E component has a few degrees deviation from the twin of the γ_D. Furthermore, the angle between (0001) planes of two α_2 texture components in fig. 4.9 (c) is measured to be 60 ° from their (0001) pole figures and the corresponding angles matrix between $<11\bar{2}0>$ directions measured from their $\{11\bar{2}0\}$ pole figures match the standard angle matrix for Burgers variants. Therefore, these two α_2 texture components in fig. 4.9 (c) are also Burgers variants. This is the same as was observed before which confirms that peritectic α nucleated on the β dendrites which transformed into Burgers variants during quenching.

The demonstration of the existence of Burgers variants in Ti4522 Bridgman sample indicates that this alloy solidified from the β phase. As observed from the microstructures shown in fig. 4.1 and 4.2, once the liquid completely solidified into solid, α began to precipitate from β and finally all the β grains would transform to α as the temperature was

further lowered. According to the above OR analysis and discussion, the solidification route for Ti4522 can be deduced:

$L \rightarrow L + \beta \rightarrow L + \beta + \alpha \rightarrow \beta + \alpha \rightarrow \alpha \rightarrow \alpha + \gamma \rightarrow \alpha_2 + \gamma$

In which the α grains between liquid and β dendrites are formed by a peritectic reaction:

$L + \beta \rightarrow \alpha$

During quenching, the Burgers α would be ordered to α_2 grains.

4.1.3 Orientation relationship analysis of Ti4522XD Bridgman sample

To analyse the solidification behaviour of the Ti4522XD Bridgman sample, the OR between each grain quenched in from the liquid and mushy zone were analysed. However, as seen from fig. 4.1 (b) there are three distinctive subregions which can be classified into fine dendrite, coarse dendrite and very coarse dendrite depending on the dendrite size. The method used for OR analysis is the same as that described above which is based on EBSD mapping and mathematical calculation.

4.1.3.1 Orientation relationships in the liquid region

Fig. 4.10 (a) shows the BSE image of the frozen-in liquid region in Ti4522XD Bridgman sample used for EBSD mapping. The phase map in fig. 4.10 (b) indicates that it is composed of α_2 and γ grains which account for 30 vol.% and 65 vol.%, respectively. There is about 5 vol.% that were not resolved, which may be due to the existence of small borides. The γ grains are mainly located around borides. However, no borides were detected by EBSD mapping due to their small size. Actually, most of the γ grains are from lamellar colonies, as seen from fig. 4.3 (a). Therefore, the first solidified phase was α in the areas around borides during quenching, because the formation of borides consumed a certain amount of Ti, leading to the enrichment of Al around borides.

Fig. 4.10 (c) and (d) show the α_2 grain map and its grain size distribution graph. The average α_2 grain size was measured to be about 4 μm. Interestingly, no texture map can be obtained from the EBSD mapping which indicates there are no α_2 grains and γ grains that have the same texture. Therefore, the α_2 and γ normal orientation maps were used for OR analysis, as shown in fig. 4.10 (e) and (f), with their own orientation colour key in fig. 4.10 (g) and (h), respectively, which indicates roughly the normal orientation of each grain. On the whole, it is seen that both α_2 and γ grains are randomly orientated. Actually, the pole figures derived from the orientation maps are more accurate than those from texture components, since one texture component may contain many grains with low angle grain boundaries or with different orientations even though they are in the same texture family. However, the normal orientation map and its corresponding rolling direction orientation map, which was discussed in the Chapter 3, should be used together to differentiate the grains that have different orientations. In the following discussion, all the grains labelled in normal orientation maps are actually judged from both normal and rolling direction orientation maps. To save space, all the rolling direction orientation maps are not presented.

Since there are so many grains in this map, the OR analysis is focused on one particular area as labelled in fig 4.10 (e) and (f) in white dashed rectangles, and these regions are enlarged in fig. 4.11 (a) and (b) which refer to the α_2 and γ orientation maps. In each map, the α_2 grains and γ grains are numbered by numbers and English letters, respectively. As seen from the maps, 20 α_2 and 11 γ grains were selected for OR analysis. In this case, individual pole figure from each individual grain are used.

Through measurement of angles between (0001) planes and $<11\bar{2}0>$ directions and comparison between those measured angle matrixes with standard angle matrixes in Appendix 3, it is found that of all those 20 grains, α_2 grain labelled 1, 2 and 3 are one

group of Burgers variants, and the others are not. Therefore, the α_2 grain 1, 2 and 3 are from the same parent β grain by solid phase transformation. It is also found that α_2_1 and γ_A, α_2_5 and γ_F, α_2_6 and γ_G, α_2_13 and γ_H and α_2_9 and γ_I follow Blackburn's OR. Therefore, during quenching the first solidified α which was around borides nucleated on the β. Parts of the pole figures of α_2 and γ grains are shown in fig. 4.11 (c).

The existence of Burgers variants and Blackburn's OR indicates that the basic solidification route for Ti4522XD is the same as Ti4522. However, no apparent peritectic α grains and fewer Burgers variants are found and the grains are smaller.

4.1.3.2 Orientation relationships in fine dendrites

The microstructure of fine dendrites in Ti4522XD Bridgman sample is shown in fig. 4.12 (a). The phase map in fig. 4.12 (b) confirms that the dendrites are composed of α_2 grains which account for 40 vol.% in the map, and the interdendritic regions are composed of γ grains which account for the remaining 60 vol.%. The α_2 grain map in fig. 4.12 (c) and its corresponding grain size distribution graph in fig. 4.12 (d) show that the average α_2 grain size is about 10 μm. Again, the α_2 and γ normal orientation maps in fig. 4.12 (e) and (f) with their own orientation colour key in fig. 4.12 (g) and (h) are used for OR analysis. It is seen that there are hundreds of α_2 and γ grains. To save analysing time, one particular dendrite at the bottom of this region, as marked in fig. 4.12 (e) and (f), was selected for further OR analysis.

The selected area is enlarged in fig. 4.13 (a) and (b) which refer to the α_2 and γ orientation maps, in which 20 α_2 grains and 15 γ grains were picked up and labelled. It is seen that there are two dendrites. In the bottom one only α_2_4, α_2_6 and α_2_17 are not in Burgers family. All in the top dendrite have no relation with the bottom dendrite. Some in the top dendrites, such as α_2_7 and α_2_8, belong to another Burgers family. It is also found that of

all the α_2 grains and γ grains, α_2_1 and γ_B, α_2_12 and γ_E, α_2_2 and γ_E, α_2_4 and γ_G and α_2_11 and γ_J follow Blackburn's OR. In addition, γ_C and γ_D, γ_F and γ_G and γ_K and γ_L are identified to be γ twins. No borides were detected by EBSD mapping due to their small size. Fig. 4.13 (c) shows parts of pole figures from α_2 grains and γ grains.

Again, the solidification behaviour in the fine dendritic region is similar to that in Ti4522 Bridgman sample, but without apparent peritectic α grains and with fewer Burgers variants and with smaller grain size.

4.1.3.3 Orientation relationships in coarse dendrites

Fig. 4.14 (a) shows the microstructure of coarse dendrites. In this image, the possible peritectic α grains which already existed before quenching can be identified which have the intermediate contrast between β dendrites and the interdendritic liquid as indicated in fig. 4.14 (a). In conjunction with the phase map in fig. 4.14 (b), it is seen that most of those peritectic α grains transformed into γ during quenching. Fig. 4.14 (b) also shows that borides were also detected, in addition to α_2 phase and γ phase. This is due to their big size. The crystal structure of these detected borides is identified to be TiB with B27 structure which belongs to space group Pnma (No. 62). The indexing of Kikuchi pattern from one of those borides is shown in fig. 4.14 (h). In this coarse dendritic region, the average α_2 grain size was measured to be 18 μm, bigger than those in the fine dendritic region, as shown in its grain map and grain size distribution graph in fig. 4.14 (c) and (d). Orientation maps of α_2, γ and borides are all obtained as shown in fig. 4.15 (e) to (g). Fig. 4.15 (i) to (k) are the orientation colour keys to α_2, γ and TiB orientation maps.

To analyse the OR in the dendrites, three regions are selected which are labelled as I, II and III as shown in fig. 4.14 (e). For the region I, the enlarged α_2, γ and TiB orientation maps are shown in fig. 4.15 (a), (b) and (c), respectively. The (0001) and the corresponding

$\{11\bar{2}0\}$ α_2 pole figures of 31 α_2 grains marked by numbers in fig. 4.15 (a), the {111} and the corresponding {110} γ pole figures of 6 γ grains marked by English letters in fig. 4.15 (b) and the {001} and the corresponding {010} TiB (B27) pole figures of the marked boride in fig. 4.15 (c) are analysed. Part of those pole figures are shown in fig. 4.15 (d).

The results of the analysis indicate that of all those 28 α_2 grains only α_2_1, α_2_9, α_2_10 and α_2_11 are from one Burgers family. However, α_2_1 and α_2_11 are parallel. In addition, many α_2 grains which are separated by interdendritic γ grain have the same orientation, such as α_2_3 and α_2_30, α_2_5 and α_2_31, α_2_12 and α_2_29, α_2_18 and α_2_28, α_2_20 and α_2_27, α_2_22 and α_2_24, α_2_21 and α_2_25, and α_2_19 and α_2_26, as marked by elliptical circles in fig. 4.15 (a), half of which are from one dendrite. This is quite similar to the situation in the original mushy zone of Ti4522 Bridgman samples as shown in fig. 4.8. However, those α_2 grains are not Burgers variants which is very different from the situation observed in fig. 4.8. In addition, all the selected γ grains in the interdendritic regions still follow the Blackburn's OR with their neighbouring α_2 grains in the dendrite, i.e. γ_A and α_2_3, γ_B and α_2_12, γ_C and α_2_16, γ_D and α_2_20, γ_E and α_2_22, and γ_F and α_2_15.

As observed in the boron-free Ti4522 Bridgman sample in fig. 4.8, if the α_2 grains in the dendrites were formed by solid phase transformation from original β during quenching they should be Burgers variants. However, the majority of them, especially those adjacent to interdendritic γ grains, are non-Burgers variants in Ti4522XD. The break-down of Burgers relationships must have happened during quenching. Considering that the α_2 grains that are adjacent to the interdendritic γ grains still have the Blackburn's OR with their neighbouring γ grains, many of which are peritectic α grains before quenching, and that many α_2 grains separated by interdendritic γ grains have the same orientation, it is assumed that those non-Burgers variants were formed by nucleation on the peritectic α

grains during quenching, which in turn nucleated on the small borides in the liquid in the interdendritic regions. In this way, the peritectic α grains do not have to obey Burgers relationships. However, in the whole process the Blackburn's OR between non-Burgers variants and the γ grains that formed from peritectic α during quenching remains. Those non-Burgers variants might be the main reason for the grain refinement in Ti45222XD, which will be discussed in detail in Chapter 6. As observed from fig. 4.11 and fig. 4.13, those non-Burgers variants in the liquid region and the fine dendrites in the mushy zone in Ti4522XD are not evident. This is because at the early stage of solidification there are not many peritectic α grains which can only form in the late stage of solidification when the Al is enriched in the interdendritic liquid regions.

What is more, the α_2_1 is found to have certain ORs with TiB:

(0001)α_2 // (001) TiB (B27)

<11$\bar{2}$ 0>α_2 // [010] TiB (B27)

It is worth noting that this α_2 _1 is a Burgers variant, indicating the original β dendrite nucleated on this boride and during quenching, the α_2_1 grain which is located inside the dendrite and adjacent to the boride inherited the OR with the boride from the parent β. However, the other α grains that are close to the interdendritic liquid transformed in another way as discussed before, leading to the breakdown of Burgers OR.

In addition, it is observed that the growth direction of TiB type boride is parallel to the spot in the {010} TiB (B27) pole figure, as shown in fig. 4.15 (d), which indicates the fastest growing direction of TiB with B27 structure is along the [010] direction.

For the regions II, the ORs between 12 α_2 grains in fig. 4.16 (a), 7 γ grains in fig. 4.16 (b) and one boride in fig. 4.16 (c) are also analysed using the same method. Similar conclusions are found. That is:

i. α_2 _1 has the OR with TiB (B27):

   (0001)α_2 // (001) TiB (B27)

   <11$\bar{2}$ 0>α_2 // [010] TiB (B27)

ii. The growth direction of TiB (B27) boride is along the [010] direction

iii. γ grains in the interdendritic regions follow Blackburn's OR with their neighbouring α_2 grains, i.e. γ_A and α_2_9, γ _B and α_2_8, γ _D and α_2_7 and γ _G and α_2_2

iv. Some γ grains in the interdendritic regions are twins, i.e. γ_B and γ_C, and γ_D and γ_E

v. α_2_6 and α_2_11, and α_2_2 and α_2_10 are possible Burgers variants from two different Burgers families.

It is noticed that the α_2 _1 that has the OR with TiB is not Burgers variant. Therefore, it is possible that the α_2 _1 grain was formed by heterogeneous nucleation on this boride during β to α solid phase transformation during quenching. That means the borides can act as inoculants, hence increasing the number of nuclei for α phase transformation and furthermore refining the as-cast grain size again. Parts of pole figures from α_2 grains, γ grains and TiB (B27) are presented in fig. 4.16 (d), from which the above ORs can be deduced.

In region III, 9 α_2 grains, 4 γ grains and one boride are marked in their enlarged orientation maps in fig. 4.17 (a), (b) and (c) associated with parts of their pole figures in fig. 4.17 (d). The ORs between them are found to be:

i. No Burgers variants
ii. No OR between TiB (B27) and neighbouring α_2 grains
iii. The growth direction of TiB (B27) is along [010]
iv. γ grains in the interdendritic regions follow Blackburn's OR with their neighbouring α_2 grains, i.e. γ_A and α_2_5, and γ _B and α_2_4

From the above analysis, it is seen that the majority of α_2 grains in the dendrites, especially those adjacent to interdrendritic regions, are not Burgers variants as the growth of dendrites and both Burgers and non-Burgers α_2 grains were found to have the OR with borides.

4.1.3.4 Orientation relationships in very coarse dendrite

Fig. 4.18 (a) shows the microstructure of very coarse dendrites in Ti4522XD Bridgman sample, which contains 55 vol.% α_2 phase, 43 vol.% γ phase and 1 vol.% TiB with the other 1 vol.% unsolved, as shown from the phase map in fig. 4.18 (b). It is also observed from fig. 4.18 (a) and (b) that there is a lot of peritectic α between β dendrites and interdendritic liquid which transformed into γ during quenching, as indicated in fig. 4.18 (a). It is seen that the α_2 volume fraction is constantly increasing from the fine dendrites to the very coarse dendrites. Fig. 4.18 (c) and (d) give the α_2 grain map and its corresponding grain size distribution graph, from which the average α_2 grain size was measured to be 20 μm. Compared with α_2 grain sizes in the fine and coarse dendrites, the α_2 grains are coarsened significantly.

Four regions marked as I, II, III and IV in fig. 4.18 (e) are selected for OR analysis, in which the borides are contained. Since there are only 18 α_2 grains in total that have

different orientation and the α_2 grain boundaries are long and clear, misorientation mapping is utilised in advance to define the neighbouring α_2 grains that make misorientations close to 10.53 °, 60 °, 60.83 °, 63.26 ° and 90 °. Only when the misorientation is close to those five values can the neighbouring α_2 grains be possible Burgers variants. It is found that only α_2_4 and α_2_5 labelled in fig. 4.18 (e) and (k) make a misorientation close to 60 °. However, further calculation based on the above method reveals that they are not Burgers variants, which indicates that the traditional misorientation-based method is not an accurate way to judge whether the neighbouring α/α_2 grains are Burgers variants. Nevertheless, the new method was used to check if there are any Burgers variants among those that are not adjacent, and found that only α_2_5 and α_2_6 are possible Burgers variants. Therefore, only the OR between α_2 grains and γ grains and OR between metallic phases and borides are considered in the four selected regions.

In the region I, (0001) and its corresponding $\{11\bar{2}0\}$ pole figures of α_2_2, {111} and its corresponding {110} pole figures of γ_F, and {001} and its corresponding {010} pole figures of TiB (B27) are shown fig. 4.19. Evidently, the following OR can be concluded:

i. α_2_1 and γ_F follow Blackburn's OR
ii. The growth direction of TiB (B27) is along [010], but they do not have OR with α_2_1

In the region II and III, the same analysing processing based on α_2 and γ pole figures shown in fig. 4.20 and fig. 4.21 leads to:

i. The γ grains in the interdendritic regions always follow Blackburn's OR with their neighbouring α_2 grains, such as α_2_4 and γ_A / γ_C, α_2_5 and γ_B, α_2_14 and γ_D / γ_E, in which γ_A and γ_C, γ_D and γ_E are twins

ii. The growth direction of TiB (B27) is along [010], but they do not have OR with their neighbouring α_2 grains

However, according to the α_2 and γ pole figures in the region IV, in fig. 4.22, where two TiB (B27) borides are enclosed in α_2_11, TiB (B27)_IV-2 is found to have the ORs with α_2_11 and also the γ_G which is adjacent to α_2_4:

(001)TiB (B27) // (0001)α_2 // {111}γ

[010] TiB (B27) // <11$\bar{2}$0>α_2 // <110>γ

Since α_2_11 grain has the above OR with the boride in the core of dendrite, it could not be formed by nucleation on the adjacent peritectic α during quenching. On the other hand, the α_2_11 grain could not be formed by nucleation on this TiB (B27)_IV-2, either. Otherwise, there should be no Blackburn's OR between α_2_11 and γ_G. Therefore, the possibility for the above ORs is that before quenching the β dendrite nucleated on this boride and the peritectic α nucleated on the β dendrite, and during quenching the α grain inherited the OR with the boride from the parent β dendrite and the γ grain inherited the OR with the neighbouring α grain from the parent peritectic α, meanwhile, the other α grains in this dendrites nucleated on the adjacent peritectic α grains which nucleated on the small borides in the interdendritic liquid. In this way, the other α_2 grains can be non-Burgers variants after quenching. It is also possible that the γ_G nucleated directly on the neighbouring α during quenching. In this case, α_2_11 and γ_G can also follow Blackburn's OR. In addition, another boride TiB (B27)_IV-1 has no such ORs with α_2_11, but the growth direction of TiB (B27) borides is also along [010].

From the OR analysis in the original mushy zone, it is seen that during the growth of dendrites more and more α_2 grains become non-Burgers variants. It is also noticed that

fewer borides in the core of dendrites were found to have OR with their neighbouring α_2 grains in the very coarse dendrites compared with the situation in coarse dendrites. Those borides in the core of dendrites can act as inoculants for both β solidification as demonstrated in fig. 4.15 and fig. 4.22 and α precipitation from β to α solid phase transformation as demonstrated in fig. 4.16.

In summary, from the microstructural observation and orientation relationship analysis of Ti4522 and Ti4522XD Bridgman samples, it is found that:

1. Ti4522XD Bridgman sample has smaller dendrite length, dendrite spacing and lamellar colony size than those in Ti4522 Bridgman.
2. Both Ti4522XD and Ti4522 solidify from β, along the following pathways:

   $L \rightarrow L + \beta \rightarrow L + \beta + \alpha \rightarrow \beta + \alpha \rightarrow \alpha$

   In which the α grains between the liquid and β dendrites are formed by peritectic reaction:

   $L + \beta \rightarrow \alpha$
3. The borides in Ti4522XD Bridgman sample formed directly from the melt, and changed from curvy bright to long bright in terms of morphologies and BSE contrast from the liquid to the fully lamellar. The long bright borides in the dendrites were identified to be TiB with B27 structure with fastest growing direction along the [010].
4. In Ti4522 Bridgman sample, the majority of α_2 grains in both frozen-in liquid region and mushy zone were found to be Burgers variants, while during the growth of dendrites in Ti4522XD Bridgman sample, more and more α_2 grains become non-

Burgers variants and fewer and fewer α_2 grains were found to have OR with the borides in the core of dendrites no matter they are Burgers or non-Burgers variants.

5. In the coarse dendrites of Ti4522XD Bridgman samples, some TiB borides with B27 structure were found to have specific ORs with their adjacent α_2 grains which could be Burgers or non-Burgers variants, and those ORs are:

   $(0001)\alpha_2$ // (001) TiB (B27)

   $<11\bar{2}0>\alpha_2$ // [010] TiB (B27)

   In the very coarse dendrites of Ti4522XD Bridgman samples, ORs between Burgers α_2 grain, γ grain and TiB (B27) boride were found to be:

   (001)TiB (B27) // $(0001)\alpha_2$ // $\{111\}\gamma$

   [010] TiB (B27) // $<11\bar{2}0>\alpha_2$ // $<110>\gamma$

The significance of the above observations on the solidification behaviour and grain refinement in Ti4522XD castings will be discussed in Chapter 6.

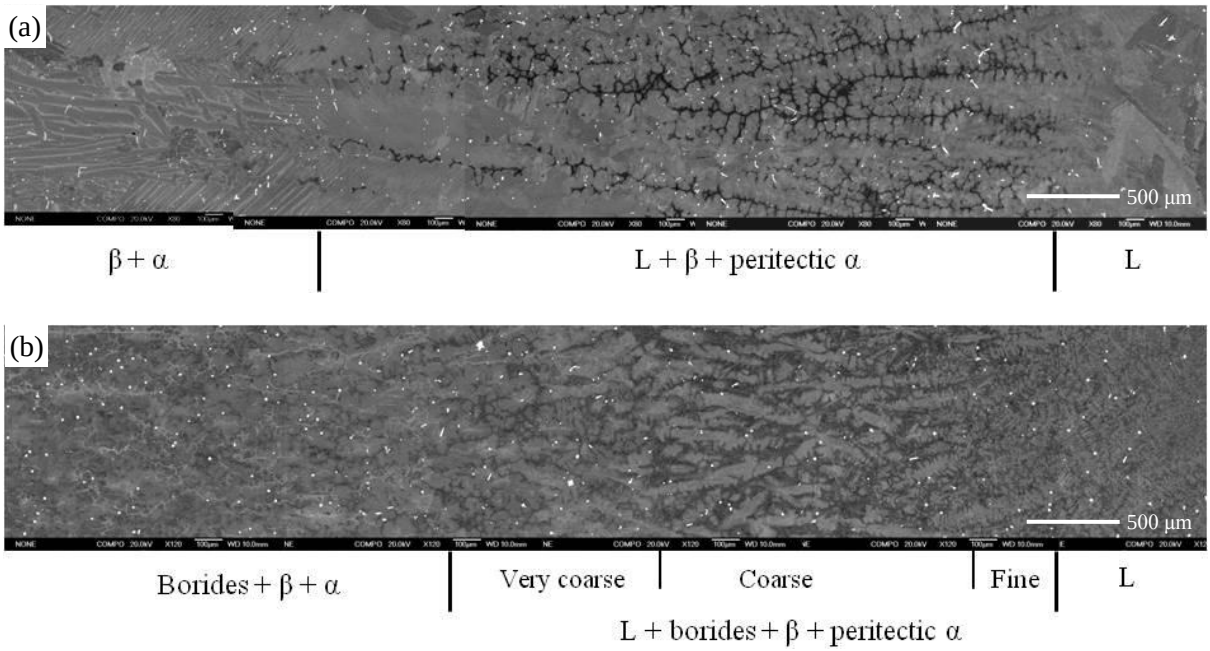

Figure 4.1 SEM images taken using back scattered electrons (BSE) of the overall microstructures of Bridgman samples in longitudinal section along the unidirectional solidification, which is along the temperature gradient in the furnace. (a) is from Ti4522 and (b) from Ti4522XD. L refers to liquid.

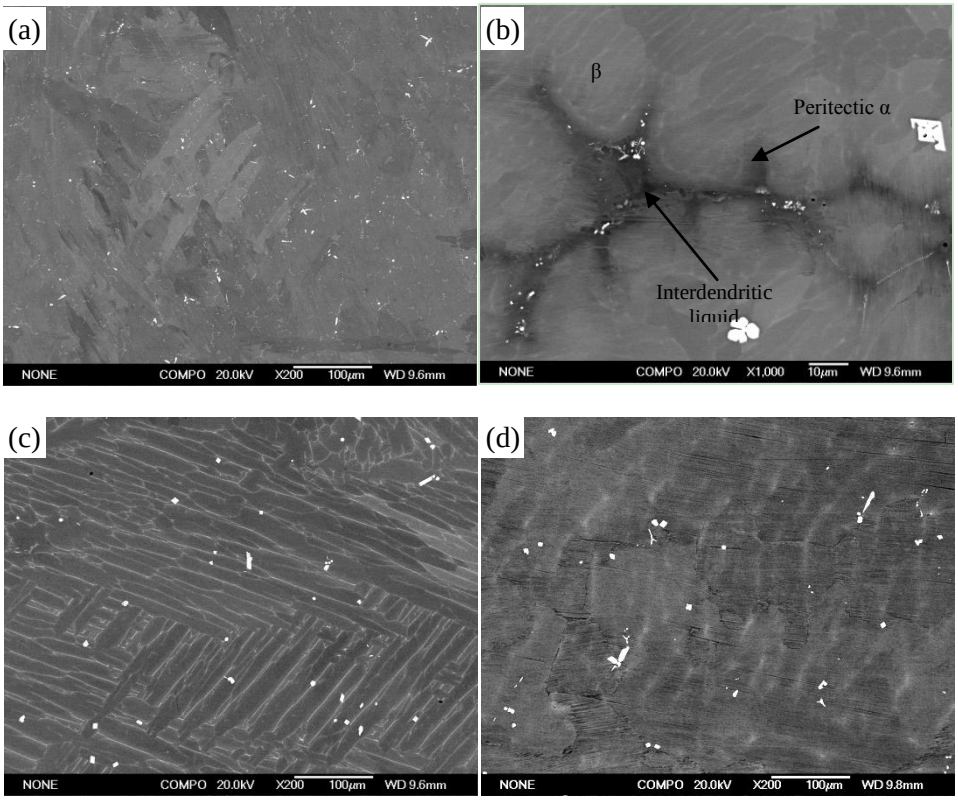

Figure 4.2 SEM BSE images of enlarged microstructures quenched from (a) liquid, (b) β dendrites with liquid in the inderdendritic region and peritectic α in between, (c) (β+ α) region with Widmanstätten structure and (d) lamellar structure which is close to the unmelted area in unidirectionally solidified Ti4522.

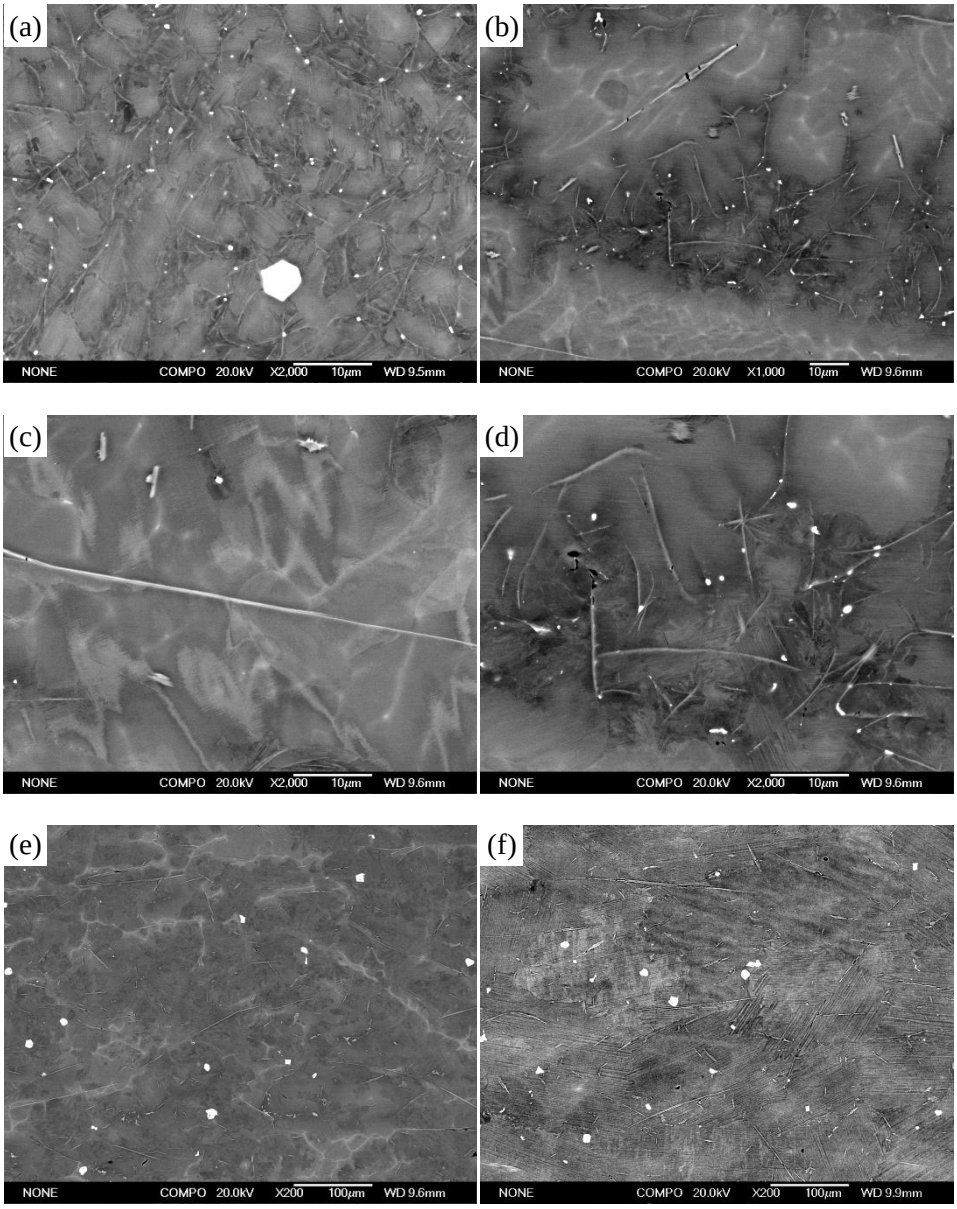

Figure 4.3 SEM BSE microstructures of (a) mushy zone, (b) dendritic region, (c) enlarged image of dendrite in dendritic region, showing the long boride in the core, (d) enlarged image of interdendritic area in dendritic region, showing the very fine lamellar structure (e) (α + massive γ) region and (f) lamellar which is close to the unmelted region in unidirectionally solidified Ti4522XD. From the mushy zone to lamellar zone, the borides change from curvy bright to long bright.

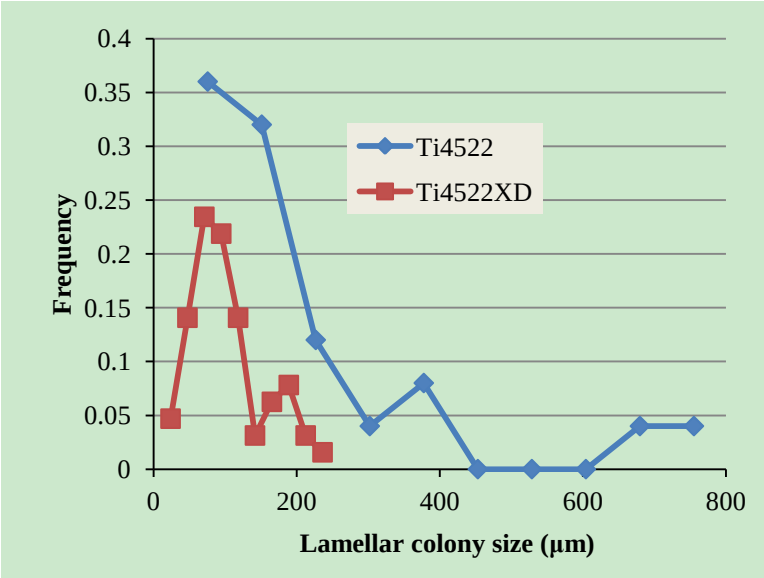

Figure 4.4 The lamellar colony size distribution in the Ti4522 and Ti4522XD Bridgman samples.

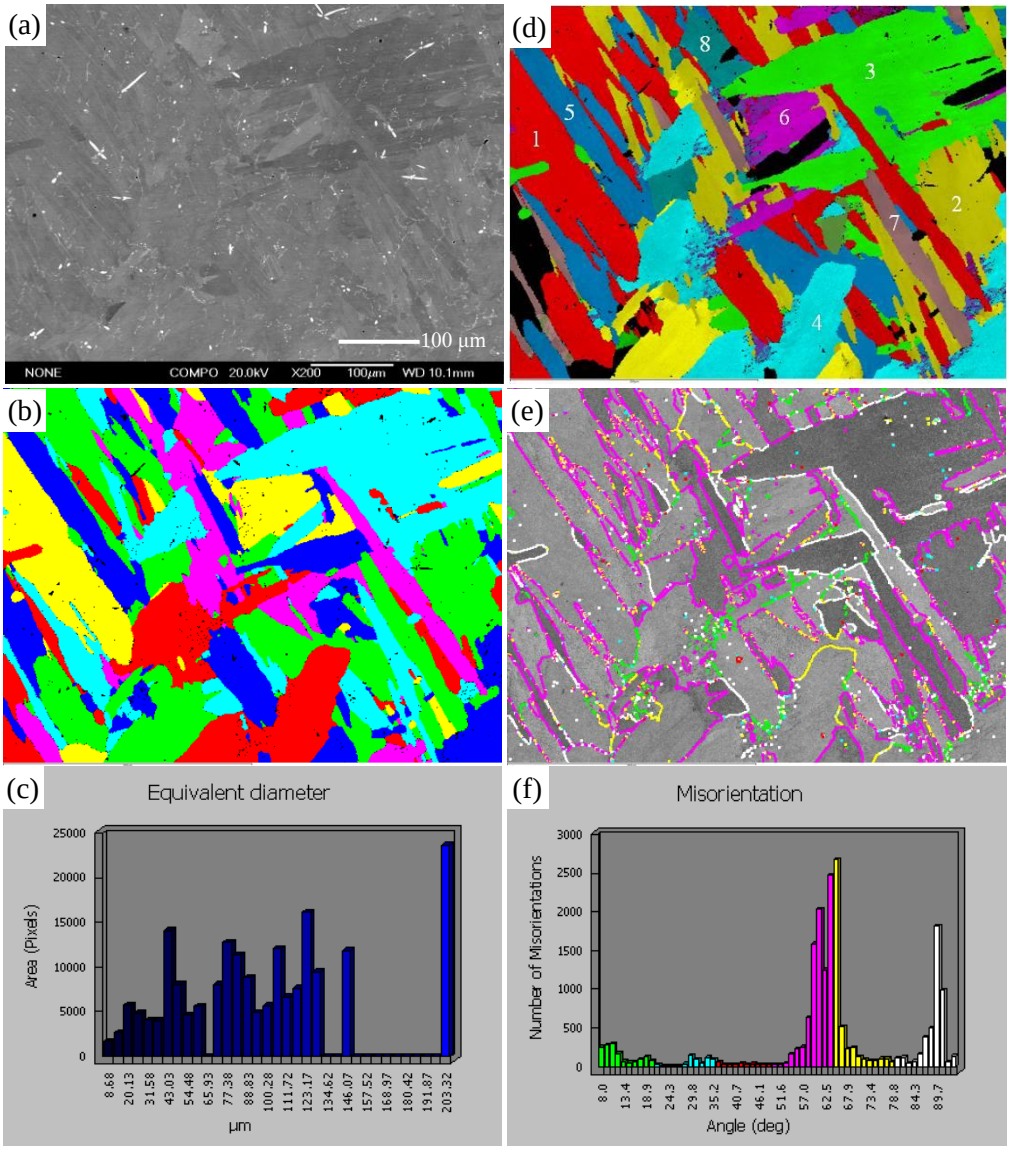

Figure 4.5 (a) BSE microstructure of the region quenched from the liquid in Ti4522 Bridgman sample with the corresponding α_2 grain map and grain size distribution graph in (b) and (c), the α_2 texture map in (d), and the misorientation map and the misorientation distribution graph in (e) and (f). It is shown in (d) that there are 8 α_2 texture components as labelled in the image.

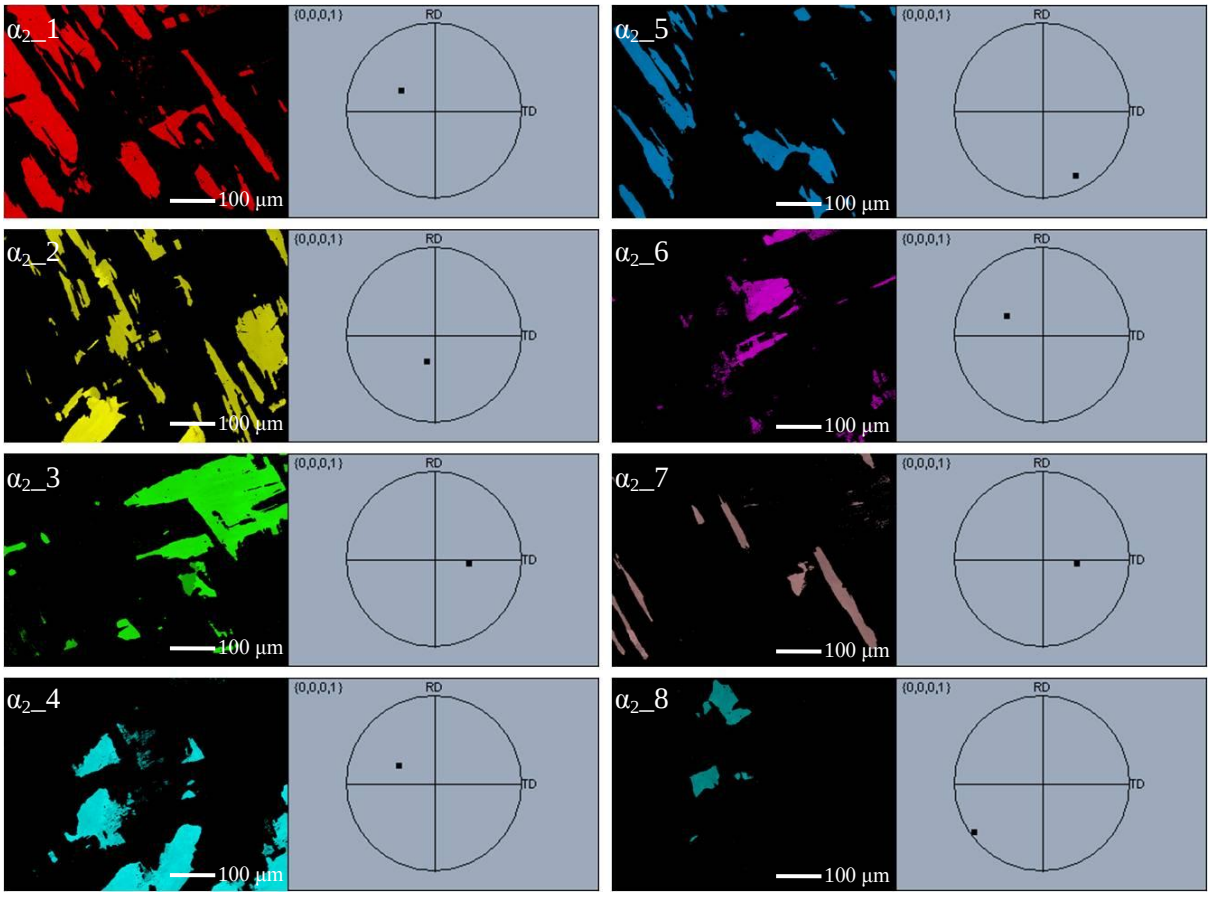

Figure 4.6 Each texture component from the texture map in fig. 4.5 (d) with their variants and their corresponding (0001) pole figures.

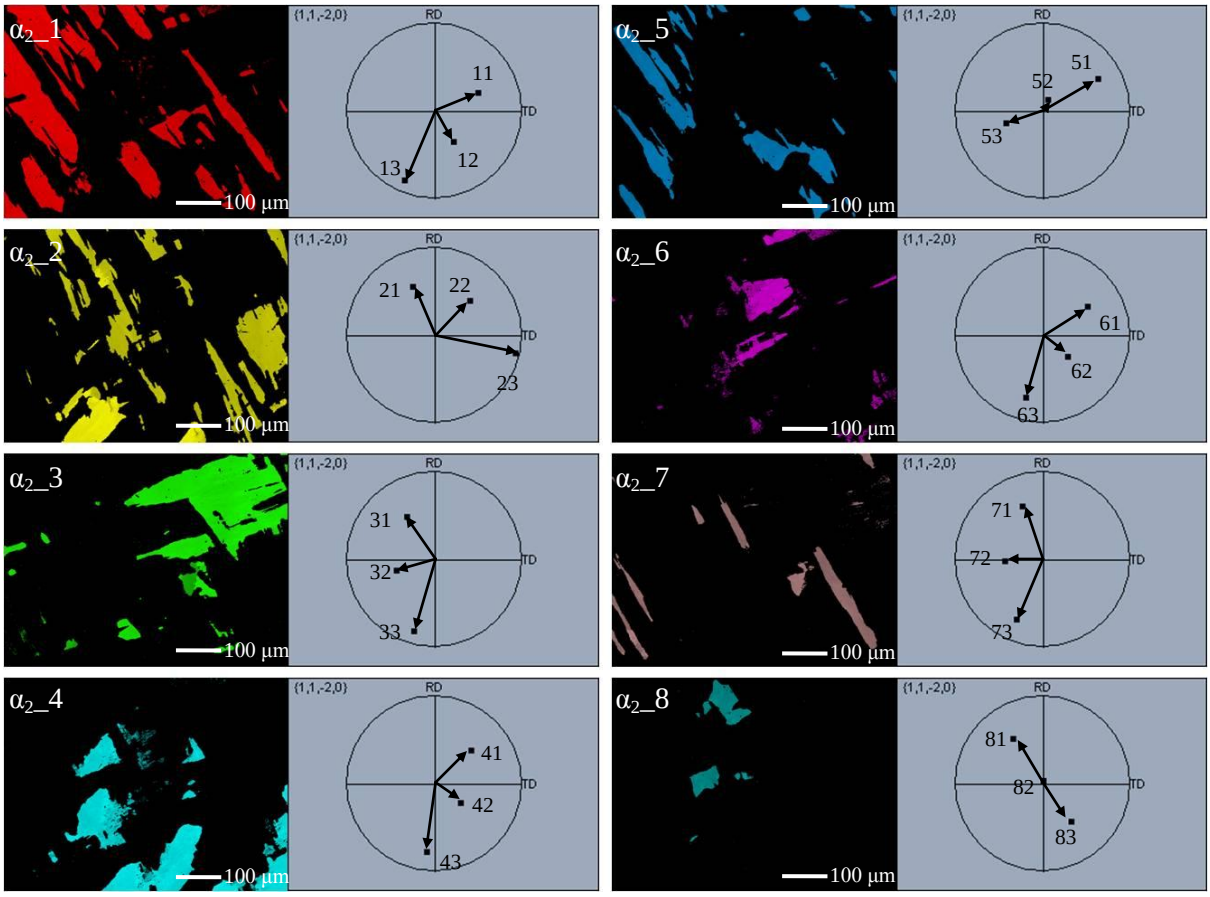

Figure 4.7 Each texture component from the texture map in fig. 4.5 (d) with their variants and their corresponding $\{11\bar{2}0\}$ pole figures.

Angle between (0001)	α_2_2	α_2_3	α_2_4	α_2_5	α_2_6	α_2_7	α_2_8
α_2_1	64	90	4	123	4	90	72
α_2_2		58	64	58	64	59	62
α_2_3			92	61	93	1	120
α_2_4				122	1	92	68
α_2_5					123	62	82
α_2_6						93	68
α_2_7							121

Table 4.1 The angles between (0001) planes from each texture component in fig. 4.5 (d).

Angle between <11$\bar{2}$0>	α_2_21	α_2_22	α_2_23
α_2_11	77.8	18.0	45.6
α_2_12	71.9	76.5	59.4
α_2_13	57.7	42.1	78.4
Angle between <11$\bar{2}$0>	α_2_61	α_2_62	α_2_63
α_2_11	12.3	48.3	70.3
α_2_12	73.4	12.8	48.6
α_2_13	45.5	74.9	13.5
Angle between <11$\bar{2}$0>	α_2_71	α_2_72	α_2_73
α_2_11	76.4	70.2	63.4
α_2_12	69.9	77.2	55.7
α_2_13	53.0	66.9	8.7

Table 4.2 Some examples of the angles between <11$\bar{2}$0> in each texture components in fig. 4.7, in which their (0001) planes make angles close 0 °, 60 ° and 90 °.

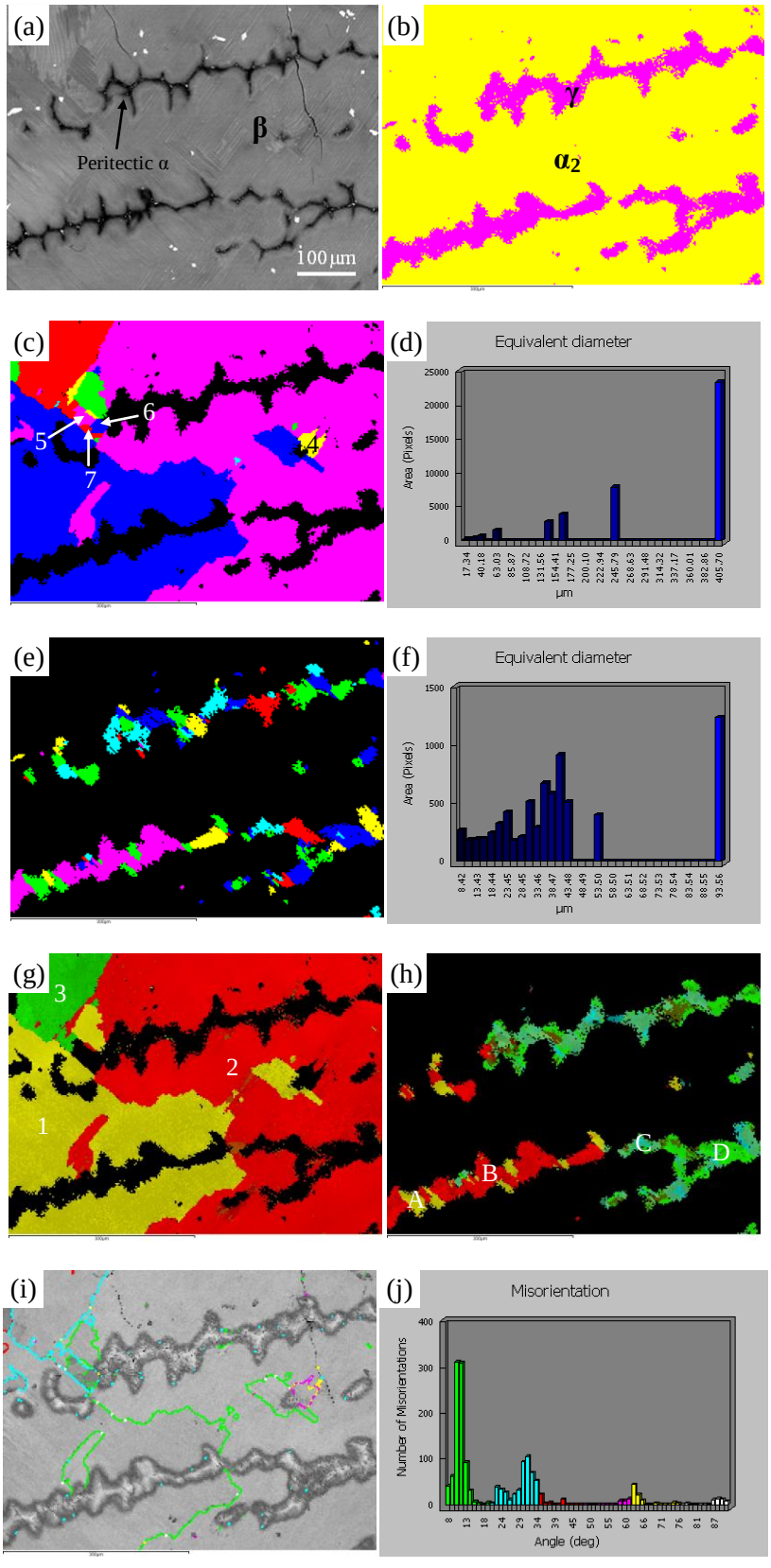
(a)
β
Peritectic α
100 µm
(b)
γ
α2
(c)
6
5
4
7
(d)
Equivalent diameter
Area (Pixels)
µm
(e)
(f)
Equivalent diameter
Area (Pixels)
µm
(g)
3
2
1
(h)
C
D
B
A
(i)
(j)
Misorientation
Number of Misorientations
Angle (deg)

(k)

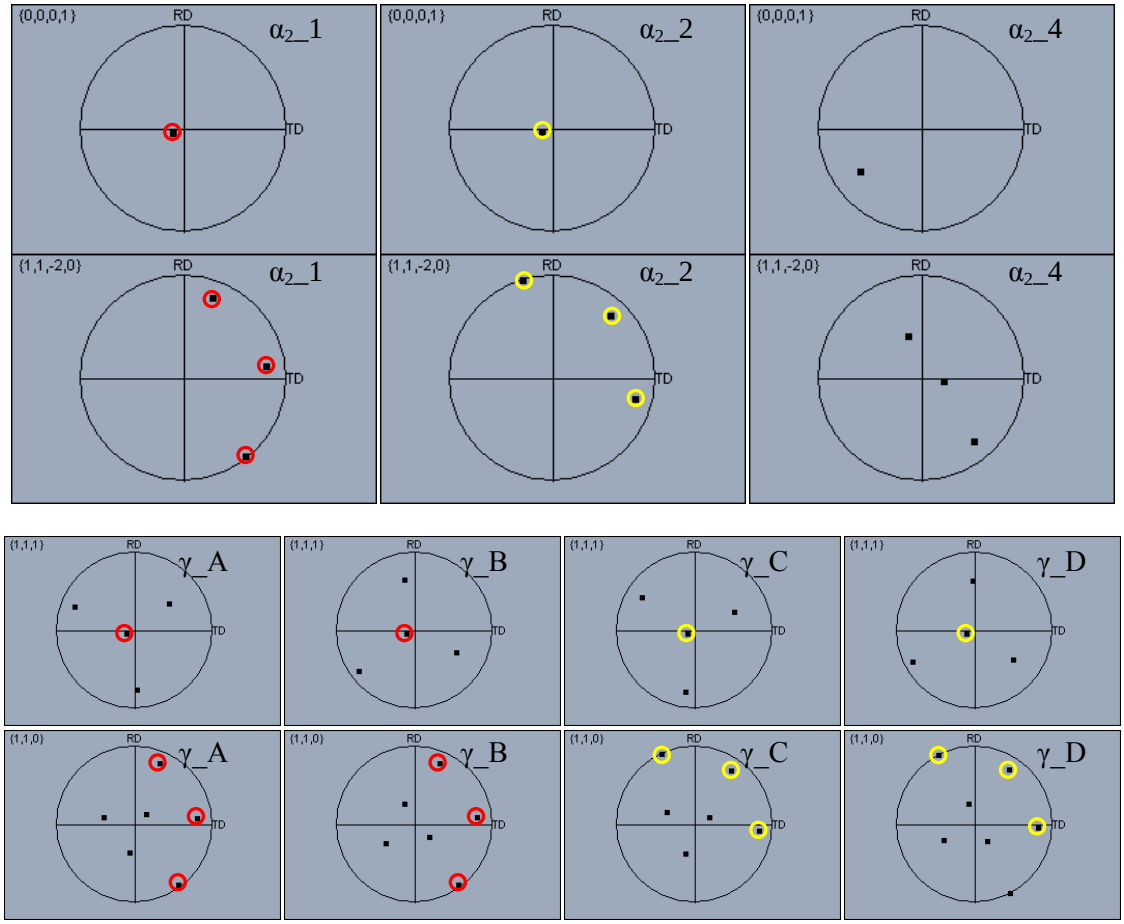

Figure 4.8 Results of orientation mapping of mushy zone in Ti4522, showing (a) the area of mapping, (b) phase map in which ■ and ■ stand for α_2 and γ phase, respectively, (c) and (d) the α_2 grain map and grain size distribution graph, (e) and (f) the γ grain map and grain size distribution graph, (g) and (h) the α_2 and γ texture map, (i) and (j) the α_2 grain misorientation map and its distribution graph, and (k) parts of the (0001) and $(11\bar{2}0)$ pole figure of α_2 and (110) and (111) pole figure of γ. The same colour circle marks in (k) indicate that the γ grains and α_2 grains follow Blackburn's OR, and twin structure among γ grains.

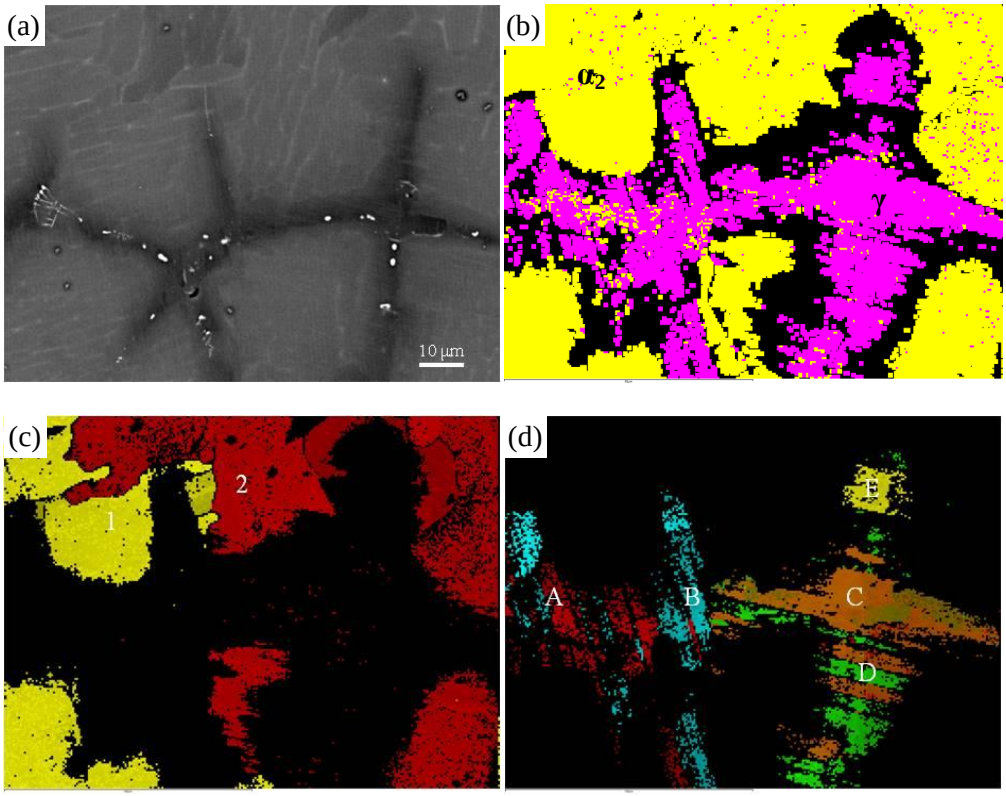

Figure 4.9 To be continued in the next page.

(e)

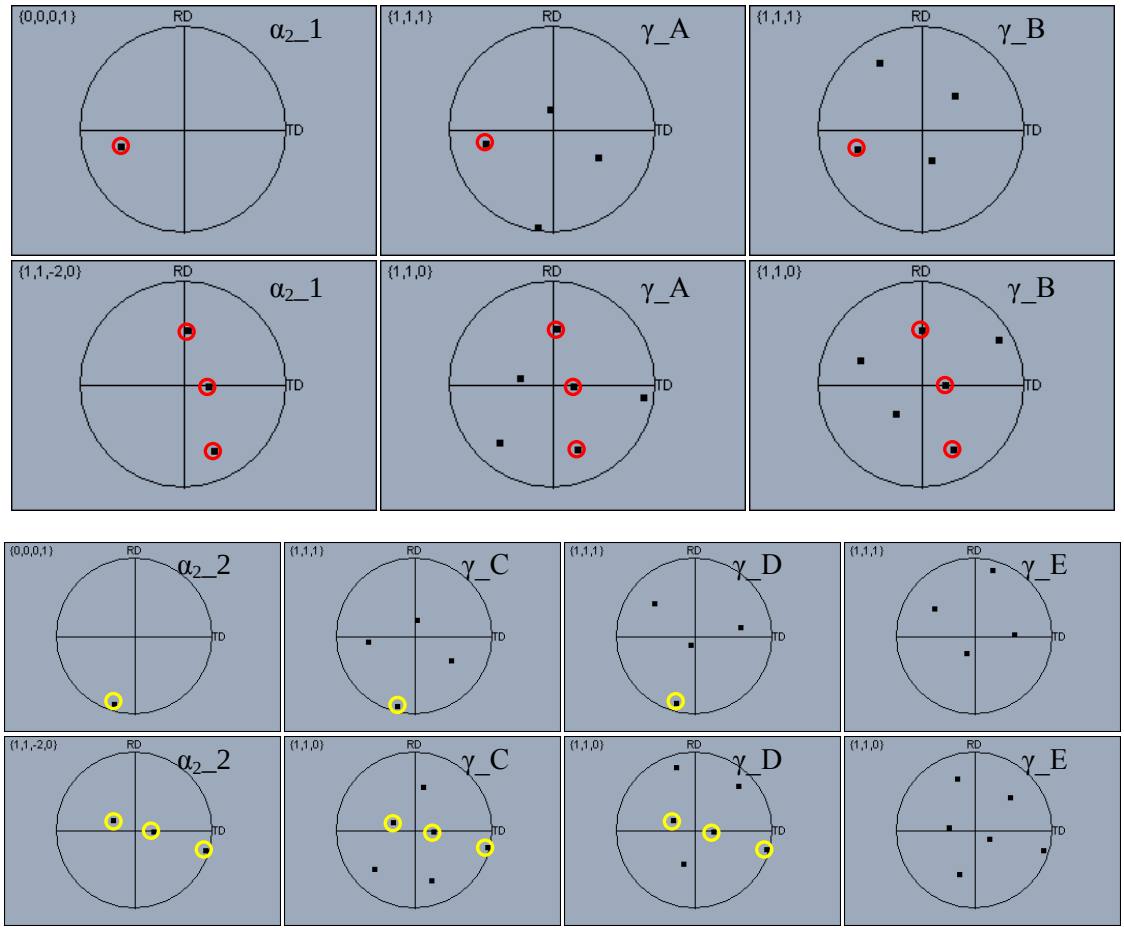

Figure 4.9 Enlarged orientation mapping of dendritic region in Ti4522, showing (a) the area of mapping, (b) phase map in which ■ and ■ stand for α_2 and γ phase, respectively, (c) and (d) the α_2 and γ texture map, (e) the (0001) and $\{11\bar{2}0\}$ pole figures of α_2, and {111} and {110} poles figures of γ. The circle marks in (e) indicate that the γ grains in the interdendritic regions and α_2 grains in the dendrites follow Blackburn's OR and the twin structure among γ grains.

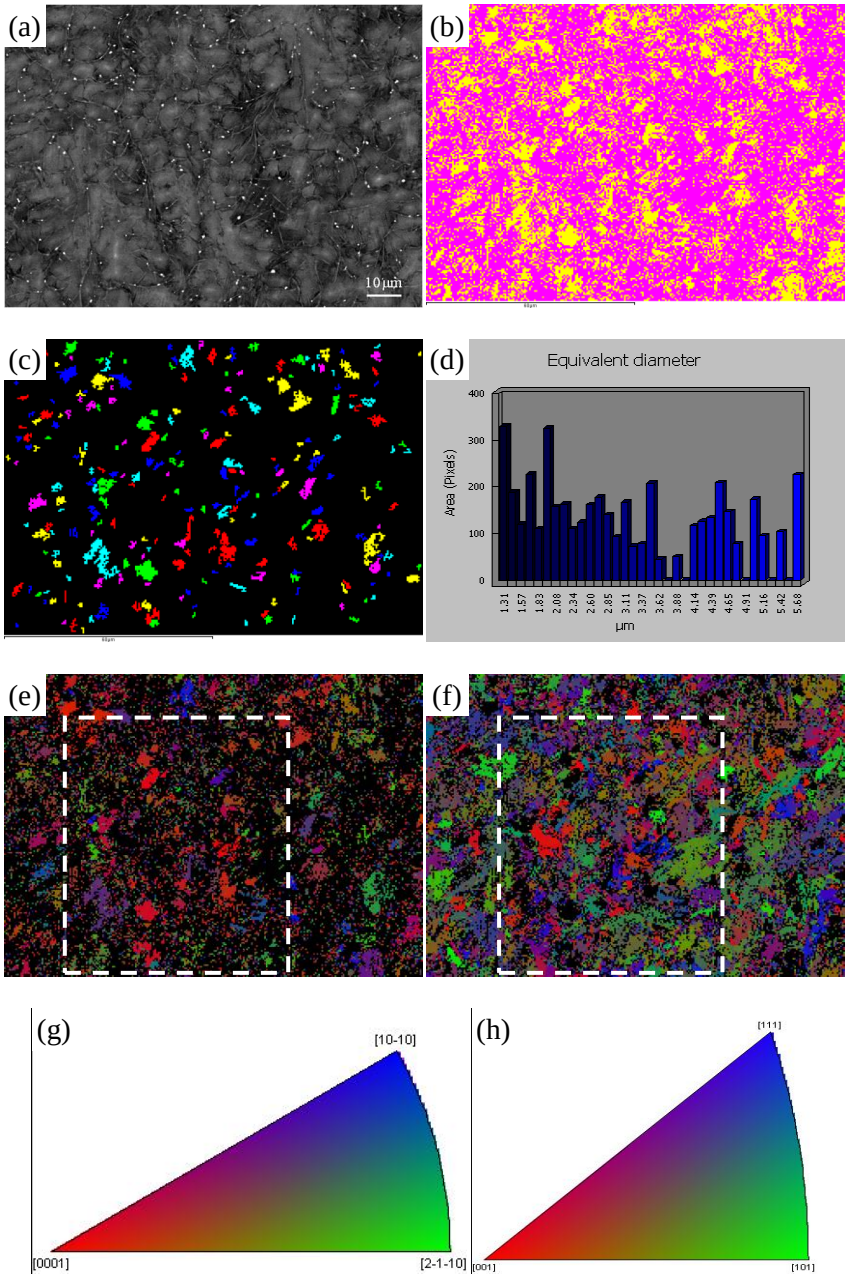

Figure 4.10 Mushy zone in Ti4522XD Bridgman sample with (a) BSE image, (b) phase map in which ■ and ■ stand for α_2 and γ phase, respectively, (c) α_2 grain map with grain size distribution graph in (d), and (e) and (f) α_2 and γ normal direction orientation map with orientation colour key in (g) and (h), respectively.

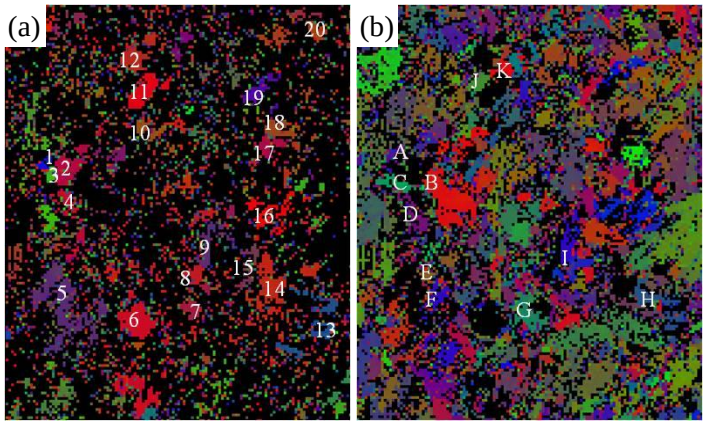

(c)

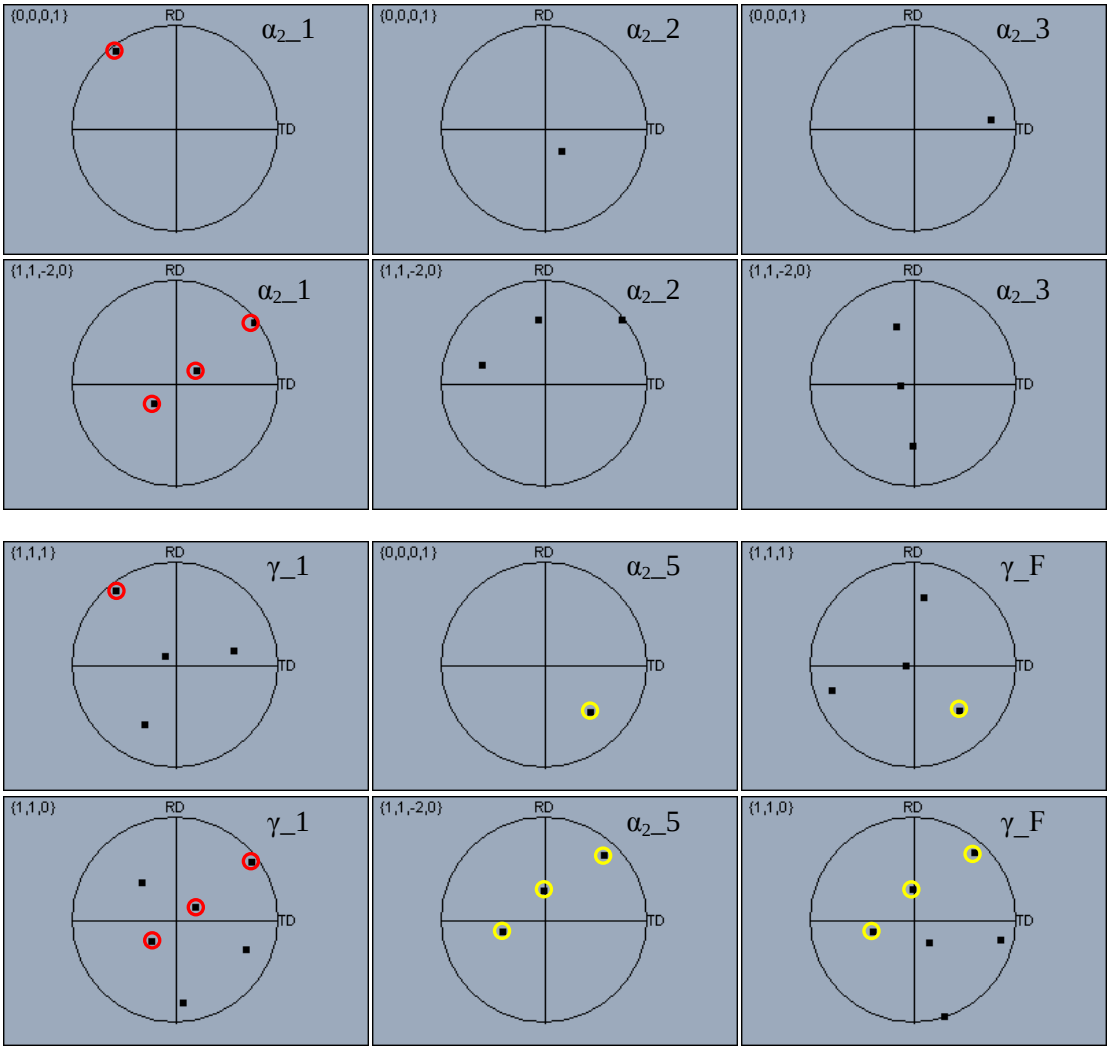

Figure 4.11 Normal orientation maps of α_2 in (a) and γ in (b) from the selected area in fig. 4.10 (e) and (f), (c) part of the pole figures of α_2 grains in both (0001) and $\{11\bar{2}0\}$ poles and γ grains in both $\{111\}$ and $\{110\}$ pole figures.

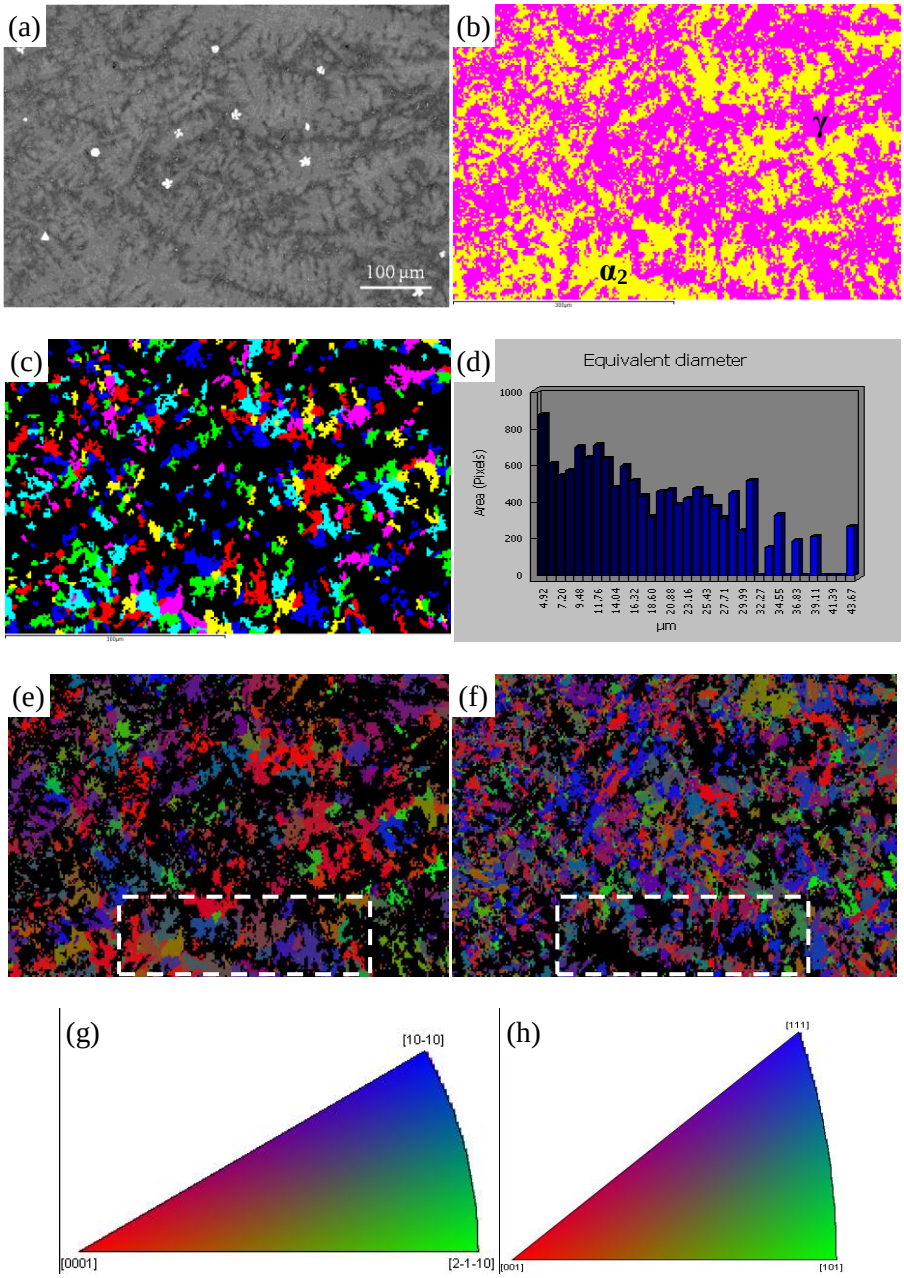

Figure 4.12 Fine dendrites in Ti4522XD Bridgman sample with (a) BSE image, (b) phase map in which ■ and ■ stand for α_2 and γ phase, respectively, (c) α_2 grain map with grain size distribution graph in (d), and (e) and (f) α_2 and γ normal direction orientation map with orientation colour key in (g) and (h), respectively.

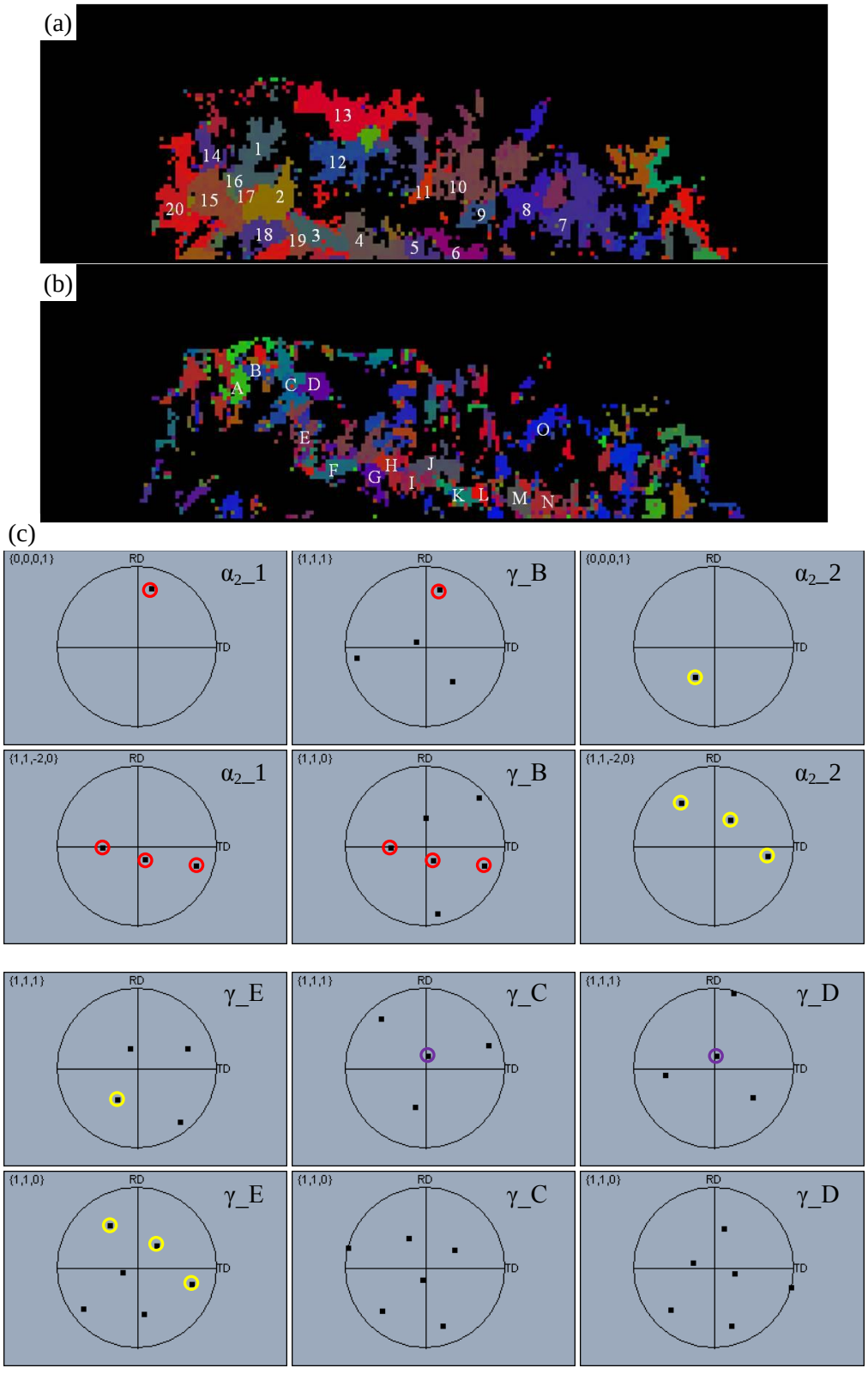

Figure 4.13 Normal orientation maps of α_2 in (a) and γ in (b) from the selected area in fig. 4.13 (e) and (f), respectively, (c) parts of the pole figures of α_2 grains and γ grains.

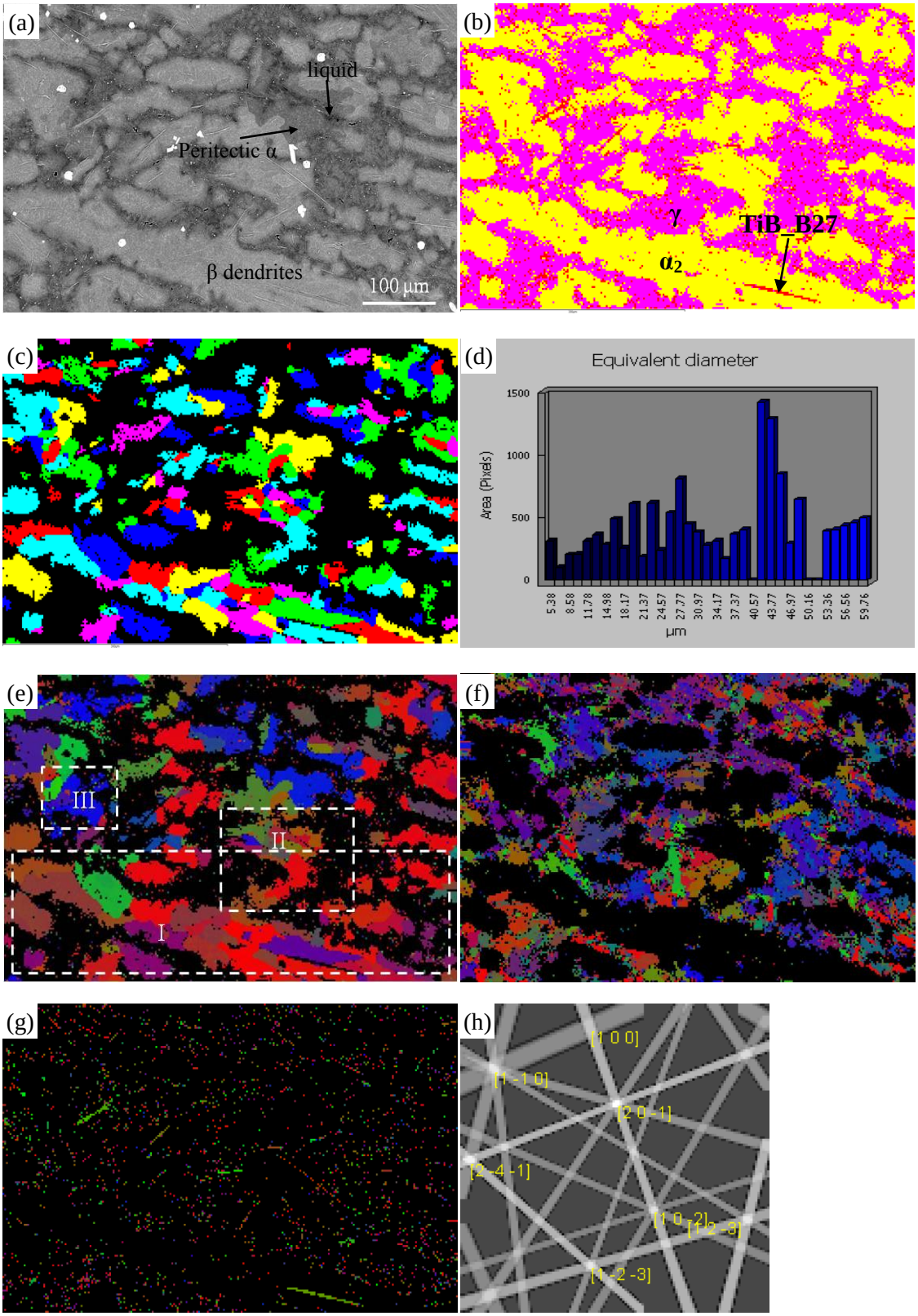
(a)
liquid
Peritectic α
β dendrites
100 μm
(b)
γ
TiB_B27
α2
(c)
(d)
Equivalent diameter
Area (Pixels)
1500
1000
500
0
5.38
8.58
11.78
14.98
18.17
21.37
24.57
27.77
30.97
34.17
37.37
40.57
43.77
46.97
50.16
53.36
56.56
59.76
μm
(e)
III
II
I
(f)
(g)
(h)
[1 0 0]
[1 -1 0]
[2 0 -1]
[2 -4 -1]
[1 0 -2]
[1 2 -3]
[1 -2 -3]

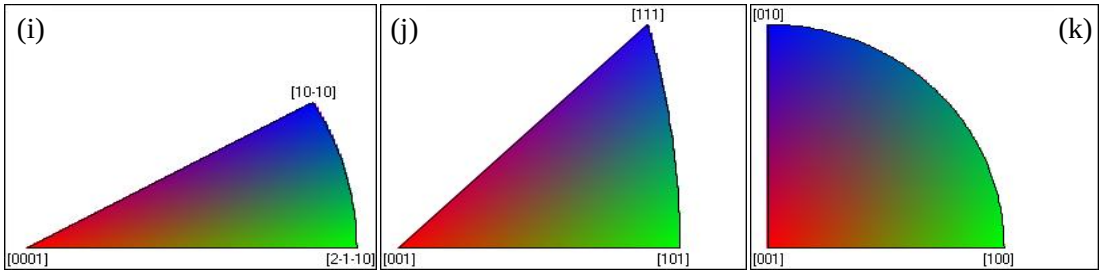

Figure 4.14 Coarse dendrite in Ti4522XD Bridgman sample, showing (a) BSE image with original phase before quenching indicated, (b) phase map in which ■, ■ and ■ stand for α_2, γ and TiB (B27) phase, respectively, (c) α_2 grain map with grain size distribution graph in (d), (e) , (f) and (g) α_2, γ and TiB (B27) normal direction orientation maps with orientation colour keys in (i), (j) and (k), respectively, (h) the indexing of TiB which is identified to belong to space group Pnma (No.62) which is B27 structure.

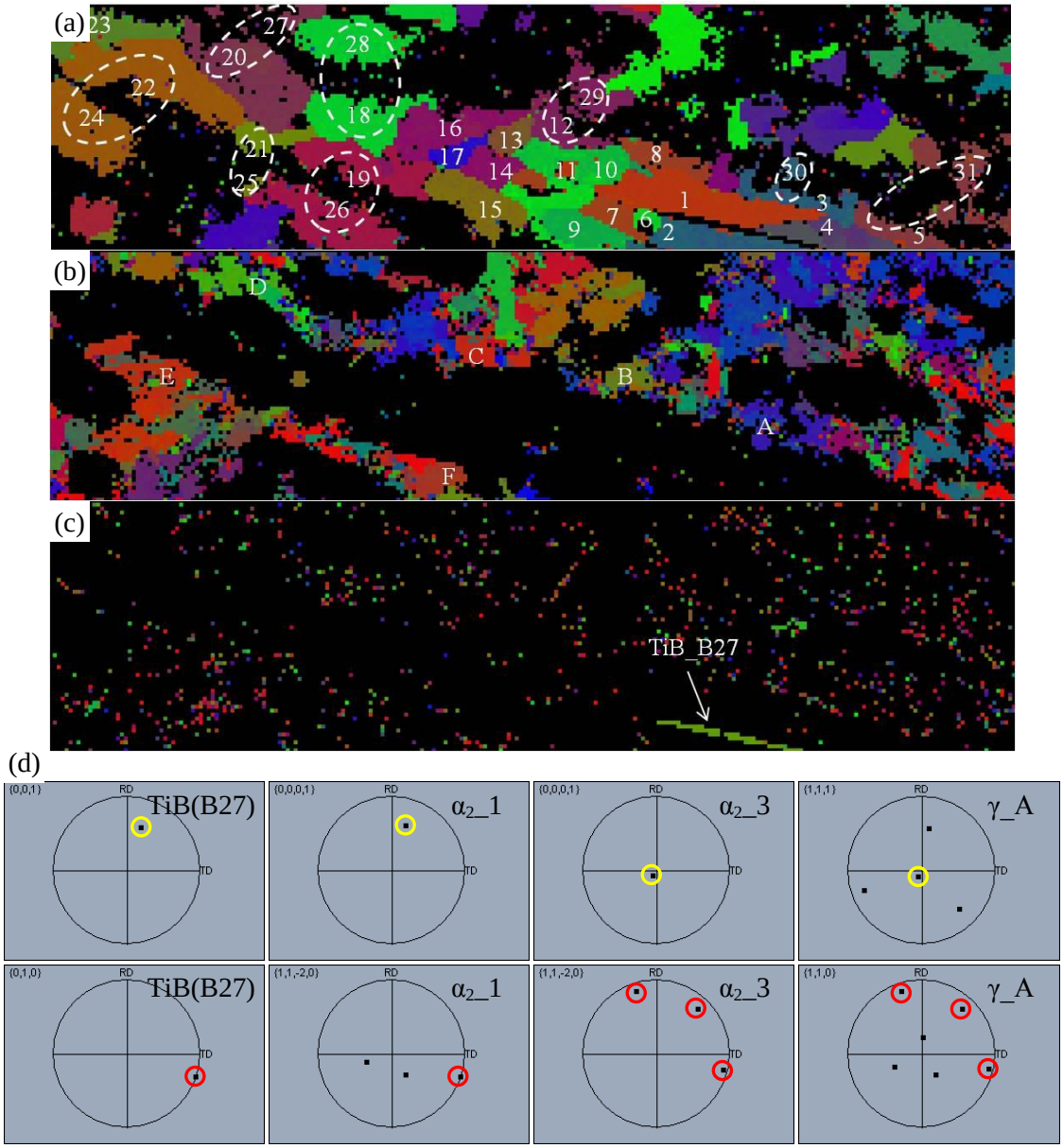

Figure 4.15 Enlarged orientation maps of (a) α_2, (b) γ and (c) TiB (B27) associated with parts of their pole figures in (d) from region I in fig. 4.14 (e), indicating the white circled α_2 grains have the same orientation, the γ grains follow Blackburn's OR with their neighbouring α_2 grains and α_2 grain 1 has OR with TiB.

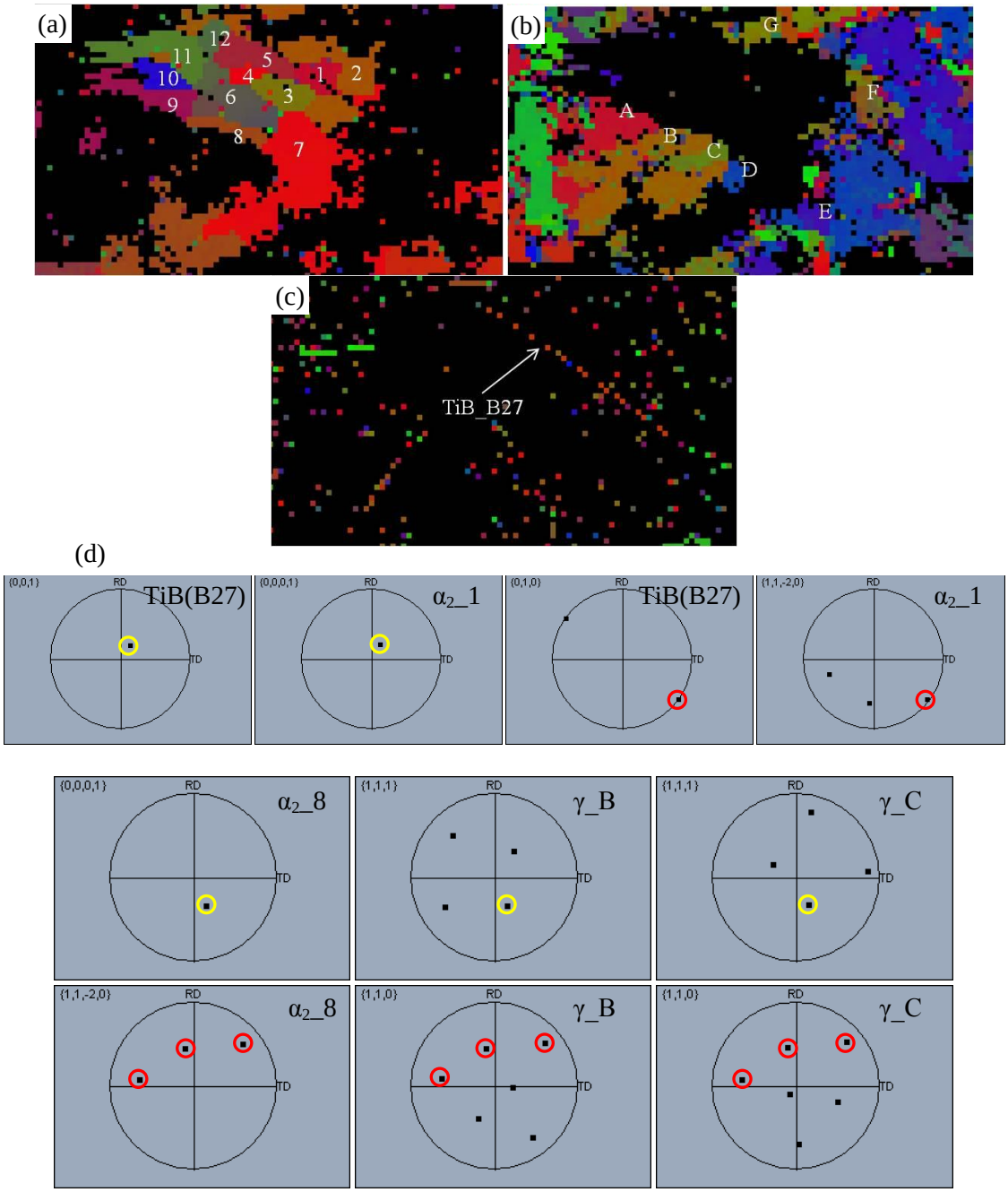

Figure 4.16 Enlarged orientation maps of (a) α_2, (b) γ and (c) TiB (B27) associated with parts of their pole figures in (d) from region II in fig. 4.14 (e).

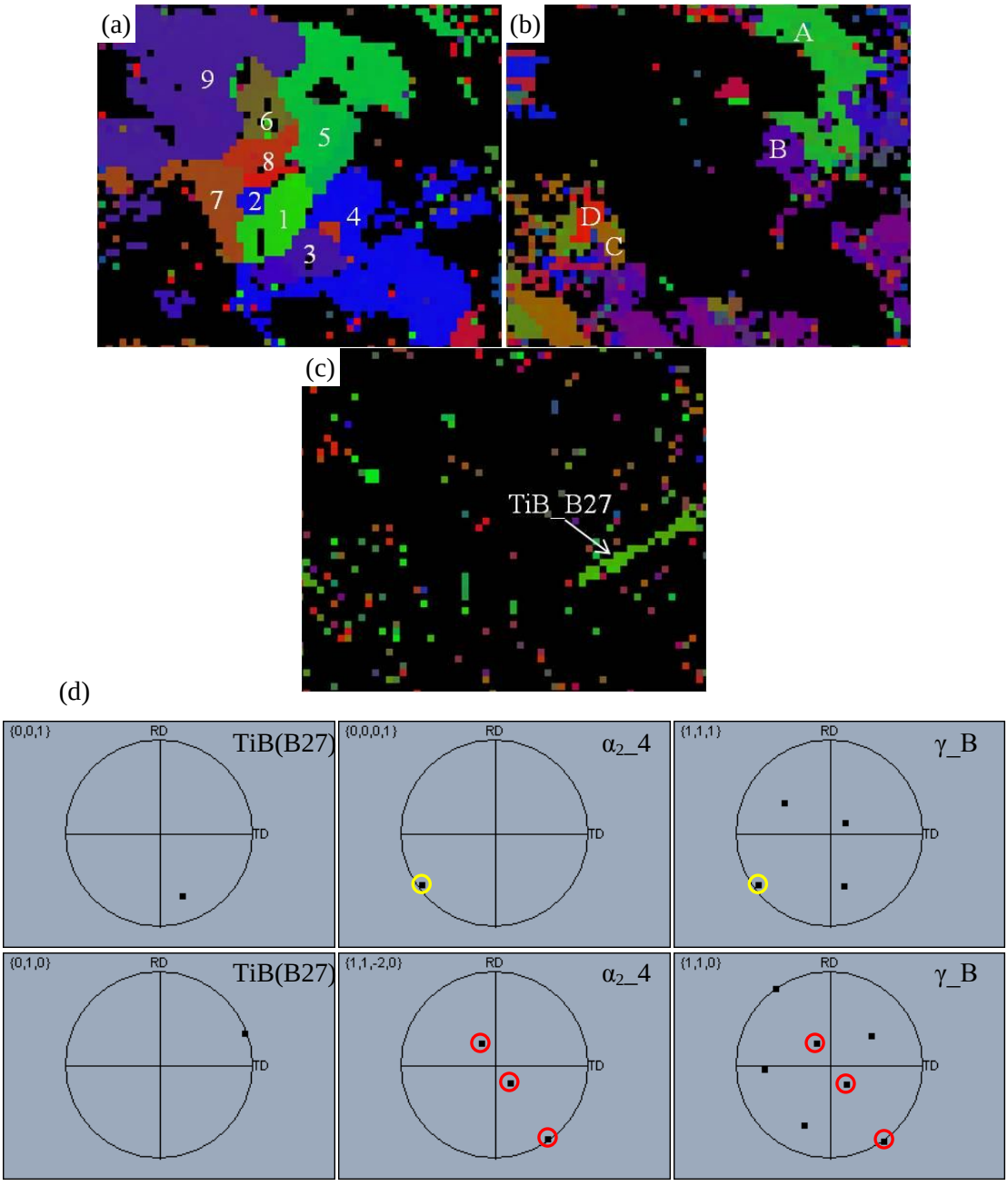

Figure 4.17 Enlarged orientation maps of (a) α_2, (b) γ and (c) TiB (B27) associated with parts of their pole figures in (d) from region III in fig. 4.14 (e), indicating the γ grains follow Blackburn's OR with their neighbouring α_2 grains.

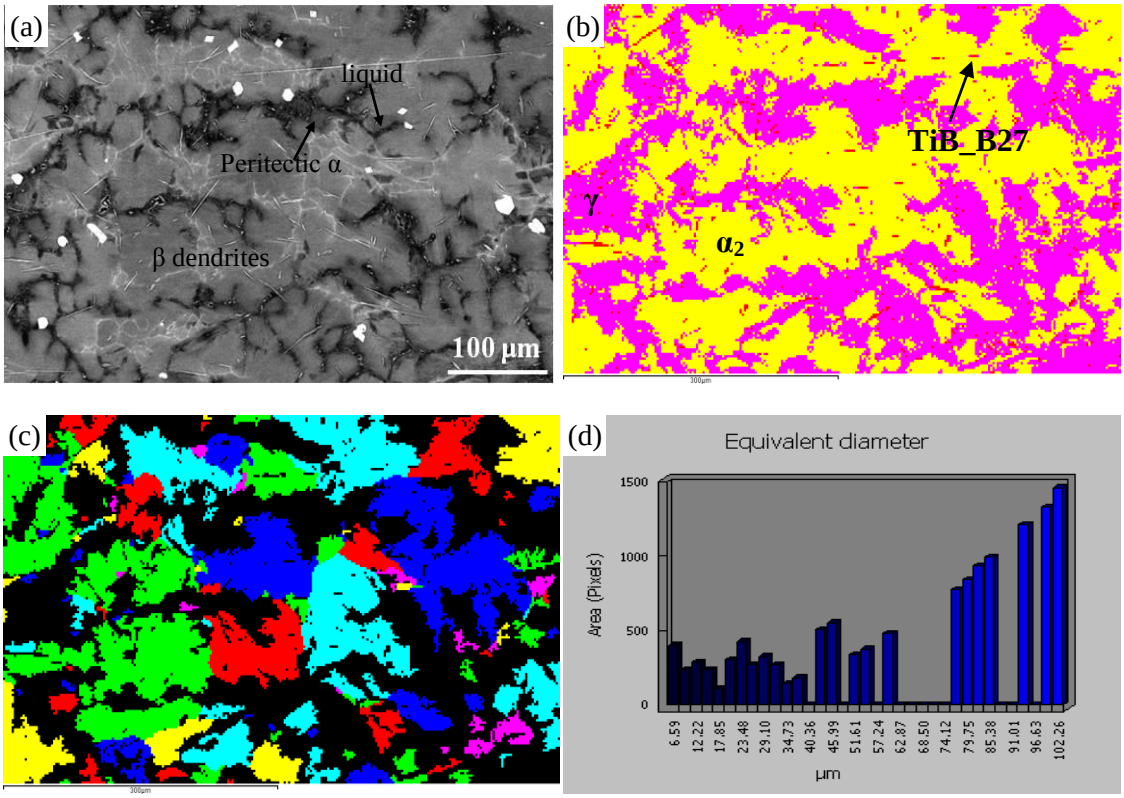
(a)
liquid
Peritectic α
β dendrites
100 μm
(b)
TiB_B27
γ
α2
(c)
(d)
Equivalent diameter
Area (Pixels)
1500
1000
500
0
6.59
12.22
17.85
23.48
29.10
34.73
40.36
45.99
51.61
57.24
62.87
68.50
74.12
79.75
85.38
91.01
96.63
102.26
μm
(e)
I
II
III
IV
1
2
4
5
6
7
8
9
10
11
12
13
14
15
16
17
18
19
(f)
A
B
C
D
E
F
G
(g)
TiB (B27)_i
TiB (B27)_ii
TiB (B27)_iii
TiB (B27)_iv-1
TiB (B27)_iv-2

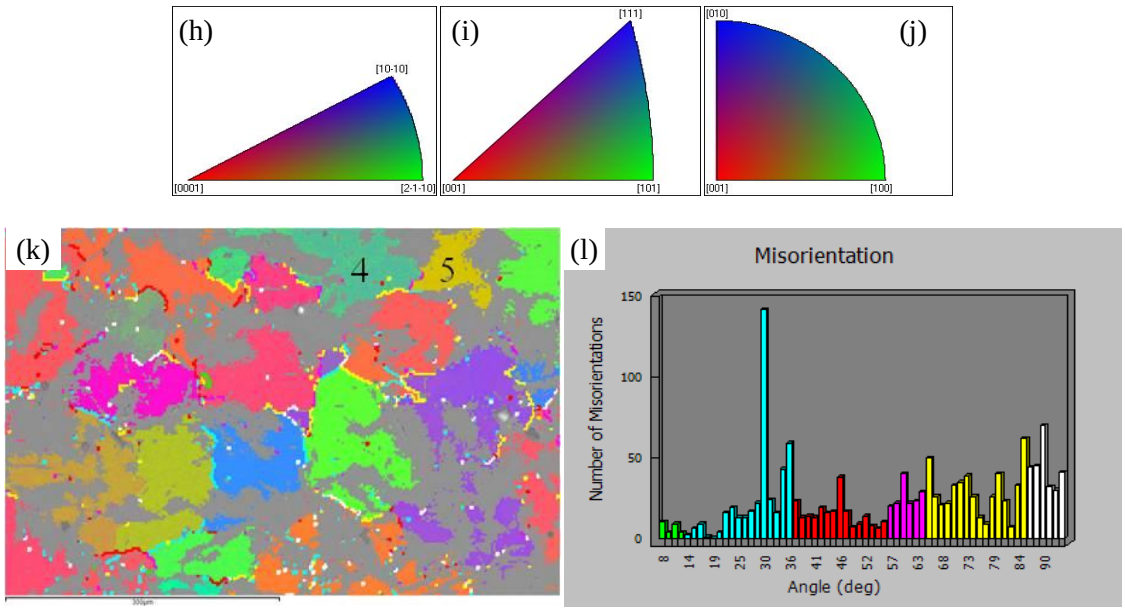

Figure 4.18 Very coarse dendrites in Ti4522XD Bridgman sample, showing (a) BSE image, (b) phase map in which ■, ■ and ■ stand for α_2, γ and TiB (B27) phase, respectively, (c) α_2 grain map with grain size distribution graphs in (d), (e), (f) and (g) α_2, γ and TiB (B27) normal direction orientation maps with orientation colour keys in (h), (i) and (j), respectively, (k) α_2 phase misorientation map with its corresponding misorientation distribution graph in (l).

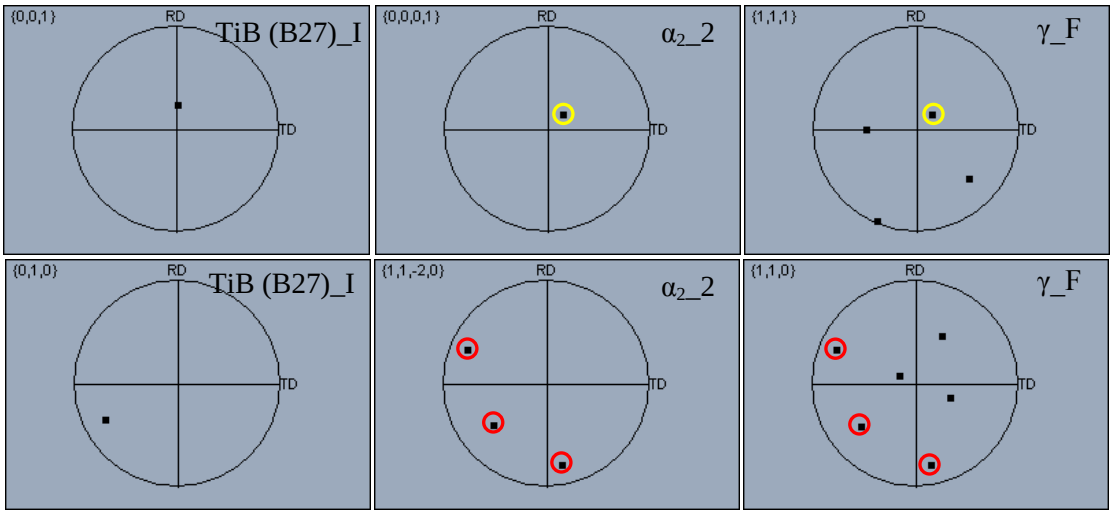

Figure 4.19 Pole figures of TiB (B27), α_2 and γ from region I in fig. 4.18 (e).

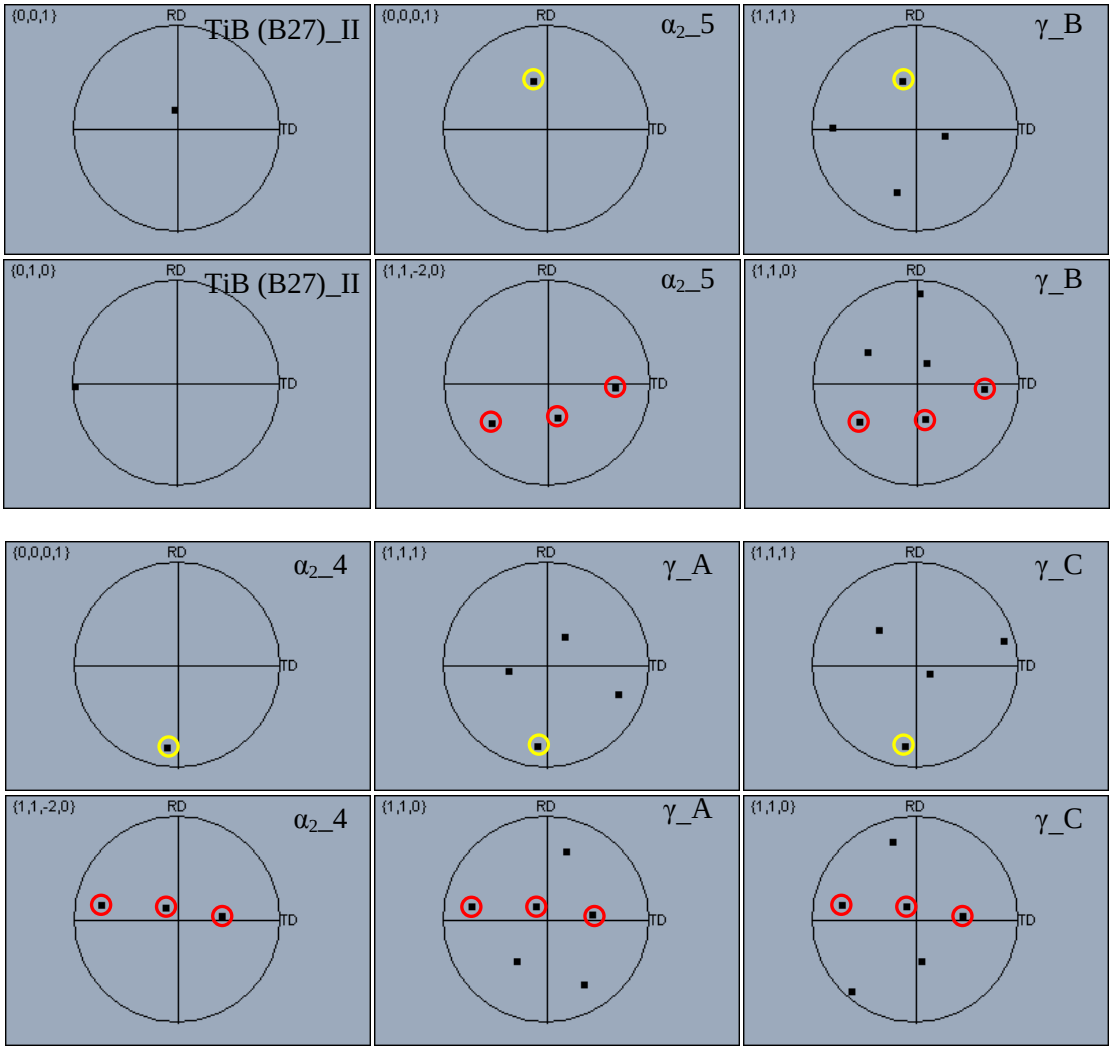

Figure 4.20 Pole figures of TiB (B27), α_2 and γ from region II in fig. 4.18 (e).

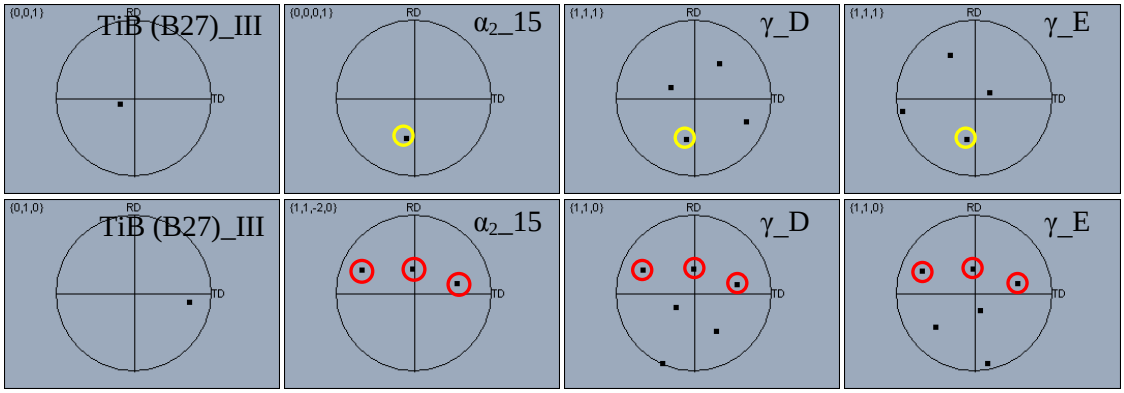

Figure 4.21 Pole figures of TiB (B27), α_2 and γ from region III in fig. 4.18 (e).

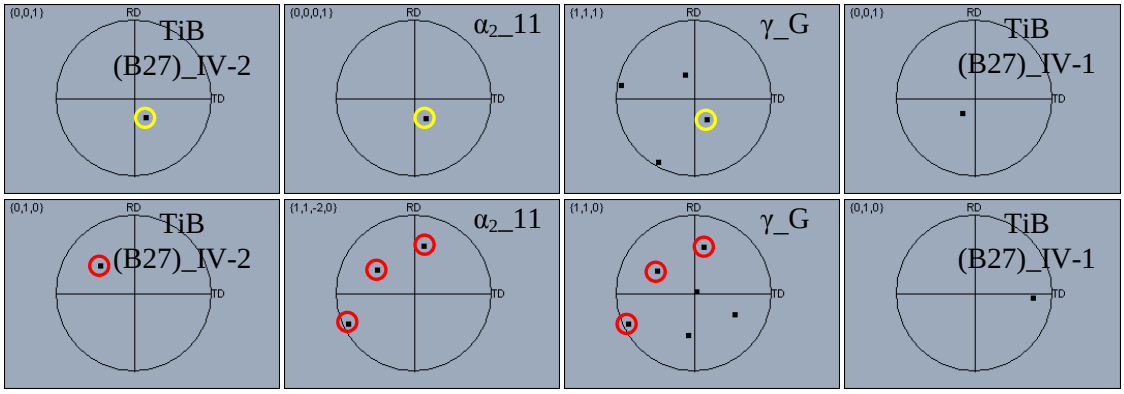

Figure 4.22 Pole figures of TiB (B27), α_2 and γ from region IV in fig. 4.18 (e).

4.2 Solidification behaviours of Ti4522XD powders

The cooling rate of gas atomised Ti4522XD powders can be up to 10^3 ℃/s, therefore, the investigation of the solidification behaviours of Ti4522XD powders can shed some light on the understanding of the influence of solidification rate on the solidification behaviour of Ti4522XD alloy. In this thesis, the solidification behaviours of gas-atomised Ti4522XD powders with different particle size have been studied in terms of microstructure, phase constitution and orientation.

4.2.1 Microstructural characteristics of Ti4522XD powders

The microstructures of a large number of powder particles were investigated. It was found that there are two distinctive microstructures which depend on the particle size. Generally, if the particle size is less than 100 μm, they had the same type of microstructure, and if the particle size is larger than 100 μm they would have another one. Therefore, the microstructural characteristics of Ti4522XD powders were investigated separately according to their particle size. However, there is no sudden change at 100 μm diameter. It is more of a continuum.

4.2.1.1 Microstructural characteristics of fine powders

Fig. 4.23 (a) and (b) show both typical secondary electron (SE) and backscattered electron (BSE) SEM microstructures of fine powders with particle size less than 100 μm. The SE image was taken from etched powder which was mounted and polished before etching. The SE image in fig. 4.23 (a) reveals that the fine powders are mainly composed of equiaxed grains with a grain size about 2-5 μm, but a few dendritic colonies are also always observed, as indicated in the image. In the grain boundaries, it is seen that there is at least a second phase. However, the BSE image in fig. 4.23 (b) does not show any dendritic

microstructure, but a microstructure with many equiaxed colonies. In addition, the contrast in the BSE images is fairly low, suggesting a low segregation in composition. On the other hand, the average dendritic size in SE images is similar to the average colony size in the BSE image, both of which are about 10 μm.

Fig. 4.24 presents a detailed SE microstructure of fine Ti4522XD powders at high magnification. This image shows there are at least three phases existing in the powders, the matrix phase accounting for the most of the powder, the particles exhibiting bright contrast and a very thin layer in the grain boundaries of intermediate intensity which is temporarily called the second solid phase. All these phases are indicated in the fig. 4.24. In terms of particles, it is worth noting that there are two kinds of morphologies, one of which is long and curvy and another short and straight and almost parallel or perpendicular to each other.

XRD scanning observations on these fine powders show a single α_2 phase as indicated in fig. 4.25. Thus, the matrix phase in fig. 4.24 is α_2 phase, which is confirmed by TEM work in fig. 4.26, in which the fig. 4.26 (a) shows the many beam bright field (BF) image of matrix α_2 phase and fig. 4.26 (b), (c) and (d) are its corresponding selected area diffraction (SAD) patterns with zone axis $[11\bar{2}\,0]$, $[14\bar{5}\,0]$ and $[11\bar{2}\,3]$, respectively.

To determine the crystal structure of the second solid phase shown in fig. 4.24, an etched Ti4522XD powder was used for FIB milling, since in this case the second solid phase is bulged out compared with the matrix, and thus could be easily identified for milling and found during TEM operation. Otherwise, it is very difficult to identify the second solid phase from the polished powders. As shown in fig. 4.27 (a), the bulged grain A is the so called second solid phase and the grain B is the matrix α_2 phase. The indexing of SAD patterns from fig. 4.27 (b) to (d) from A grain, which are in the α_2 zone axis of $[01\bar{1}\,2]$, $[11\bar{2}\,0]$ and $[\bar{1}\,2\bar{1}\,6]$, respectively, reveal that the second solid phase is actually a α_2 phase.

The OR between grain A and grain B was further investigated through the combined TEM and mathematical calculation. Fig. 4.27 (e)-(g) shows that when grain A is in $[11\bar{2}6]$ zone axes, grain B is close to $[4\bar{5}16]$ and the SAD pattern, in fig. 4.27 (f) taken from the interface between A and B, indicates that they have a common plane $(\bar{2}021)$. Based on this crystal information, the plane pole figures of α_2 in poles $[11\bar{2}6]$ and $[4\bar{5}16]$ can be plotted and superimposed together, making $(\bar{2}021)$ in each pole figure overlapped, as shown in fig. 4.28. Then the angle between (0001) in each pole figure can be calculated, which is 60 °. The angles between $<11\bar{2}0>$ directions in each grain were also calculated in the direction pole figures as shown in fig. 4.29, and the resulting angle matrix is summarised in table 4.3. Comparing this angle matrix with the standard angle matrix for Burgers variants in Appendix 3, it is revealed that it matches one of the three standard angle matrixes when the angle between (0001) planes is 60 °, therefore, grain A and grain B are possible Burgers variants. However, if there are only two grains in an area that have specific Burger's OR, they cannot be guaranteed to be Burgers variants, since it can be a coincidence. Only in the case there are more than three grains having the Burger's OR can they be identified Burgers variants.

Even though both grain A and matrix grain B are α_2 phase, they are different in compositions. Table 4.4 gives the EDS analysis results of these two grains by TEM and it shows that the grain A contains higher Al level than grain B. This is consistent with microstructural observation that higher content of Al could make the alloy more resistant to 2 % HF etchant as demonstrated in fig. 4.30, which shows the lamellar microstructure of an etched Ti4522XD casting. In this image, the γ phase, which is bulged out and contains higher Al level than α_2 phase, is more resistant to 2 % HF etchant. Since the enrichment of Al occurs in interdendritic regions, the second solid phase is essentially an interdendritic α_2

phase. Therefore, grain A and grain B are not Burgers variants and this possible Burgers relation between A and B might be formed simply by the nucleation of grain A on grain B which was transformed from prior β dendrite during solidification, since peritectic reaction would be suppressed due to high cooling rate.

The long curvy particles shown in fig. 4.24 were also studied by TEM. The bright field (BF) and dark field (DF) images of one long curvy particle are shown in fig. 4.31 (a) and (b). It is seen that the thickness of those particles is about 100 nm. The analysis of the corresponding SAD patterns in fig. 4.31 (c) and (d) indicates that those long curvy particles are monoborides (TiB) with an orthorhombic B_f structure, the lattice parameters of which are shown in table 2.1. It is worth noting that this curvy boride is actually composed of two segments, each of which is straight and has lots of ledges. In addition, there are some extra diffraction spots in both fig. 4.31 (c) and (d) which came from neighbouring α_2 matrix, and no low index orientation relationship between the curvy boride and the adjacent α_2 grain was found.

Short straight particles can be in the α_2 grains or on α_2 grains boundaries. Fig. 4.32 (a) and (b) show both the BF and DF images of one short straight particles lying in an α_2 grain and with thickness of about 30 nm. The SAD pattern shown in fig. 4.32 (c) shows these particles are also monoborides with B_f structure. A cluster of parallel and perpendicular short straight particles was also observed in the α_2 grain boundaries as shown in fig. 4. 33, in which the fig. 4.33 (a), (b) and (c) show the BF, DF and SAD pattern of horizontal particles, while fig. 4.33 (d), (e) and (f) show those of the vertical particles. Both fig. 4.33 (c) and (f) show the [012] zone axes of B_f boride, superimposed with diffraction pattern from the neighbouring α_2 grain. It is worth noting that when the horizontal borides were observed about a zone axes, the vertical borides and neighbouring α_2 grains were not, and

the sample had to be tilted 4.4 ° about the 100* of B_f from the zone axis of horizontal borides to the zone axis of vertical borides, and 15.7 ° about the other side of 001* of B_f from the zone axis of horizontal borides to the zone axis of the neighbouring α_2 grain, which is $[11\bar{2}0]$ as shown in fig. 4.33 (g), in which the superlattice spots are very weak. It is seen that the parallel borides have the same orientation and furthermore, when the vertical borides were in zone axis, they were in edge-on condition and their (100) planes were parallel to $(1\bar{1}00)$ plane of neighbouring α_2 grain, therefore, one of the α_2 grain's habit plane for B_f precipitates is $\{1\bar{1}00\}$. Fig. 4.33 (g) shows that when the horizontal borides were tilted 15.7 ° about the 001* of B_f, the neighbouring α_2 grain was in $[11\bar{2}0]$ zone axes and at the same time the borides became narrower and sharper at the horizontal edges. According to B_f (100) pole figure in fig. 4.34, there is a low index plane $(01\bar{1})$ in B_f, which is normal to (100) and 15.9 ° away from $(02\bar{1})$, therefore, it seems that for these horizontal borides, their $(01\bar{1})$ planes were parallel to (0001) plane of their neighbouring α_2 grain and another α_2 grain's habit plane for B_f precipitates may be (0001). However, it merits further investigation.

In some Ti4522XD powders, dark blocky particles were found in the BSE image, as shown in fig. 4.35 (a), and the EDS analysis, with the result shown in table 4.5, indicates those particles are highly enriched in boron. In addition, those particles are much bigger than the curvy and the short straight borides and sometimes can act as inoculants for dendrites solidification as shown in fig. 4.35 (b). Fortunately, they were also found in TEM samples. Fig. 4.35 (c) shows a BF image of this kind particle. The SAD pattern analysis from this particle revealed that it was a TiB_2 boride with a C32 crystal structure. The zone axes corresponding to the SAD patterns in fig. 4.34 (b)-(d) are $[01\bar{1}0]$, $[14\bar{5}3]$ and $[01\bar{1}0]$, respectively.

4.2.1.2 Microstructural characteristics of coarse powders

Coarse powders with particle sizes larger than 100 μm have slower cooling rate during solidification than that of fine powders. Fig. 4.36 (a) shows a BSE image of a coarse Ti4522XD powder with a diameter of about 150 μm. Compared with the BSE image in fig. 4.23 (b), the coarse powders have an evident dendritic microstructure with Al enriched in interdendritic regions, where long curvy borides are clearly discernable as shown in fig. 4.36 (b). The BSE image in fig. 4.36 (b) also shows some white traces within dendrites. Those white traces are typical products of β to α transformation and they are the location where the last bit of β was. As discussed before, those areas are enriched in β stabiliser, Nb in this alloy. Their presence is an evidence of the occurrence of β to α transformation and that β was the first solidifying metallic phase. For the etched surface, fig. 4.36 (c) did not show too much difference compared with that in fig. 4.23 (a). However, in the enlarged image shown in fig. 4.36 (d), it is seen that a large amount of long curvy borides exist. For those long curvy borides, Ti_3B_4 borides with $D7_b$ were also identified by TEM as shown in fig. 4.37, within which a twin structure is evident, apart from TiB with B_f structure. In addition, no or very few α_2 layers which were apparent in the α_2 grain boundaries in fine powders were found in coarse powders.

According to the XRD analysis results of those particular coarse powders as shown in fig. 4.38, the matrix phase is still α_2. However, the TEM analysis on the grains in the interdendritic regions which was prepared by FIB milling reveals that those grains in the interdendritic regions which are rich in Al are γ grains. The BF image and its corresponding SAD patterns of γ grain in the interdendritic region are shown in fig. 4.39. In addition, it is also noted that borides are also found in the interdendritic region and those

γ grains of about 2-3 μm are much smaller than the matrix α_2 grains, which are generally larger than 5 μm.

4.2.2 Orientation relationship analysis of Ti4522XD powders

As seen from the Ti4522 Bridgman samples, if these α_2 grains were formed through precipitation from the parent β grains there should be lots of Burgers variants. However, it is also seen from the Ti4522XD Bridgman that the addition of boron could break down the Burgers relationships when the cooling rate is 2 ℃/s. Therefore, it is assumed that many α grains nucleated on the peritectic α grains which nucleated on the small borides in the interdendritic liquid. However, it is not known whether this mechanism still works if the peritectic reaction could be suppressed by high cooling rate during solidification of gas-atomised Ti4522XD powders. To find out this answer, it is of importance to find out if there are enough Burgers variants and if there are Blackburn's OR between α_2 grains and their neighbouring γ grains in the interdendritic regions in the coarse powders, which need to be analysed through the above EBSD-based method.

4.2.2.1 The OR between α_2 grains in fine Ti4522XD powders

Fig. 4.40 (a) shows the typical BSE image of fine Ti4522XD powder, and fig. 4.40 (b) gives the corresponding α_2 orientation map. The α_2 grain map in fig. 4.40 (c) and its corresponding α_2 grain size distribution graph in fig. 4.40 (d) show that this powder has a relatively homogenous microstructure and the average α_2 grain size is about 4 μm.

It is seen from fig. 4.40 (b) that there are 151 α_2 grains. If all the grains are considered for Burgers OR analysis, there will be 11,325 pairs of α_2 grains for angle measurement and calculation from their individual pole figures, which is a huge amount of work. To save analysis time, only neighbouring α_2 grains are considered. Actually, most of Burgers

variants are adjacent as observed before. In this case, the misorientation map in fig. 4.40 (e) and its corresponding misorientation distribution graph in fig. 4.40 (f) were used to exclude the neighbouring α_2 grains, between which the misorientation is obviously not close to 10 °, 60° and 90°. Generally speaking, the misorientation distribution of all those α_2 grains is random and the majority of grain boundaries do not show clear misorientation lines as shown in fig. 4.40 (e) due to the existence of borides. However, they still helped a little bit to save the analysis time. Based on the same method used before, it is found that only α_2_73 and α_2_74, and α_2_100 and α_2_110 are potential Burgers variants. The majority of them are not.

It is worth noting that some of those 151 α_2 grains are similar in size to the developed dendrite in fig. 4. 23 (a) and the α_2 colonies in fig. 4.23 (b) which is about 10 μm. Given no unambiguous Burgers variants were found in those fine powders, it is reasonable to assume that those large α_2 grains may correspond to the original β dendrites which transformed to one single α grain during fast cooling. In this case, the fine powder can appear as a random distribution of misorientations.

To investigate the above assumption, an etched powder where the well developed dendritic structure can be identified, as marked by the black curvy line in the SE image in fig. 4.41 (a), was used for EBSD analysis, but with the compromise in the EBSD quality since it has a rough surface which causes unevenly distributed back-scattered electrons. The corresponding orientation map of this dendrite is shown in fig. 4.41 (b). As a result, it is seen that some large α_2 grains span over more than one dendrite. For example, the numbered α_2_1 and α_2_2 grains which are marked by dotted blue and green lines respectively in fig. 4.41 (a) not only cover the outlined dendrite but also others outside it. This feature indicates the nucleation of those α_2 grains should be related to something in

the interdendritic areas and independent of dendrites. In addition, the grains α_2_1, α_2_2, α_2_3 and α_2_5 all contain several cellular subgrains as observed in the etched surface that have the same orientation. That is why α_2 colonies observed in BSE images of fine Ti4522XD powders, as shown fig. 4.23 (b), appear to be much bigger than the equiaxed α_2 grains observed in SE images of etched Ti4522XD powders, as shown in fig. 4.23 (a). OR analysis between those 6 α_2 grains also reveals that none of them belongs to Burgers variants.

4.2.2.2 The OR analysis in coarse Ti4522XD powders

As shown again in fig. 4.42 (a), coarse Ti4522XD powders with diameter generally larger than 100 μm always exhibit a clear dendritic structure. The phase map in fig. 4.42 (b) confirms the TEM work that they are γ grains in the interdendritic regions. Grain maps of both α_2 and γ phase in fig. 4.42 (c) and (e) and their corresponding grain size distribution graphs in fig. 4.42 (d) and (f), respectively, indicate that the average α_2 grain size is about 5.5 μm, slightly bigger than that in fine Ti4522XD powders, while the average γ grain size is about 2 μm. Fig. 4.42 (g) and (h) show the normal orientation maps of α_2 and γ, respectively. In fig. 4.42 (g), the ellipses indicate that there are many α_2 grains within these ellipses which are separated by interdendritic γ grains have the same orientation. This is the same phenomenon as that in the coarse dendrites in Ti4522XD Bridgman sample. Therefore, the solidification behaviour in coarse Ti4522XD powder is the same as Ti4522XD Bridgman sample.

To confirm the above assumption, a particular dendrite is selected which is marked by dashed rectangles in fig. 4.42(g) and (h) for OR analysis between the α_2 grains and between α_2 grains and their neighbouring γ grains. Fig. 4.43 (a) and (b) show the enlarged α_2 and γ orientation maps of the selected area. In fig. 4.43 (a), it is shown that there are 57

α_2 grains. The corresponding misorientation map and misorientation distribution graph of this selected region, as shown in fig. 4.43 (c) and (d), show that those α_2 grains are randomly distributed. To save analysis time, only neighbouring α_2 grains were analysed. Through series of measurements of angles, calculation and comparison, it was finally revealed that no neighbouring α_2 grains are Burgers variants. This is also the similar situation as in coarse dendrites in Ti4522XD Bridgman sample.

The OR between α_2 grains in a dendrite and neighbouring γ grains in interdendritic regions were analysed by comparing α_2 grains' (0001) and $\{11\bar{2}0\}$ pole figures and γ grains' {111} and {110} pole figures in a particularly selected area, and it was found that no single pair of α_2 and γ grains follows Blackburn's OR. One example is shown in fig. 4.44, in which the (0001) pole figures of each α_2 grain in the dendrite labelled in fig. 4. 44 (a) and {111} pole figures of each neighbouring γ grain in the interdendritic region labelled in fig. 4.44 (b) are displayed and it is seen that no spots in (0001) pole figures can be overlapped with those in {111} pole figure. Furthermore, no γ twins as observed in the interdendritic regions of Bridgman samples were found in the interdendirtic regions of Ti4522XD powders and the γ grains were always in equiaxed morphology. This is different from Ti4522XD Bridgman samples. However, in coarse Ti4522XD powders the solidification rate is much higher, therefore, the peritectic α grains which acted as nuclei for those α grains that had the same orientation have no time to grow into liquid. As a result, the liquid solidified directly into equiaxed γ grains.

4.2.3 Solidification behaviours of Ti4522XD powders

As described above, the microstructural and OR characteristics of Ti4522XD powders are particle size dependent and can be summarised as:

For fine powders,

1. They have an equiaxed microstructure with a few visible dendrites on the etched powder surface by SE SEM images.
2. They are composed of matrix α_2 phase, interdendritic α_2 phase, fine curvy TiB type borides with B_f structure and very fine B_f precipitates. Sometimes, big blocky TiB_2 borides were also found in the Ti4522XD powders, but those borides are probably the unmelted borides from a prealloyed electrode. No specific OR between borides and adjacent α_2 grains were found.
3. The majority of α_2 grains are non-Burgers variants and the α_2 grain boundaries observed in EBSD do not correspond to β dendrite boundaries with some α_2 grains covering more than one adjacent β dendrites.

For coarse powders,

1. They have a typical dendrite structure.
2. They are composed of matrix α_2 grains, γ grains in the interdendritic regions and curvy borides which were found to be TiB with B_f structure or Ti_3B_4. No specific OR between borides and adjacent metallic phases were found.
3. The majority of matrix α_2 grains are non-Burgers variants and no Blackburn's OR between matrix α_2 grains and the neighbouring γ grains in the interdendritic regions was found.

The particle size-related microstructural characteristics are related to the cooling rate during the solidification of Ti4522XD powders. The coarser the powders are, the slower the cooling rate is. However, the solidification rates of all Ti4522XD powders are much higher than that in Bridgman samples.

4.2.3.1 Solidification behaviour of fine Ti4522XD powders

Even though the cooling rate during solidification of fine Ti4522XD powders can be up to 10^3 ℃/s, the first solidified metallic phase is still β phase. During solidification, the growth of β grains was in a columnar or in a dendritic way as seen from the SE images in fig. 4.23 (a). As a result, Al would be enriched in the columnar boundaries or the interdendritic regions and the enrichment could result in the interdendritic α_2 phase as was observed. The dendritic growth of β grains and the formation of interdendritic α_2 phase make each β grain seem to contain several subgrains. But actually those subgrains have the same orientation. That is why the α_2 grain sizes in BSE images taken from the as-polished fine Ti4522XD powders appeared much larger than those in the SE images taken from the etched powders.

As discussed before that the most likely way for the formation of the thin interdendritic α_2 layers is through direct nucleation on the original β grain during solidification, since they contain higher Al level and the peritectic reaction can be suppressed at such a high cooling rate. According to the equilibrium Ti-Al phase diagram, α cannot be formed directly from the liquid in Ti4522XD. On the assumption that interdendritic α_2 layers were formed directly from the interdendritic liquid, the high cooling rate probably shift the α liquidus line to the lower Al level.

In addition, the facts that the majority of matrix α_2 grains are not Burgers variants, even in the apparent dendrites, and that the α_2 grain boundaries observed in EBSD do not correspond to β dendrite boundaries with some α_2 grains covering more than one adjacent β dendrites, reveal that the solid phase transformation from β to α did not follow Burgers OR in gas-atomised Ti4522XD powders and the nucleation of the α during β to α transformation is associated with something in the interdendritic regions. There are only two phases in the interdendritic areas, boride and interdendritic α_2. The primary boride

precipitates have no OR with β dendrites and with the assumption that there is no peritectic α during solidification at high cooling rate boride can only inoculate α during β to α solid phase transformation. In this way, the observed phenomena can be interpreted. However, since there are so many fine curvy borides in those fine powders, no direct evidence for nucleation of α on borides was found yet.

The TiB curvy borides with B_f structure are always found to grow together with interdendritic α_2 layers and are located in the interdendritic regions where B and Al can be enriched. The 'curvy' shape, the location in the interdendritic regions and the metastable structure all indicate that they were formed directly from the melt and later than the β phase, which will be discussed in the next section.

Apparently, the short straight borides with B_f structure are secondary borides precipitated from α_2 matrix during cooling. Due to the low solubility of boron in β and high solidification rate, the boron must be supersaturated in the matrix during solidification. In the following cooling process, the metastable borides were precipitated from α_2 grains.

Based on the above discussion, the solidification pathway for fine Ti4522XD powders can be:

L → L + β → L + β + primary TiB (B_f) → β + interdendritic α + TiB (B_f) → α + interdendritic α + TiB (B_f) → α_2 + secondary TiB (B_f) + interdendritic α_2 + primary TiB (B_f)

4.2.3.2 Solidification behaviour of coarse Ti4522XD powders

It has been shown that the first solidifying metallic phase is β in coarse Ti4522XD powders. During solidification, the cooling rate in coarse powders is about 10^2 ℃/s, since the BSE microstructures of coarse Ti4522XD powders are comparable to that of the quenched

liquid in Ti4522XD Bridgeman sample (fig. 4.10 (a)). Therefore, the relatively lower solidification rate in coarse powders leads to more pronounced solute segregation in the interdendritic regions such as Al and B and less supersaturation of B in the matrix. That might be the reason why γ grains and Ti_3B_4 were found in the interdendritic region and no secondary borides were found in the matrix in coarse Ti4522XD powders.

Given that many α_2 grains which are separated by interdendritic γ grains have the same orientation and most of α_2 grains in the dendrites are not Burgers variants, the solidification behaviour in coarse Ti4522XD powders that have evident interdendritic γ grains is the same as the that in Ti4522XD Bridgman samples, which means during solidification the peritectic α nucleates on the borides in the interdendritic liquid and then during solid phase transformation the α grains in the dendrites nucleate on the peritectic α grains. In this way, the as-solidified microstructure is further refined.

However, because of the fast cooling rate, the peritectic α cannot grow bigger into the liquid and the liquid which is rich in Al will solidify directly into equiaxed γ grains. Therefore, no peritectic α is evident and no Blackburn's OR can be found. Again, it indicates that the γ liquidus could be shifted to lower Al level as high cooling rate.

In summary, the possible solidification passway for coarse Ti4522XD powders can be:

$L \rightarrow L + \beta \rightarrow L + \beta + \text{borides} \rightarrow \beta + \text{primary } \gamma + \text{borides} \rightarrow \alpha + \text{primary } \gamma + \text{borides} \rightarrow \alpha_2 + \text{primary } \gamma + \text{borides}$

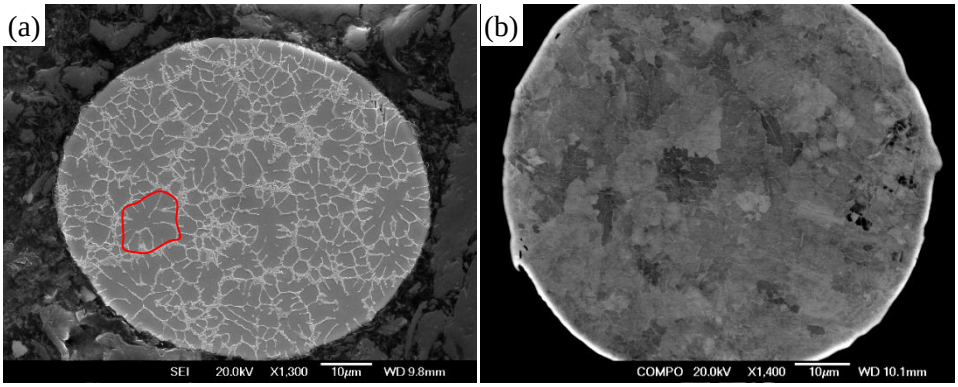

Figure 4.23 (a) SE and (b) BSE SEM images of Ti4522XD powders with particle size less than 100 μm. The SE image in (a) was taken from an etched specimen and the red line marked area refers to a dendrite area.

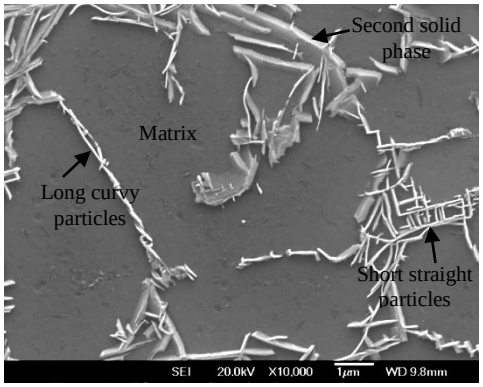

Figure 4.24 SE SEM image of etched Ti4522XD powder with diameter less than 100 μm.

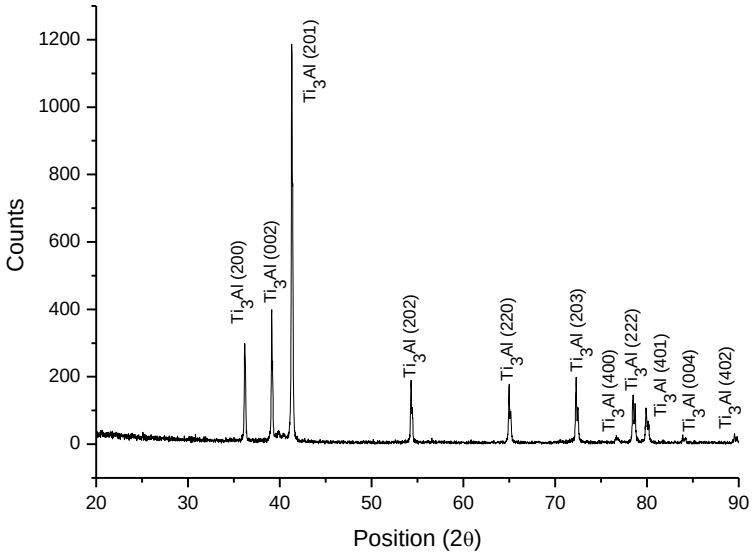

Figure 4.25 XRD result from fine Ti4522XD powders with diameter less than 100 μm, showing a single α_2 phase.

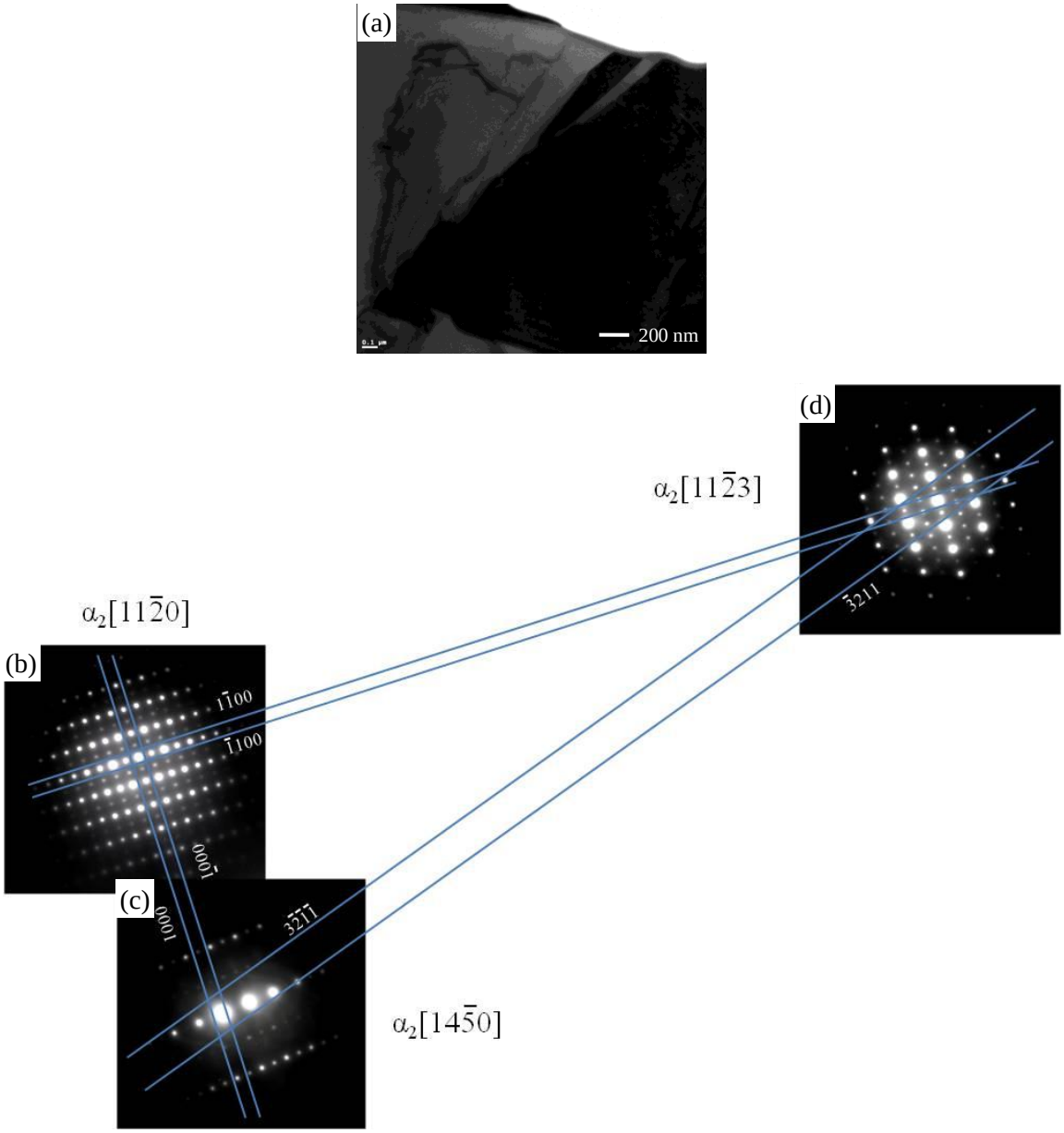

Figure 4.26 (a) many beam TEM bright field (BF) image of matrix phase (dark grain) shown in fine Ti4522XD powders, and (b), (c) and (d) are the corresponding selected area diffraction (SAD) patterns which was identified to be α_2 phase with zone axis $[11\bar{2}0]$, $[14\bar{5}0]$ and $[11\bar{2}3]$, respectively. The tilting angles between (b) and (c), (b) and (d) and (c) and (d) are 20.4 °, 39.0 ° and 43.2 °, respectively.

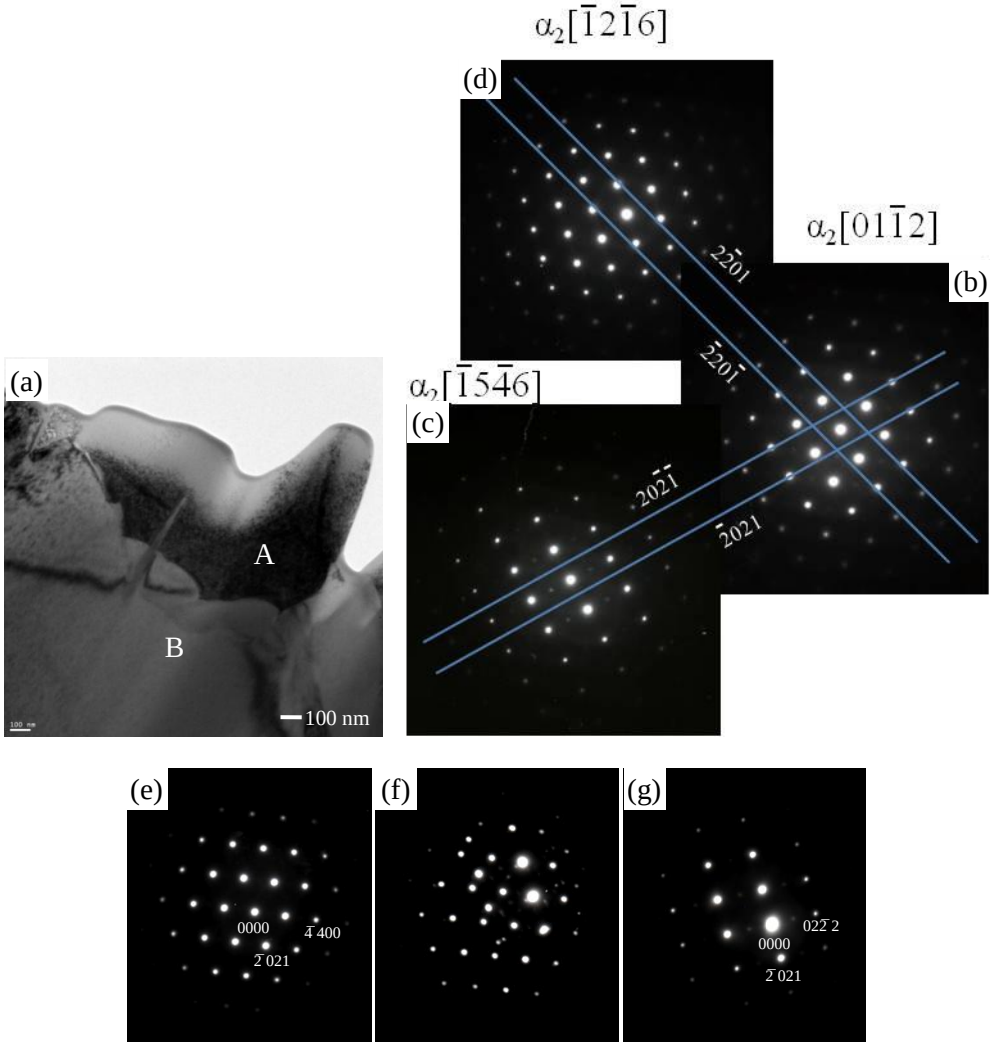

Figure 4.27 (a) many beam TEM BF image of fine Ti4522XD powder, in which grain A is the second solid phase shown in fig. 4.25 and grain B the matrix α_2 phase. SAD patterns shown in (b), (c) and (d) were taken from grain A, which was identified as α_2 phase with zone axis $[01\bar{1}2]$, $[\bar{1}5\bar{4}6]$ and $[\bar{1}2\bar{1}6]$, respectively. The tilting angles between (b) and (c), (b) and (d) and (c) and (d) are 14.4 °, 23.7 ° and 29.9 °, respectively. When A is in zone axes $[11\bar{2}6]$ as shown in (e), B is in $[4\bar{5}16]$ as shown in (g) and (f) was taken from their interface.

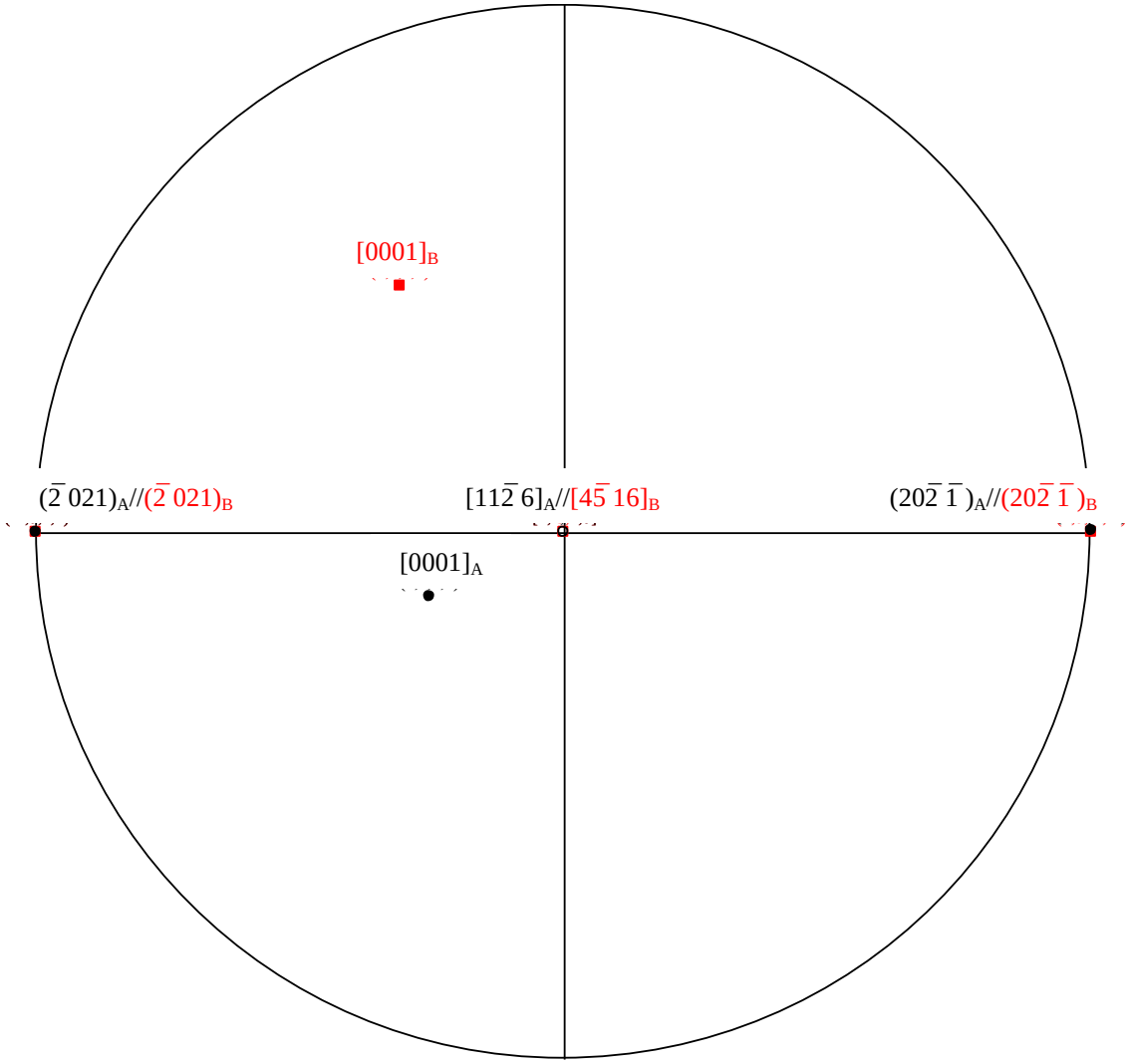

Figure 4.28 Superposed plane stereographic projections with $[11\bar{2}6]_A//[4\bar{5}16]_B$ and $(\bar{2}021)_A//(\bar{2}021)_B$. The angle between (0001) in each pole figure is calculated to be 60 °.

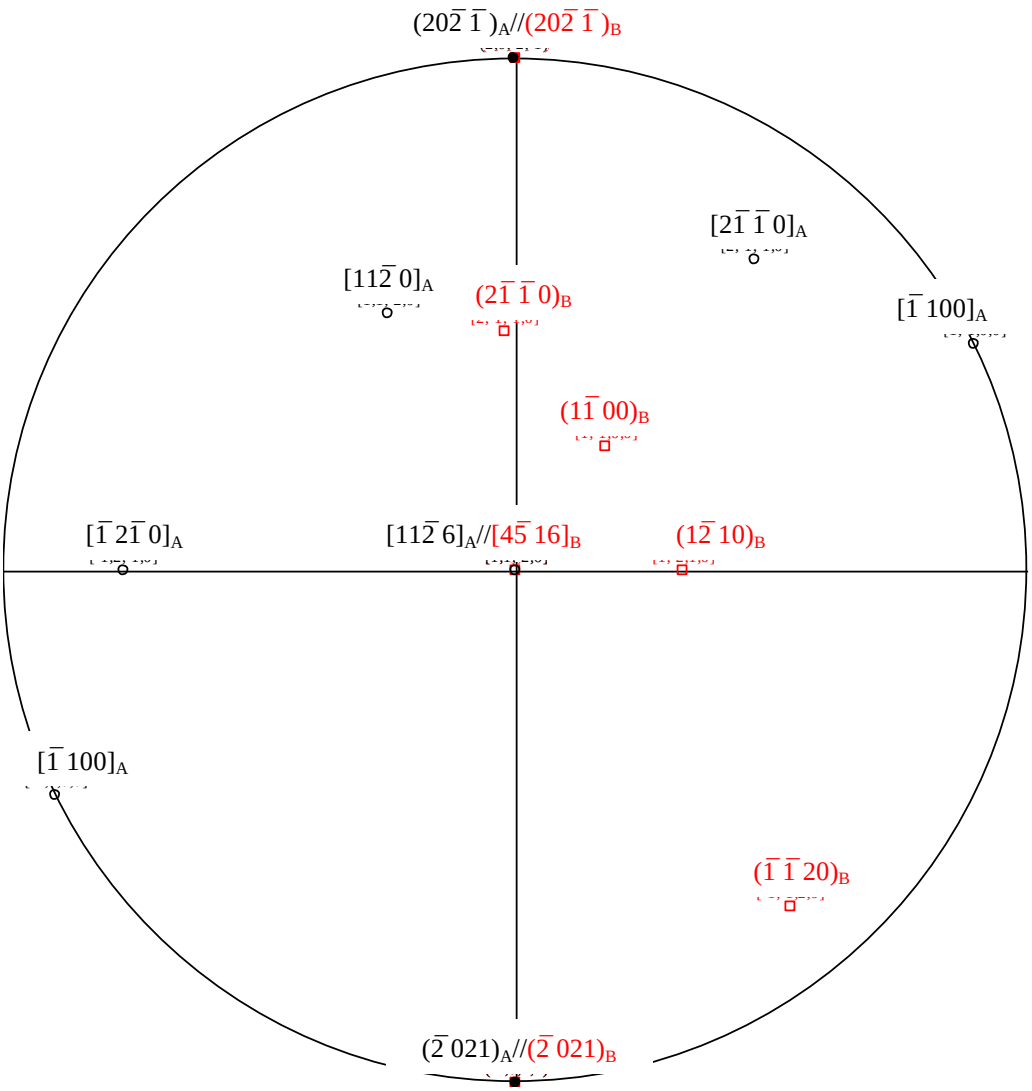

Figure 4.29 Superposed direction stereographic projections with $[11\bar{2}\,6]_A//[4\bar{5}\,16]_B$ and $(20\bar{2}\,\bar{1})_A//(20\bar{2}\,\bar{1})_B$. The angles between $<11\bar{2}\,0>$ planes in each stereographic projection are summarized in table 4.3.

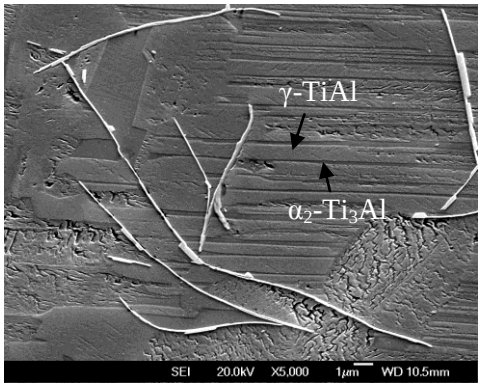

Figure 4.30 SE SEM images showing corrosion resistance of γ-TiAl and α_2-Ti_3Al to 2% HF etchant, indicating γ phase is more resistant.

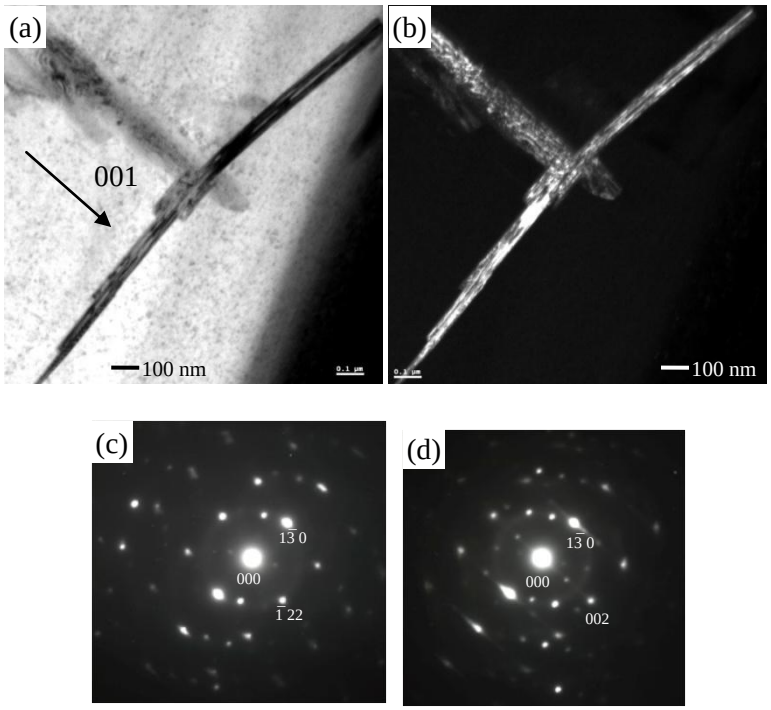

Figure 4.31 (a) many beam BF and (b) centered dark field (CDF) images of long curvy boride existing in Ti4522XD powders. The ***g*** vector used for CDF image in (b) is $1\bar{3}\,0$*. (c) and (d) are the corresponding SDA patterns from B_f [621] and [310] zone axis. The tilting angle between (c) and (d) is 9.4 °.

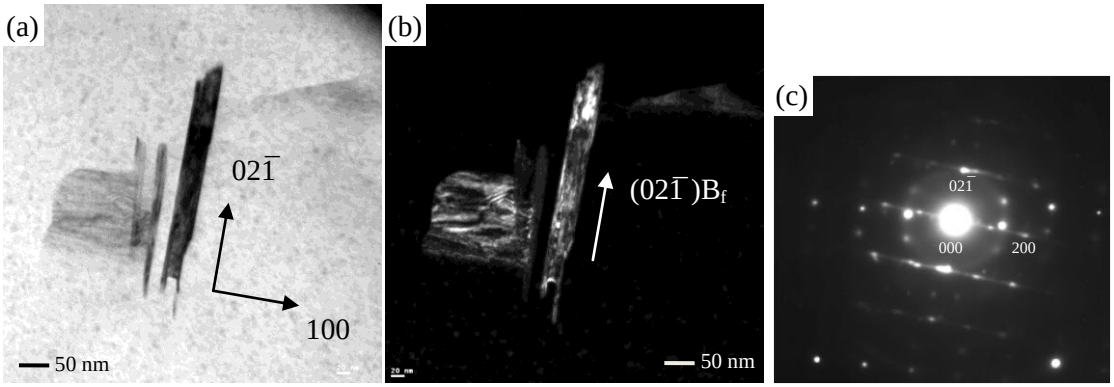

Figure 4.32 (a) BF and (b) DF images of short straight borides in Ti4522XD powder with SAD in (c) showing the zone axis of [012] in B_f.

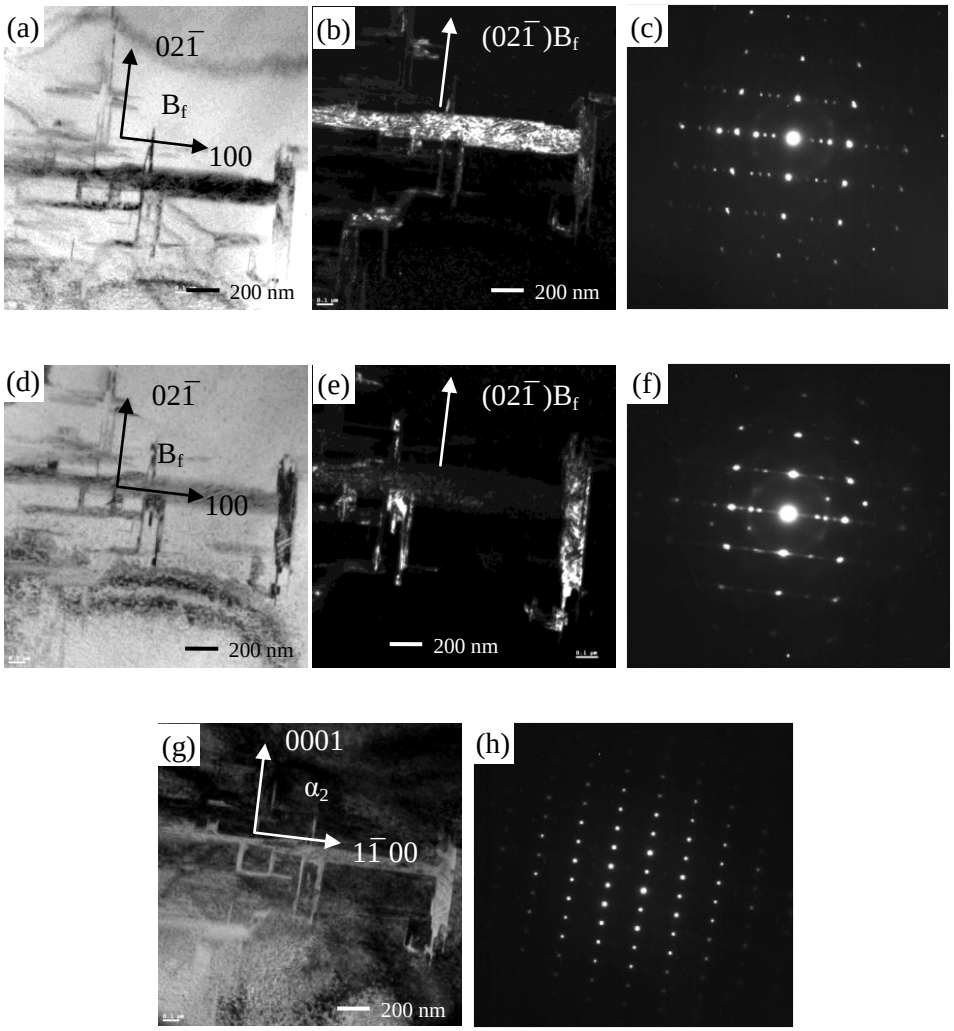

Figure 4.33 (a), (b) and (c) are BF image, DF image and SAD pattern of horizontal particles when it is in the B_f boride zone axis [012]; (d), (e) and (f) are BF image, DF image and SAD pattern of vertical particles when it is in the B_f boride zone axis [012], which was tilted 4.4 ° about 001* of B_f from (c); (g) and (h) show the BF image and the corresponding SAD pattern of the neighbouring α_2 phase in the zone axis of $[11\bar{2}0]$, which was tilted 15.7 ° about the other side 001* of B_f from (c).

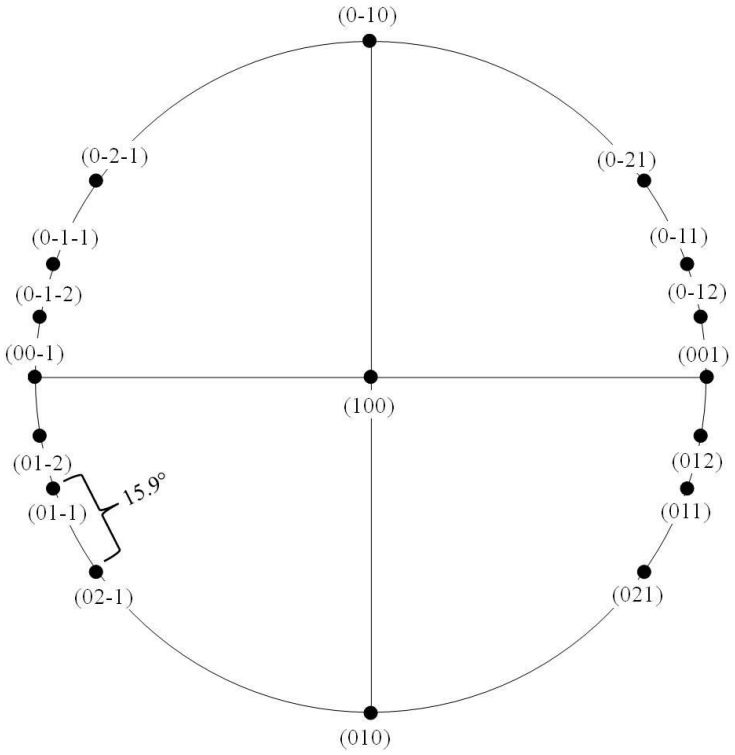

Figure 4.34 TiB (B_f) (100) pole figure showing the angle between $(02\bar{1})$ and $(01\bar{1})$ is 15.9°.

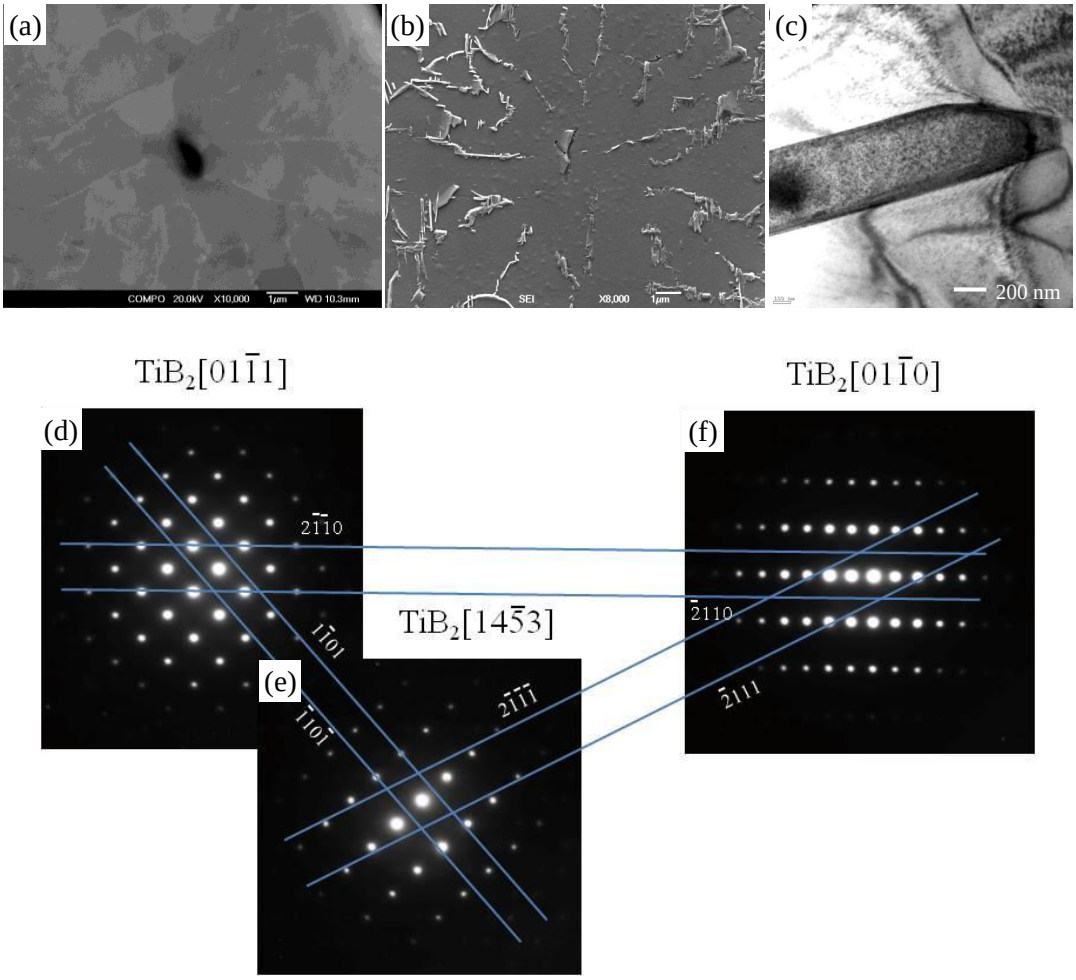

Figure 4.35 (a) BSE and (b) SE images of Ti4522XD powders at high magnifications, showing blocky particles, (c) many beam BF image of a blocky particle and their corresponding SAD patterns in (d)-(f), showing a TiB_2 particle. The zone axis in (d)-(f) are [01$\bar{1}$ 1], [14$\bar{3}$ 5] and [01$\bar{1}$ 0], respectively. The tilting angles between (d) and (e), (d) and (f) and (e) and (f) are 14.6 °, 31.4 ° and 23.4 °, respectively.

	$[11\bar{2}0]_A$	$[\bar{1}2\bar{1}0]_A$	$[2\bar{1}\bar{1}0]_A$
$[2\bar{1}\bar{1}0]_B$	21.02 °	78.52 °	42.74 °
$[1\bar{2}10]_B$	78.52 °	68.82 °	55.91 °
$[\bar{1}\bar{1}20]_B$	42.74 °	55.91 °	79.98 °

Table 4.3 The angles between <$11\bar{2}0$> variants in grain A and B shown in fig. 4.27.

Grain	Ti	Al	Mn	Nb
A	48.1	48.6	1.9	1.5
B	52.3	43.9	2.4	1.5

Table 4.4 Compositions (at.%) of α_2 grains in Ti4522XD powder shown in fig. 4.27 through TEM EDS analysis.

	B	Ti	Al	Mn	Nb
at.%	56.7	29.6	12.3	0.3	1.2

Table 4.5 EDS analysis of the dark blocky particle in fig. 4.34 (a), indicating an enrichment of boron.

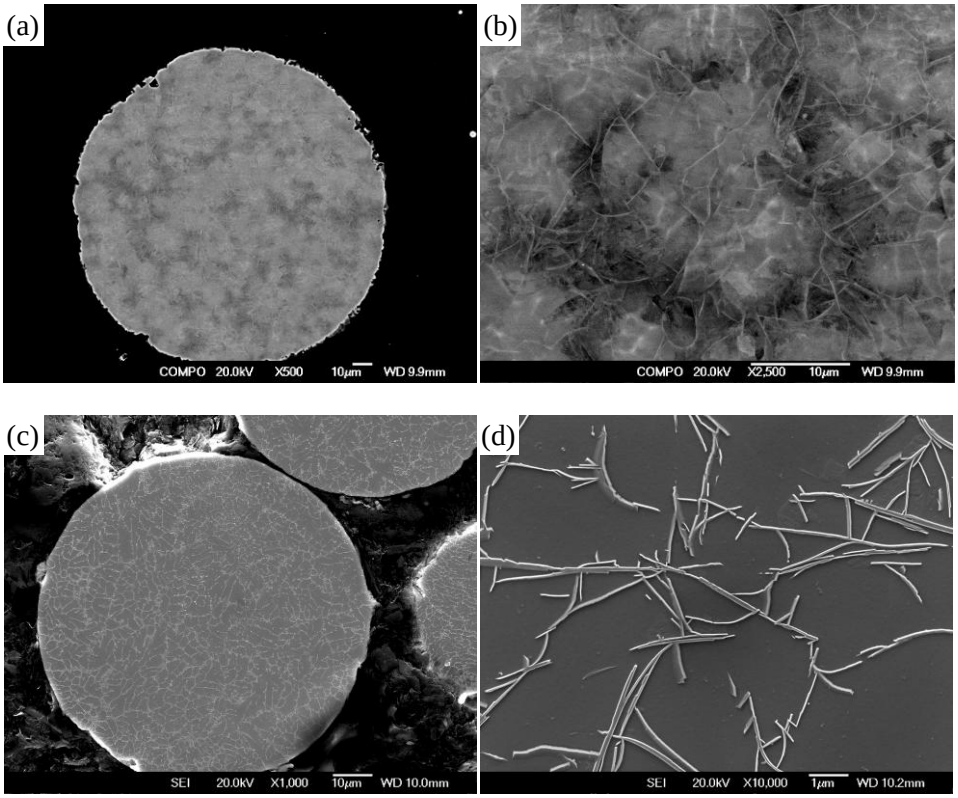

Figure 4.36 BSE SEM images of (a) the overall and (b) the interdendritic BSE images of coarse Ti4522XD powder, SE SEM images of (c) the overall and (d) the enlarged SE images of coarse Ti4522XD powder with specimen surface etched.

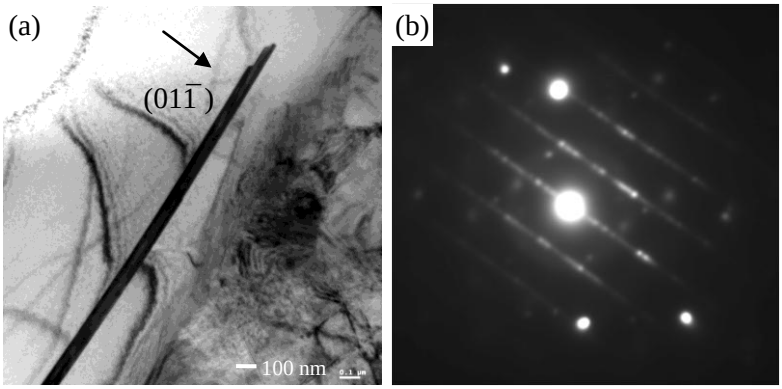

Figure 4.37 (a) many beam BF image of Ti_3B_4 in coarse Ti4522XD powder and their corresponding SAD patterns in (b) with zone axis [311].

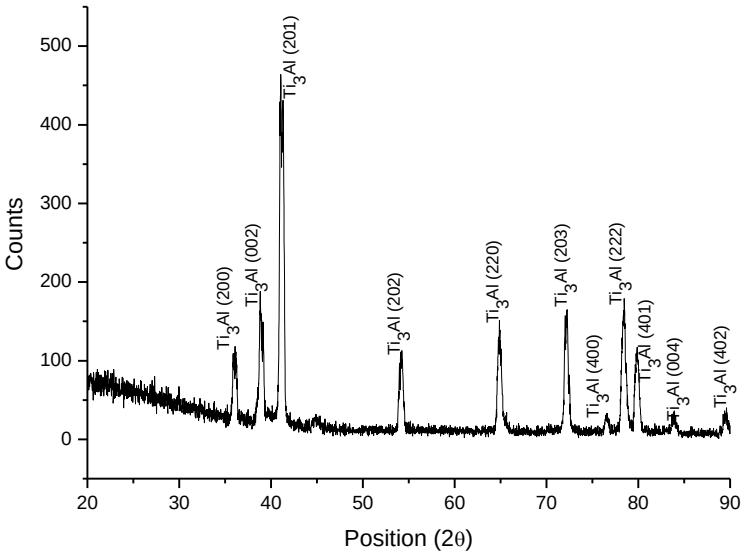

Figure 4.38 XRD result from fine Ti4522XD powders with diameter larger than 100 μm, showing a single α_2 phase.

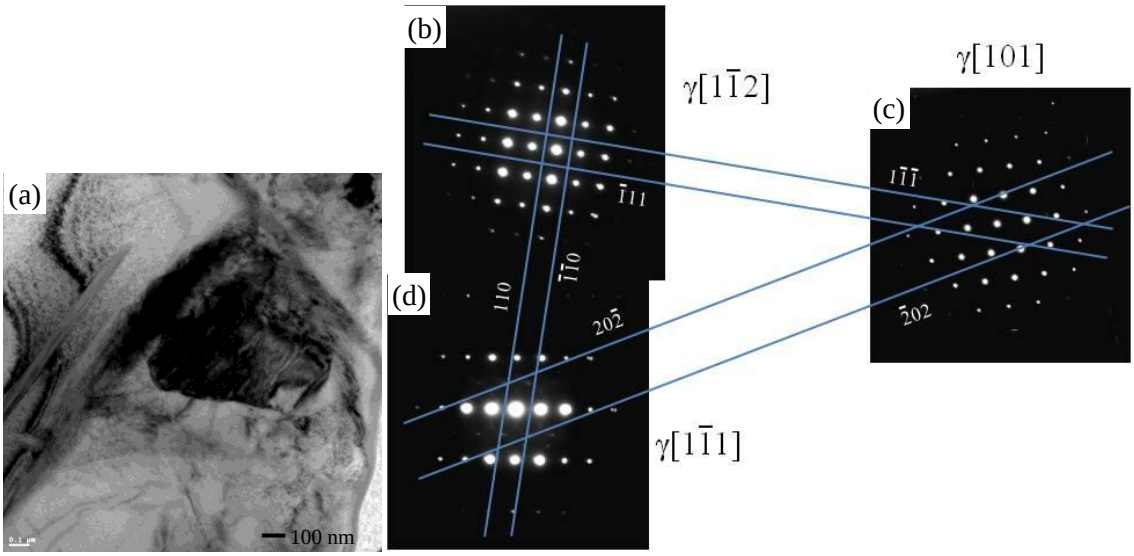

Figure 4.39 (a) many beam BF image of γ grains in the interdendritic regions of coarse Ti4522XD powder and their corresponding SAD patterns in (b)-(d) with zone axis [1$\bar{1}$2], [101] and [1$\bar{1}$1], respectively. The tilting angles between (b) and (c), (b) and (d) and (c) and (d) are 30.5 °, 17.1 ° and 34.4 °, respectively.

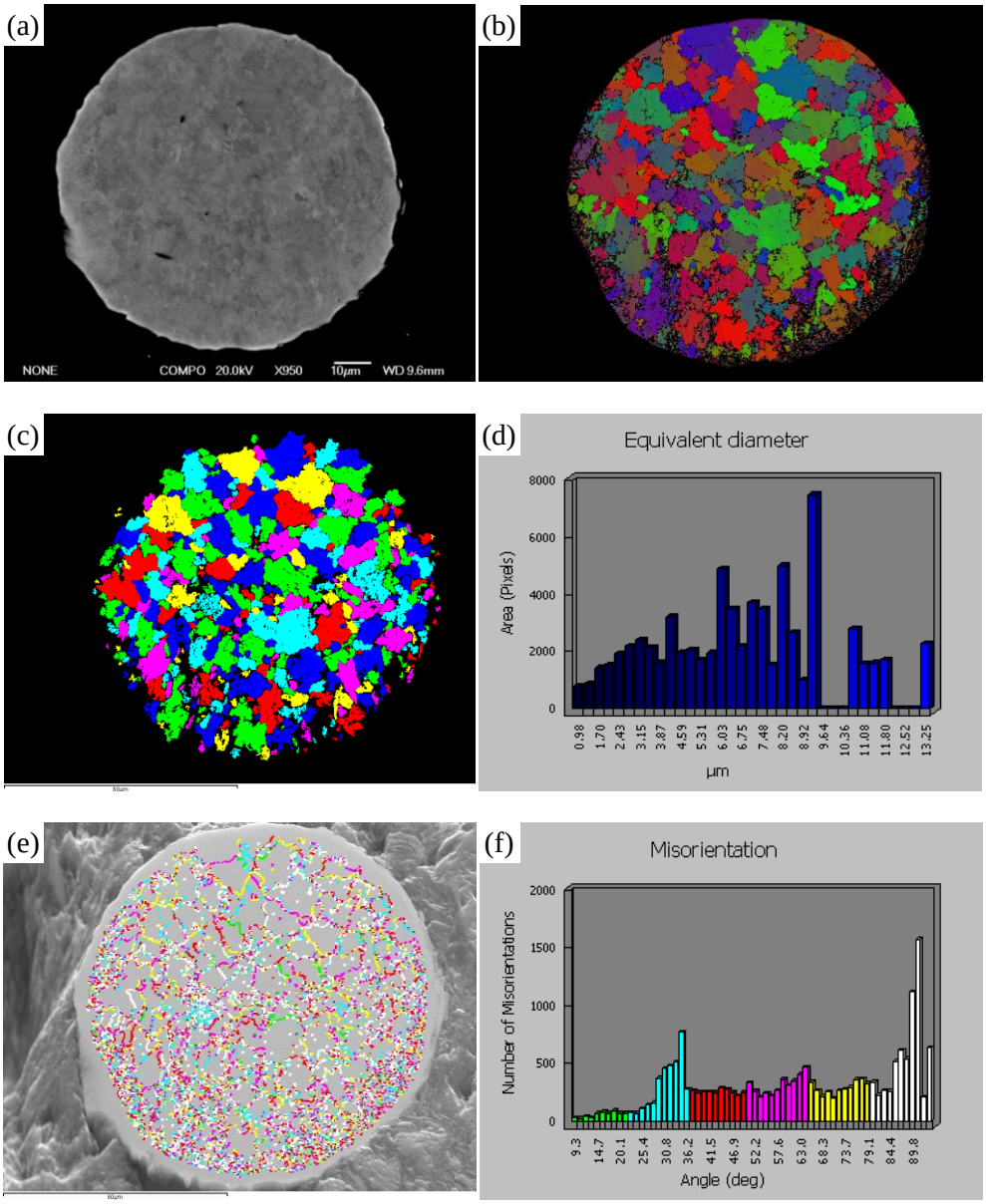

Figure 4.40 To be continued in the next page.

(g)

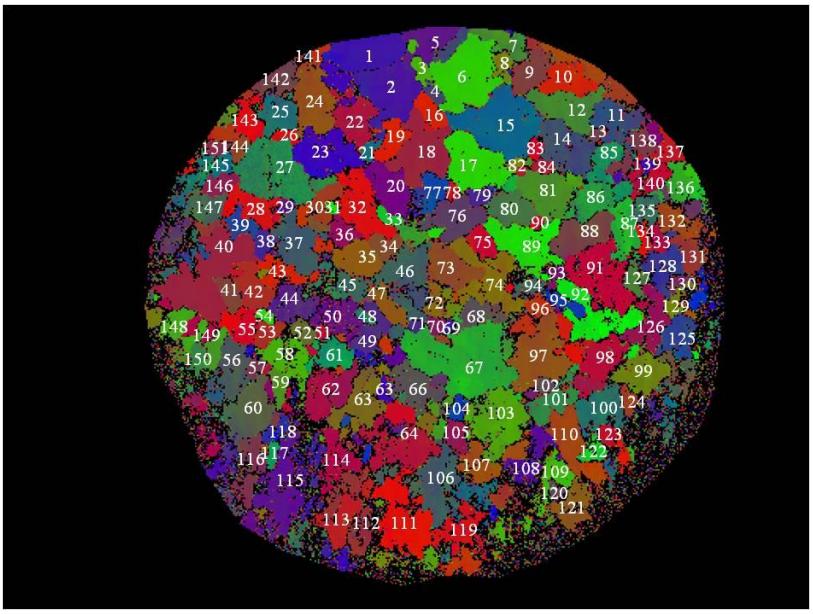

Figure 4.40 BSE image of fine Ti4522XD powder in (a) and its corresponding α_2 orientation map in (b), (c) and (d) are the α_2 grain map and its corresponding grain size distribution graph; (e) and (f) are the α_2 grain misorientation map and its corresponding misorientation distribution graph; (g) shows that of all the 151 α_2 grains in this powder, only grains labelled 73 and 74, 100 and 110 are possible Burgers variants which are neighboured.

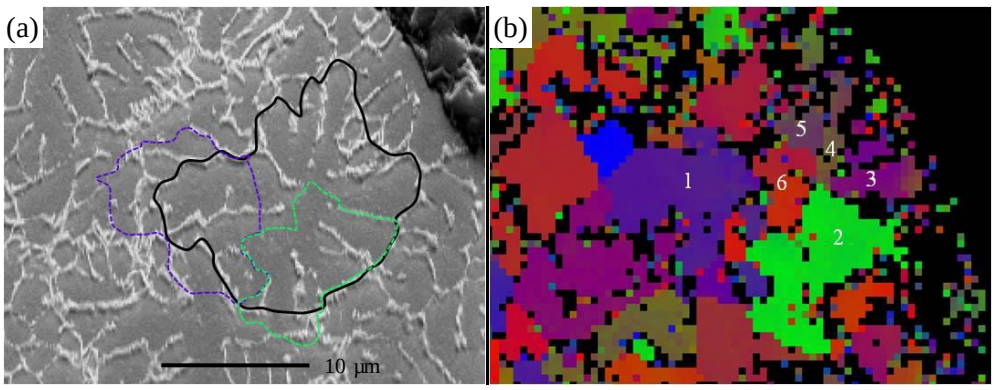

Figure 4.41 (a) SE image of etched fine Ti4522XD powder and (b) its corresponding α_2 normal orientation map.

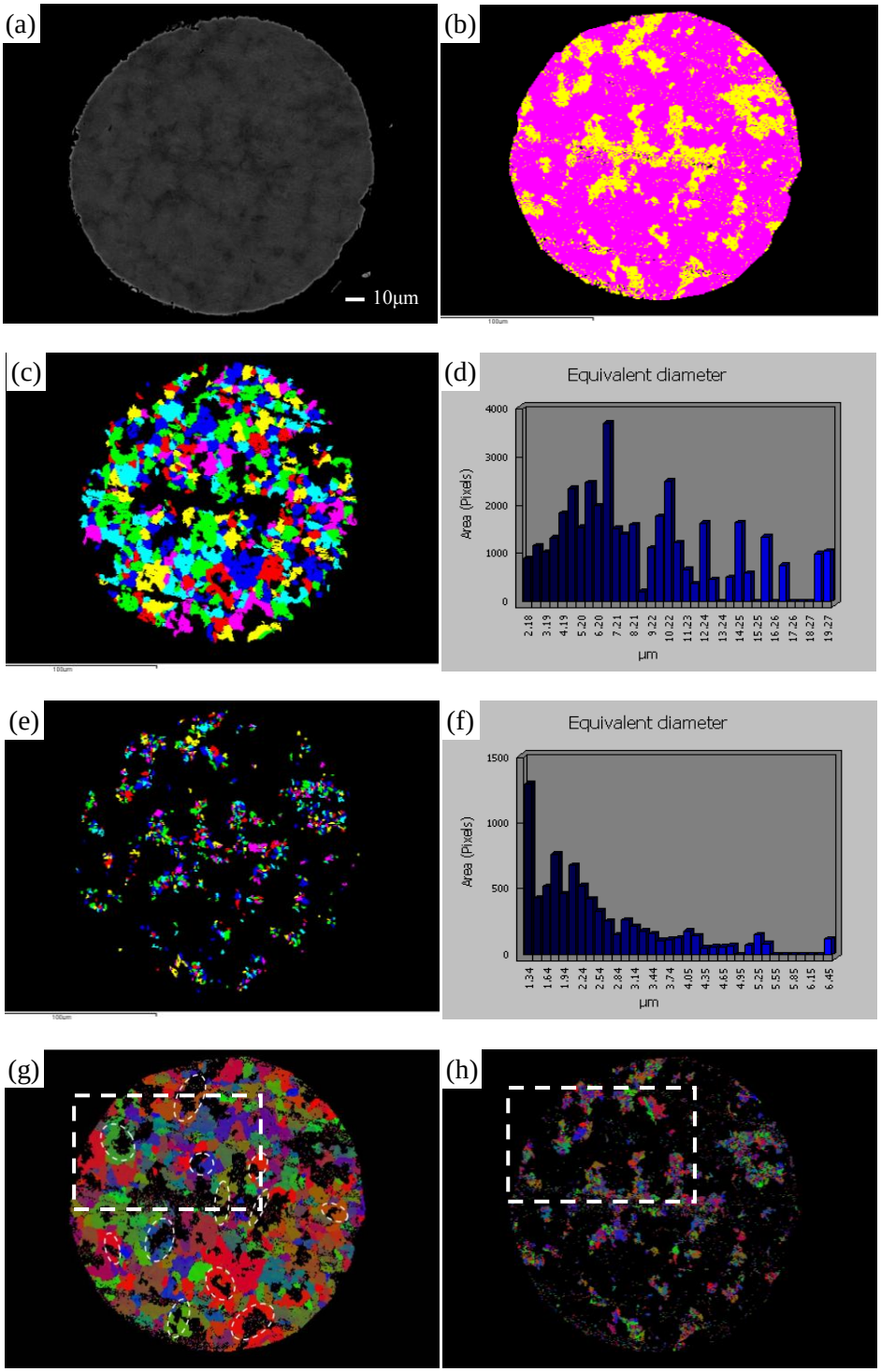

Figure 4.42 Coarse Ti4522XD powder with BSE image in (a), phase map in (b), α_2 grain map and α_2 grain size distribution graph in (c) and (d), γ grain map and γ grain size distribution graph in (e) and (f), α_2 and γ normal orientation map in (g) and (h), respectively.

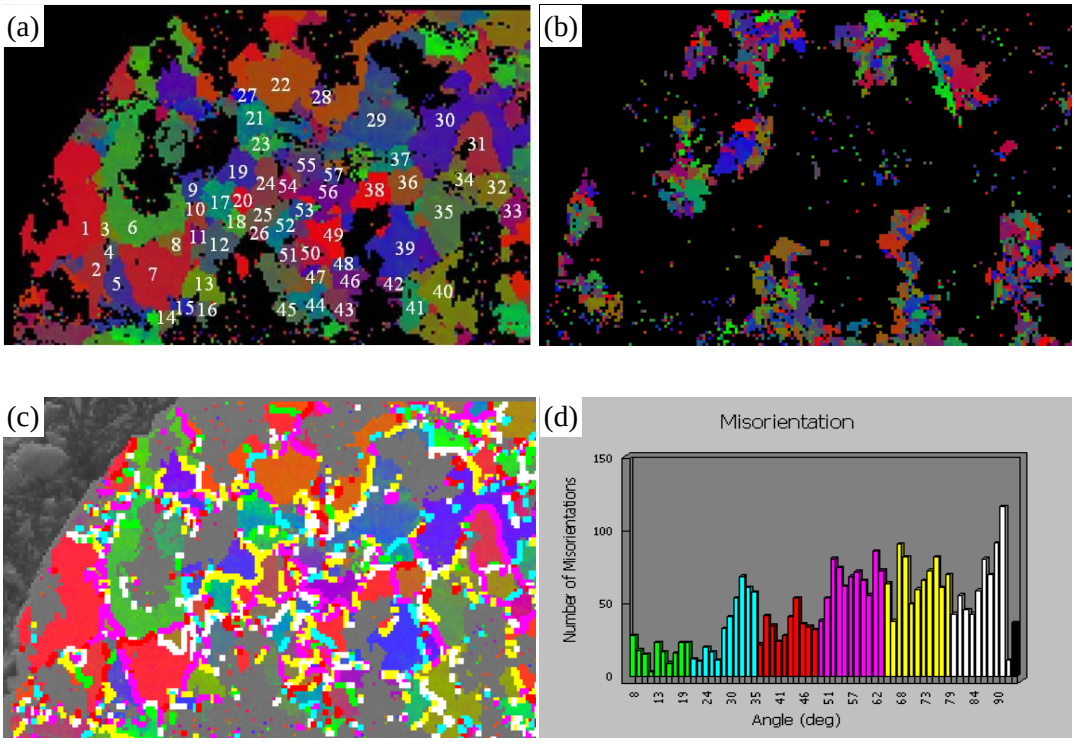

Figure 4.43 Enlarged α_2 and γ normal orientation maps in (a) and (b) from the selected dendritic region in fig. 4.21 (g) and (h); (c) and (d) are the corresponding α_2 misorientation map and its misorientation distribution graph.

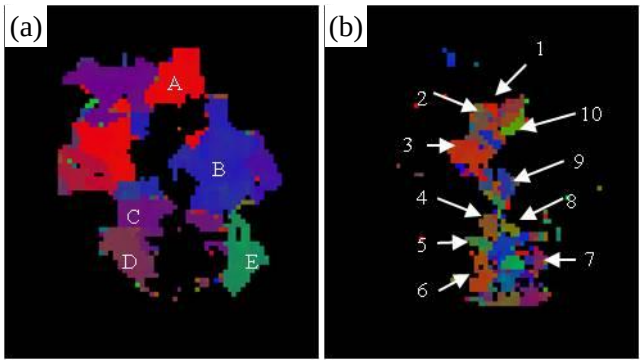

Figure 4.44 To be continued in the next page.

(c)

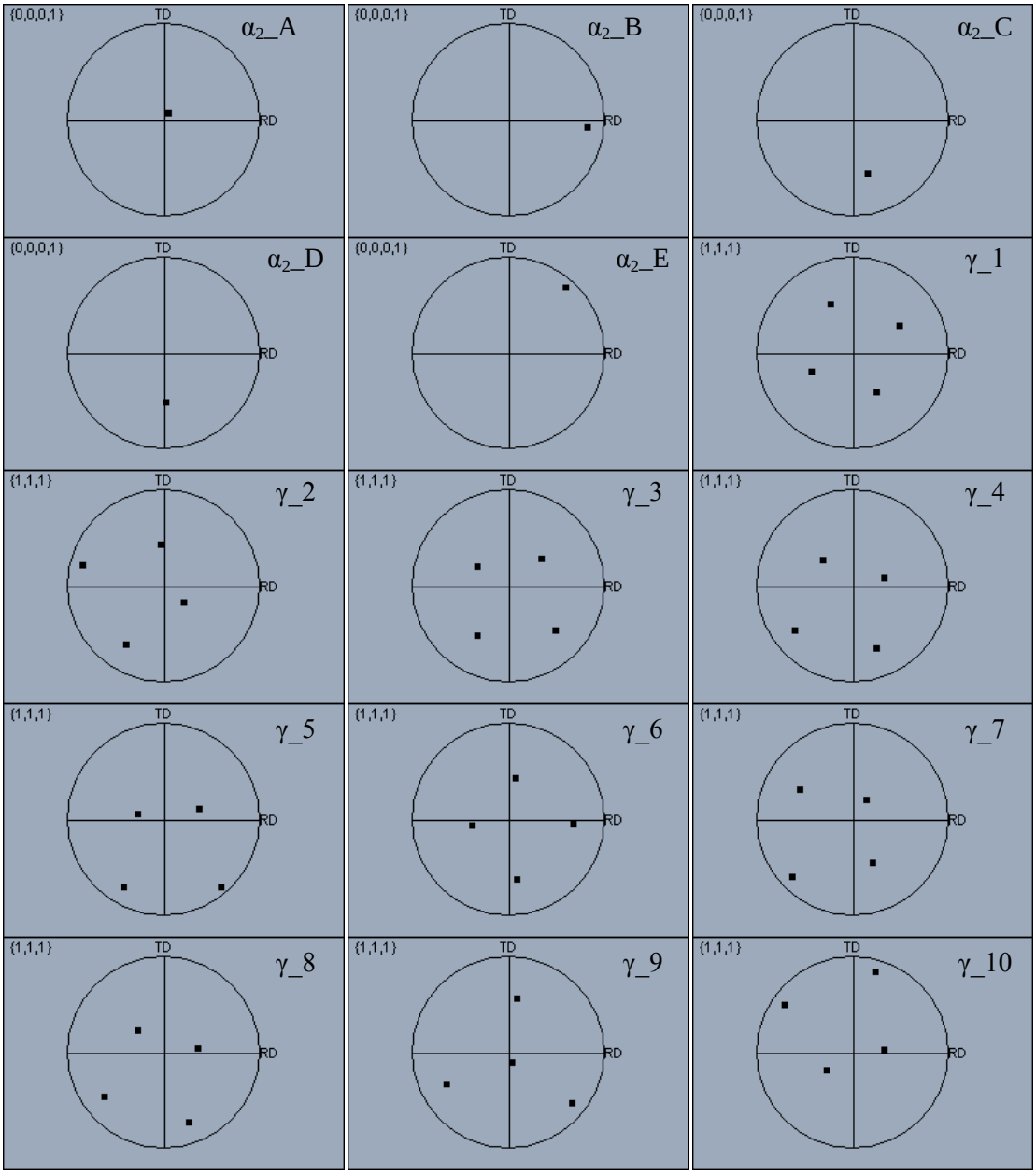

Figure 4.44 Enlarged α_2 and γ normal orientation maps in (a) and (b) from a selected dendritic region in fig. 4.22; (c) shows the (0001) α_2 pole figures and {111} γ pole figures of the labelled α_2 and γ grains in (a) and (b), respectively.

4.3 Solidification behaviour of borides in boron-containing TiAl alloys

As observed and discussed in literature review and previous sections, the addition of boron is a very effective way to refine the microstructures of TiAl-based alloys. Regardless of the mechanisms for the refinement introduced by the addition of boron, the solidification behaviours of borides themselves are so far not well understood. Even though it has been established that the cooling rate can affect the morphologies of borides during solidification[32] and the crystal structures of borides are affected by alloy compositions[31], no thorough investigation of the influence of cooling rate and alloy compositions on both morphologies and crystal structures of borides has been reported. This part of work is dedicated to solve this problem through the investigation of microstructural and crystal structural evolution of borides in Ti4522XD and Ti48Al2Cr2Nb1B buttons.

4.3.1 Microstructural evolution of borides under different cooling rate and alloy compositions

The microstructural characteristics of a Ti4522XD button from the edge to the centre along the solidification direction are shown in fig. 4.45 (a) to (c). Fig. 4.45 (a) shows the BSE image of a polished sample taken from the edge of the button, which had the fastest cooling rate because this is close to the water-cooled copper crucible. The cooling rate is gradually reduced along the solidification direction from the chill zone to the last solidified region. No detectable borides were found in this chill zone. However, small equiaxed particles can be seen in the same area in an etched sample as shown in fig. 4.46 (a), which are assumed to be small borides particles. About 150 μm away from the chill zone, fine curvy borides were observed as shown in fig. 4.45 (b), Most of which were located in

interdendritic regions. In the centre of Ti4522XD button which has the slowest cooling rate during solidification, most borides appeared blocky shaped as shown in fig. 4.45 (c). The morphological evolution of borides in the Ti48Al2Cr 2Nb1B button was similar to that in Ti4522XD button, as shown from fig. 4.45 (d) to (f). Fig. 4.46 (b) shows small borides particles in the chill zone from an etched Ti48Al2Cr 2Nb1B specimen.

The above observations are consistent with those of Hyman et al.[32], in which the studied alloys were Ti-Al-B ternary systems with Al content more than 49 at.%. It should be noted that the contrast of borides in the BSE images changed from bright to dark. That is attributed to the increase of boron content in borides as their morphologies changed from the long curvy to the blocky, since more boron content in the borides leads to a lower molecular weight of those borides which in turn yields fewer back scattered electrons.

4.3.2 Crystal structural evolution of borides under different cooling rate and alloy compositions

Determination of the crystal structures of those small boride particles in the chill zones of remelted buttons, as shown in fig. 4.46, were not attempted due to the difficulty in the TEM sample preparation by both conventional methods and FIB milling, since they are too small.

TEM analysis of crystal structures of the fine curvy borides in Ti4522XD found some are Ti_3B_4 borides with an orthorhombic $D7_b$ crystal structure with lattice parameters of a = 0.326 nm, b = 1.373 nm and c = 0.304 nm, as shown in fig. 4.47, in which the fig. 4.47 (a) shows the many beam BF image of a segment of this long curvy boride and fig. 4.47 (b) to (d) are the corresponding SAD patterns from this Ti_3B_4 boride in the zone axis of [100], [201] and [10,1,0], respectively. However, most of them were found to have the B_f

structure interspersed with layers of ordered B2. B_f also has an orthorhombic structure with lattice parameters of a = 0.323 nm, b = 0.856 nm and c = 0.305 nm. B2 is an ordered cubic structure with a lattice parameter of a = 0.32 nm. The BF image of the B_f boride and the indexing of the SAD patterns are shown in fig. 4.48. The orientation relationships between B_f and B2 are found to be:

(010)B_f //(010)B2 and [001]B_f //[001]B2

For the blocky borides in the centre of Ti4522XD button EBSD was used to identify their crystal structures. Fig. 4.49 (a) shows BSE images of borides with both bright and dark contrast and the phase map in fig. 4.49 (b) reveals that bright borides are TiB with an orthorhombic B27 structure with lattice parameters of a = 0.611 nm, b = 0.305 nm and c = 0.456 nm and dark borides are TiB_2 with a hexagonal C32 structure with lattice parameters of a = 0.303 nm and c = 0.323 nm. The identification of each phase is through the indexing of Kikuchi pattern yielded from back scattered electrons. Fig. 4.49 (c) and (d) are the Kikuchi patterns and the corresponding indexings from the bright boride and the dark boride, respectively, reflecting their own B27 and C32 structures. In addition, the (010) pole figure of TiB (B27) from the bright boride, in fig. 4.49 (e), and (0001) pole figure of TiB_2 from the dark boride, in fig. 4.49 (f), show the long axis of TiB with B27 structure and TiB_2 are parallel to the [010] and [0001] directions, indicating that the fastest growing direction of TiB with B27 structure and TiB_2 are along [010] and [0001], respectively.

In Ti48Al2Cr2Nb1B button, all the long curvy borides appeared bright and blocky borides dark. Since long curvy borides in Ti48Al2Cr2Nb1B only appeared in a small area close to the chill zone, TEM samples containing those long curvy borides were prepared by FIB milling. Fig. 4.50 (a) shows the original SE image of an etched Ti48Al2Cr2Nb1B button containing long curvy borides and fig. 4.50 (b) illustrates the area selected for sectioning.

The final morphology of an FIB milled TEM sample is shown in fig. 4.50 (c), from which it is seen that those long curvy borides observed from the etched surface actually stretches deep into the matrix. This means those long curvy borides are two dimensional with two directions growing much faster that the third one which is normal to those two.

BF image of one of those long curvy borides is shown in fig. 4.51 (a) and the SAD pattern taken from this boride is shown in fig. 4.51 (b), which has been indexed to be in the $[11\bar{2}0]$ zone axes of TiB_2 type boride.

Tilting one end of this long curvy boride in Ti48Al2Cr2Nb1B button to edge-on condition, as shown in fig. 4.52 (a), it was found that the TiB_2 is in the $[1\bar{1}00]$ zone axes, as shown in fig. 4.52 (d), and the plane normal the long axes of this boride is (0001) which is illustrated in fig. 4.52 (a). This is an indication that the two fastest growing directions in the long curvy TiB_2 are [0001] and $<1\bar{1}00>$. Fig. 4.51 (b) and (c) show the corresponding BF images of this boride when they were in the TiB_2 zone axis $[01\bar{1}1]$ and $[01\bar{1}2]$, respectively, as shown in fig. 4.52 (e) and (f), which are not in the edge-on condition.

Some of those long curvy TiB_2 borides are also found to be interspersed with very thin layers of ordered B2 phase, as shown in fig. 4.53 (a). The superimposed SAD pattern in fig. 4.53 (b) indicates that the orientation relationships between TiB_2 and B2 are:

$\{1\bar{1}00\}TiB_2$ // {001}B2 and $<11\bar{2}3>TiB_2$ // <110>B2

Fig. 4.53 (c) and (d) show the other two SAD patterns from TiB_2 zone axis of $[01\bar{1}2]$ and $[\bar{1}2\bar{1}3]$, where no diffraction spots from B2 were detected. This is due to the small volume fraction of B2 phase in this boride.

In addition, none of the borides which were imaged and analysed, appeared to have any specific orientation relationships with the neighbouring matrix phases.

For the big blocky borides in Ti48Al2Cr2Nb1B button which have dark contrast in BSE images as shown in fig. 4.54 (a), EBSD phase mapping was utilised again. The resulting phase map of a selected area in fig. 4.54 (a) is shown in fig. 4.54 (b), revealing that the analysed borides are also TiB_2 type boride with its Kikuchi pattern and the corresponding indexing shown in fig. 4.54 (c). From the (0001) pole figure of this boride, in fig. 4.54 (d), it was also found that the long axes of blocky TiB_2 borides is along [0001], confirming one of the fastest growing direction for TiB_2 is along [0001] as observed in fig. 4.49 and fig. 4.52.

In summary, the crystal structures of borides in Ti4522XD button change from Ti_3B_4 and metastable TiB with B_f structure for curvy borides to stable TiB with B27 structure and TiB_2 for blocky borides, while all the borides in Ti48Al2Cr2Nb1B button are TiB_2, regardless of their morphologies.

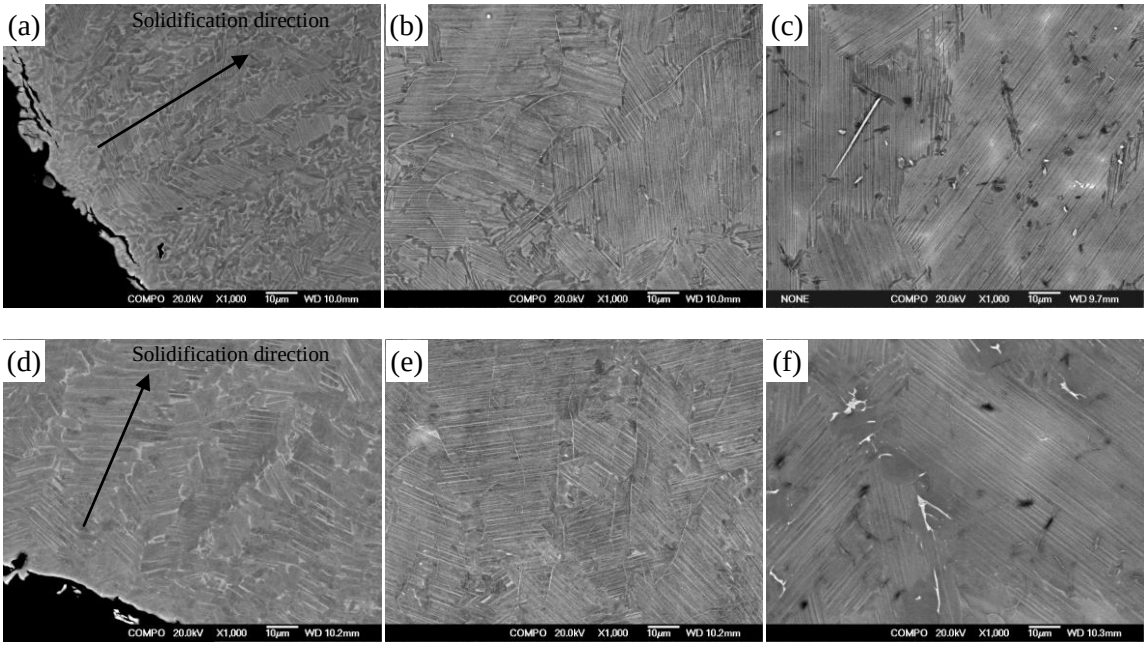

Figure 4.45 BSE SEM images of (a), (b) and (c) in Ti4522XD button along the solidification direction; and (d), (e) and (f) in Ti48Al2Cr2Nb1B button along the solidification direction.

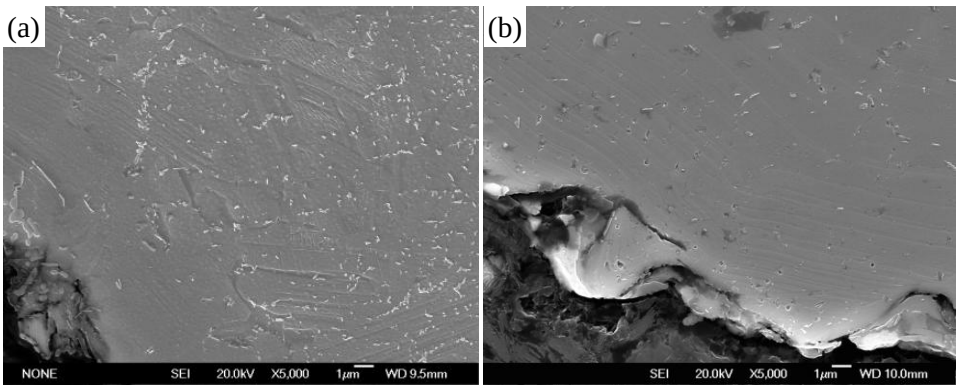

Figure 4.46 SE SEM images of the edge areas in etched samples (a) Ti4522XD button and (b) Ti48Al2Cr2Nb1B button, indicating the existence of equiaxed small borides particles.

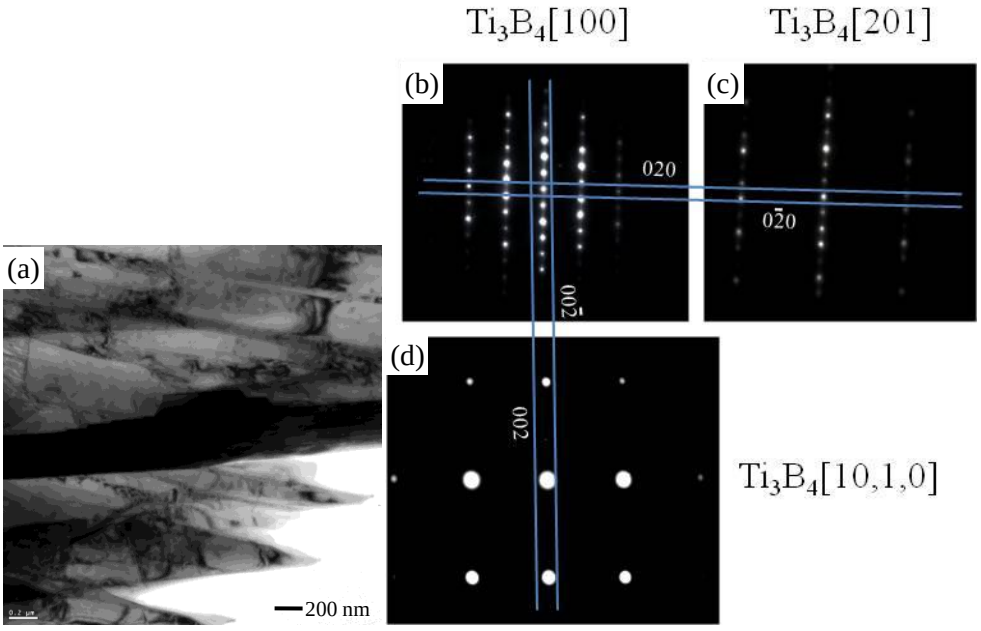

Figure 4.47 Long curvy boride in Ti4522XD button, (a) many beam BF TEM image with SAD patterns in the Ti_3B_4 zone axes (b) [100], (c) [201] and (d) [10,1,0]. The tilting angles between (b) and (c), (b) and (d) and (c) and (d) are 25.2 °, 21.1 °and 33.4 °, respectively.

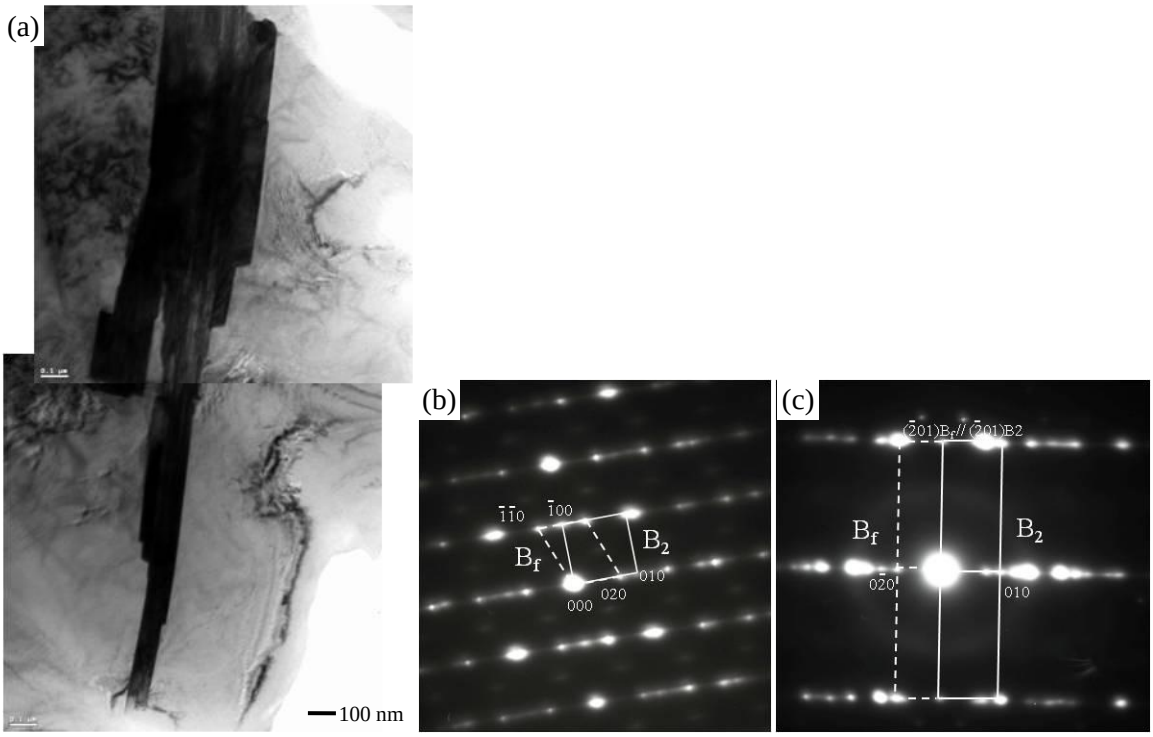

Figure 4.48 Long curvy boride in Ti4522XD button, (a) many beam BF TEM image with SAD pattern in zone axes (b) $[001]B_f$ // [001]B2 and (c) $[102]B_f$ // [102]B2. The tilting angle between (b) and (c) is 29.6 °.

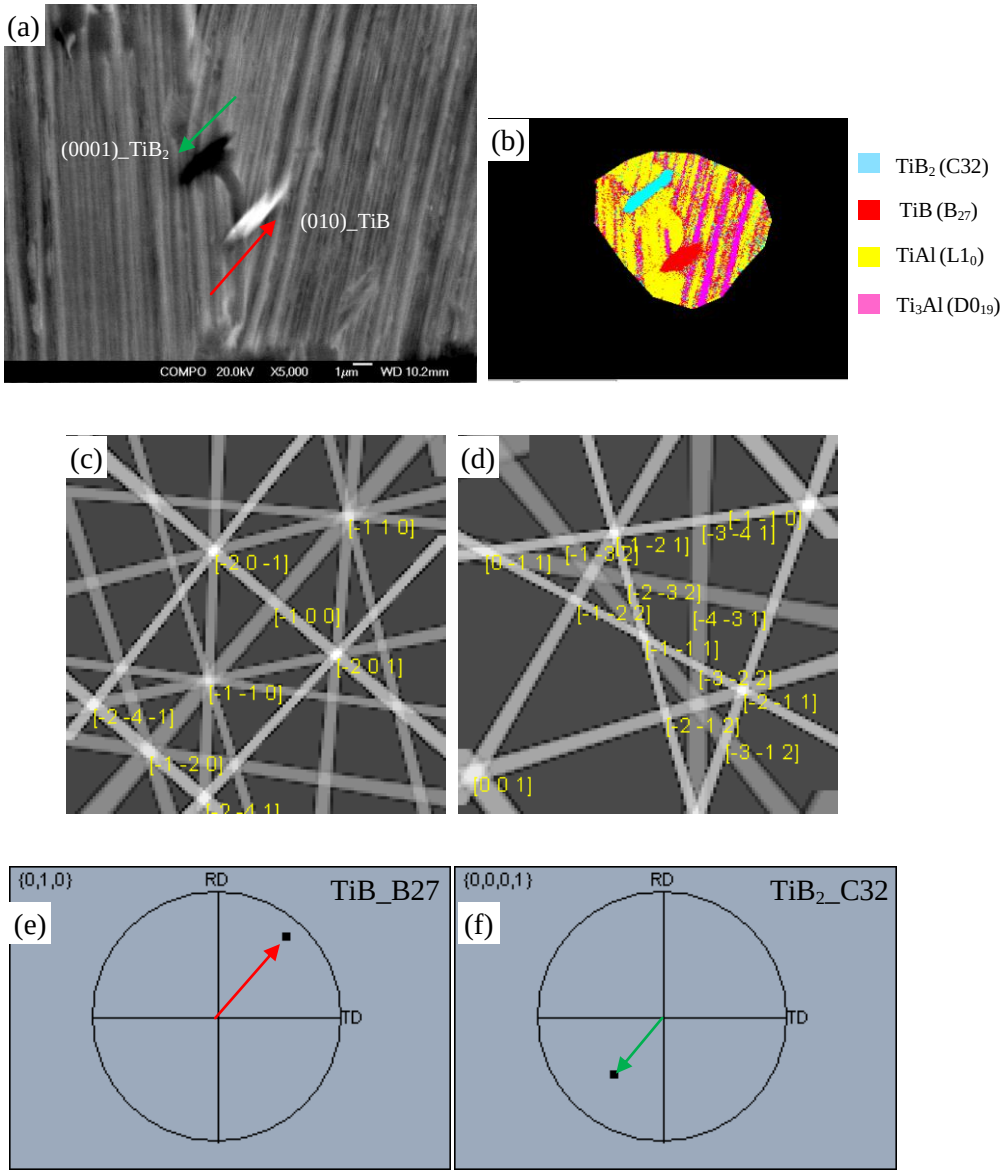

Figure 4.49 (a) BSE images of both bright and dark borides in Ti4522XD button, (b) the corresponding EBSD phase map, showing dark boride is TiB_2 with C32 structure and bright boride TiB with B27 structure. The principle for the identification of the crystal structures of those borides is through the indexing of the Kikuchi patterns in (c) and (d) yielded from bright boride and dark boride, respectively. (e) and (f) are the (010) and (0001) pole figures from bright and dark boride, indicating the fastest growing directions of TiB with B27 structure and TiB_2 are along [010] and [0001], respectively.

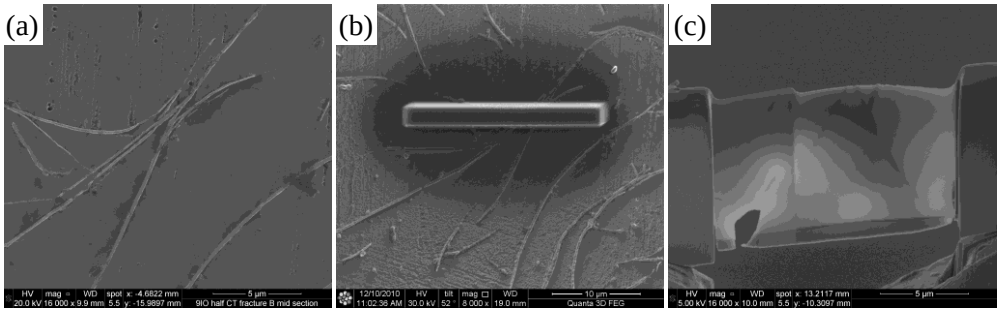

Figure 4.50 (a) SE image of etched Ti48Al2Cr2Nb1B button containing long curvy borides; (b) marks the area sectioned for TEM sample preparation by FIB milling; and (c) shows the final morphology of TEM sample selected from the region marked in (b), indicating that those long curvy borides are two dimensional.

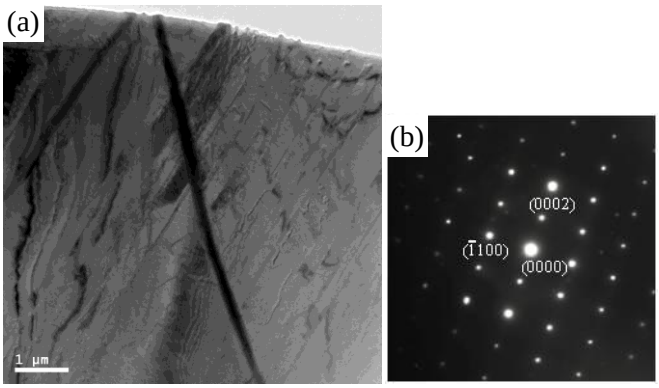

Figure 4.51 (a) Many beam BF TEM image of long curvy boride in Ti48Al2Cr2Nb1B button with (b) SAD pattern in $[11\bar{2}\,0]$ zone axes of TiB_2.

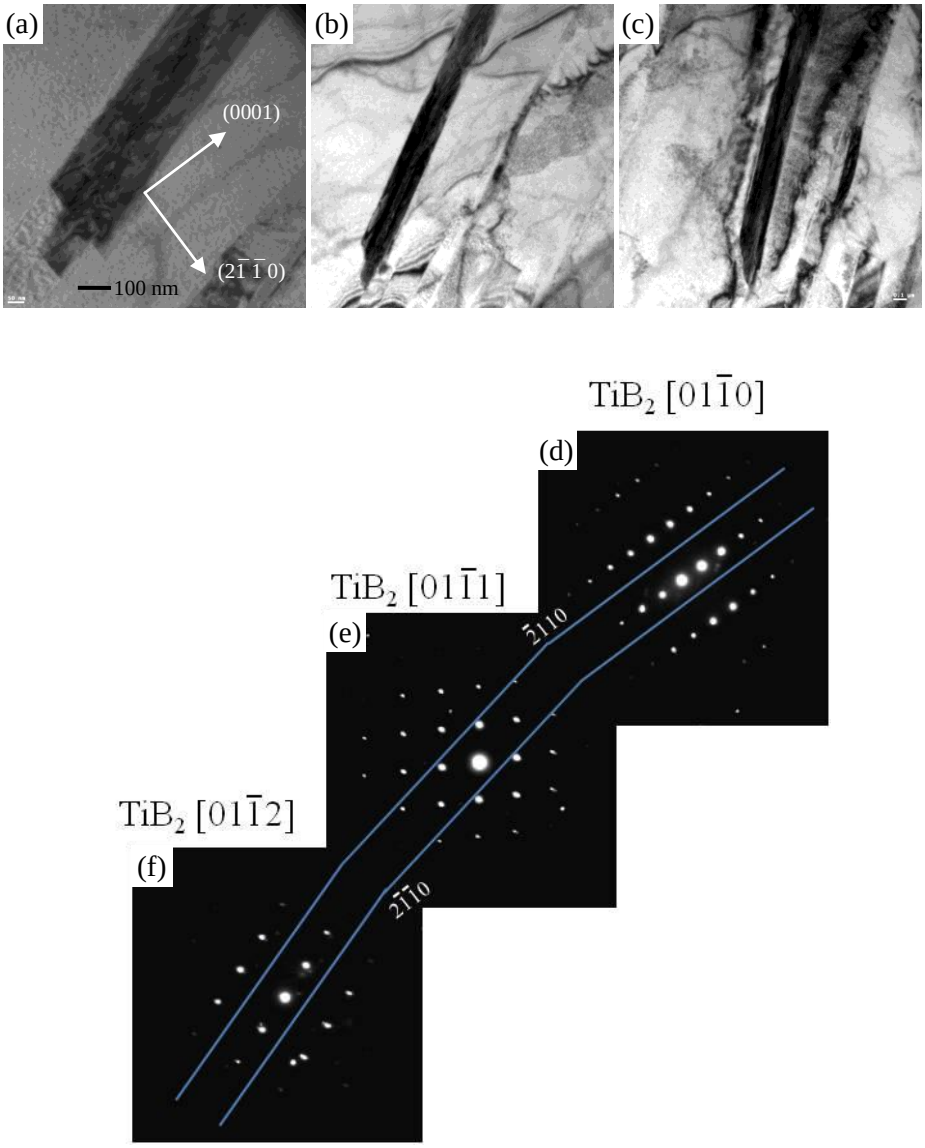

Figure 4.52 (a), (b) and (c) are many beam BF TEM images of one end of long curvy TiB_2 boride in Ti48Al2Cr2Nb1B button with their corresponding SAD patterns from zone axis $[1\bar{1}00]$ in (d), $[01\bar{1}1]$ in (e) and $[01\bar{1}2]$ in (f). The tilting angles between (d) and (e) and (d) and (f), are 27.1 °and 47.7 °, respectively. It is noticed that the end of boride in image (a) is in edge-on condition.

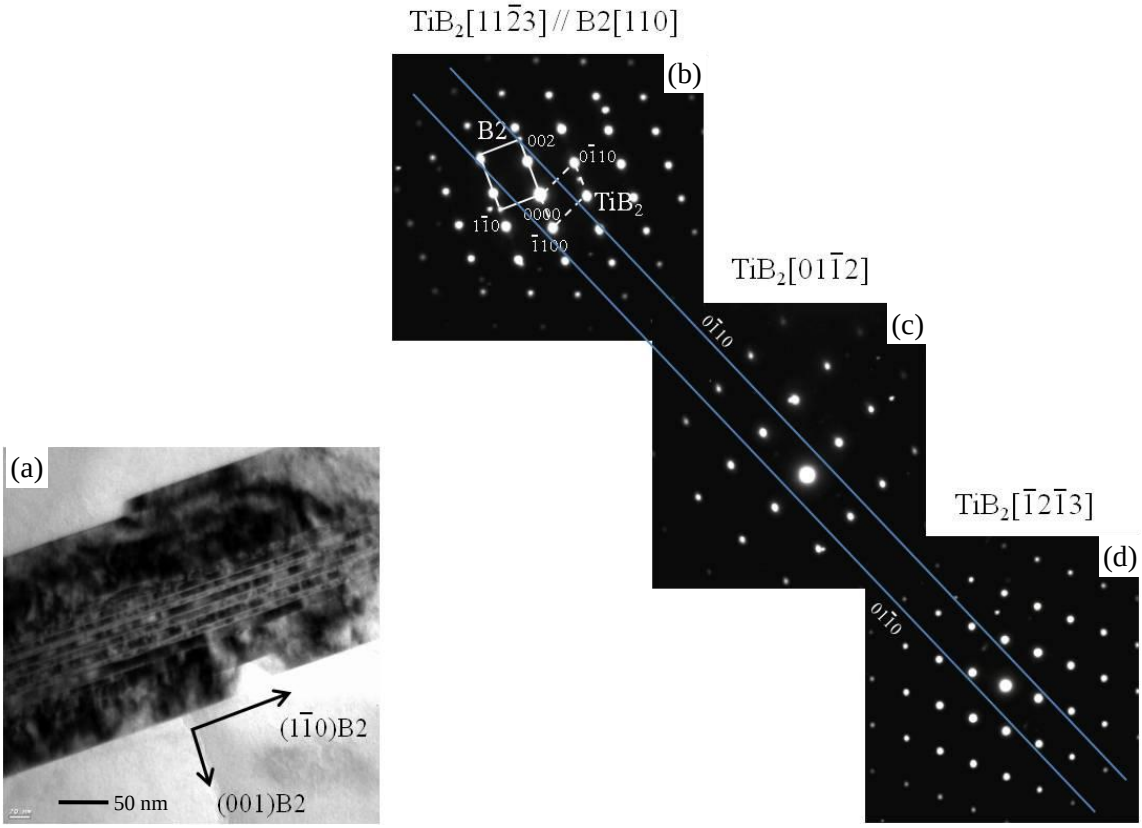

Figure 4.53 (a) Many beam BF TEM images of one section of long curvy TiB_2 boride in Ti48Al2Cr2Nb1B button with its corresponding SAD patterns from zone axis [11$\bar{2}$3] in (b), [01$\bar{1}$2] in (c) and [$\bar{1}$2$\bar{1}$3] in (d). The tilting angles between (b) and (c), and (b) and (d) are 19.6 °and 39.9 °, respectively.

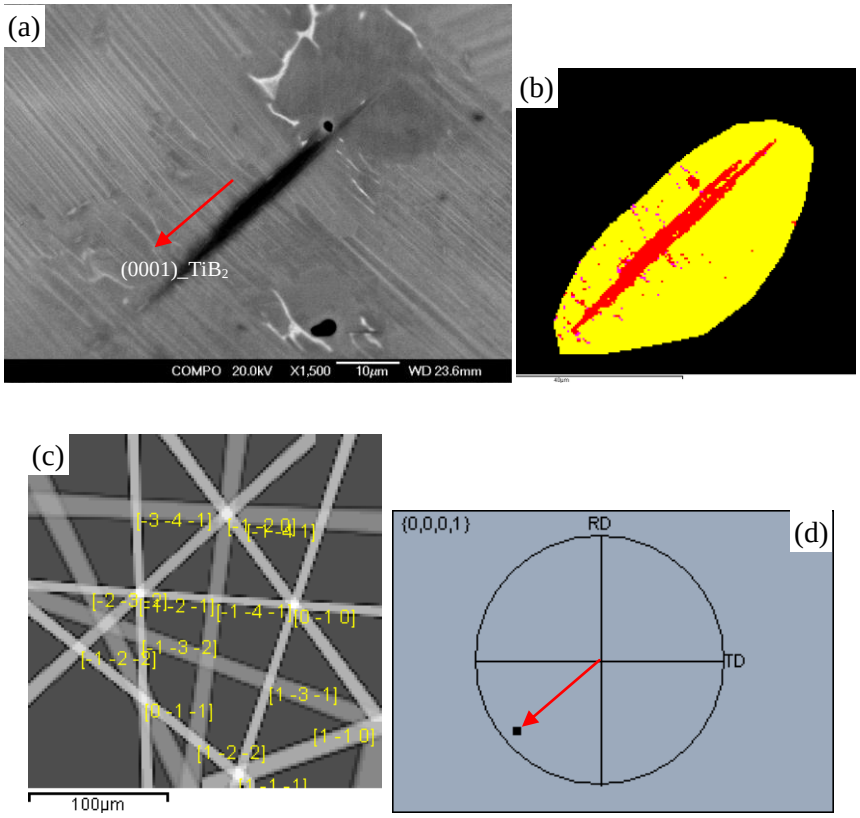

Figure 4.54 (a) BSE image of the centre of Ti45Al2Cr2Nb1B button containing blocky boride with dark contrast, (b) the corresponding EBSD phase map, showing this boride is TiB_2 with C32 structure, (c) the Kikuchi pattern from this boride and its corresponding indexing by TiB_2 structure, (d) the (0001) pole figures from this boride, indicating the fastest growing direction of TiB_2 is along [0001].

CHAPTER 5 MICROSTRUCTURES AND PROPERTIES OF HIPPED Ti4522XD CASTINGS

5.1 Microstructures of cast Ti4522XD before and after HIPping

The microstructure of near net shape cast Ti4522XD low pressure (LP) turbine blade, which is fully lamellar, is show in fig. 5.1 (a). In this backscattered electron (BSE) SEM image, the light laths and relatively grey laths are α_2 phase and γ phase, respectively, since α_2-Ti_3Al has higher molecular weight than γ-TiAl. The dark spots in fig. 5.1 (a) are pores formed during casting due to gas trapping or shrinkage. As mentioned in the literature review, it is difficult to avoid porosity when producing castings and HIPping is required to remove those defects. Fig. 5.1 (b) shows the microstructure of as-HIPped Ti4522XD from the same LP turbine blade under standard HIPping conditions which are 1260 ℃, 4 hours and 150 MPa using a heating and cooling rate of 5 ℃/min as described in the Chapter 3. It is seen that almost all the internal pored have been removed, but some equiaxed γ grains and α_2 grains have appeared, as shown in the magnified image in fig. 5.1 (c), due to recrystallisation, especially in the positions where original pores existed. The small dark spots in fig. 5.1 (b) are borides. In addition, evidence for micro-segregation can be seen in fig. 5.1 (a) from the changes in background intensity. EDS line-scanning analysis of the white streak in the as-cast microstructure revealed the enriched elements in those micro-segregated regions are Mn and Nb, while Al is depleted, as shown more clearly in fig. 5.2.

Micro-segregation of Al in the interdendritic region is also evident. However, the micro-segregation-caused white streaks were not clear after HIPing, even though Al segregation in interdendritic region was still there as seen from fig. 5.1 (b).

5.2 Structure of HIPped surface under standard HIPping conditions

5.2.1 Microstructures and crystal structures of HIPped surfaces

Apart from the changes in the microstructure of the bulk material, it was also found that when the cast Ti4522XD alloy was HIPped under these standard conditions the surface developed a complex microstructure very different from that of the substrate. The aim of the work described in this section is to understand the origin and the nature of these surface layers and their influence on the mechanical properties. This is important since these net shape investment cast blades will retain their as-HIPped surface.

The as-received Ti4522XD alloy for the study of HIPped surface was in the form of 34 × 34 × 23 mm blocks which were cut from original cast ingot using EDM. Bars of 10 × 10 × 23 mm were cut again with EDM from those blocks. The bars were firstly ground with silicon carbide grinding paper from 240× to 1200× on all six surfaces, then finally electropolished in order to remove the surface residual stress introduced by manual grinding. Typical BSE SEM image of cross-section microstructure and SE SEM image of top morphology of electropolished surface are shown in figs. 5.3 (a) and (c). Both the cross-section microstructure and surface morphology show that the electropolished surfaces were smooth and had little surface deformation because the lamellae were almost straight. However, when those cast Ti4522XD bars were HIPped under standard HIPping

conditions, the cross-section microstructure and surface morphology changed as shown in fig. 5.3 (b) (which was Ni-plated to preserve the microstructure) and (d), respectively. Fig. 5.3 (b) shows that the surface microstructure changed significantly after HIPping and contained a few apparently different layers. The dark layer around 2-3 μm in thickness below the Ni-plating was shown in fig. 5.3 (d) to contain oxide layers, as shown in fig. 5.4.

XRD analysis on those HIPped surfaces indicates the oxides were composed of Al_2O_3, TiO_2 and other Ti oxides, as shown in fig. 5.4. This oxide layer is more clearly revealed in fig. 5.5 (a) and (b) using SE and BSE mode from the same region. The oxides layer exhibits a dark contrast in fig. 5.5 (b), but the same region contains both bright and grey grains in fig. 5.5 (a). Since Al_2O_3 particles are not good electrical conductors and have a lower molecular weight, they show bright contrast in SE mode and dark contrast in BSE mode, while even though Ti oxides also have a lower molecular weight and show a dark contrast in BSE image in the oxides layer in fig. 5.5 (b), they are semiconductors and as a consequence, showing almost the same contrast in SE image as the substrate. Therefore, Al_2O_3 particles and Ti oxides particles can be distinguished in the oxide layers as indicated in fig. 5.5 (a). This is proven by EDS analysis as shown in table 5.1. It is clear that the bright particles in the oxide layer shown in fig. 5.4 (a) are Al_2O_3 particles and the grey particles are Ti oxides particles. Furthermore, EDS analysis results indicate that both Al_2O_3 and Ti oxides have a certain solubility of other metallic elements, especially a great amount of Al was detected in Ti oxides.

XRD results also revealed the possible existence of carbides on the HIPped surface. The carbon may come from the HIPping vessel which was contaminated by the other HIPping runs such as the HIPping of metal powders which were encapsulated within carbon-containing mild steel cans.

EDS line-scanning analysis on the cross-section of the HIPped surface revealed the layer underneath the oxide layer which was about 8 μm thick was enriched in Ti and depleted in Al and the layer between the Ti-rich layer and substrate was an Al-rich layer which ranged from 10 to 25 μm. The elemental distribution of HIPped surface is illustrated in fig. 5.6. Apart from the enrichment of Ti and Al in their particular layer, oxygen was identified in the oxide layer and Nb was found to be enriched in the interface between the Ti-rich layer and Al-rich layer. In addition, the concentration of Mn in Ti-rich layer was very low compared with that in matrix. On the other hand, the Ti and Al concentration fluctuated in the matrix which is related to the change in compositions of the α_2 laths and γ laths in the lamellae. Relative analysis of the compositions in each layer by EDS is summarised in table 5.2, which were not standardised by the standard Ti4522XD sample, and the Al concentration was a little lower than actual values. However, the tendency reflected in this table is consistent with line scanning results.

The crystal structures of those Ti-rich grains were analyzed by TEM. The results revealed that the majority of Ti-rich grains are α_2 phase. Fig. 5.7 shows the TEM image of α_2 grain and their corresponding selected area diffraction (SAD) patterns in zone axes $[2\bar{1}\,\bar{1}\,6]$, $[2\bar{1}\,\bar{1}\,3]$ and $[1\bar{1}\,03]$. However, investigation also revealed that there were some other crystal structures in this Ti-rich layer. Fig. 5.8 shows a Ti-rich grain from which the SAD patterns were indexed as a face centered cubic (fcc) crystal structure with lattice parameter a≈0.43 nm. The zone axes for those SAD patterns were indexed as [001], [112] and [101], respectively. Fig. 5.9 displays another Ti-rich grain which had been shown to have a tetragonal crystal structure with a≈0.81 nm and c≈ 1.39 nm. The SAD patterns obtained from this grain were from the zone axes of [101], [001] and [011]. The superlattice diffraction spots in the [011] SAD pattern, shown in fig. 5.9 (d), indicates that it was

actually an ordered tetragonal crystal structure. It is noted that, in this Ti-rich layer there were lots of oxides particles embedded inside the grains or along grains boundaries, as shown in fig. 5.10 (a). The growth of those oxide particles made this layer appear loose. Fig. 5.8 also shows lots of pores with nano-scale small particles inside (fig. 5.10 (b)) which were located in the interface between the Ti-rich layer and Al-rich layer. According to the EDS analysis in table 5.3, those small particles had a high content of Ti and O. Therefore, they were supposed to be Ti oxides.

For the identification of the Al-rich layer which was between the Ti-rich layer and substrate, a HIPped sample with the oxides layer and Ti-rich layer sand blasted off was used for XRD analysis. In this case only the Al-rich layer was left. The cross-section microstructure of the sample containing only the Al-rich layer is shown in fig. 5.11 (a) and the corresponding XRD result, in fig. 5.11 (b), revealed it was a pure γ-TiAl phase. Some Al_2O_3 peaks were also indentified, but it is believed that those Al_2O_3 peaks were from the sand particles remaining on the surface. TEM analysis on these Al-rich grains confirmed that they were γ grains, as are shown in fig. 5.12 in SAD patterns which correspond to [$3\bar{2}$ 3], [101] and [$2\bar{1}$ 1] γ zone axes. It is interesting to notice that there are 5 extra spots in the γ [101] diffraction pattern in the direction along the 111* diffraction maximum, as shown in fig. 5.12 (c), which would totally disappear when the sample was tilted along 111* for 5.3 °. The reason for this phenomenon is not understood.

Table 5.4 is a summary of the EDS results analysed by TEM from the above identified grains, indicating the level of elemental enrichment in each grain. In summary, for the Al-rich grains, the main phase was γ phase, while for the Ti-rich grains there was α_2 phase which was the majority phase and phases with cubic and ordered tetragonal crystal structures which contained a certain amount of light elements like C and O.

5.2.2 Oxygen distribution along the HIPped surface

The average oxygen distribution in the HIPped surface and matrix was examined by WDS using point measurement and the result is shown in fig. 5.13. It was found that the Ti-rich layer was enriched in oxygen and the α_2 phase in the matrix has a higher capability to dissolve oxygen than does the γ phase. Since most of the Ti-rich grains were α_2, it is reasonable to believe that α_2 grains in this Ti-rich layer were enriched in oxygen.

Further WDS analysis of the oxygen distribution as a function of distance away from the HIPped surface was carried out. Fig. 5.14 (a) shows the positions where point measurements were conducted and fig. 5.14 (b) is the corresponding result. It is shown that in the oxygen-enriched Ti-rich layer, the oxygen concentration decreases with increase in distance from the surface. However, the grain boundaries could be highly enriched with oxygen in this Ti-rich layer as shown in fig. 5.14 (b) in the last few dark points. The oxygen concentrations in the γ-layer and the two metallic phases in matrix, however, do not change a lot. This may be due to the low solubility of oxygen in γ and no penetration of oxygen in the matrix.

5.3 Affecting factors

5.3.1 The influence of HIPping time

When HIPping time was increased from 1 hour to 10 hours with all the other conditions unchanged, it was found the surface microstructures changed. Fig. 5.15 shows the SE and the corresponding BSE cross section microstructures of 1 hour and 10 hours HIPped samples. For 1 hour HIPped surface, the γ layer formed directly under the oxide layer which was identified by BSE image in fig. 5.15 (b) in which the oxides layer appeared in

dark contrast and the γ layer grey contrast similar to that of γ laths in the neighbouring lamellae. Two hours HIPped surface exhibited a similar cross section microstructure. However, when the HIPping time reached 10 hours the surface microstructure was like that shown in fig. 5.15 (c) and (d). EDS analysis in table 5.5 and XRD analysis in fig. 5.16 revealed if the HIPping time was no more than 2 hours Ti oxides were predominant in the oxide layer, while if the HIPping time reached 10 hours Al_2O_3 was dominant. Quantitative EDS analysis in table 5.5 also revealed that the oxygen concentration in the oxide layer of 1 hour HIPped surface was much less than that in the oxide layer of the 10 hour HIPped sample. In addition, XRD analysis on both the 1 hour and 10 hours HIPped surfaces found Mn oxides and Nb oxides, in addition to some carbides. In samples HIPped for 10 hours, many grains in the Ti-rich layer were oxidised and furthermore the γ layer disappeared and was replaced by a subsurface of coarsened α_2 laths. Fig. 5.17 shows the change of thickness for each layer as the HIPping time is increased. The thickness of the γ layer was not plotted in this chart because it did not exist in the surface layers formed by HIPping for 10 hours and because it was uneven in thickness thus difficult to measure. The thickness of the oxide layer increases as the HIPping time is increased, but there was no obvious change for the Ti-rich layer when the HIPping time was more than 4 hours.

5.3.2 The influence of HIPping temperature

HIPping temperature was also found to have a great effect on the structures of HIPped surfaces. Fig. 5.18 shows the SE and BSE cross section microstructures of 900 ℃ and 1100 ℃ HIPped surfaces both of which were HIPped for 4 hours under 150 MPa. EDS analysis in table 5.6 shows that for both the 900 ℃ and 1100 ℃ HIPped surfaces the top surfaces layers were enriched in O and the subsurface layers enriched in Ti. They are different from the typical cross-section microstructure of the HIPped surface shown in fig.

5.3, since there were no Al-rich layers underneath the Ti-rich layers. In conjunction with XRD analysis in fig. 5.19 and BSE images in fig. 5.18 (b) and (d), it is reasonable to believe that in both conditions the top surfaces were composed of both Ti oxides and Al_2O_3 and Ti-rich layer contained mainly α_2 grains. On average, the thickness of oxides layer and α_2 layer of 900 ℃ HIPped surface was about 2.5 μm and 1.5 μm, respectively, while the thickness of oxides layer and α_2 layer of 1100 ℃ HIPped surfaces was about 2.0 μm and 2.5 μm, respectively. Obviously, the ratio of the thickness of the oxide layer to α_2 layer was increased with increase of HIPping temperature. It is worth noting that the brightness of some α_2 grains in the Ti-rich layer of the 900 ℃ HIPped surface in the BSE image was stronger than the α_2 laths in the matrix. This may be due to the interstitial dissolution of a certain amount of oxygen as indicated by the EDS analysis in table 5.6, effectively increasing the molecular weight of the α_2. Orientation effect may also be the reason, since the coarsened end of the thick α_2 lath in fig. 5.18 (b) still has the same contrast as those in matrix. Moreover, the higher the HIPping temperature, the more oxides particles, especially more Al_2O_3 particles would form on the surface as reflected by the XRD intensities of oxides.

5.3.3 The influence of oxygen concentration in the Argon

Under 150 MPa HIPping pressure, the oxygen partial pressure in the argon is about 1.5×10^{-3} mbar, which is sufficient for the occurrence of oxidation as observed above. The introduction of Ti sponge as a getter during HIPping could absorb the oxygen in the HIPping vessel. Under such an environment with much lower oxygen concentration in argon, the HIPped surface, which had an originally electropolished surface, had the microstructure like that shown in fig. 5.20 (a). It is seen that the top surface was covered by loose particles which was about 7 μm thick. There is no γ layer. Instead, there was a layer

about 15 μm thick of α_2 laths coarsened subsurface. XRD analysis on such a surface revealed the top surface layer was mainly covered by metastable Ti oxides, like TiO, as shown in fig. 5.20 (b).

HIPping with higher oxygen level than normal was realised by the introduction of not completely densified Al_2O_3 blocks which would release some oxygen during HIPping. The resulting cross-section microstructure of a HIPped surface is shown in fig. 5.21. There was a thick oxidised layer of about 130 μm and beneath this layer was a α_2 phase enriched layer which was around 10 μm thick.

Even though it is not clear how much the oxygen concentration could be reduced by the introduction of a getter or how much it could be increased by the introduction of Al_2O_3 blocks, it is clear that the oxygen partial pressure in the argon has a huge influence on the structure of the HIPped surfaces.

5.3.4 The influence of HIPping pressure

The standard HIPping pressure used in the present study is 150 MPa which is used to get rid of internal porosity. To understand the influence of HIPping pressure on the formation of the HIPped surface, heat treatment in argon with 1 atm pressure at 1260 ℃ for 4 hours was carried out by back filling 0.2 atm argon at room temperature in the glass tube which was used to encapsulate the specimen that was wrapped with Ta foil. The cross section microstructure of the surface after this heat treatment is shown in fig. 5.22. There is no obvious oxides layer and neither γ layer. The surface is actually an Al-depleted layer, as indicated by EDS analysis in table 5.7, which is supposed to be formed because of evaporation of Al since it has a high saturation vapour pressure. However, when the

pressure was reduced the oxygen level in the argon environment was also reduced. That may be the reason why no obvious oxidation occurred.

5.3.5 The influence of surface deformation

All the observation mentioned above are based on the originally electropolished surfaces which are supposed to be deformation free. To investigate the influence of surface deformation on the formation of HIPped surface layers, a machine ground sample in fig. 5.23 (a) and a sand blasted samples in fig. 5.23 (b) were prepared to compare with the electrochemically polished sample in fig. 5.23 (c). The severeness of surface deformation is manifested by the curvature of the lamellae in the region below the sample's surfaces. In the ground sample, the lamellae were bent to the right which was the moving direction of the grinding wheel surface. The deformation depth which can be judged from the SEM image is about 20 μm. The lamellae beneath the deformed surface are fairly straight. Compared to the ground surface the deformation on the blasted surface is moderate since curvy lamellae can only be seen at some places and to a small depth. In the electrochemically polished sample all the lamellae are straight, indicating a deformation-free state. Moreover, the Al_2O_3 blasted surface had an obvious high surface roughness compared with the other two.

However, those three samples exhibited almost identical surface structures after HIPping under the standard HIPping conditions as shown in fig. 5.23 (d), (e) and (f) which correspond to ground, blasted and electropolished surfaces, respectively. The difference is that the severer the original surface deformation had, the thicker the HIPped surface layers, especially the γ layers, would be.

Another effect of surface deformation on the formation of HIPped surface is on the mechanism of the growth of the γ layer. As shown in the EBSD orientation map in fig. 5.24 (b), for the originally electropolished samples the γ grains in the γ layer had the same orientation as γ laths in the neighbouring lamellae. This means the growth of γ grains was through the growth of γ laths by compositional diffusion. However, if the surface was deformed before HIPping, the γ grains did not inherit the orientation relationship from the neighbouring γ laths as shown in fig. 5.24 (e) and had random orientation distribution relative to the other γ grains. Therefore, they were formed by recrystallisation. Compared with fig. 5.24 (b) and (c) it is clear that the γ grains in γ layer were much bigger than the α_2 grains in the Ti-rich layer which were around 15 μm and 4μm, respectively, and in both conditions the equiaxed α_2 grains were randomly orientated. Thus, the formation of α_2 grains in Ti-rich layer was through a nucleation and growth process.

5.4 The influence of surface layers on properties

5.4.1 Tensile properties

Tensile test pieces with and without HIPped surfaces were tested at ambient temperature. To prepare the tensile test pieces with and without a surface layer, all the as-machined tensile test pieces were hand ground with silicon carbide grit paper from 400× to 1200× to a depth of 100 μm and then electrochemically polished to a depth of 50 μm to completely remove the surface residual stress introduced by machining[156]. Then those surface treated test pieces were HIPped again at 1260 ℃ for 4 hours at 150 MPa. In this case, all the test pieces formed surface layers, of which half of them were hand ground 50 μm to get rid of all the surface layers formed during HIPping with silicon carbide grit papers. The cross-section microstructures of tensile test pieces with and without surface layers, in which γ

layer was contained, are shown in fig. 5.25 (a) and (b). The tensile properties are summarised in table 5.8. It is seen that the there is no significant difference between the test pieces with and without surface layers. However, the whole batch of test pieces exhibited a low ductility, which was only about 0.3 %.

The tensile testing at room temperature was repeated in order to check the influence of the γ layer in the hope that the matrix has good ductility. Unfortunately, no γ layer was contained in the HIPped surfaces, instead, there was an α_2 layer contained in the HIPped surface due to the problem of the leakage of oil in the pump which allowed oil into the argon and increased the oxygen concentration by decomposition during HIPping. The cross-section of the second batch of tensile test pieces are shown in fig. 5.26 and the tensile results are summarised in table 5.9. Even though the α_2-layer-containing HIPped surfaces were not expected and the matrix's ductility was still not good, it reveals that the α_2-layer-containing HIPped surfaces are very detrimental to both tensile strength and ductility, as indicated in table 5.9.

The investigation of fracture surfaces reveals that if the HIPped surface contained γ layer before testing, whether or not the γ layer remained or not, the crack initiated through interlamellar fracture in the near surface as shown in fig. 5.27 (b) and (d). However, if the HIPped surface contained an α_2-layer, the crack would initiate from the α_2 layer by intergranual fracture as shown in fig. 5.28 (b). When this layer was removed, the strength and ductility recovered and exhibited the typical interlamellar fracture for crack initiation as shown in fig. 5.28 (d). The overall fracture surfaces in fig. 5.27 (a) and (c), and fig. 5.28 (a) and (c) exhibit a quite flat morphology, indicating a brittle fracture mode. Once the crack is initiated in TiAl alloys, the cracks propagate through translamellar, interlamellar and lamellar colony boundaries as indicated by the secondary cracks underneath the

fracture surface in fig. 5.29 (a) and fracture surface in fig. 5.29 (b), which also indicates that the cracks could propagate through the debonding between borides and matrix or between borides themselves.

5.4.2 Micro-hardness

The micro-hardness of each layer in the HIPped surface and also the matrix were tested as a function of distance away from the surface and the results are shown in fig. 5.30. Fig. 5.30 (a) and (b) refer to the SE and BSE images of cross-section of HIPped surface containing a γ-layer with the indication of the indentation for hardness testing. From fig. 5.30 (b), it is seen the hardness testing were carried out in oxide/Ti-rich layer, γ-layer and matrix. The results in fig. 5.30 (e) show that the oxide/Ti-rich layer has the highest hardness and the γ layer has the lowest. On the contrary, if it was a HIPped surface containing an α_2-layer as shown in the SE image in fig. 5.30 (c) and BSE image in fig. 5.30 (d), the α_2 layer is much harder than the matrix even though it was still softer than the oxide/Ti-rich layer.

5.4.3 High cycle fatigue (HCF) properties

For the HCF testing with and without surface layers, the test pieces were prepared in the same way as described in section 5.4.1, but test pieces with HIPped surface layers were further polished to contain only the γ layer to avoid the micro-cracks existing in the oxide layer and Ti-rich layer. The polishing process included sand blasting and vibration polishing. In this way, two groups of test pieces with and without γ layer for the HCF testing were prepared, of which the cross-section microstructures are shown in fig. 5.31. From fig. 5.31 (a), it is known that the thickness of the remaining γ-layer was about 20 μm.

Room temperature HCF tests of cast Ti4522XD alloy with and without γ layer were carried out and the resulting S-N curves are shown in figure 5.32. The HCF failure strengths for more than 10^7 cycles in both cases are about 400 MPa. In addition, in both cases there was a scatter in the strength. Therefore, there is actually no significant difference in the room temperature HCF properties for the test pieces with and without a γ layer.

Fractography of fracture surfaces of both cases is shown in fig. 5.33. In terms of crack initiation, both the test pieces with and without a γ layer failed by interlamellar fracture in the near surfaces as shown in fig. 5.33 (b) and (d). The cracks propagated in the same way as was observed in fig. 5.29 by translamellar, interlamellar and lamellar boundaries fracture and also debonding between borides and matrix or between borides themselves.

5.4.4 Corrosion property and HCF properties after corrosion

5.4.4.1 Hot corrosion properties

HIPped Ti4522XD samples with and without γ layers were prepared. The surface cross-section microstructures of those specimens with and without a γ layer were similar to those shown in fig. 5.25. As described in the experimental section, there were two groups of materials which were immersed in two different corrosion solutions. In each group, there were samples with and without a γ layer.

Surface cross-section microstructures of these samples after hot corrosion are shown in fig. 5.34. For the hot corrosion experiment of the first group of specimens which had the less severe corrosion environment, samples with a γ layer retained their γ layer after corrosion as shown in fig. 5.34 (a). However, samples without a γ layer displayed rough surface morphology as shown in fig. 5.34 (b). Clearly, samples with a γ layer had better corrosion resistance than those without.

However, in the tougher corrosion environment with higher acid concentration and corrosion temperature, the surfaces of both samples with and without a γ layer had been severely corroded, as shown in fig. 5.34 (c) and (d), exhibiting a gear teeth shaped surface morphology underneath the top surface layer. In addition, the BSE images shown in fig. 5.34 (c) and (d) also indicate that the γ phase was more corrosion-resistant than the α_2 phase in this corrosion environment, since in the gear teeth shaped region α_2 laths were more severely corroded than γ laths. In addition, the EDS analysis determined by point measurement as a function of distance in the γ lath, as shown in fig. 5.35, revealed that during hot corrosion process metallic elements in the specimen surfaces such as Ti and Al, especially Al, dissolve and light elements, especially O, N and Cl, diffuse into metallic phases.

XRD analysis on the corroded surface with and without a γ layer revealed the top surfaces were mainly covered by metallic oxides. The results are shown in fig. 5. 36. They also revealed that the γ layer made no difference on the corroded surface products. For the corroded specimens which originally had a γ layer, the top oxides layer might be enriched in Al_2O_3, while for those without the γ layer, the corroded surfaces were enriched in Ti oxides, as indicated in fig 5.37 and their corresponding EDS analysis results in table 5.10 which was determined by point measurement.

In some areas, the specimen surfaces formed a multilayered structure after severe hot corrosion as shown in fig. 5.38 (a). The corresponding EDS line scanning in fig. 5.38 (b) along the cross-section of this corroded surface indicates that the top layer, which was about 5 μm thick, was enriched in Ti and the second thin layer, which was about 1 μm thick, was rich in Al. The third layer and the fourth layer were again enriched in Ti and Al,

respectively. In the whole corroded surface layer, oxygen was apparently enriched and was richer in Al-rich layer than that in Ti-rich layer.

5.4.4.2 RT HCF property after hot corrosion

To investigate the influence of the γ layer on HCF property in corrosion environment, the HCF test pieces with and without γ layer were prepared in the same way as mentioned in 5.3.3. Then those test pieces were corroded in the second type of $NaCl/SO_x/H_2O$ solution which was tougher and had 300 ppm sulphide concentration at 700 ℃ for 200 hours. After corrosion, the surfaces of thread areas of the HCF test pieces were cleaned by screw die which has the same diameter of the thread. Then all the corroded test pieces were tested at room temperature.

Fig. 5.39 shows the RT HCF results of all test pieces with and without γ layer. Considering the scattering of the values, it is actually difficult to say if there was any difference between these two groups of specimens, but on the whole the fatigue strength of the corroded specimens is about 320 MPa, much lower than that without corrosion which is about 400 MPa.

Fractures surfaces of those failed HCF test pieces, shown in fig. 5.40, indicate similar crack initiation and propagation behaviours like those without corrosion. For instance, for both test pieces with and without γ layer, it is seen that the cracks initiated from the near surface through interlamellar fracture as shown in fig. 5.40 (b) and (d) which is similar to that in fig. 5.28, fig. 5.29 and fig. 5.33. Therefore, the γ layer does not have a significant influence on HCF properties after severe corrosion. However, it is not clear whether the γ layer has some beneficial influence on HCF properties if the test pieces are corroded in a less severe corrosion environment, say the $NaCl/SO_x/H_2O$ solution with only 100 ppm sulphide concentration and lower corrosion temperature at 650 °C, in which the γ layer has

a better corrosion resistant property. But because of the limitation of material and time, the influence of γ layer on HCF properties in less severe corrosion environment will be investigated in future.

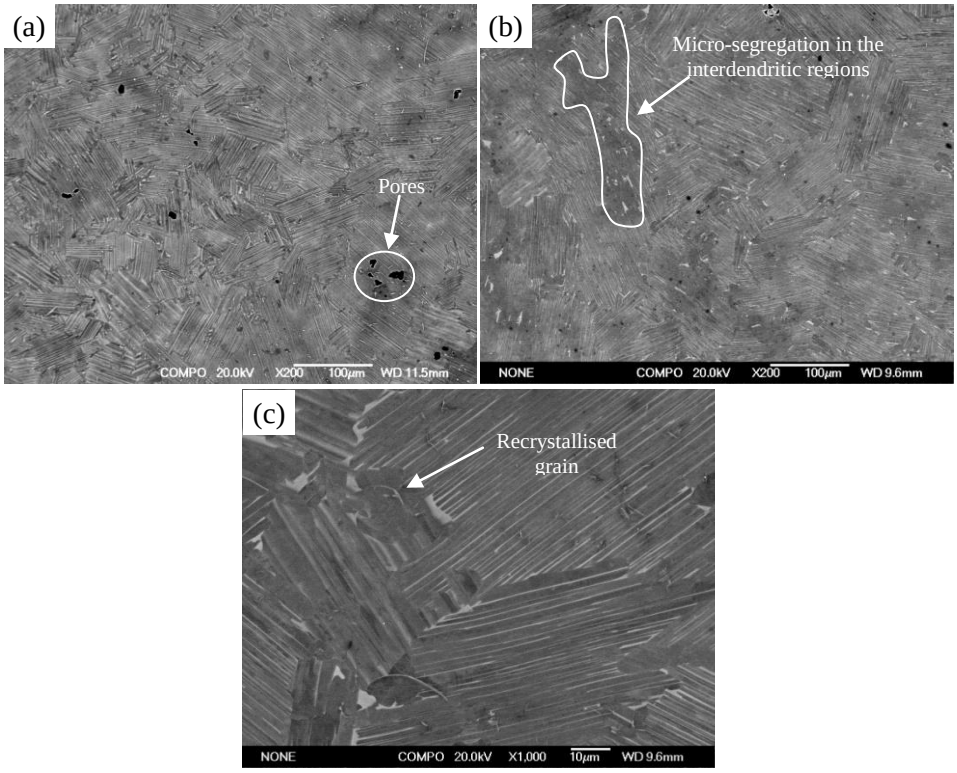

Figure 5.1 Backscattered SEM (BSE) images of (a) as-cast and (b) and (c) as-HIPped Ti4522XD from LP turbine blades.

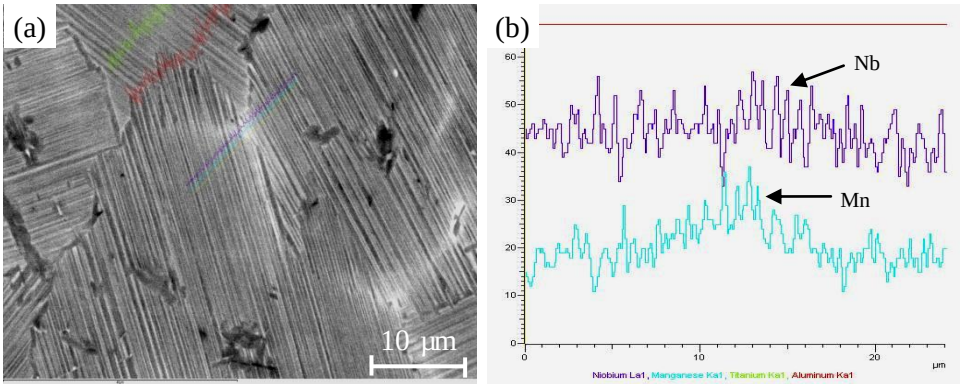

Figure 5.2 (a) BSE image of as-cast Ti4522XD and (b) the corresponding EDS line scan in the micro-segregation region, indicating Mn and Nb are slightly enriched.

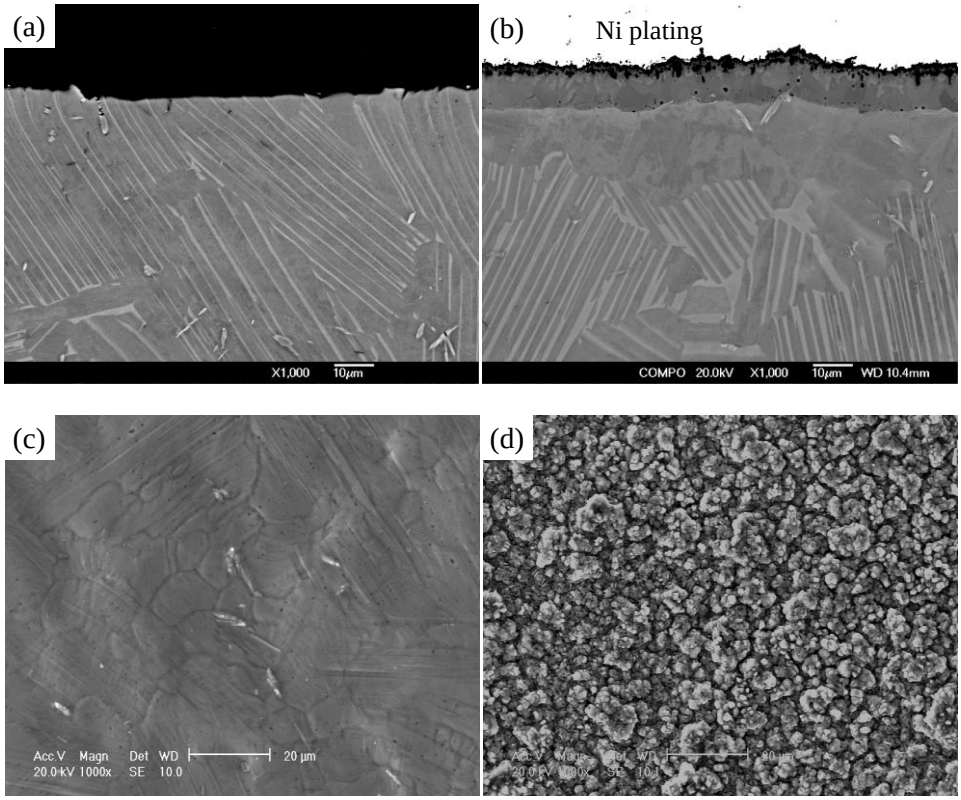

Figure 5.3 BSE SEM images of cross-sections of cast Ti4522XD (a) as-electropolished and (b) after HIPing at 1260 ℃/4 h/150 MPa and Ni-plating; Secondary electron (SE) SEM images of surface morphologies of cast Ti4522XD (c) as-electropolished and (d) after HIPping at 1260 ℃/4 h/150 MPa.

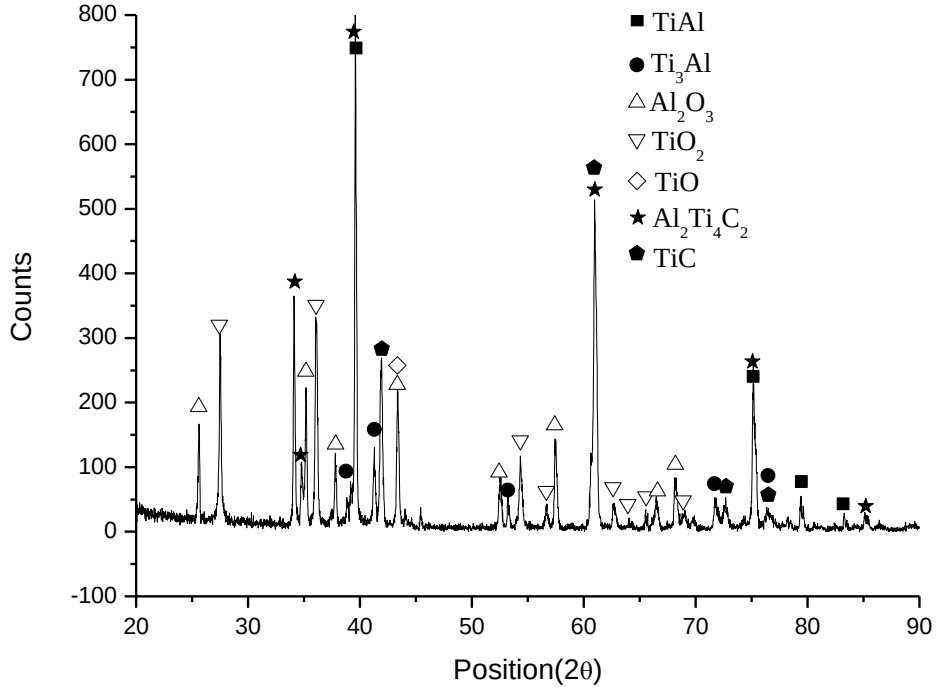

Figure 5.4 Analytical XRD results from the surface of 1260 ℃/4 h/150 MPa HIPped 4522XD castings.

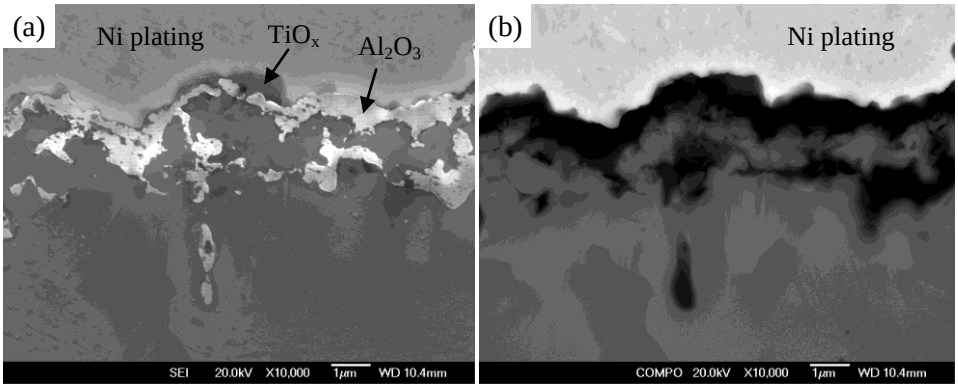

Figure 5.5 (a) SE and (b) BSE SEM images of the cross-sections of 4522XD casting HIPped at 1260 ℃/4 h/150 MPa.

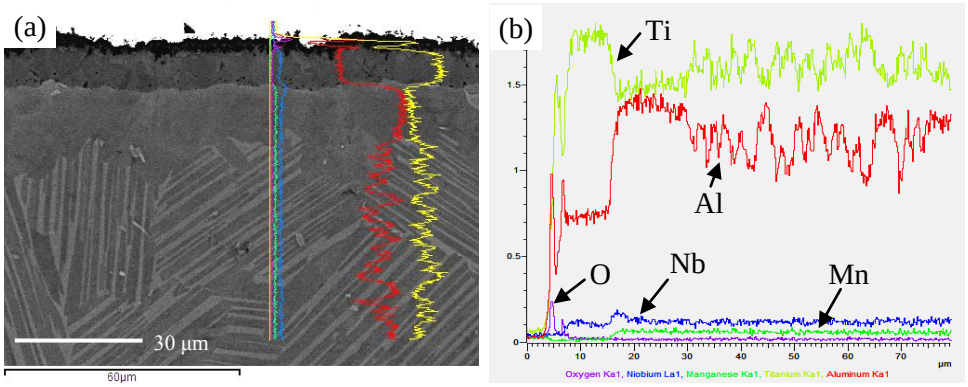

Figure 5.6 EDS line scans on the HIPped surface which was formed under standard HIPping conditions. (a) BSE image of cross-section microstructure of HIPped surface, indicating the area used for EDS line scan, (b) elemental distribution curves along the HIPped cross-section using EDS line scan.

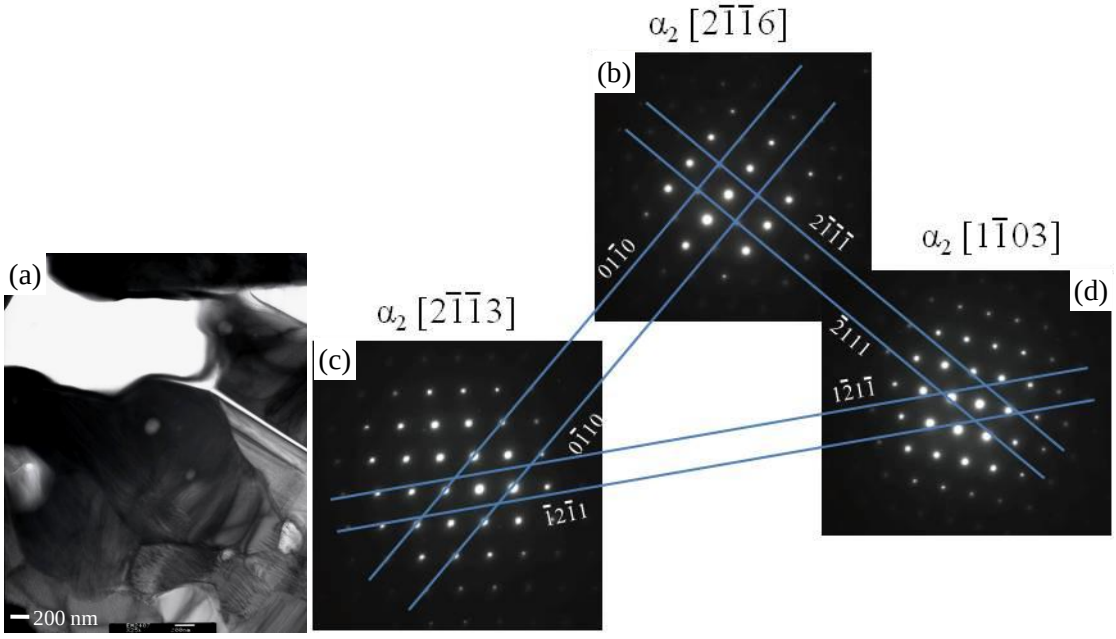

Figure 5.7 (a) α_2-Ti_3Al grain in Ti-rich layer and (b), (c) and (d) are the corresponding SAD patterns with zone axes [$2\bar{1}\,\bar{1}\,6$], [$2\bar{1}\,\bar{1}\,3$] and [$1\bar{1}\,03$] respectively. The tilting angles between (b) and (c), (b) and (d) and (c) and (d) are 18.3 °, 15.8 °and 23.7 °, respectively.

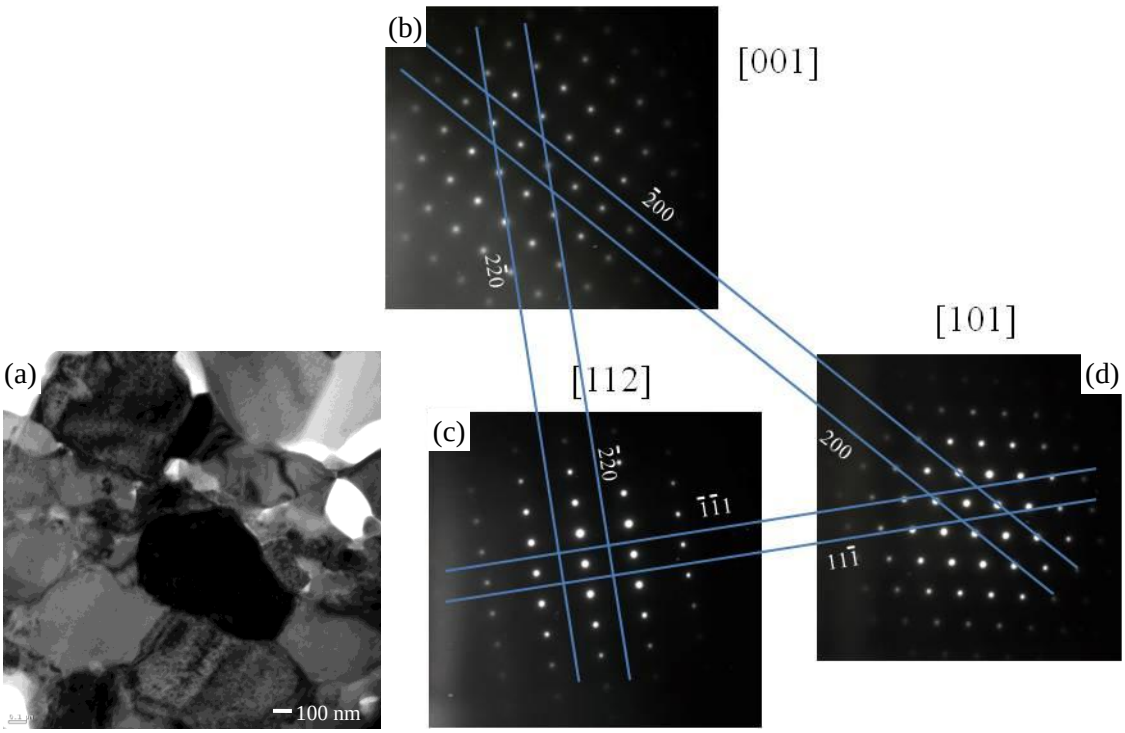

Figure 5.8 (a)Ti-rich grain in the Ti-rich layer showing a cubic crystal structure; (b), (c) and (d) are the corresponding SAD patterns with zone axes [001], [112] and [101] respectively. The tilting angles between (b) and (c), (b) and (d) and (c) and (d) are 35.4 °, 44.6 °and 29.3 °, respectively.

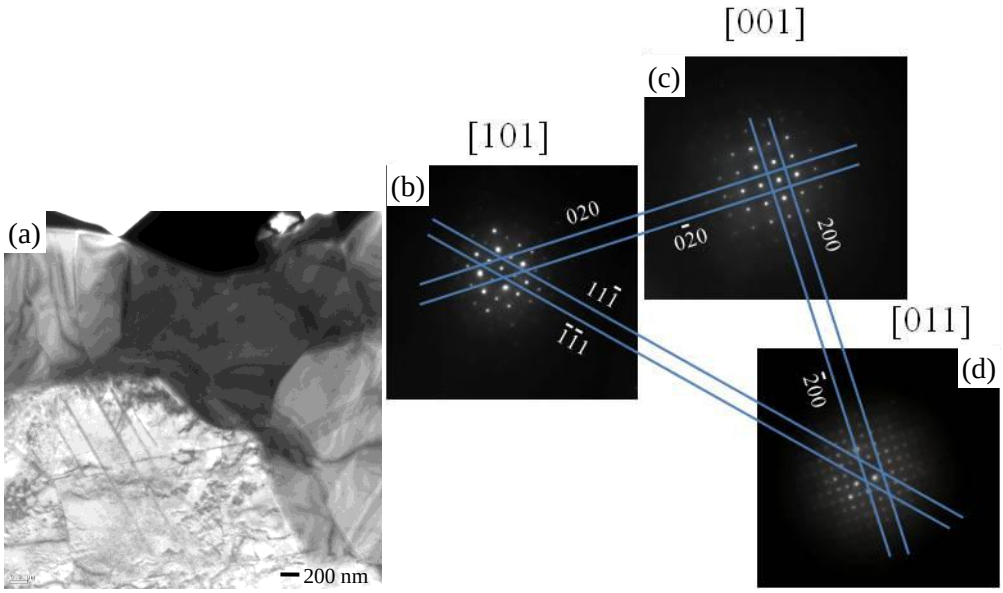

Figure 5.9 Ti-rich grain in the Ti-rich layer showing an ordered tetragonal crystal structure; (b), (c) and (d) are the corresponding SAD patterns with zone axis [101], [001] and [011] respectively. The tilting angles between (b) and (c), (b) and (d) and (c) and (d) are 30.5 °, 41.8 °and 30.3 °, respectively.

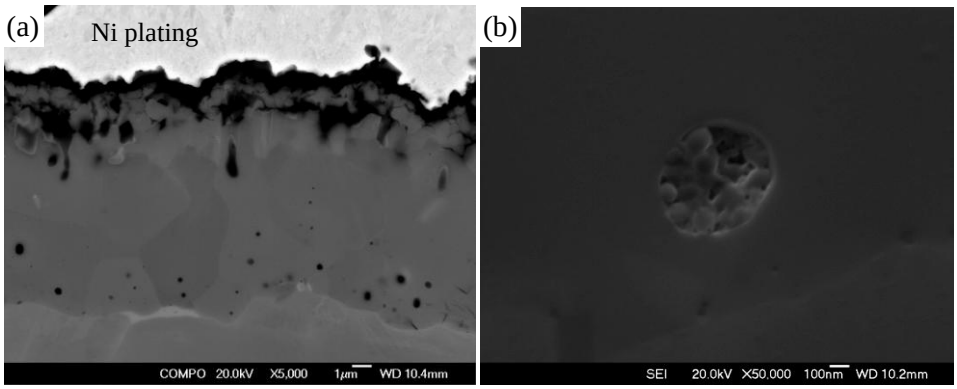

Figure 5.10 (a) BSE and (b) SE SEM image of oxides particles and pores in the Ti-rich layer and interface between Ti-rich layer and Al-rich layer.

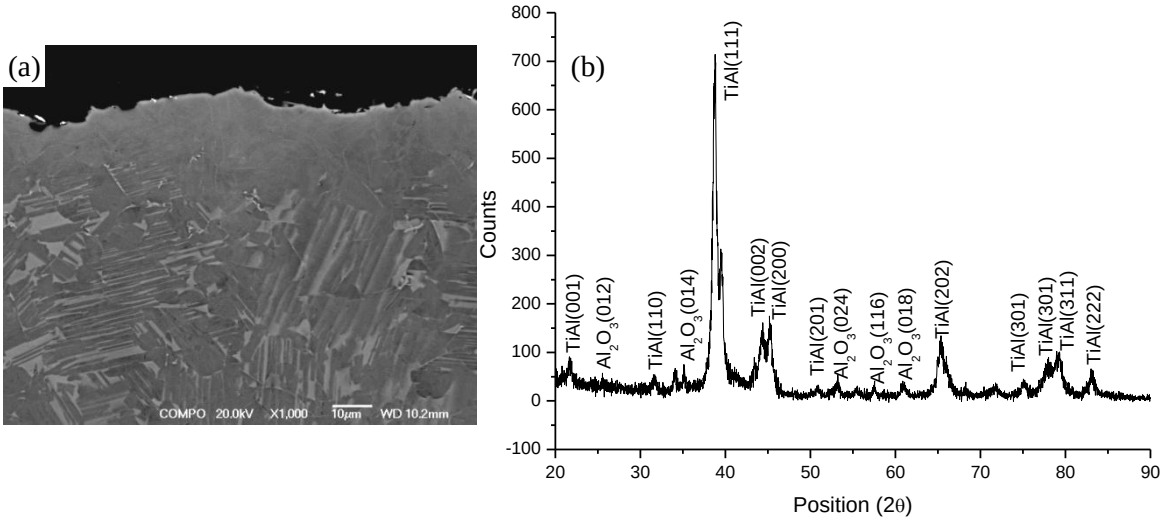

Figure 5.11 (a) BSE SEM image of 1260 ℃/4 hours/150 MPa HIPped surface containing only Al-rich layer; (b) XRD analysis on this surface indicated it was a γ-TiAl layer. Al_2O_3 came from the sand blasting medium.

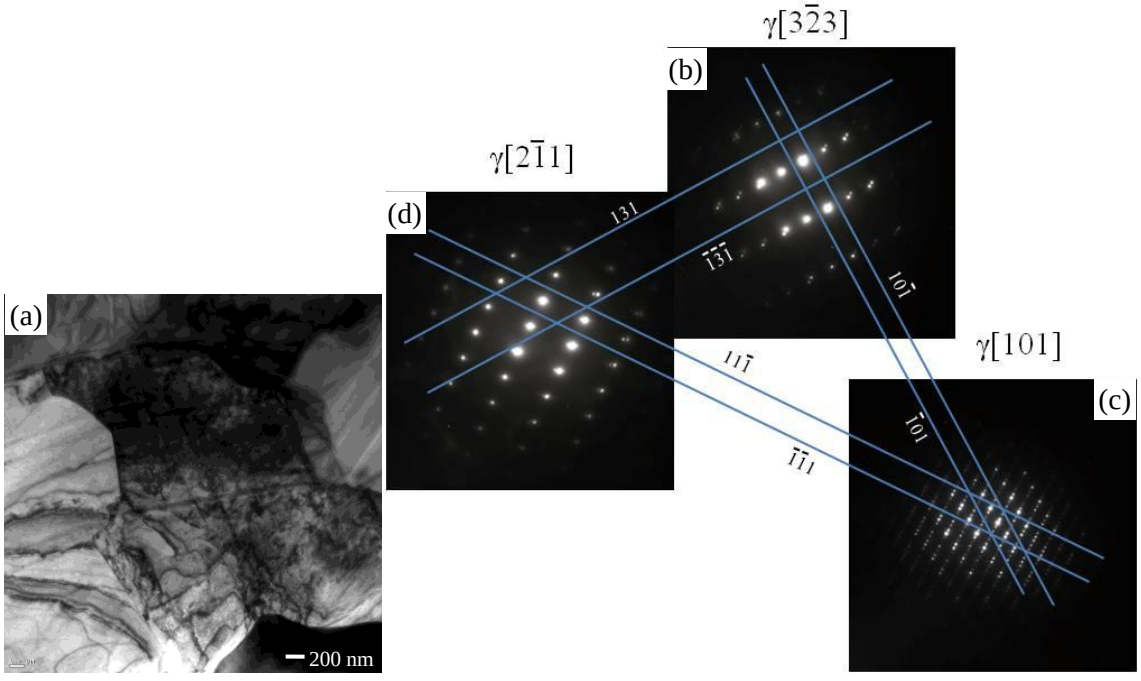

Figure 5.12 (a) γ grains in Al-rich layer and corresponding SAD patterns with zone axis [3$\bar{2}$3], [101] and [2$\bar{1}$1] for (b), (c) and (d) respectively. The tilting angles between (b) and (c), (b) and (d) and (c) and (d) are 25.3 °, 17.2 ° and 30.4 °, respectively.

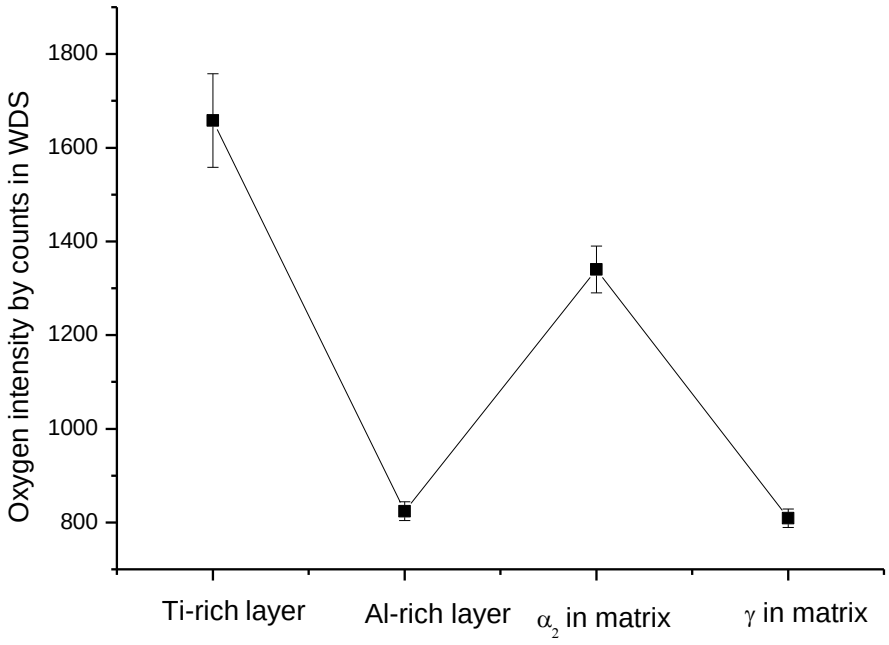

Figure 5.13 WDS analysis of oxygen distribution from the HIPped surface to matrix by point measurements.

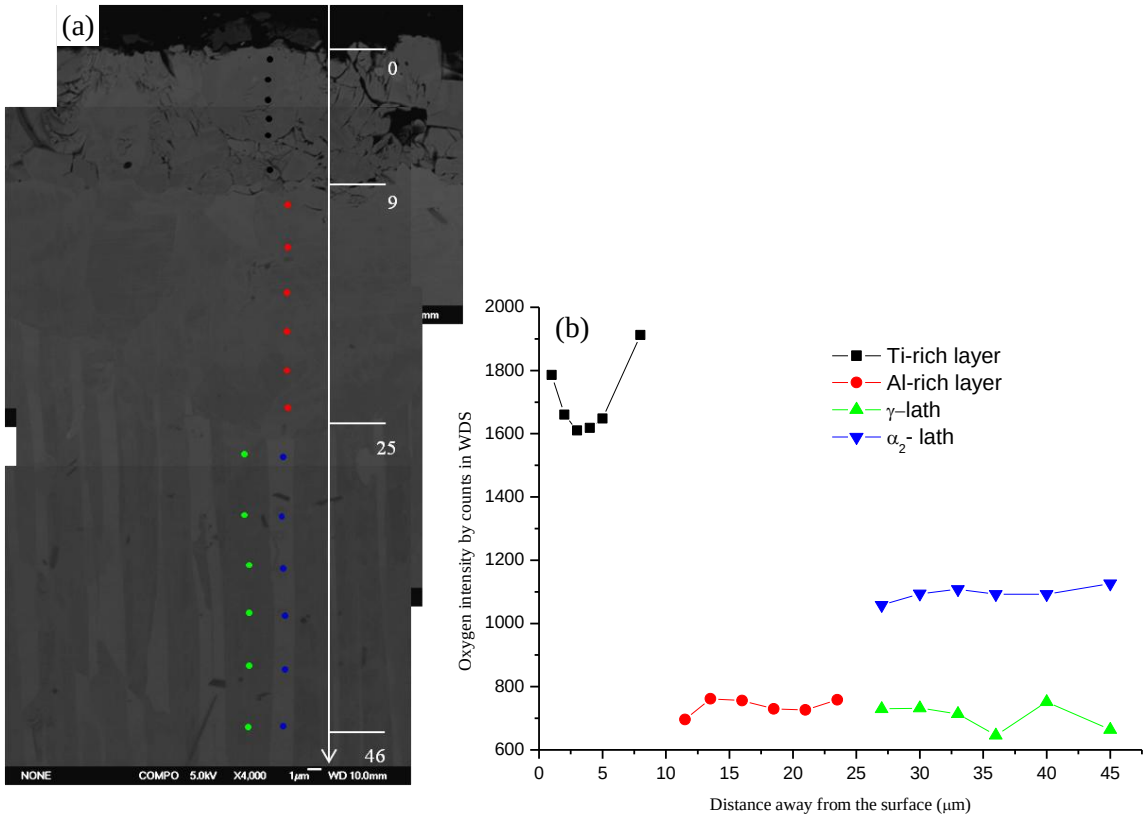

Figure 5.14 WDS analysis of oxygen distribution as a function of distance away from the HIPped surface. (a) BSE image of the HIPped surface; (b) the oxygen distribution graph.

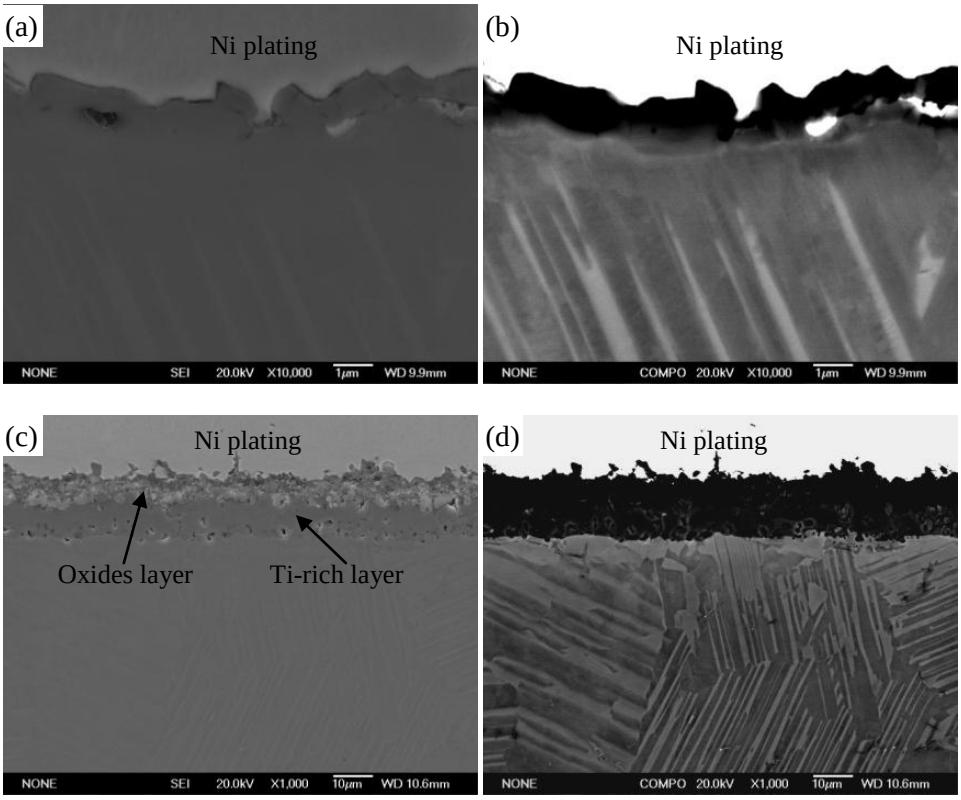

Figure 5.15 (a) SE and (b) the corresponding BSE image of 1 h HIPped surfaces; (c) SE and (d) the corresponding BSE image of 10 h HIPped surfaces. Both were HIPped at 1260 ℃ and 150 MPa.

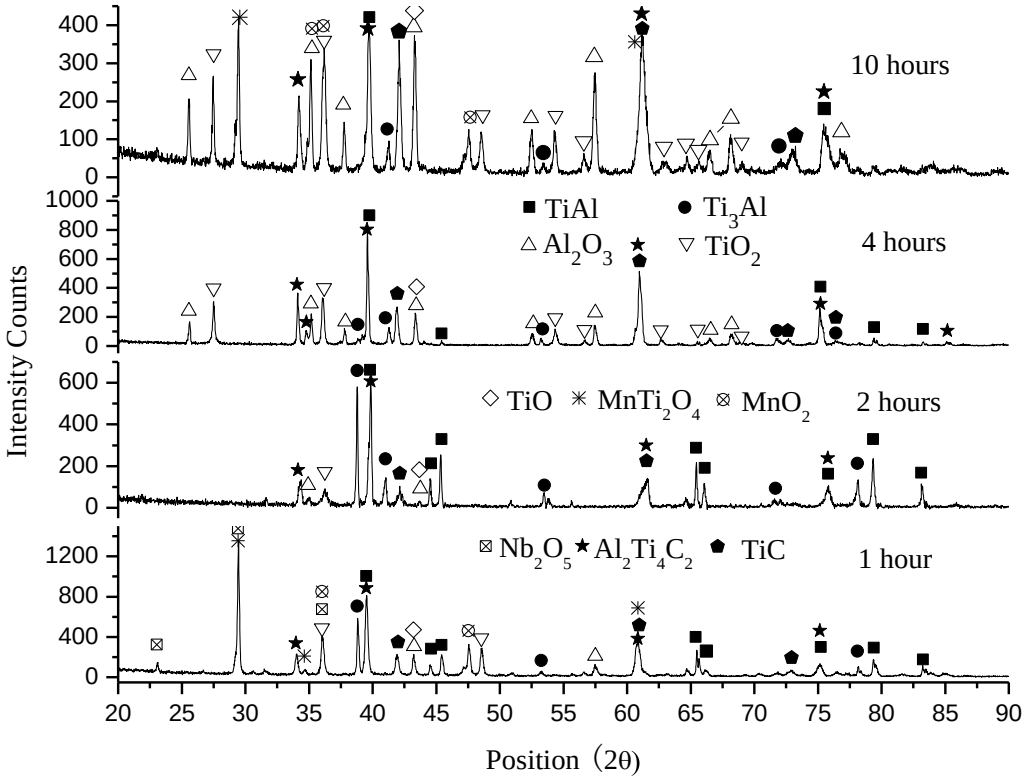

Figure 5.16 XRD results of various time HIPped surfaces (at 1260 ℃ and 150 MPa).

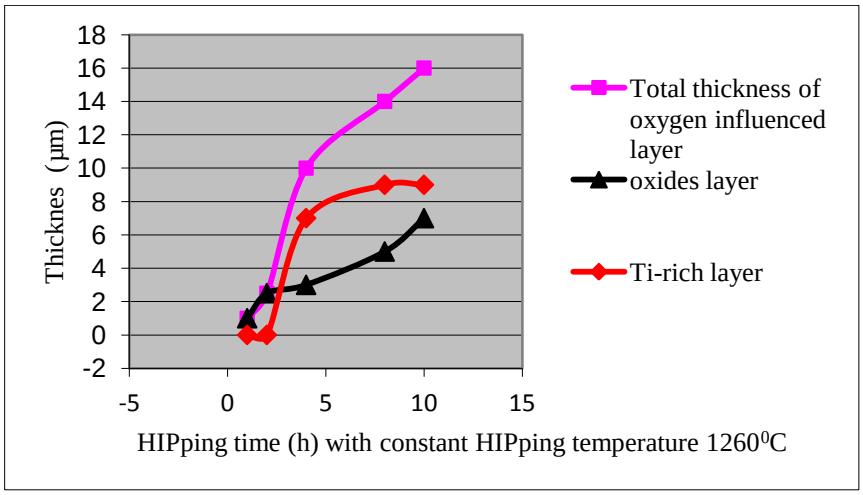

Figure 5.17 The thickness of the various layers on the HIPped surface as a function of HIPping time (at 1260 ℃ and 150 MPa).

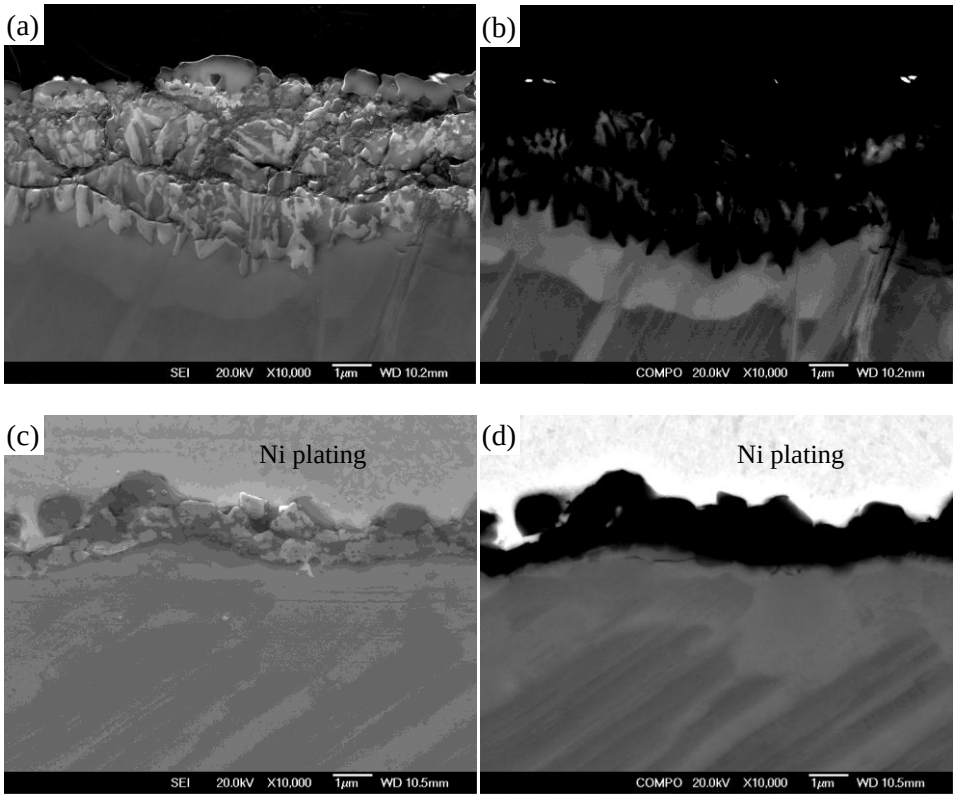

Figure 5.18 (a) SE and (b) the corresponding BSE image of 900 ℃ HIPped surfaces; (c) SE and (d) the corresponding BSE image of 1100 ℃ HIPped surfaces. Both of them were HIPped for 4 hours at 150 MPa.

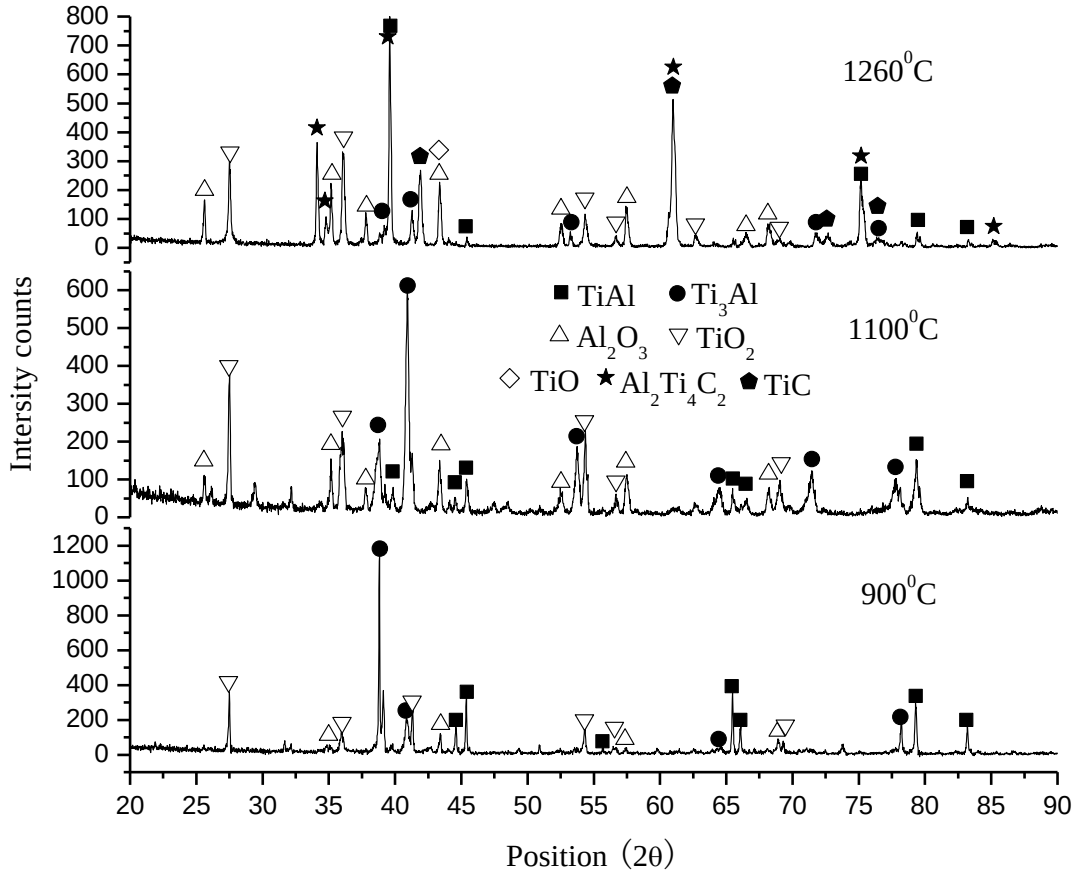

Figure 5.19 XRD results of different temperature HIPped surfaces (for 4 hours at 150 MPa).

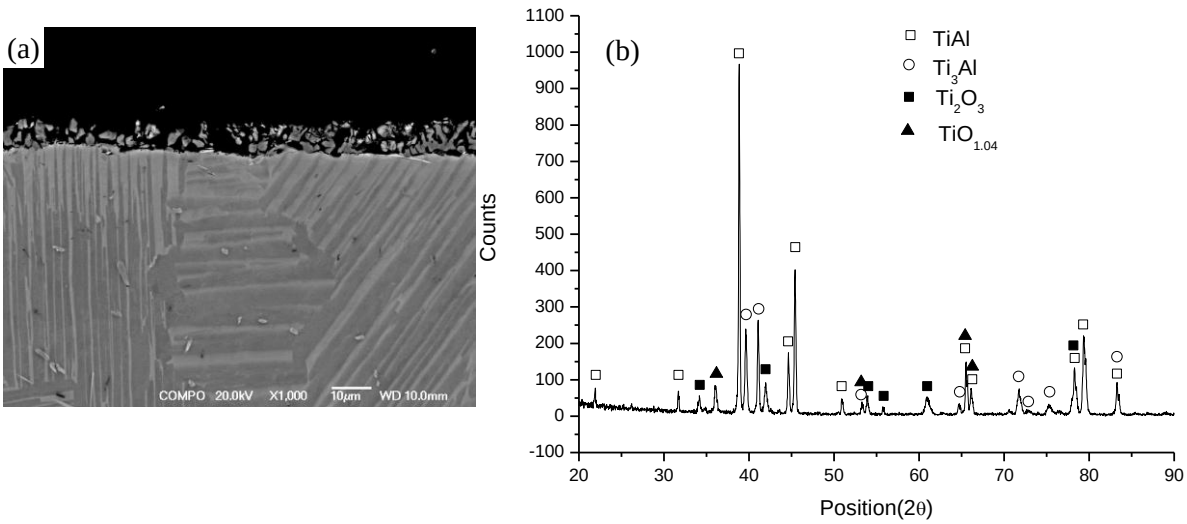

Figure 5.20 (a) BSE cross-section microstructure of 1260 ℃/4 h/150 MPa HIPped Ti4522XD casting which was HIPped with getter (Ti sponge); (b) the corresponding XRD analysis results from the surface, indicating the existence of metastable Ti oxides.

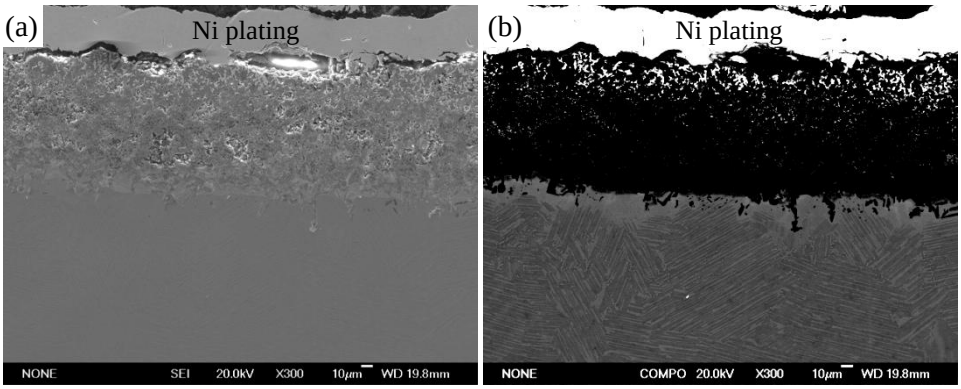

Figure 5.21 (a) SE and (b) BSE images of cross section microstructures of Ti4522XD casting which was HIPped with Al_2O_3 blocks at 1260 ℃/4 h/150 MPa.

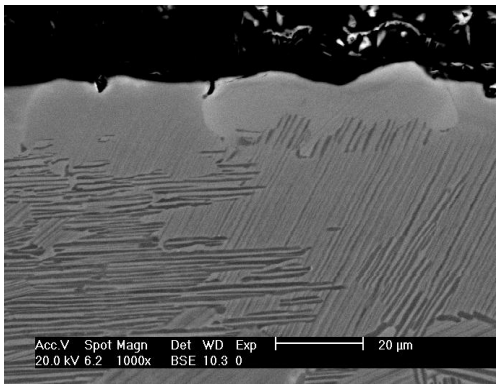

Figure 5.22 BSE image of cross-section microstructure of 1260 ℃/4 h heat treated Ti4522XD sample which was encapsulated in a glass tube back filled with 0.2 bar argon.

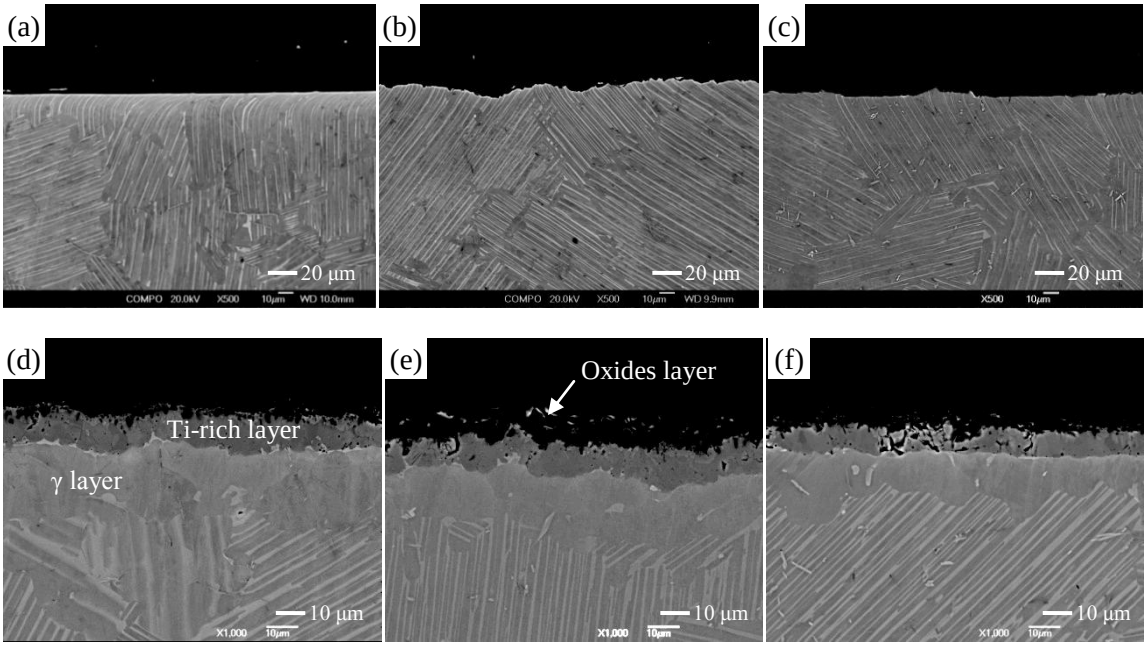

Figure 5.23 BSE images of cross-sections of (a) ground, (b) Al_2O_3 sand blasted, and (c) electropolished surfaces; (d), (e) and (f) are the corresponding cross-section microstructures to (a), (b) and (d) respectively, after HIPping under standard conditions.

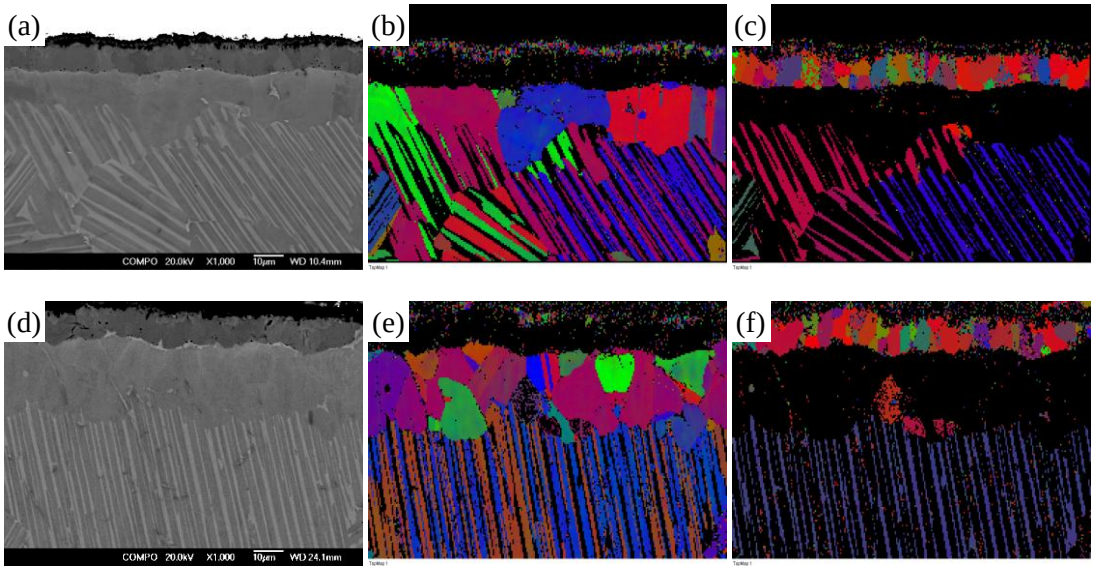

Figure 5.24 (a) BSE image, (b) γ phase and (c) α_2 phase normal orientation map on the cross-section of originally electropolished sample which was HIPped under standard conditions; (d) BSE image, (e) γ phase and (f) α_2 phase normal orientation map on the cross-section of originally machine ground sample which was HIPped under standard conditions.

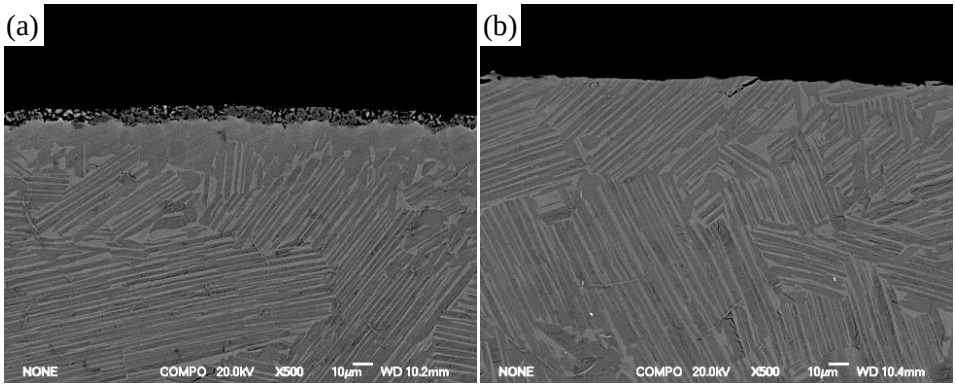

Figure 5.25 BSE cross-section microstructures of tensile test pieces, (a) with as-HIPped surface layer; (b) with HIPped surface hand ground.

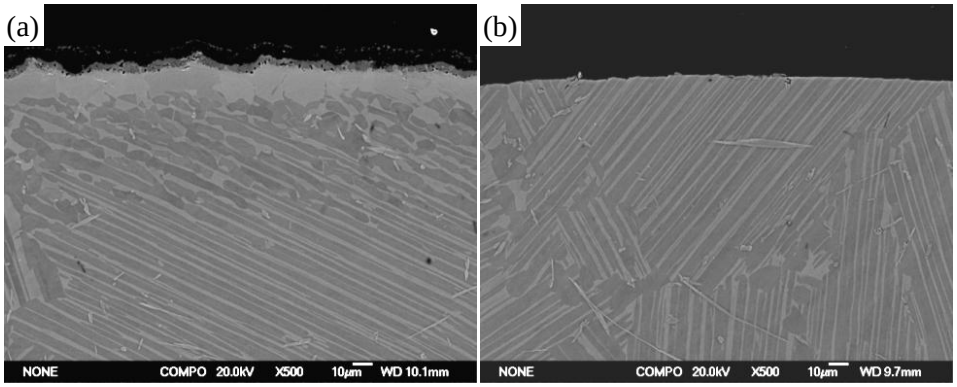

Figure 5.26 BSE cross-section microstructures of the second batch of tensile test pieces, (a) with as-HIPped surface layer; (b) with HIPped surface hand ground.

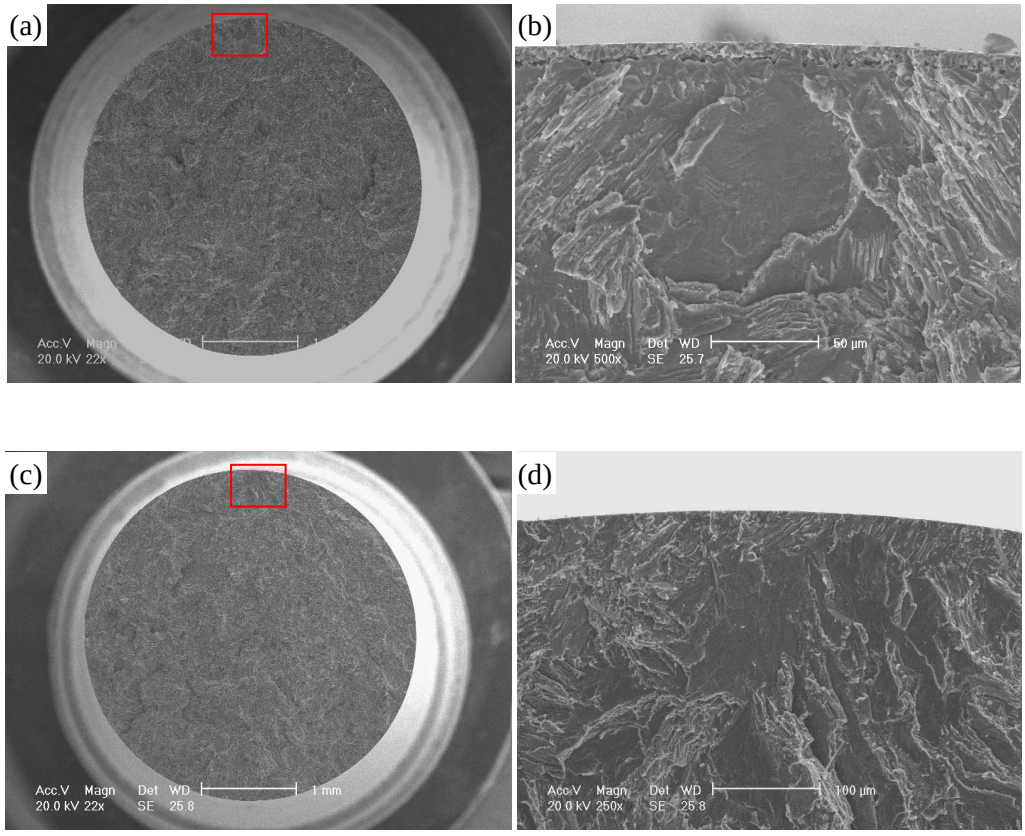

Figure 5.27 SE SEM images of fracture surfaces of failed tensile test pieces, showing (a) and (b) from the as-HIPped test pieces containing γ layer and (c) and (d) from the HIP + γ layer hand ground test pieces. (a) and (c) are overall surface morphologies and (b) and (d) the corresponding crack initiation areas from the regions marked with red rectangles in (a) and (c), respectively.

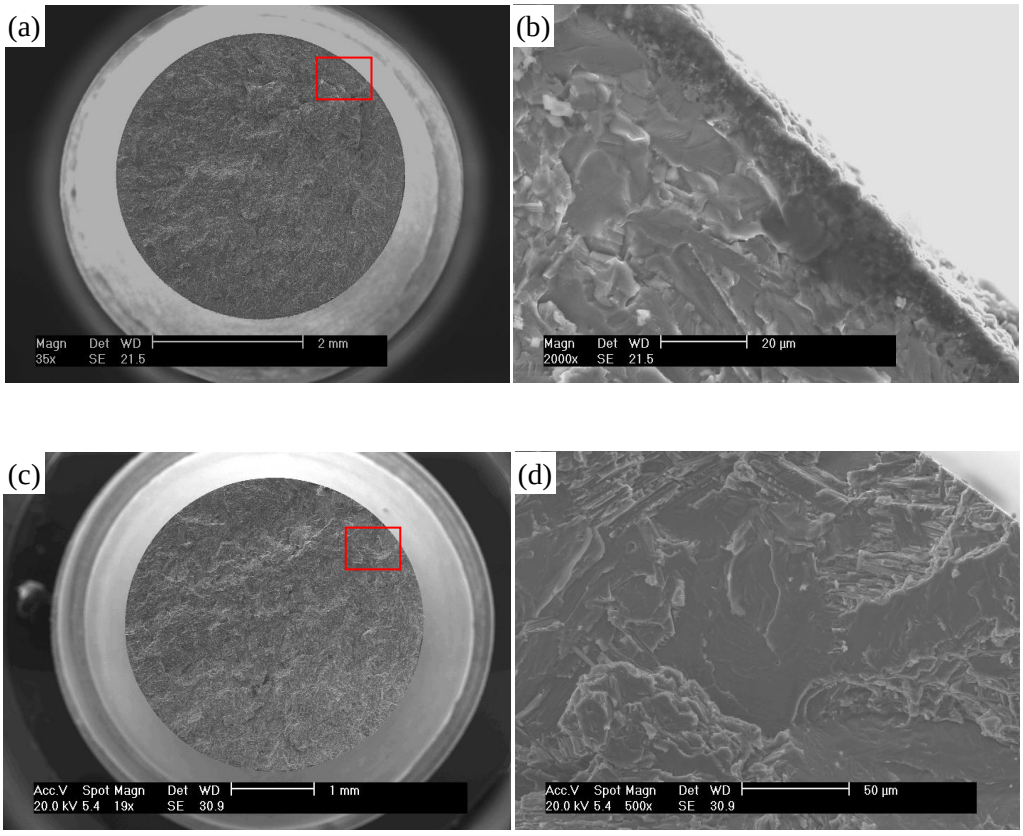

Figure 5.28 SE SEM images of fracture surfaces of failed tensile test pieces, showing (a) and (b) from the as-HIPped test pieces containing α_2 layer and (c) and (d) from the HIP + α_2 layer hand ground test pieces. (a) and (c) are overall surface morphologies and (b) and (d) the corresponding crack initiation areas from the region marked with red rectangles in (a) and (c), respectively.

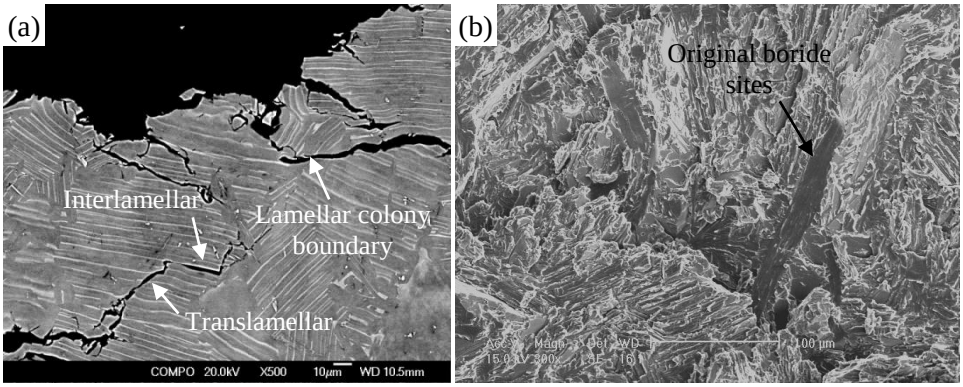

Figure 5.29 SE SEM images of (a) cross-section microstructure and (b) fracture surface of failed tensile test pieces, indicating the crack propagated either through translamellar, interlamellar or lamellar colony boundaries, or the debonding between borides and matrix.

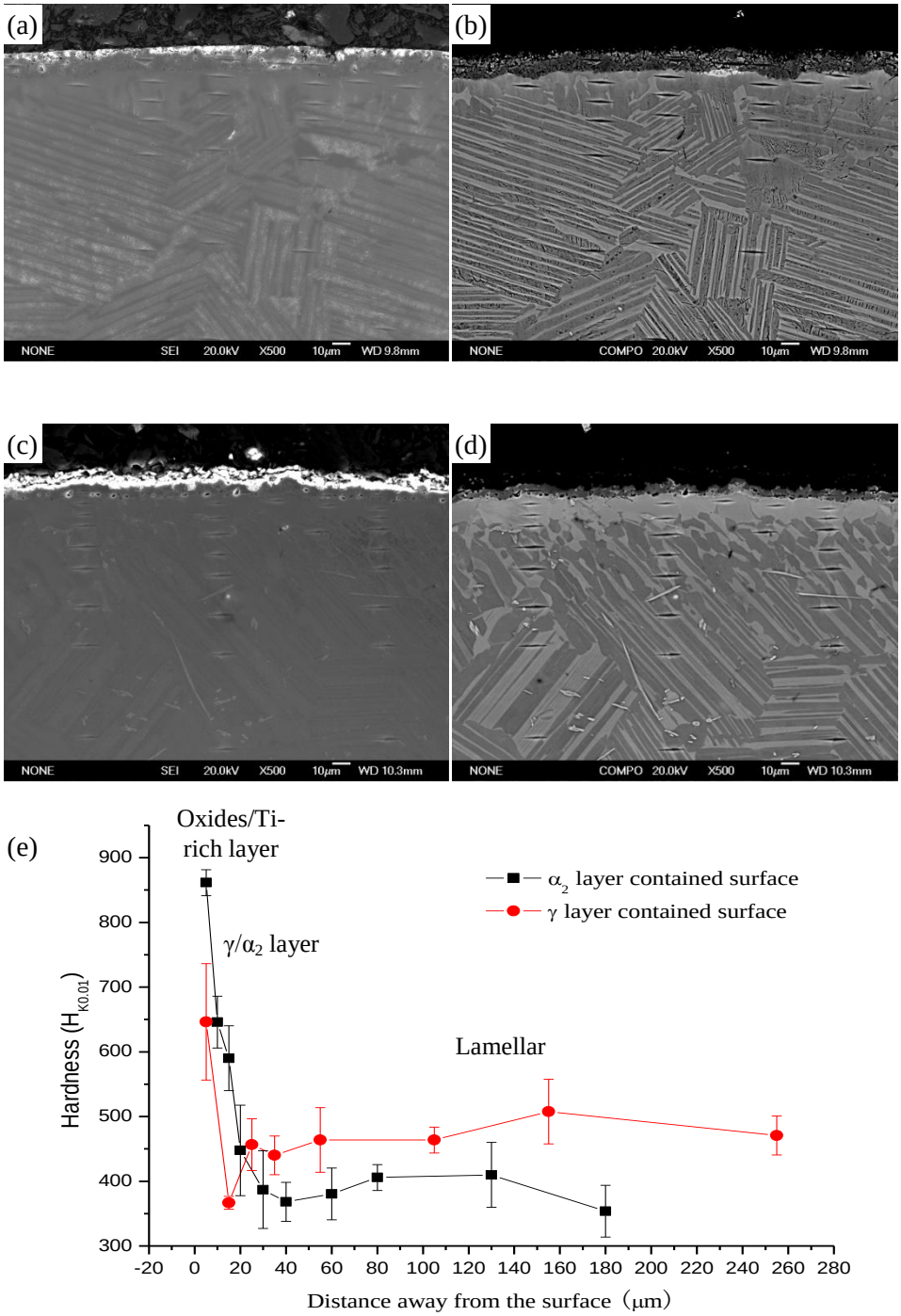

Figure 5.30 Cross-section microstructures of the tensile test pieces with hardness indentations. For the HIPped surfaces, (a) and (b) have γ layer and (c) and (d) have α_2 layer. (a) and (c) are SE images and (b) and (d) are the corresponding BSE images. (e) shows the microhardness results as a function of distance from the surface.

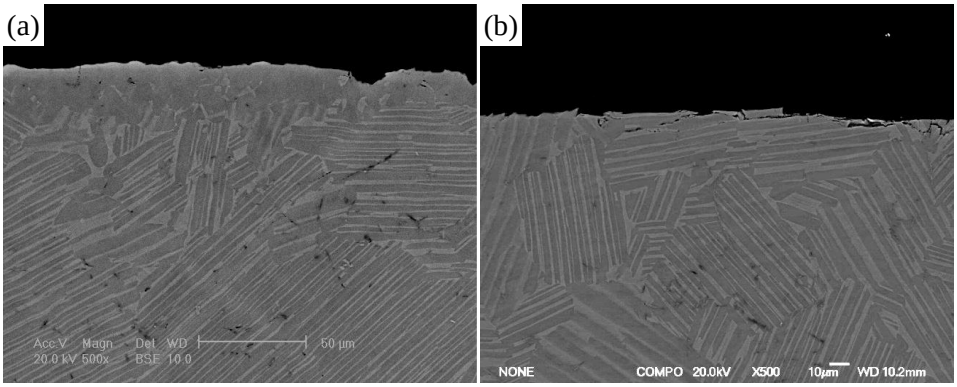

Figure 5.31 BSE cross-section microstructures of HCF test pieces, (a) with γ layer; (b) without γ layer.

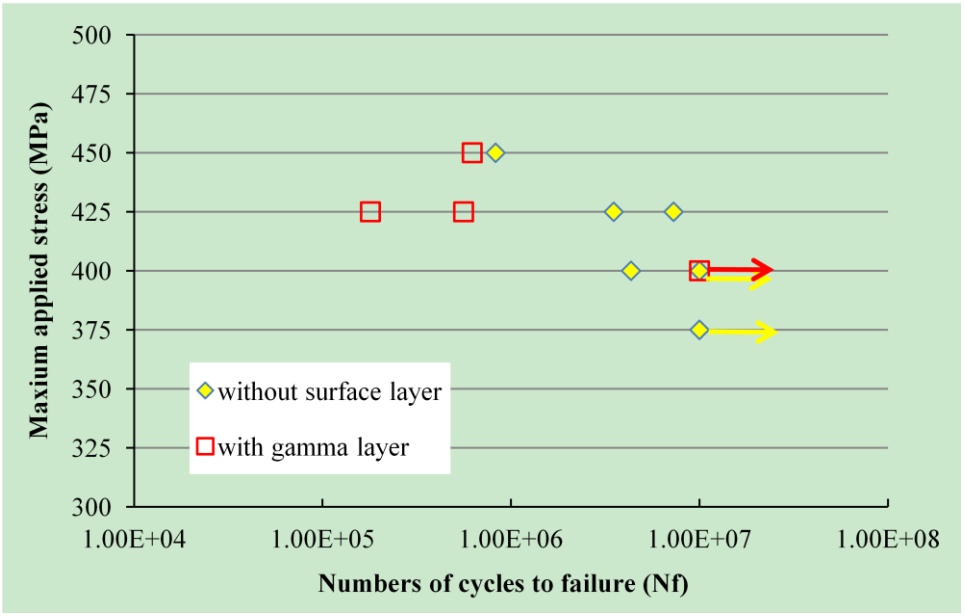

Figure 5.32 Room temperature HCF properties of 1260 ℃/4 h/150 MPa HIPped Ti4522XD castings with and without γ layer.

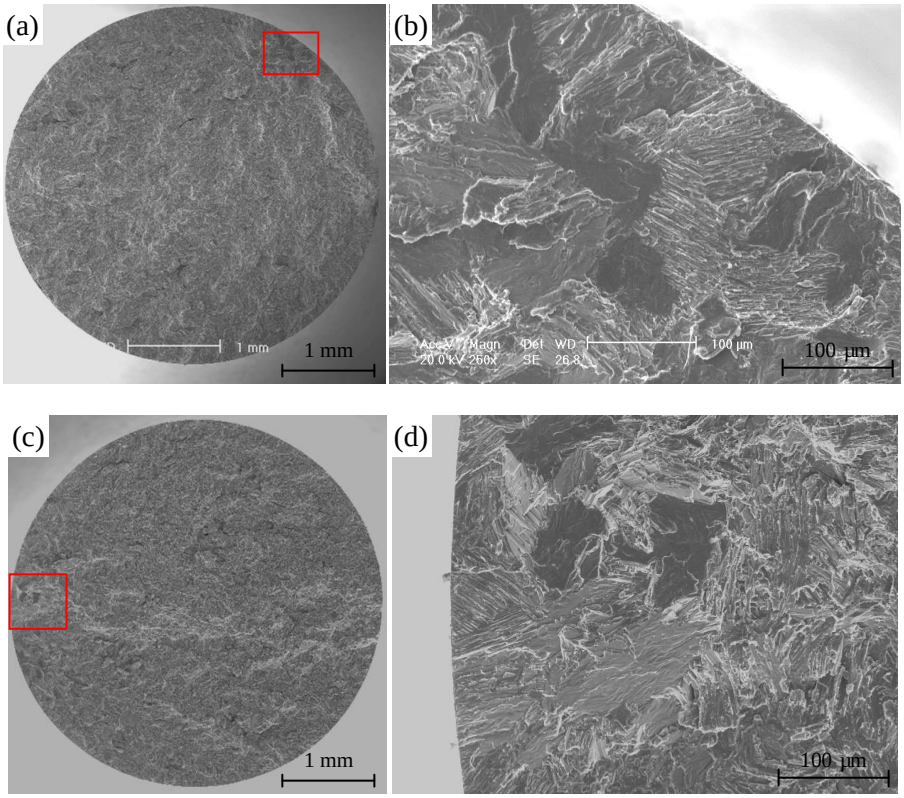

Figure 5.33 SE SEM images of fracture surfaces of room temperature HCF test pieces, (a) and (b) with γ layer; (c) and (d) without γ layer. (b) and (d) show the corresponding crack initiation areas from the region marked with red rectangles in (a) and (c), respectively.

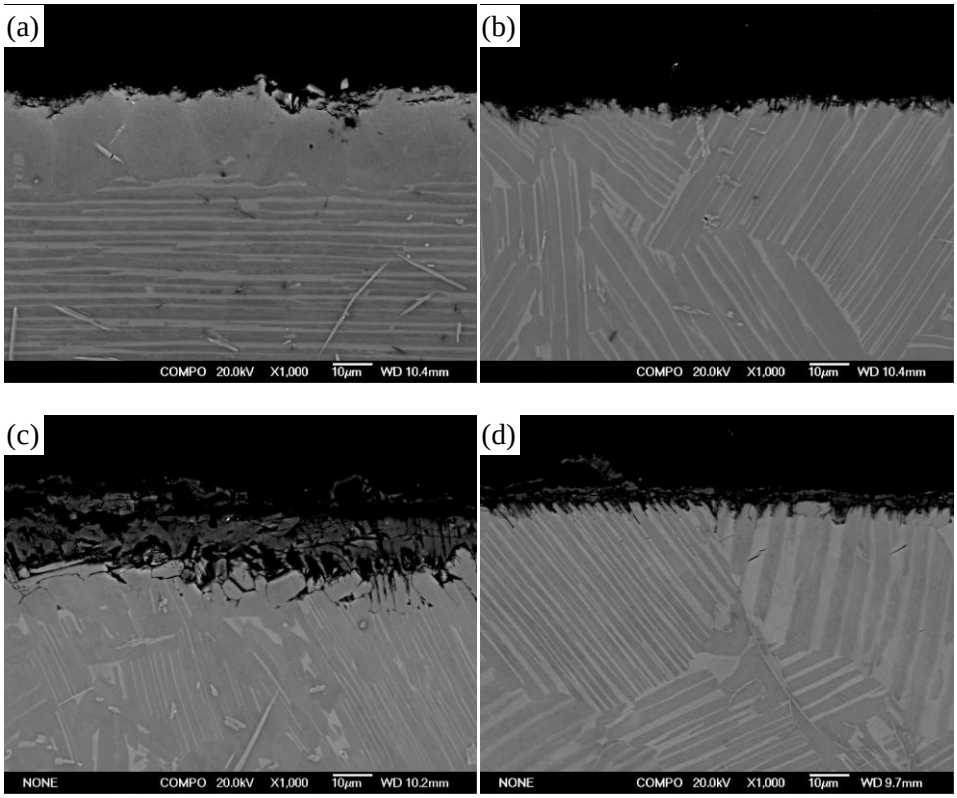

Figure 5.34 BSE SEM images of cross-section microstructures after hot corrosion in (a) and (b) NaCl/SOx solution with salt depositing rate of 0.75 μg/cm^2/h and sulphide concentration 100 ppm at 650 ℃ for 200 hours, (c) and (d) NaCl/SOx solution with salt depositing rate of 0.75 μg/cm^2/h but sulphide concentration 300 ppm at 700 ℃ for 200 hours. (a) and (c) had γ layer before corrosion, and (b) and (d) did not have γ layer before corrosion.

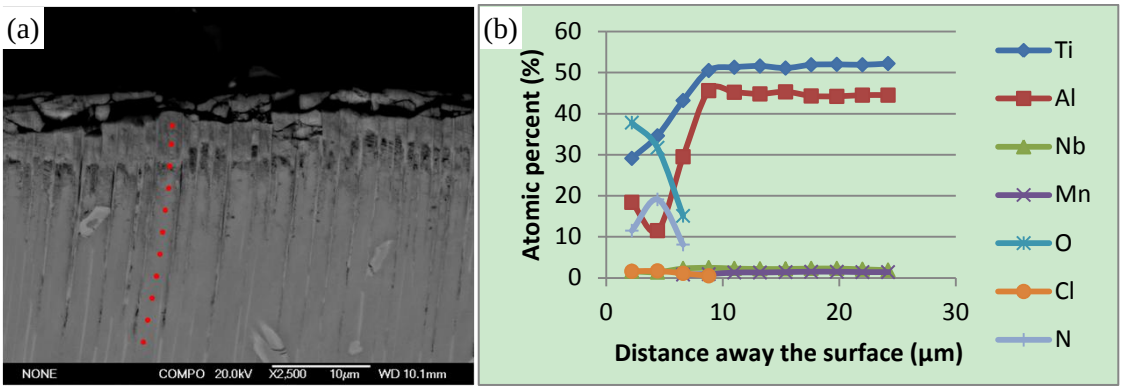

Figure 5.35 (a) Cross-section microstructure of 700 ℃ corroded surface, (b) the element distribution after corrosion as a function of distance away from the surface in the γ lath labelled with the red dots in (a).

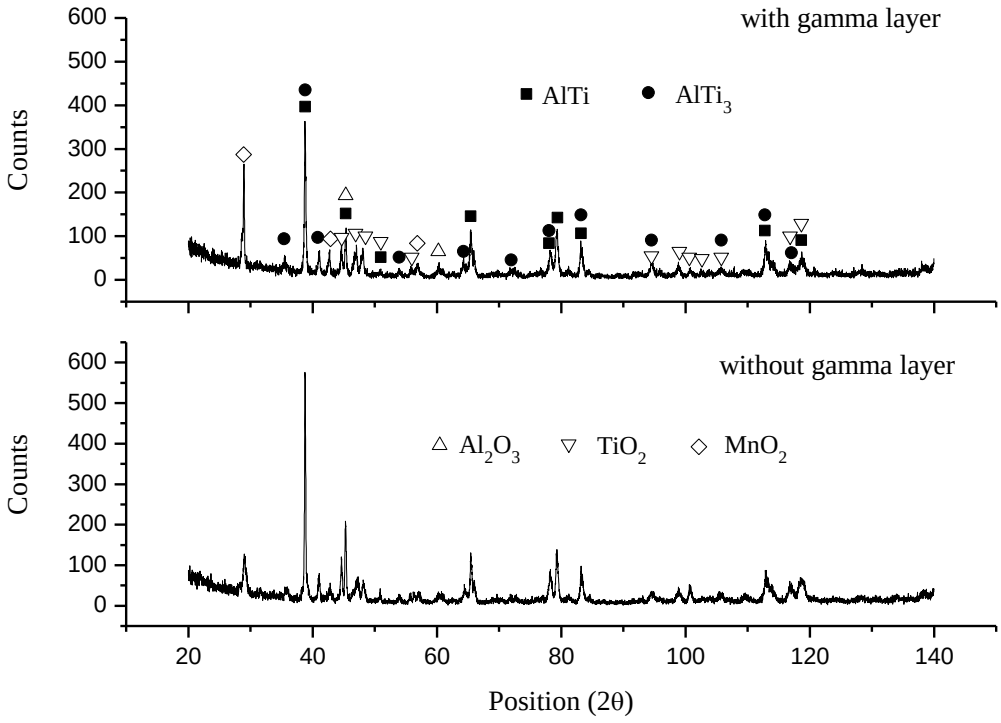

Figure 5.36 XRD results on the 700 °C corroded surfaces of specimens with and without γ layer.

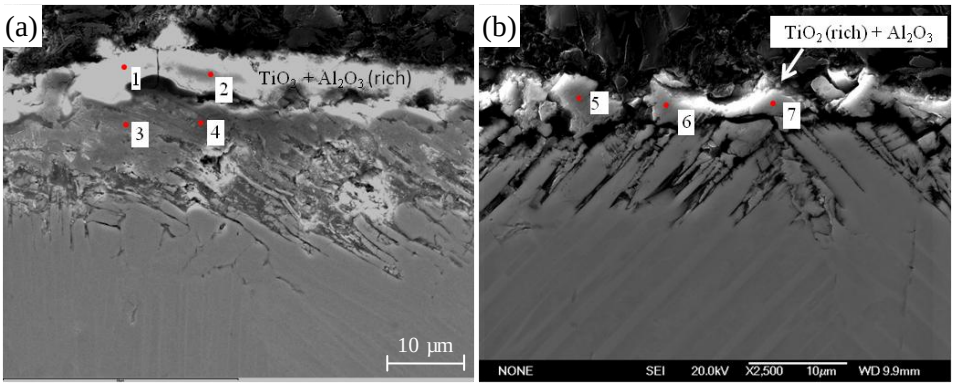

Figure 5.37 SE SEM images of 700 ℃ corroded surfaces of specimens (a) with γ layer and (b) without γ layer.

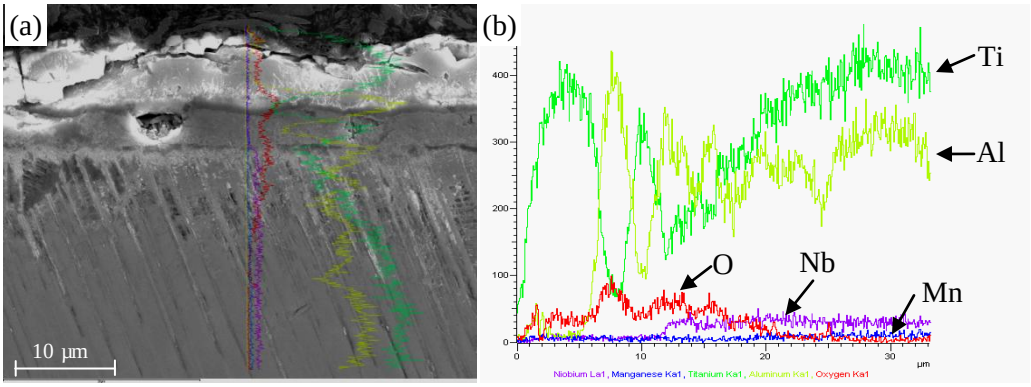

Figure 5.38 (a) SE SEM image of 700 ℃ corroded surface of specimen without γ layer, (b) the EDS line scanning along the surface cross-section in (a).

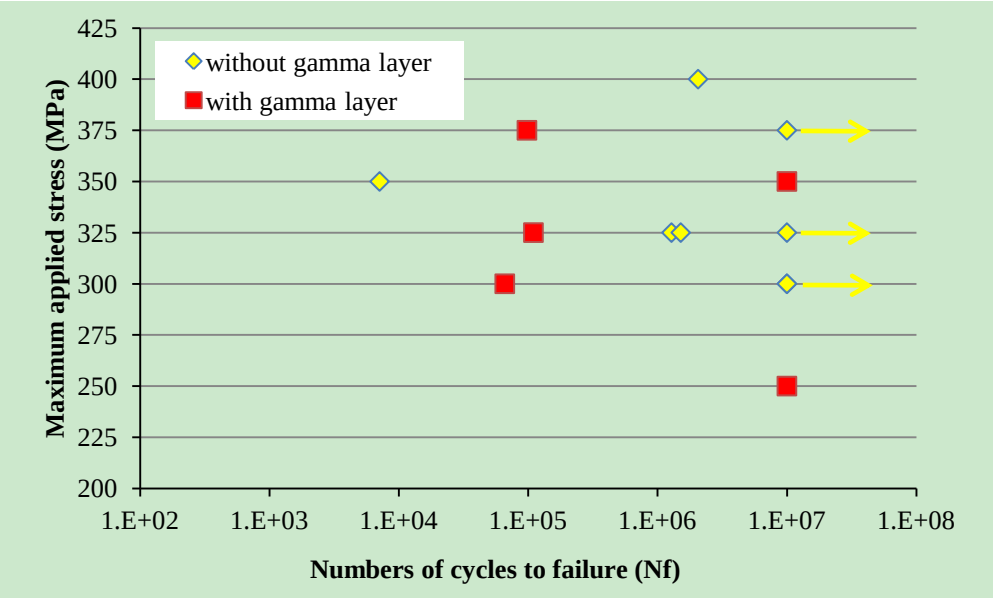

Figure 5.39 HCF properties of corroded Ti4522XD castings with and without γ layer.

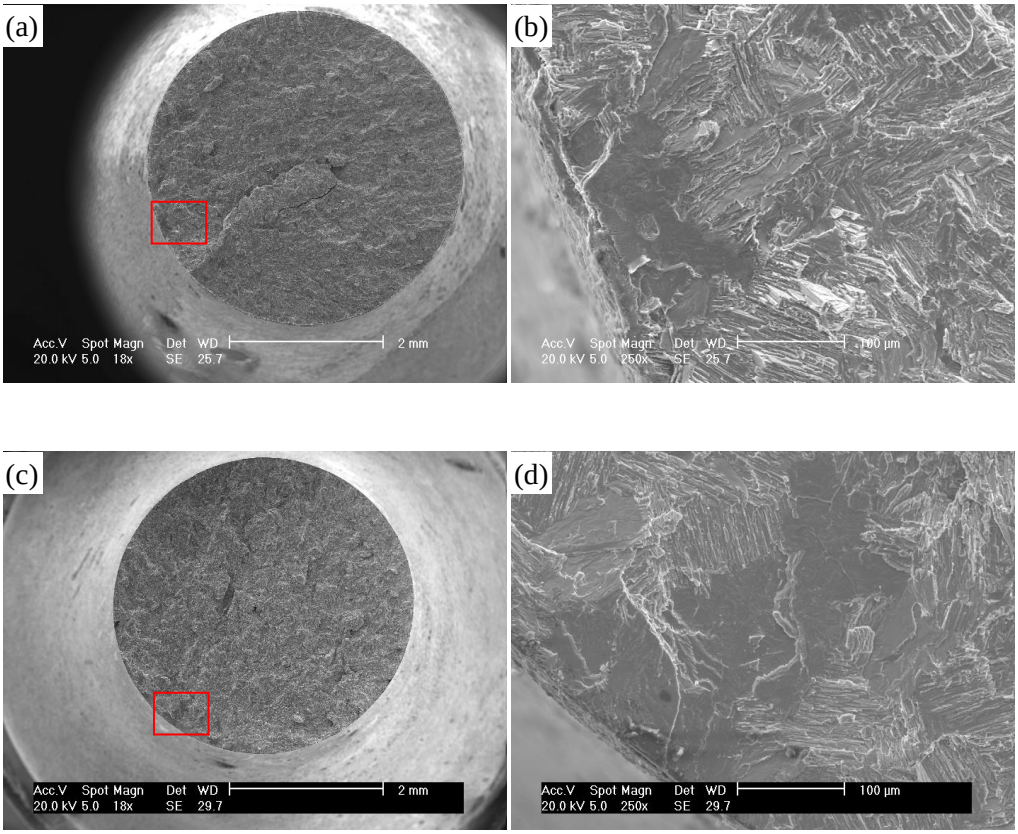

Figure 5.40 SE SEM images of fracture surfaces of corroded HCF test pieces. Before corrosion, (a) and (b) had γ layer and (c) and (d) did not have γ layer. (b) and (d) are the magnified images of red rectangle areas labelled in (a) and (c), respectively.

	O	Ti	Al	Nb
White oxides particles	65.8±2.0	6.4±4.0	27.7±5.0	
Grey oxides particles	45.9±8.0	38.2±8.0	15.6±2.0	0.5±0.2

Table 5.1 Quantitative analysis of composition (at.%) in oxides particles by EDS in which the results were not standardised.

	Ti	Al	Mn	Nb
Ti-rich layer	66.0±0.5	32.0±0.6		2.0±0.1
Al-rich layer	47.1±0.4	48.4±0.8	2.2±0.2	2.3±0.2
Matrix	52.3±0.2	43.7±0.1	2.0±0.2	2.0±0.2

Table 5.2 Quantitative analysis of compositions in each HIPped surface layer by EDS in atomic percent (at.%) in which the results were not standardised.

	O	Ti	Al	Mn	Nb
Atomic percent (at%)	38.7±2.1	41.6±2.9	18.4±3.0	0.2±0.2	1.2±0.2

Table 5.3 EDS analysis results (at.%) of the small particles inside the pores, as shown in fig. 5.10.

	Ti	Al	Nb	Mn	O	C
Ti-rich grain in fig. 5.7	66.3	31.9	1.8			
Ti-rich grain in fig. 5.8	66.4	0.3			7.1	26.3
Ti-rich grain in fig. 5.9	65.4	22.5	0.7	5.3	6.4	
Al-rich grain in fig. 5.12	44.4	50.5	3.1	2.1		

Table 5.4 EDS analysis by TEM on the grains in the HIPped surface (at.%).

	O	Ti	Al	Nb
Oxides layer in 1 hour HIPped surface	8.7±3.9	63.7±3.0	26.5±4.0	1.3±0.1
Oxides layer in 10 hours HIPped surface	66.6±1.6	6.2±1.7	27.2±3.6	

Table 5.5 EDS analysis results (at.%) on oxide layers in 1 hour and 10 hours HIPped surfaces.

		O	Ti	Al	Mn	Nb
900℃	Top surface	58.7	17.9	22.7	0.3	0.6
	Subsurface	18.0	50.0	28.9	1.0	2.1
1100℃	Top surface	66.6	15.3	17.5	0.4	0.2
	subsurface		57.4	38.6	1.8	2.0

Table 5.6 Average EDS analysis results (at.%) of 900 ℃ and 1100 ℃ HIPped surfaces, as shown in fig. 5.18, determined by area measurements.

	Ti	Al	Mn	Nb
Surface layer	59.7±0.2	39.6±0.2	1.3±0.0	2.4±0.1
Matrix	54.3±0.3	41.7±0.3	1.9±0.1	2.1±0.0

Table 5.7 EDS analysis results (at.%) of the 1260 ℃/4 h heat treated sample, as shown in fig. 5.22, in argon at 1 atm.

Surface conditions	$YS_{0.2}$ (MPa)	UTS(MPa)	EL(%)
As-HIPped (containing γ layer)	-/-/-	454/422/457	0.17/0.13/0.14
With HIPped surface hand ground	463.8/-/-	471/453/456	0.21/0.12/0.14

Table 5.8 Room temperature tensile properties of HIPped Ti4522XD with and without γ layer.

Surface conditions	$YS_{0.2}$ (MPa)	UTS(MPa)	Plastic Elongation (%)
As-HIPped (containing α_2 layer)	-/-/-	357.9/367.0/377.6	0.08/0.06/0.10
With HIPped surface hand ground	428.9/422.1	448.8/448.2	0.33/0.28

Table 5.9 Room temperature tensile properties of the second batch of Ti4522XD with and without α_2 layer.

Positions	Ti	Al	Mn	Nb	O	Cl	S
1	5.5	33.5	0.2		60.6	0.2	
2	10.9	25.2	0.7	0.7	62.5	0.2	
3	26.9	5.9		1.3	65.5		0.5
4	31.8	2.7		0.5	65.1		
5	28.4	3.0	0.2	0.6	67.8		
6	28.4	3.2	0.5	0.7	67.0		
7	28.6	1.1	0.2	0.6	69.6		

Table 5.10 EDS results of the oxide layers in the corroded surfaces determined by point measurement. The position of each measurement is labelled by red spots in fig. 5.37.

CHAPTER 6 GENERAL DISCUSSION

Two aspects of the work reported in Chapters 4 and 5 will be discussed in this chapter. These are firstly a discussion of the grain refinement mechanism which operates in castings and in powders and secondly the mechanism of the formation of surface layers during HIPping and their impact on properties. These two aspects are the most important areas investigated since grain size control is vital in castings and the nature of the surface in net shape cast HIPped blades is clearly important.

6.1 Solidification behaviour of boron-containing TiAl alloys

6.1.1 The basic solidification behaviour for Ti4522 and Ti4522XD

In both Ti4522 and Ti4522XD Bridgman samples, the Burgers variants were found in the quenched liquid regions or in the dendrites which indicates that the first solidified solid is β phase. The fact that in both coarse dendrites in Ti4522 and in Ti4522XD Bridgman samples peritectic α_2 grains were found indicates that the peritectic reaction occurs during solidification of both alloys. The observation of lamellar structure in the regions quenched from low temperatures further indicates that finally both alloys transform to α grains. Therefore, the basic solidification pathways for both Ti4522 and Ti4522XD Bridgman samples are the same which follow the sequence below:

$$L \rightarrow L + \beta \rightarrow L + \beta + \alpha \rightarrow \beta + \alpha \rightarrow \alpha \rightarrow \alpha + \gamma \rightarrow \alpha_2 + \gamma$$

In which the α grains between the liquid and β dendrites are formed by the peritectic reaction:

$$L + \beta \rightarrow \alpha$$

In Ti4522 Bridgman sample, the peritectic α grains nucleate on the adjacent β dendrites as demonstrated by the OR analysis in dendrites in Ti4522. However, with 1 at.% addition of boron in Ti4522XD the formation of borides occurs mainly after β solidification, as discussed in regions quenched from the liquid and mushy zones in Ti4522XD Bridgman sample, without changing the pathway of metallic phases. Therefore, the formation of borides should be added to the solidification pathway for Ti4522XD Bridgman sample:

$$L \rightarrow L + \beta \rightarrow L + \beta + \text{borides} \rightarrow L + \beta + \alpha + \text{borides} \rightarrow \beta + \alpha + \text{borides} \rightarrow \alpha + \text{borides}$$

Furthermore, in the Ti4522XD Bridgman samples, the solidification behaviour of peritectic α and the nucleation of α during solid phase transformation will also be changed which will be discussed later.

6.1.2 The influence of the addition of boron on the solidification behaviour of Ti4522XD

As observed from the overall microstructures of unidirectionally solidified Ti4522 and Ti4522XD Bridgman samples, the addition of boron could effectively refine the grain size. The mechanism for the microstructure refinement in other TiAl alloys has been reviewed in the literature review. There are mainly two widely accepted mechanisms. One is the constitutional supercooling related refinement mechanism proposed by Cheng[17]. For this mechanism, the addition of boron is supposed to cause constitutional supercooling in the solidification front and thus increase the number of nuclei of β. The second one was proposed by Hecht et al.[48]. They suggested that for low boron-containing TiAl alloys, the microstructure can be refined by heterogeneous nucleation of α grains on the borides during solid phase transformation. However, neither of these mechanisms is supported by direct evidence, and moreover, in Cheng's mechanism β dendrites are not obvious in the

refined as-solidified alloys and Hecht's mechanism is restricted to solidification without a peritectic reaction. In Ti4522 and Ti4522XD Bridgman samples, however, both β dendrites and the peritectic reaction were demonstrated to exist during solidification in Chapter 4, but the addition of 1 at.% boron to Ti4522 can also refine the microstructure significantly. Apparently, these two mechanisms are not applicable here. Therefore, a new refinement mechanism for the high boron-containing TiAl alloys which go through a peritectic reaction is proposed below through the analysis of microstructure and OR characteristics of those Ti4522 and Ti4522XD Bridgman samples.

6.1.1.1 The influence on the nucleation of β grains during solidification

The smaller grain size in the liquid region and the smaller primary and secondary dendrite arm spacing and the shorter dendrite length in the mushy zone in Ti45422XD Bridgman sample than those in the Ti4522 Bridgman sample, as shown in fig. 4.1, indicate that the addition of boron could increase of the number of nuclei for the nucleation of β grains, leading to the decrease of the size of the original β dendrites. The problem is how the nucleation rate is increased through the addition of boron. In Cheng's theory, the constitutional supercooling is the main reason, whereby the boron is rejected into the melt as the alloy solidifies, since boron has a low solubility in the β phase, and a boron-rich layer can build-up ahead of the solidification front if the critical boron content is added, which can enhance the formation of β dendrites and reduce the dendrite arm spacing. As a result, no obvious dendritic structure can be observed. Since the dendrites in Ti4522XD Bridgman sample is pronounced, the constitutional supercooling mechanism is inapplicable here. In the Ti4522XD Bridgman sample long borides located in the cores of coarse dendrites were observed, which are assumed to be formed slightly later than the leading β dendrites, and were found to have specific OR with their neighbouring Burgers

α_2 variants, as evidenced in fig. 4.15 and fig. 4.22. This is the direct evidence that the β dendrites can nucleate on the primary borides during solidification. Thus, the increase of the number of nuclei for β solidification in Ti4522XD is more likely to be due to the formation of primary borides acting as inoculants.

In addition, the OR between Burgers variants and TiB (B27) was found to be:

(0001)α_2 // (001) TiB (B27) and <11$\bar{2}$ 0>α_2 // [010] TiB (B27)

Given the Burgers OR between α and β, the OR between β and TiB (B27) can be deduced:

{110}β // (001)TiB (B27) and <111>β // [010] TiB (B27)

Actually, detailed OR between β and TiB (B27) has been found in the study of grain refinement in Ti44Al8Nb1B[252], and their OR can be written as:

{110}β // (001)TiB (B27), {111}β // (010)TiB (B27) and {211}β // (100)TiB (B27)

6.1.2.2 The influence on the solidification of peritectic α grains and the subsequent solid phase transformation

As demonstrated in Chapter 4, the peritectic reaction in boron-free Ti4522 Bridgman sample occurred in a normal way, where peritectic α nucleated on the β dendrites which transformed into Burgers α variants during cooling. However, it was observed that as the growth of dendrites in Ti4522XD Bridgman samples, more and more α_2 grains in the dendrites became non-Burgers variants and many pairs of α_2 grains that are adjacent to the interdendritic γ grains but opposite to each other had the same orientation and followed Blackburn's OR with the γ grains in between, most of which were transformed from peritectic α grains during quenching. This means more and more α grain in the dendrites in Ti4522XD will not form through β transformation during cooling as the growth of dendrites, but will nucleate on the adjacent peritectic α which will grow toward both β

dendrites and interdendritic liquid and will get bigger and bigger as the growth of dendrites. Since those α_2 grains that nucleated on peritectic α grains are non-Burgers variants, those peritectic α cannot have nucleated on the β dendrites. Otherwise, those α_2 grains that nucleated on peritectic α grains should be Burgers variants. Furthermore, those peritectic α grains must nucleate on something else in the interdendritic liquid, which, most possibly, are borides which have been observed in the interdendritic liquid. Only in this way can the Burgers relation among α_2 grains be broken down after quenching or cooling. However, in the study of Ti43Al5Nb0.2C0.2B alloy which also experiences peritectic reaction during solidification, Hecht et al.[48] found that the borides in the interdendritic region did not cause grain refinement. The reason is that the studied Ti4522XD has a higher boron content, 1 at.%, which makes the formation of borides prior to the peritectic reaction, but in Ti43Al5Nb0.2C0.2B, peritectic reaction occurs before the formation of borides. Therefore, the grain refinement mechanism through peritectic reaction does not apply to the low-boron containing TiAl systems and that is why there is a switch on/off effect for the grain refinement in the boron-containing TiAl systems that have peritectic reaction.

Thus, in the solidification of Ti4522XD, peritectic α will nucleate on the borides in the interdendritic liquid, and then will pass the OR to the neighbouring α grains during the subsequent cooling. Since there are so many fine borides in the liquid, there are many nucleation sites for peritectic α grains. Therefore, the peritectic α grains are firstly refined. In the subsequent cooling process, the massive peritectic α grains in turn provide the nucleation sites for formation of α grains in the dendrites during solid phase transformation. Then the microstructure could be refined again. More importantly, this grain refinement mechanism leads to randomly oriented α grains which is also very beneficial for mechanical properties[131].

6.1.2.3 The influence on the nucleation of α grains during solid phase transformation

Heterogeneous nucleation of α grains on the borides in the dendrites during solid phase transformation may also contribute to grain refinement as indicated by the OR between borides and non-Burgers α_2 grain in fig. 4.16.

Whether the constitutional supercooling, which was suggested by Cheng, could help refine the cast microstructure is not clear, since no direct evidence was found in Ti4522XD.

In summary, the microstructure refinement in cast Ti4522XD through the addition of 1 at.% boron is a combined effect of heterogeneous nucleation of β dendrites on primary borides, heterogeneous nucleation of peritectic α grains on the borides in the interdendritic liquid and the subsequent α nucleation on the peritectic α grains during solid phase transformation, along with the heterogeneous nucleation of α grains on the borides in the dendrites during solid phase transformation.

Considering that there are more and more randomly oriented non-Burgers variants and fewer and fewer Burgers and non-Burgers variants that have the OR with borides as the growth of dendrites, it is suggested that non-Burgers α nucleated on peritectic α grow faster than Burgers α precipitated from parent β and non-Burgers α nucleated on borides during β to α solid phase transformation in Ti4522XD. Even though the β dendrites have already been refined before the peritectic reaction occurs, the sizes of β dendrites are still larger than the final α grains which are about 400 and 100 μm, respectively, as shown in fig. 4.1 (b) and fig. 4.4, and moreover, the β dendrites need to be broken up somehow. Therefore, in the whole solidification process heterogeneous nucleation of peritectic α on the borides in the interdendritic liquid and the subsequent α nucleation on the peritectic α grains play a very important role in the microstructure refinement in the slowly solidified Ti4522XD castings and its role is more important than the other two mechanisms which

are caused by borides inoculating β dendrites during solidification and α grains during β to α solid phase transformation. However, it is believed that all the grain refinement mechanisms are interlocked and cannot be separated. It should be emphasised that the grain refinement mechanisms in the as-cast boron-containing TiAl alloys and their interactions are directly related to their alloy systems, the boron content and the solidification and cooling rate. In the other alloys systems, the solidification behaviours are different and thus their grain refinement mechanisms are different. The above mechanisms are only applicable to the slowly solidified Ti4522XD castings and the other alloy systems that have the similar solidification behaviours.

6.1.3 The influence of cooling rate on the solidification behaviour of Ti4522XD

The above mechanism for the grain refinement in Ti4522XD will be affected by the cooling rate, since at high cooling rate during solidification such as the solidification of quenched liquid in Ti4522XD Bridgman samples and gas-atomised fine Ti4522XD powders, the peritectic reaction will be restricted. At such a high cooling rate the grain size will always be much smaller than that in the as-cast ingot, since increasing cooling rate can increase supercooling which can in turn increase the number of nuclei for the primary β grains or dendrites. However, with the addition of 1 at.% boron to Ti4522XD, the microstructures of fast solidified Ti4522XD can be further refined. Grain refinement has two meanings here: one is that the α/α_2 grains should be smaller than their parent β grains and the second is that most of the α/α_2 grains should be randomly oriented. Obviously the microstructures of fast solidified boron-free base alloy do not meet the criteria. Even though some α_2 grains in the quenched liquid of Ti4522 Bridgman sample are only around 100 μm (fig. 4.5), most of them have the orientations defined by the Burgers OR with their

parent β phase. The Burgers OR was broken down by boron addition in the quenched liquid of Ti4522XD Bridgman sample and gas-atomised Ti4522XD powders, leading to randomly oriented fine grains.

As to the fine Ti4522XD powders solidifying at a cooling rate about 10^3 ℃/s, the peritectic reaction is not assumed to occur, and the grain refinement mechanism is not certain. However, as discussed in section 4.2.3.1, the most possible way for the grain refinement introduced by the addition of boron is through the heterogeneous nucleation α grains on the borides in the interdendritic regions during β to α solid phase transformation. In terms of coarse powders solidifying at a cooling rate around 10^2 ℃/s, the solidification behaviour and grain refinement mechanism are similar to the Ti4522XD Bridgman sample, since there are many α_2 grains surrounding the interdendritc γ grains have the same orientation, even thought the peritectic α grains are not obvious.

As discussed before, another important influence of high cooling rate on the solidification behaviour of Ti4522XD is that the α and γ grains can solidify directly from the liquid when the Al content reaches a critical level without peritectic reactions. In coarse Ti4522XD powders, the cooling rate is about 10^2 °C/s and the primary β grain grows in a dendritic way. In this way, Al can be segregated into the interdendritic regions, leading to possible peritectic reactions. Even though peritectic α grains are not obvious in coarse Ti4522XD powders, they are proven to exist as discussed above. However, the observation that the γ grains in the interdendritic regions had equiaxed microstructure, random orientation and no Blackburn's OR with neighbouring α_2 grains indicates that they were formed by direct solidification from liquid by homogenous nucleation or by nucleation on the interdendritic borides, rather than by solid phase transformation from peritectic α as observed from Ti4522(XD) Bridgman samples. In fine Ti4522XD powders the cooling rate is even higher

and can be up to 10^3 ℃/s, no diffusion controlled peritectic reactions are expected. The observation of the interdendritic α_2 grains with higher Al than matrix α_2 grains is also assumed to be caused by direct solidification from the liquid by nucleating on the neighbouring β grains or on the interdendritic borides. In the former case the Burgers relation between interdendritic α_2 grains and their adjacent matrix α_2 grains can be retained as observed in fig. 4.27 to fig. 4.29.

6.1.4 The influence of cooling rate and alloy composition on the solidification behaviour of borides

It has been established that as the decrease of cooling rate during solidification the morphologies of borides in boron-containing TiAl alloys can be changed from fine curvy to blocky. At very high cooling rate, boron can be supersaturated within the matrix during solidification, but in the cooling process the secondary borides can be precipitated as shown in fig. 4.32 in fine Ti4522XD powders. The fact that both the fine curvy borides and blocky borides have no evident OR with the matrix phases indicates that they were formed directly from the melt. Since both the β phase and the α phase have a very small solubility for boron[20, 106], the liquid will become enriched in boron during the formation of primary metallic phases, and when a critical amount of boron is accumulated, the borides form.

However, the onset of primary boride precipitation is also affected by the cooling rate during solidification. In slowly solidified Ti4522XD Bridgman sample the start of primary boride precipitation was found just slightly later than the leading β phase since coarse boride precipitates in the cores of the β dendrites and interdendritic areas were frequently observed through most of the mushy zone. In fast solidified Ti4522XD, especially in the powder particles, all the primary boride precipitates are fine and curvy and located in the

interdendritic areas. This indicates that the primary boride formation occurred well after the β dendrites were formed, probably at a stage when the β dendrite growth was almost to its end.

The formation of fine curvy borides in rapidly cooled regions in the interdendritic areas appears to be influenced by the constraint of the neighbouring matrix as they grow concurrently; the long axes for the curvy borides depend on the structure of borides[16, 32]. The observation that the long curvy TiB_2 in Ti48Al2Cr2Nb1B is two dimensional indicates that there are two directions growing much faster than the third one which is normal to the other two, and those two fastest growing directions were found to be along $<1\bar{1}00>$ and [0001] by TEM observation.

When the cooling rate is lower, the onset for boride precipitation is earlier, slightly later than the solidification of leading dendrite. As a result, there is enough space for them to grow freely in all directions even though the fastest growing directions are still favoured; hence blocky borides are formed in the slow cooling areas, most of which are located inside of as-solidified lamellar colonies. Pole figures from EBSD mapping have confirmed that the fastest growing direction for blocky TiB with B27 structure is along [010], while the fast growing direction for blocky TiB_2 is along [0001]. The fastest growing directions of each boride are thought to be related to its intrinsic crystal structures. Consider TiB with B27 structure and TiB_2 for example. The (010) plane and (0001) plane are the closest packed planes in TiB and TiB_2, respectively. Growth along the closest packed planes needs the least nucleation activation energy, therefore, the axis normal to those closest packed planes are very common to be the fastest growing directions during solidification.

Meanwhile, the boron concentration in the later solidified liquid which is cooled more slowly would increase. In the equilibrium Ti-B binary system, there are three equilibrium

titanium borides, i.e. TiB with B27 structure, Ti_3B_4 and TiB_2. The areas with slowest cooling rate are the places in the middle of the buttons. As a result, they have the highest possible enrichment of boron. This is consistent with the observation of TiB_2 borides in the middle of the button, while no TiB_2 borides were found in the chill zone of the Ti4522XD buttons.

De Graef et al.[21] reported that there was little difference in the formation energy of B_f and B27 under equilibrium conditions, and it was proposed that the B_f is metastable relative to $D7_b$ and C32 in response to a change in the melt chemistry. However, for the same monoboride TiB, metastable B_f structure was formed preferentially in the fast cooling areas in Ti4522XD button. The reason for this is not well understood yet.

Borides with similar morphologies were observed in cast Ti-48Al-2Cr-2Nb-1B, but in this alloy all the borides were TiB_2. It has been well established that increasing the Al content in the Ti-Al-B system could change the structure of primary borides as illustrated in the schematic Ti-Al-B liquidus projection in fig. 6.1[31]. When the Al concentration is more than 45 at.%, the only possible boride is TiB_2. Therefore, the cooling rate does not have any effect on the crystal structures of borides in Ti48Al2Cr2Nb1B, even though the boron content in long curvy borides and blocky borides would be different at different cooling rates. However, since Nb is a monoboride former, the single TiB_2 form was not observed in Ti4522XD, especially in the areas with fast cooling rate where the boron content was lower. It has been reported that for about 2 at.% addition of boride formers, like Ta and W, TiB-based borides can be stabilized up to 47 at.% Al[20, 253].

In addition, long curvy borides interspersed with layers of B2 phase were observed in both TiB and TiB_2 borides. This can also be interpreted based on the Ti-Al-B liquidus projection in fig. 6.1. Those long curvy borides were observed close to the chill zone in the

buttons where the cooling rate is high during solidification and the neighbouring boron content is low. As a result, the first solidified solid phase is β phase and then the borides are formed through the eutectic reaction:

$L \rightarrow \beta + TiB_x$ (x=1 or 2, depending on Al level)

Therefore, a lamellar structure could be found in those curvy borides due to the eutectic reaction and in the cooling process the β is ordered to B_2. However, in the centre of buttons both B and Al contents are increased due to the segregation caused by relatively slow solidification rate. When their concentrations reach the liquidus line in fig. 6.1, which actually is a slight increase compared with their original compositions, the first solidified solid phase is boride. Thus no lamellar structure could be found in those blocky borides. The solidification sequence for both Ti4522XD and Ti48Al2Cr2Nb1B has been indicated in fig. 6.1.

In summary, the structures of borides in TiAl alloys are both composition and cooling rate related. On one hand, the increase of boron and Al content favours the formation of TiB_2 borides and the addition of boride formers, like Nb, can stabilize TiB borides to a higher Al content. On the other hand, fast cooling rate promotes the formation of TiB rather than TiB_2 through the change of boron content in the melt and also favours B_f than B27 by non-equilibrium solidification.

Based on above discussion, it is seen that the solidification behaviour of Ti4522XD is cooling rate related. Combining the observation in this study and the published work in the literature[102], the transformation behaviour in Ti4522XD during continuous cooling (CCT) can be established in fig. 6.2, in which both the transformation behaviours of metallic phases and borides are defined.

6.2 The formation of surface layers during HIPping of Ti4522XD castings and their influence on properties

6.2.1 Mechanism for the formation of surface layers under HIPping conditions

6.2.1.1 A proposed mechanism for the formation of HIPped surface layers

The observation of oxide layers on the top surface of the HIPped samples makes it certain that oxidation occurs under standard HIPping conditions. This is possible because the equilibrium oxygen partial pressure for the oxidation of Ti and Al are about 10^{-22} and 10^{-26} atm, respectively, according to the Ellingham diagram in fig. 2.36, while the oxygen partial pressure in the argon during HIPping is around 10^{-3} atm which is actually much higher than the equilibrium oxygen pressures for oxidation of almost all metals.

The formation of other HIPped surface layers like Ti-rich layer and γ layer which is underneath the Ti-rich layer are also directly related to the oxidation process. As demonstrated in the experimental results, all factors which influence oxidation rate, like time, temperature and oxygen partial pressure, have a significant influence on the structures of HIPped surfaces.

For the oxidation of TiAl alloys, particularly Ti4522XD, it has been well established that the oxidation process is through both inward diffusion of oxygen and outward diffusion of titanium[198, 250]. Mn was also reported to diffuse outward during oxidation[250]. The main transport process is through TiO_2 if grain boundary and other short circuit diffusion are not considered. Transport in alumina is very small compared with that in TiO_2, thus it can be neglected[198]. Furthermore, studies of defect structures in TiO_2 suggested both the oxygen vacancy, $V_O^{\cdot\cdot}$, and interstitial Ti ions, $Ti_i^{\cdot\cdot\cdot}$ or $Ti_i^{\cdot\cdot\cdot\cdot}$ are the predominant defects[196]. It is

concluded that the transport process is controlled by the diffusion of point defects and influenced by temperature, time, oxygen pressure and also alloy compositions as discussed in the literature review in section 2.9.1. In general, interstitial Ti ions predominate at low oxygen pressures and high temperatures, while oxygen vacancies predominate at high oxygen pressures and low temperatures. The calculation of the formation energy of point defects has confirmed this, as shown in fig. 2.32[197]. According to thermodynamic calculation, from 900 to 1100 ℃ Ti is preferentially oxidised over Al when the Al content is less than 50 at.% in TiAl alloys, and Al is preferentially oxidised over Ti when the Al content is higher than that as shown in fig. 2.33[201]. This tendency is supposed to be the same at higher temperature.

The typical cross section microstructure of a HIPped surface as shown in fig. 5.3 which is formed under standard HIPping conditions is assumed to be an oxidation phenomenon under specific conditions. Therefore, a mechanism for the formation of surface layers during HIPping of Ti4522XD alloys is proposed based on the oxidation mechanism in TiAl alloys as discussed in section 2.9.1 and a schematic illustration for the proposed mechanism is shown in fig. 6.3.

At the very beginning of the HIPping process, the oxygen would diffuse into the metal surface until the metallic phases, TiAl and Ti_3Al in TiAl alloys, are saturated with oxygen. Then oxidation occurs. Both Ti and Al would be oxidised forming thin oxide films on the surface which might be only a few nanometers thick according to the study carried out by Maurice et al.[192]. Once a continuous oxide layer is formed on the surface, the growth of the oxide layer is controlled by the diffusion of the required elements through the oxides.

Since the diffusion rate of Ti ions is faster in both Ti oxides and metal phases than Al ions[6], the growth rate of Ti oxides is faster than Al_2O_3 at the beginning and, therefore, the

outer oxide layer is mainly composed of Ti oxides. Due to the high temperature (1260 ℃) and low oxygen pressure ($<1.5\times10^{-3}$ bar) during HIPping, the outward diffusion of interstitial Ti ions is faster than inward diffusion of oxygen in the Ti oxides which is realised by the outward diffusion of oxygen vacancies as was proven by Ref.[197]. Therefore, a thin Al-rich layer beneath the oxide layer forms. When the Al content reaches a certain level and meanwhile there is not enough oxygen diffusing in for oxidation, α transforms to γ by solid phase transformation and therefore forming a thin pure γ layer, as the situation of 1-2 hours HIPped surface structures shown in fig. 5.15 (a) and (b).

With increase in HIPping time, the thickness of oxides layer will increase as the oxides grow. On the other hand, because of the faster outward diffusion of Ti interstitials than the inward diffusion of oxygen ions, lots of extra Ti ions underneath the oxides layer could not be fully oxidised, therefore, they nucleate and grow between the oxide layer and the γ layer, leaving a Ti-rich layer in between most of which transform to α_2 grains during cooling. Since previous oxides particles which are present in large numbers can act as nuclei for the growth of Ti-rich grains, the size of Ti-rich grains is very small, less than 5 μm, as observed in fig. 5.24. The thickness of the Ti-rich layer increases as the HIPping time increases. Meanwhile, the outward diffusion of oxygen vacancies and low solubility of oxygen in γ phase leads to the formation and enrichment of pores in the interface between the Ti-rich layer and γ layer. At the same time, the continuous outward diffusion of Ti makes γ grains in the γ layer grow bigger and bigger. Since the growth of γ grains is diffusion-controlled, it is, in essence, a coarsening process of the original γ laths because of the enrichment of Al. This is evidenced by the same orientation relationships between the γ grains in the γ layer and the adjacent γ laths in the lamellae through the EBSD observation in fig. 5.24 (e).

However, with further increasing HIPping time, more and more oxides will form and more and more oxygen will diffuse into the Ti-rich layer. Finally, Ti-rich grains will get oxidised when the oxygen content reaches a certain level. At the same time, γ grains in the γ layer begin to be oxidised when the oxygen is saturated in the γ layer. However, due to the enrichment of Al in the γ layer Al is preferentially oxidised, leading to the depletion of Al or in other words, the enrichment of Ti which favours the formation of a subsurface with coarsened α_2 laths. This is consistent with the observation of 10 hours HIPped surface structures as shown in fig. 5.15 (c) and (d). However, the Al_2O_3 was not as commonly found in Ti-rich layer as that in the oxides layer. This is attributed to the interstitial dissolution of Al_2O_3 in Ti oxides as reviewed in section 2.9.1. The solubility of Al_2O_3 in Ti oxides decreases with increase of oxygen pressure. The oxygen pressure in the interface of the Ti-rich layer and substrate is much lower than that in the interface of gas and oxides scale, therefore, Al_2O_3 could precipitate on the surface oxide layer.

In addition, EDS analysis in fig. 5.6 and table 5.2 found that Mn was depleted in the Ti-rich layer. This is most likely due the oxidation of Mn, forming Mn oxides in the oxide layer by the outward diffusion of Mn[250]. Actually, MnO_2 was detected by XRD analysis on the surfaces of 1 and 10 hours HIPped specimens. But because of the small amount of Mn oxides and limited analysing area of XRD, Mn oxides were not detected every time on the HIPped surfaces.

6.2.1.2 The influence of HIPping temperature and time

At lower temperature, however, inward diffusion of oxygen ions is faster than outward diffusion of Ti ions. In this case, the Ti oxides and Al_2O_3 may alternately form because of the alternate enrichment of Al and Ti underneath the oxide layer, as oxidation or HIPping time increase. Nevertheless, only an α_2 layer was found below the oxide layer as observed

in fig. 5.18, when the specimens were HIPped at 900 and 1100 ℃ for 4 hours. The formation of an α_2 layer is actually a very common phenomenon in the oxidation of two phase TiAl alloys as discussed in 2.9.1, which is attributed to the preferential oxidation of Al in the interface between the oxide scale and metal phases and the dissolution of oxygen in the subsurface. However, according to thermodynamic calculations and Ti-Al-O ternary phase diagram[201], Ti can also be preferentially oxidised in Ti-rich TiAl alloys in low oxygen pressure environment, such as the interface between oxides scale and metal phases. As a consequence, it is assumed that an Al-rich layer can also appear if the specimens are HIPped for a longer time, since Ti should be preferentially oxidised when the subsurface is enriched in Ti, leading to the enrichment of Al. As has been summarised in the literature review in section 2.9.2, the γ layer underneath the outer oxides layer indeed was found by Yang et al.[200] and Xia et al.[216, 217] in the oxidation of a TiAl alloy at 800-900 ℃ for about 50-100 hours in air. Unfortunately, they did not give any explanation for this phenomenon, but according to the above assumption, the possible reason for the formation of this γ layer is the preferential oxidation of Ti just when the previous Ti-rich subsurface was saturated with oxygen. Therefore, in the oxidation of TiAl alloys, whether the γ layer subsurface can appear may really depend on the oxidation time. However, if the Al-rich layer is formed by the oxidation that is predominated by the inward diffusion of oxygen, there will be no Ti-rich layer between the oxide layer and the Al-rich layer as what was commonly observed after standard HIPping.

6.2.1.3 The influence of oxygen pressure

If the oxygen pressure in the HIPping environment is extremely low, like the case of HIPping with an oxygen getter, most of the oxygen is just dissolved in metal phases. That might be the reason why there was only an α_2 laths coarsened layer underneath the surface

oxide layer when samples were HIPped with Ti sponge, as fig. 5.20 (a) shows. On the other hand, XRD analysis in fig. 5.20 (b) found that when the specimen was HIPped with Ti sponge, only metastable Ti oxides were detected. As pointed out in the literature review in section 2.9.1 and fig. 2.35, when the oxygen pressure is extremely low, lower than 10^{-22} bar, the oxidation products of Ti oxides are no longer stable rutile TiO_2, but metastable TiO, Ti_2O_3, etc, which are more thermodynamically stable. Therefore, it is reasonable to believe that the oxygen pressure was lower than 10^{-22} bar when the specimens were HIPped with Ti sponge.

But if the oxygen pressure is higher than a crucial amount, the mechanism for the diffusion of point defects will change to be dominated by oxygen vacancies, the same effect as lowering the HIPping temperature. As a result, the structure of HIPped surfaces will have no γ layer either, as shown in fig. 5.21. However, severe oxidation occurs which leads to the formation of thick oxide layer due to the high temperature and oxygen content.

6.2.1.4 The influence of HIPping pressure

As seen in fig. 5.22, when the same specimen was heat treated in argon at 1 bar, the sample surface was depleted with Al and formed an α_2-rich layer. It is well known that Al has a high saturation vapour pressure which is in the range of 10^{-5}-10^{-4} bar at 1260 ℃[215]. As a consequence, it is very easy for Al to get evaporated during heat treatment at 1260 ℃ in argon at ambient pressure. However, in the HIPping environment, there is extra 1500 times pressure. Thus the actual saturation vapour pressure of Al at 1260 ℃ is reduced to 1/1500 of the original value, namely $6.7 \times (10^{-9}$-$10^{-8})$ bar. As a result, the evaporation of Al can be significantly suppressed. On the other hand, the oxygen content in the argon is also increased 1500 times higher, leading to a serious surface oxidation problem. But if the specimen was heat treated in argon at 1 bar (the specimens were encapsulated in glass

tubes, therefore, there was no continuous oxygen supply when it was consumed), there was no apparent oxide scale as indicated in Fig. 5.22. Therefore, the influence of HIPping pressure on formation of surface layers can be regarded as suppressing the evaporation of Al and providing enough oxygen. The compositional change in the metal surface can thus be excluded when considering the mechanism for the formation of the HIPped surface.

Furthermore, the HIPping pressure is considered to accelerate the oxidation rate. Since the ductility and thermal expansion coefficient are different between oxides and metallic phases, the pressure imposed by HIPping could break the oxide layer during the plastic deformation, especially when the internal pores are large, and therefore, produces lots of micro-cracks within oxides layer which could increase the diffusion rate of oxygen and titanium ions.

6.2.1.5 The influence of surface deformation

Surface deformations could introduce extra defects, such as dislocations, which can enhance the diffusion of metal ions and oxygen vacancies, thus increase the thickness of HIPped surface layers. What is more, the elastic energy stored in the deformed grains can provide a driving force for the recrystallisation. Therefore, the random orientation distribution of γ grains in the γ layer, as observed in fig. 5.24, on the surfaces of surface deformed specimens indicates that the growth of γ grains in the γ layer is through a recrystallisation process. On the contrary, for electropolished specimens which initially had deformation-free surfaces, the growth of γ grains in the γ layer is through the growth of the original γ laths in the adjacent lamellae as discussed before.

In summary, basically, the mechanism for the oxidation of TiAl alloys can be applied to explain the formation of HIPped surface in Ti4522XD. However, the specific HIPping environment and HIPping pressure add to the complexity.

6.2.2 The influence of surface layers on properties

6.2.2.1 The influence on RT mechanical properties

According to the room temperature tensile and HCF testing, the γ-layer containing HIPped surface has no significant influence on mechanical properties. However, if the HIPped surface contained an α_2 layer, it has a very detrimental effect on both tensile strength and ductility.

The influence of the γ layer on mechanical properties compared with that of the α_2 layer is related to its intrinsic properties. As indicated from micro-hardness testing and WDS analysis, the γ layer is a softer layer and has a lower solubility of oxygen than the α_2 layer which is intrinsically brittle. Therefore, it is not easy for cracks to initiate from this γ layer and should not reduce the materials' ductility. Given the thinness of the γ layer, the room temperature tensile and fatigue strength should not be reduced significantly. In addition, the fact that the crack is always initiated through interlamellar fracture in γ-layer-containing TiAl test pieces when tested at room temperature indicates that the interlamellar strength is weaker than the translamellar, lamellar colony boundaries and γ grain boundaries, but higher than α_2 grain boundaries. Considering the incompatibility of plastic deformation between α_2 laths and γ laths, the α_2/γ interlamellar strength should be weaker than the γ/γ interlamellar strength.

Actually, better mechanical properties are expected at high temperatures for a sample with a γ surface layer since γ has a higher oxidation resistance than α_2. However, because of limitation of material and time, mechanical testing at high temperatures has not been finished yet.

6.2.2.2 The influence on hot corrosion properties

The corrosion solutions used in the experiment is a simulation of air atmosphere above sea waters. The solution of SO_2 and SO_3 has acidic properties. Therefore, because of the metallic/reductive property of Ti and Al in TiAl alloys, the following dissolution will happen:

$$Ti + 4H^+ \rightarrow Ti^{4+} + 2H_2 \uparrow$$

$$2Al + 6H^+ \rightarrow 2Al^{3+} + 3H_2 \uparrow$$

Since Al has a higher reductivity than Ti, more Al can be reduced and dissolved than Ti even in the γ lath as was observed in fig. 5.35. On the other hand, due to the dissolution of oxygen in the corrosion solution and the high temperature, oxidation would also take place, leading to the formation of Ti oxides and Al_2O_3:

$$2Ti + xO_2 \rightarrow 2TiO_x$$

$$4Al + 3O_2 \rightarrow 2Al_2O_3$$

As discussed in section 2.9.1, the type of Ti oxides which will form depends on the oxygen partial pressure in the solution, but according to the XRD results in fig. 5.36, the majority of Ti oxides were TiO_2. Therefore, there should be enough oxygen dissolved in the solution. Furthermore, the preferential oxidation of Ti and Al is related to the alloy composition. When the Al content is higher than 50 at.%, Al_2O_3 is preferentially formed. Otherwise, Ti oxides are preferentially formed. Since a continuous Al_2O_3 layer could prevent further oxidation, a γ layer is supposed to increase an alloy's corrosion resistance in the mild corrosion environment like the situation in the first group of corrosion experiment with 100 ppm SO_2/SO_3. However, in the acidic environment those oxides can indeed be dissolved:

$$TiO_2 + 4H^+ \rightarrow Ti^{4+} + 2H_2O$$

$$Al_2O_3 + 6H^+ \rightarrow 2Al^{3+} + 3H_2O$$

Increasing the acidic concentration increases the dissolution of oxides, and to a certain extent like the situation in the second group of corrosion experiment with 300 ppm SO_2/SO_3, continuous Al_2O_3 layer could be destroyed and could not prevent the alloy from further corrosion and oxidation. Therefore, in this case even a γ layer could not play the protective function against the corrosion process. However, Al_2O_3 can still be the preferentially oxidised product in the γ layer contained samples.

The existence of Cl^- was reported to increase the TiAl alloys' corrosion rate by acting as a catalyst as discussed in the literature review. It is reasonable to believe that the deposition of NaCl on the surface of specimens could also increase the corrosion process and the extent of degradation would increase with increase of temperature.

Because the γ layer played no role of protecting the surfaces of specimens from severe corrosion, the HCF test pieces with γ layers did not show any advantage in the HCF properties, either, and because of the surface corrosion, the overall fatigue strength was significantly decreased.

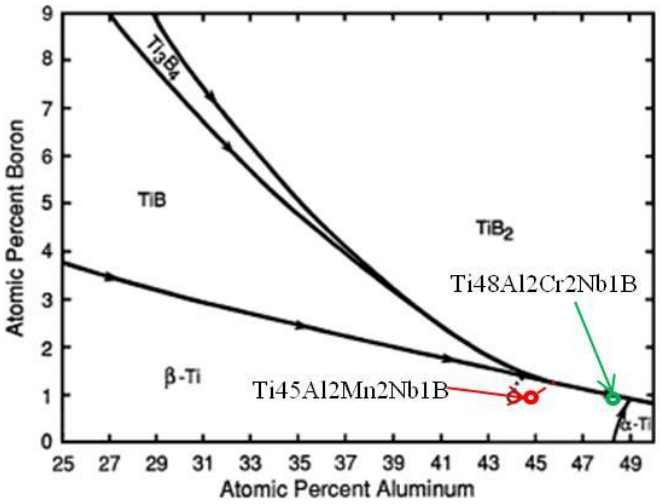

Figure 6.1 Projection of liquidus surface for the ternary Ti-Al-B system [31]. The solidification sequences of Ti4522XD and Ti48Al2Cr2Nb1B are labelled in this graph.

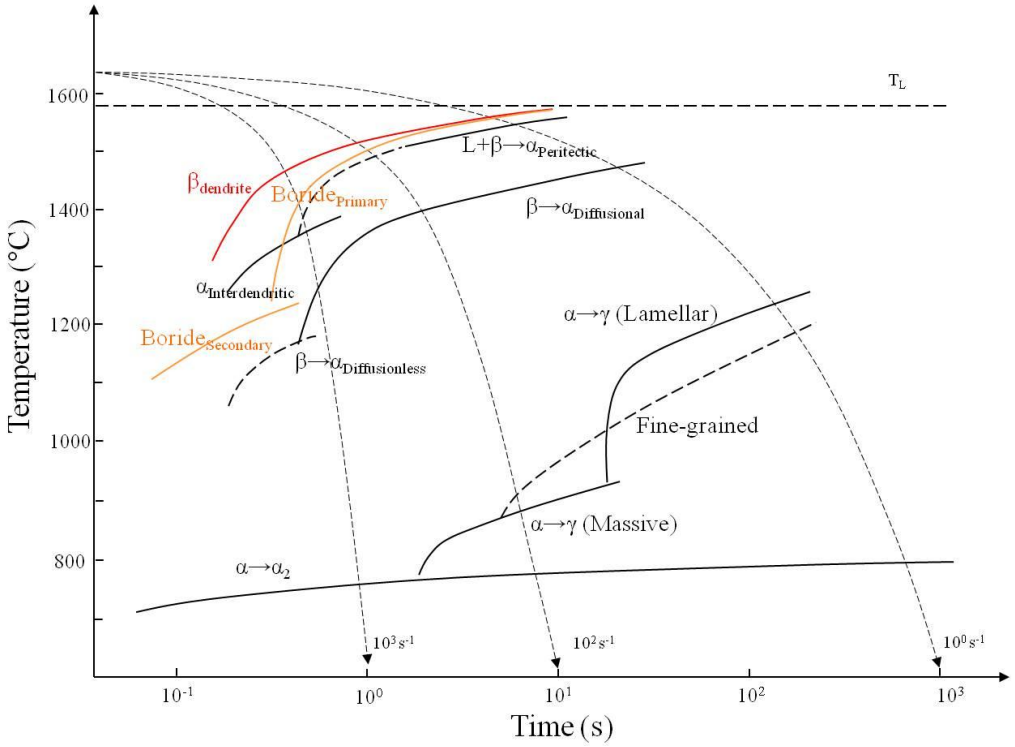

Figure 6.2 CCT curve for Ti4522XD.

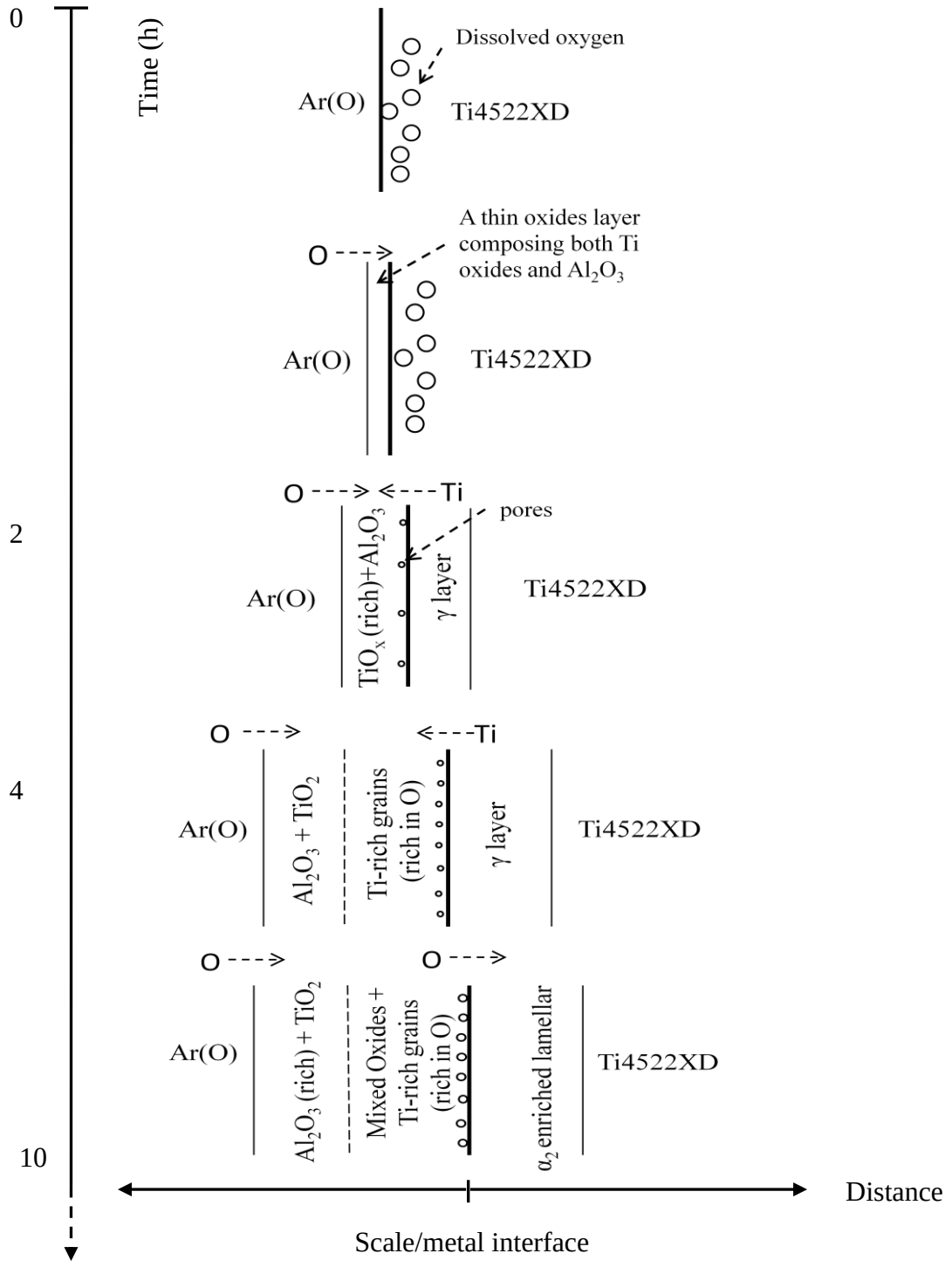

Figure 6.3 Schematic illustration of the formation of surface layers on Ti4522XD castings under standard HIPping conditions.

CHAPTER 7 CONCLUSIONS AND FUTURE WORK

This chapter covers the main conclusions drawn from the work reported in this thesis. There are several issues addressed in this thesis needing further investigation and suggestions for future work are also given following the list of main conclusions.

7.1 Conclusions

1. The basic solidification pathways for cast Ti4522XD and Ti4522 at low cooling rate are through:

   $L \rightarrow L + \beta \rightarrow L + \beta + \alpha \rightarrow \beta + \alpha \rightarrow \alpha$

   In which the α grains between the liquid and β dendrites are formed by a peritectic reaction:

   $L + \beta \rightarrow \alpha$

   While at cooling rates above 10^3 ℃/s, the peritectic reaction is suppressed in Ti4522XD, and α and γ can solidify directly from the liquid.

2. With the addition of 1 at.% boron, the microstructures of cast Ti4522XD could be effectively refined, which is attributed to three factors:

   i. Heterogeneous nucleation of β dendrites on the primary borides, which increases the number of β dendrites;

   ii. Heterogeneous nucleation of peritectic α grains on the borides in the interdendritic regions during solidification, and the subsequent nucleation of α grains in dendrites on the peritectic α during solid phase transformation,

which is the main reason for the formation of non-Burgers variants. With increase of nucleation sites for the peritectic α grains and the non-Burgers variants, the microstructure of cast Ti4522XD is refined again.

iii. Heterogeneous nucleation of α grains on the borides during β to α solid phase transformation.

For the solidification of Ti4522XD castings with slow cooling rate, all the above three mechanisms contribute to the grain refinement in the as-cast microstructure, while the third one and probably the second one are applicable when the cooling rate is up to 10^3 ℃/s.

3. The morphologies of borides are greatly influenced by cooling rate during solidification of boron-containing TiAl alloys, with fast cooling giving rise to fine curvy borides and relatively slow cooling to blocky borides, regardless of alloy compositions. The crystal structures of borides in Al-lean TiAl alloys, such as Ti4522XD, are also affected by cooling rate, with metastable B_f type TiB and Ti_3B_4 borides dominating the curvy borides, and stable B27 type TiB and TiB_2 occupying the whole blocky borides. However, in Al-rich TiAl alloys, such as Ti48Al2Cr2Nb1B, the change of cooling rate during solidification does not cause any crystal structural change in borides which are always TiB_2.
4. HIPping of Ti4522XD castings under standard conditions: 1260 ℃/4 h/150 MPa could change the surface microstructure to contain an oxide layer on the top, a Ti-rich layer in the middle and a γ layer above the matrix. The change of HIPping conditions, such as temperature, time, pressure and oxygen level in argon could change the surface microstructures. Surface deformation does not change the

surface microstructure but could cause the growth mechanism for the γ layer to be changed from diffusion-controlled growth to a recrystallisation process.

5. The γ-layer formed on the surface of Ti4522XD castings during standard HIPping at least has no negative influence on the mechanical properties. In a mild corrosion environment, a γ-layer can enhance the corrosion resistance.

7.2 Future work

1. It has been established that the refinement of as-cast Ti45422XD by the addition of 1 at.% boron can be attributed to the formation of borides from the melt which act as inoculants for the nucleation of β dendrites and peritectic α during solidification. It is also suggested that β dendrites might be refined because of constitutional supercooling by the addition of boron, however, no direct evidence has been found. It would be interesting to lower the boron level in Ti4522XD Bridgman samples and Ti4522XD powders to investigate their solidification behaviours in the case that there would be fewer borides.
2. The borides that were found to have OR with neighbouring α_2 grains in the core of Bridgman dendrites are large and long. It would be interesting to investigate the OR between fine curvy borides in the interdendritic regions with their neighbouring γ grains transformed from peritectic α_2 grains in a Ti4522XD Bridgman sample by TEM, in order to confirm if the peritectic α can nucleate on those borides. The structural and compositional features in the interface between dendrites and interdendritic regions in Bridgman samples also merit further confirmation by TEM.
3. It is known that the TiB with B_f structure is more favoured than TiB with B27 structure in Ti4522XD castings in the rapidly solidified areas. However, the reason

for this is not well understood. Thermodynamic and kinetic simulations for both borides under non-equilibrium conditions may be considered. In addition, the habit planes for the precipitation of B_f TiB from α_2-Ti_3Al in fine Ti4522XD powders can be reinvestigated.

4. Even though the α_2-layer contained on HIPped surface was found to be definitely detrimental to RT mechanical properties, no significant difference in the room temperature mechanical properties between test pieces with and without γ-layers was found. However, the mechanical properties of the matrix, especially the ductility, were poor. It has not been shown convincingly that the γ-layer does not harm room temperature properties. Therefore, it is better to repeat the mechanical testing with the Ti4522XD castings that have better ductility.
5. Since Ti4522XD castings are designed to be used as high as 650 ℃, the test pieces with and without γ-layer should be further tested at this temperature to investigate the influence of the γ-layer on high temperate mechanical properties, such as tensile properties and fatigue properties.
6. Corrosion is another important issue in the practical application of Ti4522XD. It was found that γ-layer has no evident effect on fatigue properties after severe corrosion, however, it is valuable to investigate if γ-layer can improve the fatigue properties in less severe corrosion conditions, given it has been found that γ-layer can help improve the corrosion resistance in a less severe corrosion conditions.

APPENDIX 1 LIST OF PUBLICATIONS

1. Published paper:
    i. C Yang, D Hu, X Wu, A Huang, M Dixon, *The influence of cooling rate and alloy composition on the formation of borides during solidification of boron-containing TiAl alloys*, proceedings of the 12th world conference on Titanium Beijing, 2011, In press.
    ii. D Hu, C Yang, A Huang, M Dixon, U Hecht, *Solidification and grain refinement in Ti45Al2Mn2Nb1B*, accepted by Intermetallics (doi:10.1016/j.intermet.2011.11.003).
    iii. C Yang, D Hu, X Wu, A Huang, M Dixon, *Microstructures and tensile properties of hot isostatic pressed Ti4522XD powders*, accepted by Materials Science and Engineering A.
2. Papers in the process of clearance by Rolls-Royce:
    i. C Yang, D Hu, A Huang, M Dixon, *The solidification and grain refinement in Ti45Al2Mn2Nb1B subjected to fast cooling*.
    ii. D Hu, C Yang, A Huang, M Dixon, U Hecht, *Grain refinement in Ti44Al8Nb1B*.
    iii. C Yang, H Jiang, D Hu, A Huang and M Dixon, *Effect of boron concentration on phase transformation texture in as-solidified Ti44Al8NbxB*.

APPENDIX 2 CALCULATIONS OF ANGLES BETWEEN TWO SPOTS IN POLE FIGURES

Pole figure is a two dimensional stereographic projection reflecting a three dimensional crystal structure information, including the relative position of a particular plane or direction to the pole plane or pole direction, which is very useful for the texture and orientation relationship analysis.

If the angle between two spots in a pole figure can be measured, the angle between two plane vectors or two direction vectors, which project two spots in the pole figure, in a three dimensional crystal space can be known. The method used here to measure the angle is by retrieving the two dimensional vectors in the pole figure to three dimensional vectors and then calculating the angle between those three dimensional vectors by a well known mathematic vector formula.

In a pole figure, each spot can be treated as the two dimensional vector $\boldsymbol{v}$, including two values, φ and $|\boldsymbol{v}|$, as illustrated in fig. 1(a). φ is the angle between the $\boldsymbol{v}$ and RT direction, which stands for the direction pointing upward in the pole figure, and it has the rang from -180 ºto 180 º. $|\boldsymbol{v}|$ refers to the absolute value of vector $\boldsymbol{v}$, i.e. the length. In two dimensions, each $\boldsymbol{v}$ has two components in two dimensional Cartesian coordinate system, $\boldsymbol{v_1}$ and $\boldsymbol{v_2}$. Therefore, the $\boldsymbol{v}$ can be written as:

$$\boldsymbol{v} = \boldsymbol{v}_1 + \boldsymbol{v}_2 = \boldsymbol{v} \cdot cos\varphi + \boldsymbol{v} \cdot sin\varphi \qquad (1)$$

However, if the spot is retrieved to the three dimensional unit sphere, the projected vector $\boldsymbol{v}$ corresponds to vector $\boldsymbol{V}$, as illustrated in fig. 1(b), which has three components: $\boldsymbol{V_1}$, $\boldsymbol{V_2}$ and $\boldsymbol{V_3}$ in each axis in the three dimensional Cartesian coordinate system. The stereographic projection in $\boldsymbol{V_1 0 V_2}$ plane is actually the pole figure in fig. 1(a). Therefore, the $\boldsymbol{V}$ can be written as:

$$\boldsymbol{V} = \boldsymbol{V_1} + \boldsymbol{V_2} + \boldsymbol{V_3} \qquad (2)$$

In which,

$$\boldsymbol{V_1} = \boldsymbol{V'} \cdot cos\varphi \qquad (3)$$

$$\boldsymbol{V_2} = \boldsymbol{V'} \cdot sin\varphi \qquad (4)$$

Now projecting the three dimensional unit sphere in fig. 1(b) to $\boldsymbol{V' 0 V_3}$ plane, another pole figure fig. 1(c) is formed, in which the θ is the angle between $\boldsymbol{V}$ and the RD direction and has the range from 0 to 180 º. From this pole figure, we know:

$$\boldsymbol{V_3} = \boldsymbol{V} \cdot cos\theta \qquad (5)$$

$$\boldsymbol{V'} = \boldsymbol{V} \cdot sin\theta \qquad (6)$$

Incorporating equation (3) – (6) into (2), then

$$\boldsymbol{V} = \boldsymbol{V} \cdot sin\theta \cdot cos\varphi + \boldsymbol{V} \cdot sin\theta \cdot sin\varphi + \boldsymbol{V} \cdot cos\theta \qquad (7)$$

If both φ and θ are known for projected spots in the pole figure, the corresponding three dimensional $\boldsymbol{V}$ can be calculated by equation (7). However, in some applications, the θ is not known from the resultant pole figure. In this case, the θ can be calculated from a geometric analysis as shown in fig. 1(c). Since

$$\tan\left(\frac{\theta}{2}\right) = \frac{|\boldsymbol{v}|}{|\boldsymbol{V}|} \qquad (8)$$

where $|\boldsymbol{v}|$ and $|\boldsymbol{V}|$ refer to the absolute values of $\boldsymbol{v}$ and $\boldsymbol{V}$, respectively. Therefore, θ can be replaced by

$$\theta = 2 \cdot atan\left(\frac{|\boldsymbol{v}|}{|\boldsymbol{V}|}\right) \qquad (9)$$

Then the three dimensional vector $\boldsymbol{V}$ can also be written as

$$\boldsymbol{V} = \boldsymbol{V} \cdot sin\left[2 \cdot atan\left(\frac{|\boldsymbol{v}|}{|\boldsymbol{V}|}\right)\right] \cdot cos\varphi + \boldsymbol{V} \cdot sin\left[2 \cdot \tan\left(\frac{|\boldsymbol{v}|}{|\boldsymbol{V}|}\right)\right] \cdot sin\varphi + \boldsymbol{V} \cdot cos\,[2 \cdot atan\left(\frac{|\boldsymbol{v}|}{|\boldsymbol{V}|}\right)] \qquad (10)$$

Once the two vectors, $\boldsymbol{v_1}$ and $\boldsymbol{v_2}$, in two dimensional pole figure are represented by their corresponding three dimensional vectors, $\boldsymbol{V_1}$ and $\boldsymbol{V_2}$, the angle, ψ, between these two spots in pole figure can be easily calculated from a well known mathematic formula:

$$\delta = acos\left(\frac{\boldsymbol{V_1} \cdot \boldsymbol{V_2}}{|\boldsymbol{V_1}| \cdot |\boldsymbol{V_2}|}\right) \qquad (11)$$

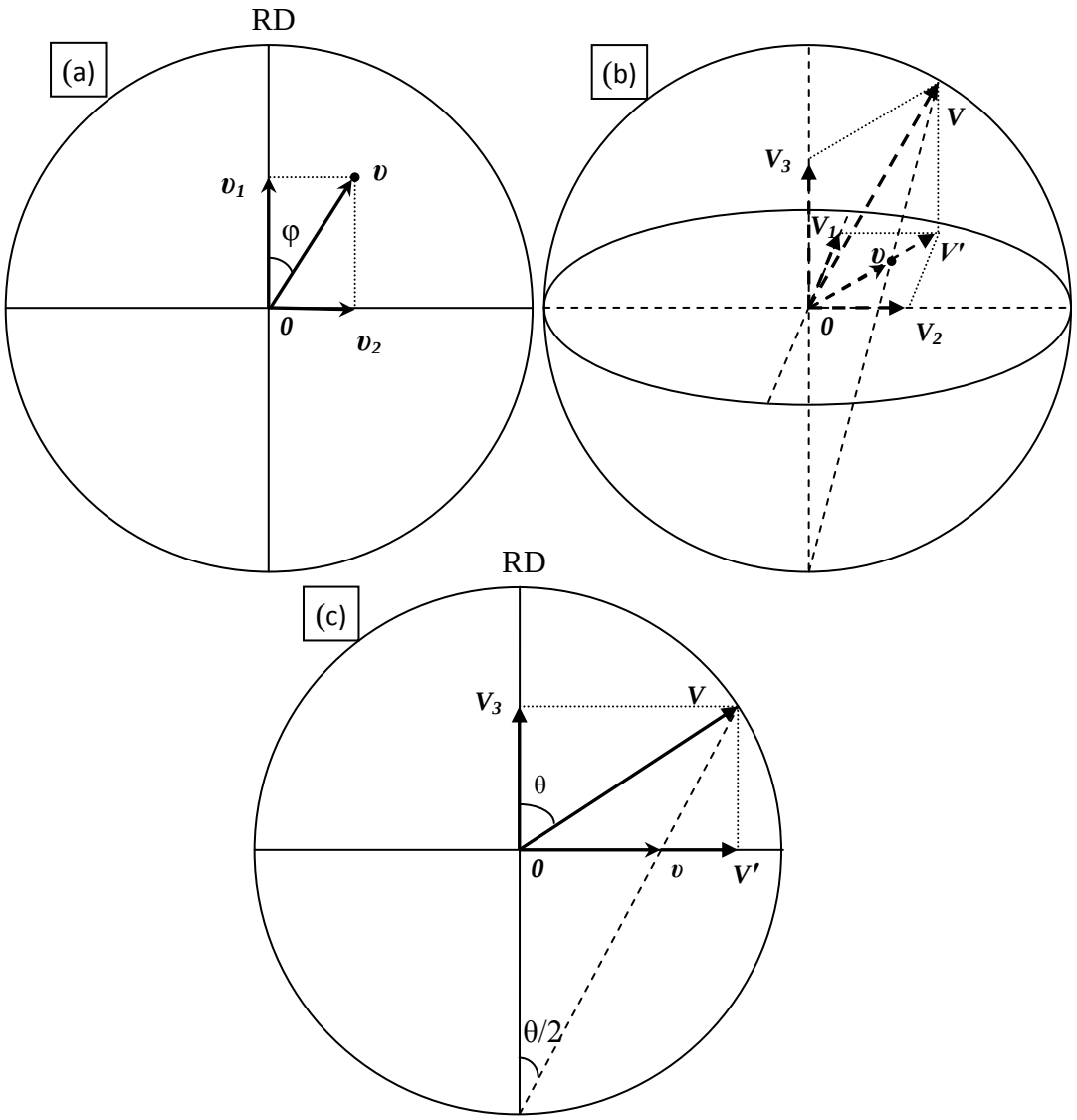

Figure 1(a) represents a pole figure with a projected spot vector $\boldsymbol{v}$. (b) is the retrieved three dimensional unit sphere with original vector $\boldsymbol{V}$ and its projected vector $\boldsymbol{v}$ in $\boldsymbol{V_1 0 V_2}$ plane. (c) is the stereographic projection of (b) in $\boldsymbol{V' 0 V_3}$ plane, forming a new pole figure.

APPENDIX 3 ORIENTATION RELATIONSHIPS BETWEEN BURGERS ALPHA VARIANTS

When hcp α is formed from bcc β by solid phase transformation, they follow Burgers orientation relationships:

$(0001)\alpha // \{110\}\beta; <11\bar{2}0>\alpha // <111>\beta$

There are 6 {110} variants in a β unit cell, namely, (110), $(1\bar{1}0)$, (101), $(\bar{1}01)$, (011) and $(0\bar{1}1)$. If α grains are precipitated from the same parent β grain, they are called Burgers α variants and the angles between (0001) in these variants can only be 0°, 60° and 90°, as illustrated in fig. 1.

When two α variants precipitate from the same {110} in β, their (0001) are parallel and the angle between them is 0°, as illustrated in fig. 1 (a).

When two α variants precipitate from two {110} in β, whose zone axes are parallel to <100>, their (0001) are perpendicular to each other and the angle between them is 90°, as illustrated in fig. 1(b).

When two α variants precipitate from two {110} in β, whose zone axes are parallel to <111> the angle between their (0001) is 60° as illustrated in fig. 1(c).

However, for each {110} in β, there are two <111> directions, to which anyone of the three $<11\bar{2}0>$ directions in the precipitated α can be parallel. For a given angle between (0001) of Burgers α variants, the angles between their corresponding $<11\bar{2}0>$ variants in each

variant are measured and calculated based on β stereographic projections (pole figures). It is worth noting that in the bcc structure of β and in the hcp structure of α, [110] is normal to (110) and $[11\bar{2}0]$ is normal to $(11\bar{2}0)$, respectively. Therefore, the OR between {110} in β and $\{11\bar{2}0\}$ in α_2 is also applicable to the OR between <110> in β and $<11\bar{2}0>$ in α_2. Therefore, only plane stereographic projections were used in the following analysis.

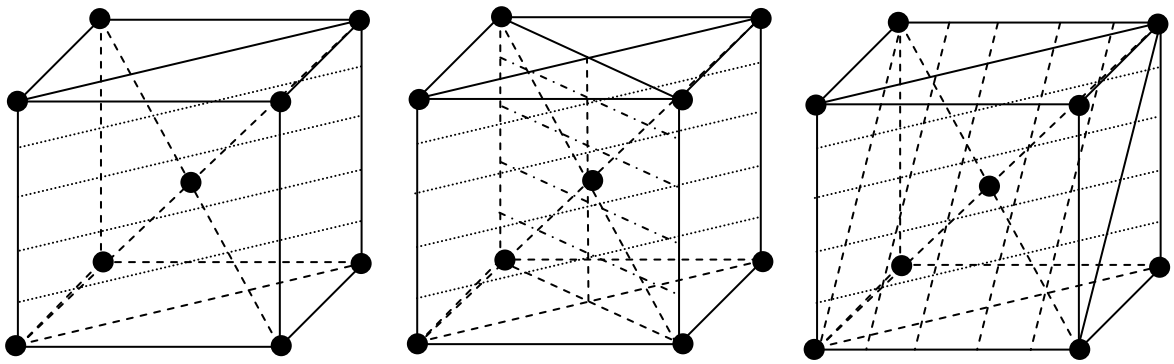

(a) (b) (c)

Figure 1 shows the schematic bcc crystal structure, with (a) parallel {110} planes, (b) two perpendicular {110} planes and (c) two {110} planes with 60 °angle.

When two α variants, VA and VB, are parallel to each other, let the (0001) plane in the two variants represented on a (110) projection in β $(00\bar{1})$ stereographic projection. Meanwhile, superpose one of $<11\bar{2}0>$ variants in VA on $(\bar{1}1\bar{1})$ in (110) plane's trace line, and one of $<11\bar{2}0>$ variants in VB on $(1\bar{1}\bar{1})$ in the same trace line. As a result, the other two $<11\bar{2}0>$ variants in VA and VB can be plotted in the trace line accordingly, based on the 60 °angle between each variant and the relationship between point projection in pole figure and its actual direction vector, which is discussed in Appendix 2. The whole projection is

illustrated in fig. 2 and the resulting angles between <11$\bar{2}$0> in each variant is summarised in table 1.

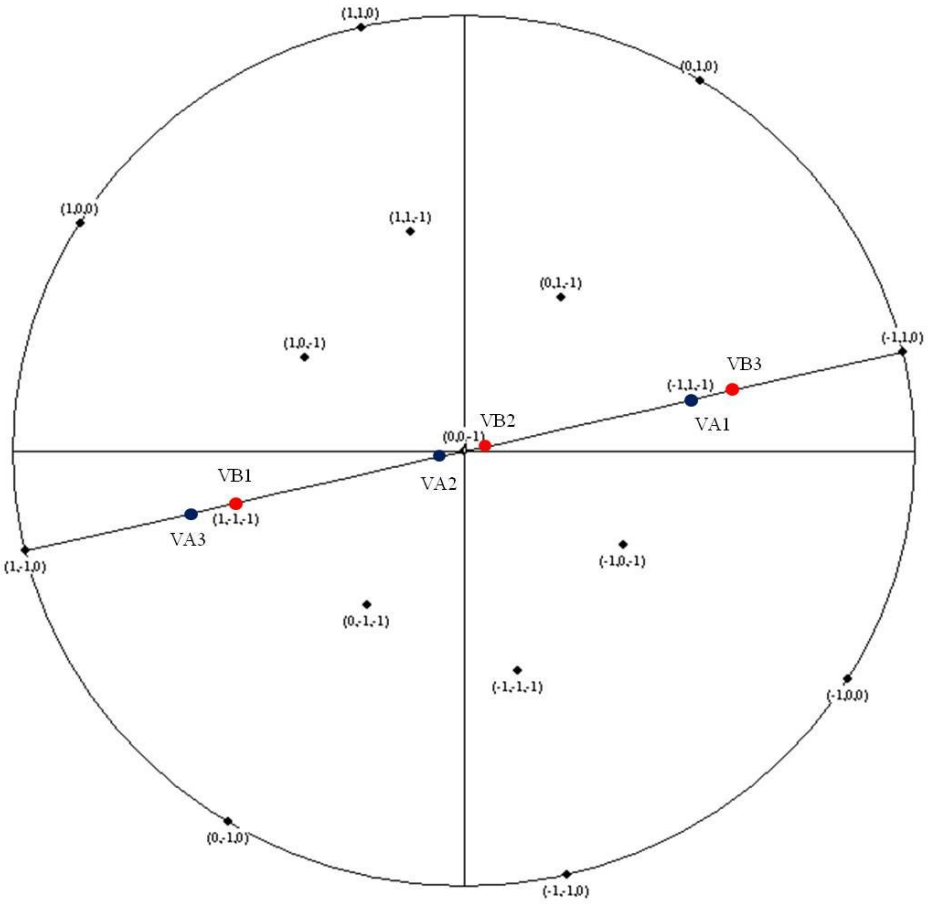

Figure 2 The stereographic projection of bcc structure in (00$\bar{1}$) pole with the (110) trace line and <11$\bar{2}$0> projections in both Burgers α variants.

0 °	VA<11$\bar{2}$0>_1	VA<11$\bar{2}$0>_2	VA<11$\bar{2}$0>_3
VB<11$\bar{2}$0>_1	70.6	49.4	10.6
VB<11$\bar{2}$0>_2	49.4	10.6	70.6
VB<11$\bar{2}$0>_3	10.6	70.6	49.4

Table 1 Angles between <11$\bar{2}$0> in each Burgers α variant when the angle between (0001) in each variant is 0 °.

If the first <11$\bar{2}$0> variant in VB is also superposed to ($\bar{1}$1$\bar{1}$), the two α variants are exactly imposed. Therefore, the two are actually one α variant.

When two α variants, VA and VB, are perpendicular to each other, let the (0001) in VA superposed to (110) projection in β (00$\bar{1}$) stereographic projection and (0001) in VB to ($\bar{1}$10). Meanwhile, make one of <11$\bar{2}$0> variants in VA superposed to ($\bar{1}$1$\bar{1}$) in (110) plane's trace line, and one of <11$\bar{2}$0> variants in VB superposed to (11$\bar{1}$) in ($\bar{1}$10) plane's trace line. As a result, the other two <11$\bar{2}$0> variants in VA and VB can also be plotted in their individual trace line accordingly. The whole projection is illustrated in fig. 3 and the resulting angles between <11$\bar{2}$0> in each α variant is summarised in table 2.

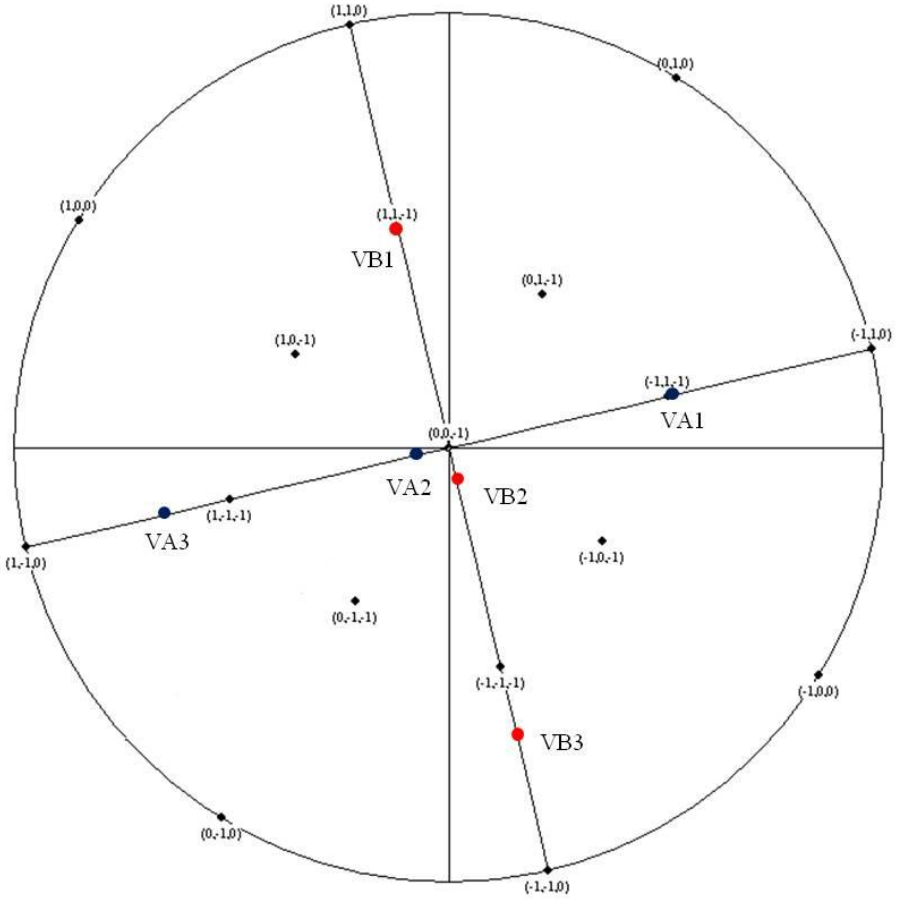

Figure 3 The stereographic projection of bcc structure in (00$\bar{1}$) pole with the (110) and ($\bar{1}$ 10) trace lines and <11$\bar{2}$ 0> projections in both Burgers α variants.

90 °	VA<11$\bar{2}$ 0>_1	VA<11$\bar{2}$ 0>_2	VA<11$\bar{2}$ 0>_3
VB<11$\bar{2}$ 0>_1	70.5	54.9	76.0
VB<11$\bar{2}$ 0>_2	54.9	7.5	65.4
VB<11$\bar{2}$ 0>_3	76.0	65.4	79.9

Table 2 Angles between <11$\bar{2}$ 0> in each Burgers α variant when the angle between (0001) in each variant is 90 °.

Actually, the first <11$\bar{2}$ 0> variant in VB can also be superposed to ($\bar{1}$ 1$\bar{1}$) projection in fig. 3, but because of the symmetry, there is no difference in the resulting angles between <11$\bar{2}$ 0> in each α variant.

When the angle between (0001) in each α variant is 60°, the situation is a little bit complicated, since there are three possibilities in arranging the parallelism between <11$\bar{2}$ 0> in α and <111> in β in each Burgers α, as illustrated in fig. 4-6.

Fig. 4 shows the first possibility, where β stereographic projection is used in the pole ($\bar{1}$ $\bar{1}$ $\bar{1}$), therefore, {110} variants with 60 ° angle can be presented in the big circle. In this stereographic projection, (0001) in VA is superposed to (01$\bar{1}$) and (0001) in VB to ($\bar{1}$ 10). In this way, the angle between (0001) in α variant VA and VB is 60°. Then, the first <11$\bar{2}$ 0> variants in both VA and VB are superposed to ($\bar{1}$ $\bar{1}$ $\bar{1}$) and the other two <11$\bar{2}$ 0> variants in each α variant can be plotted as shown in fig. 4. In case of this situation, the angles between the <11$\bar{2}$ 0> in each α variant are calculated and summarised in table. 3.

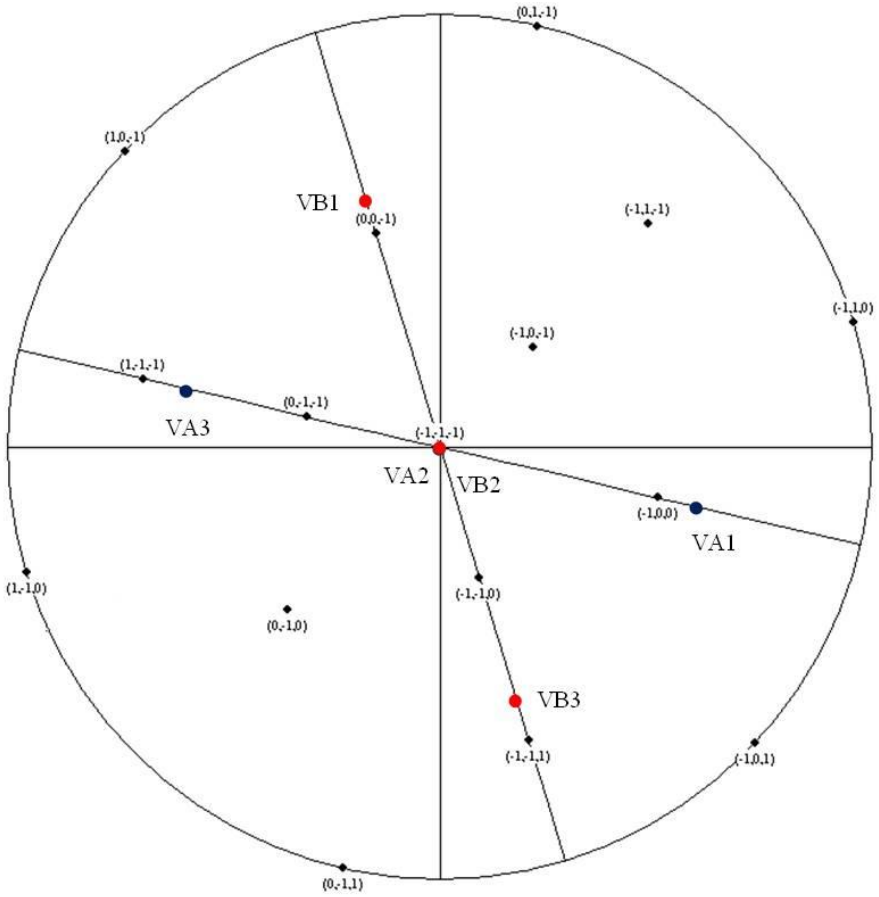

Figure 4 The stereographic projection of bcc structure in $(\bar{1}\,\bar{1}\,\bar{1})$ pole with the $(01\bar{1})$ and $(\bar{1}\,10)$ trace lines and $<11\bar{2}\,0>$ projections in both Burgers α variants. In this situation, one of the $<11\bar{2}\,0>$ in both VA and VB variants are superposed to $(\bar{1}\,\bar{1}\,\bar{1})$ in β.

60 °_1	VA$<11\bar{2}\,0>$_1	VA$<11\bar{2}\,0>$_2	VA$<11\bar{2}\,0>$_3
VB$<11\bar{2}\,0>$_1	0	60.0	60.0
VB$<11\bar{2}\,0>$_2	60.0	51.3	82.8
VB$<11\bar{2}\,0>$_3	60.0	82.8	51.3

Table 3 The first possibility for the angles between $<11\bar{2}\,0>$ in each Burgers α variant when the angle between (0001) in each variant is 60 °.

The arrangement for the second possibility is shown in fig. 5. The same β stereographic projection and the same trace lines from $(01\bar{1})$ and $(\bar{1}10)$ are used. To different from the situation shown in fig. 4, one of the $<11\bar{2}0>$ in VB is arranged to be parallel to $(\bar{1}\,\bar{1}1)$, but not $(\bar{1}\,\bar{1}\,\bar{1})$. In such a case, the resulting angles between $<11\bar{2}0>$ in each α variant are calculated and summarised in table. 4.

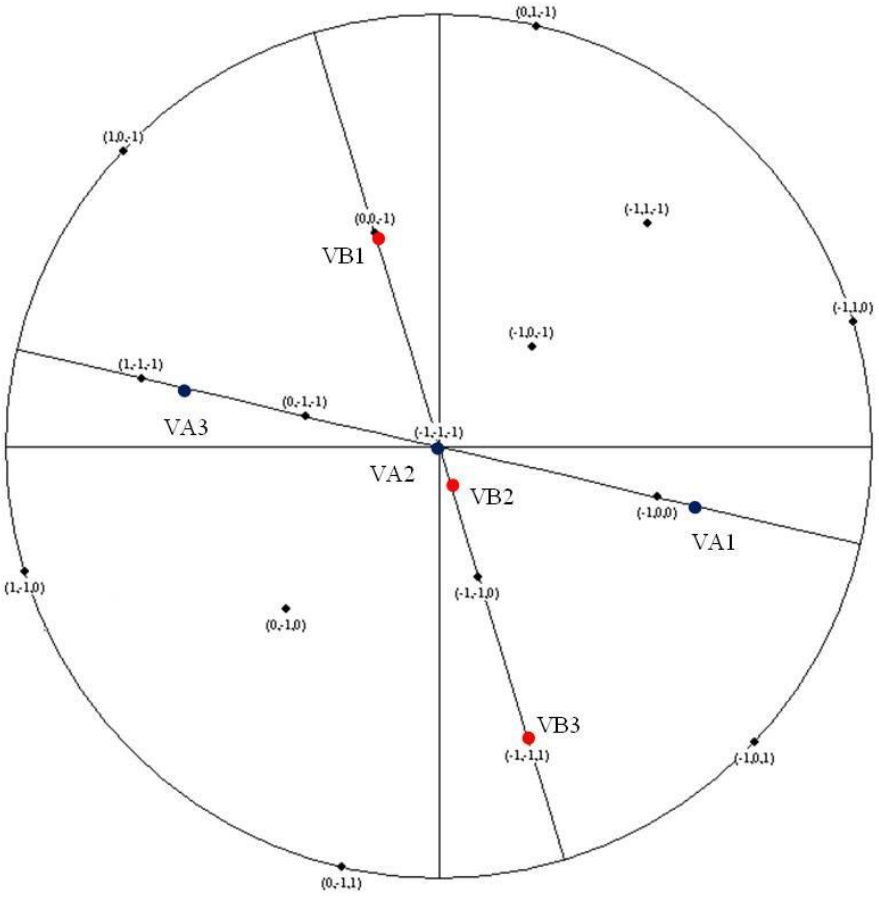

Figure 5 The stereographic projection of bcc structure in $(\bar{1}\,\bar{1}\,\bar{1})$ pole with the $(01\bar{1})$ and $(\bar{1}10)$ trace lines and $<11\bar{2}0>$ projections in both Burgers α variants. In this situation, one of the $<11\bar{2}0>$ in VA is parallel to $(\bar{1}\,\bar{1}\,\bar{1})$ and the $<11\bar{2}0>$ in VB to $(\bar{1}11)$.

60°_2	VA<11$\bar{2}$0>_1	VA<11$\bar{2}$0>_2	VA<11$\bar{2}$0>_3
VB<11$\bar{2}$0>_1	70.5	76.0	54.9
VB<11$\bar{2}$0>_2	10.5	65.6	55.2
VB<11$\bar{2}$0>_3	49.5	49.2	89.7

Table 4 The second possibility for the angles between <11$\bar{2}$0> in each Burgers α variant when the angle between (0001) in each variant is 60°.

The last possibility is through the arrangement of <11$\bar{2}$0> in each α variant like what fig. 5 shows. In this situation, one of the <11$\bar{2}$0> variants in VA is arranged to be parallel to (1$\bar{1}$ $\bar{1}$) and to ($\bar{1}$11) in VB. For this arrangement, the angles between <11$\bar{2}$0> in each α variant are also calculated and summarised in table 5.

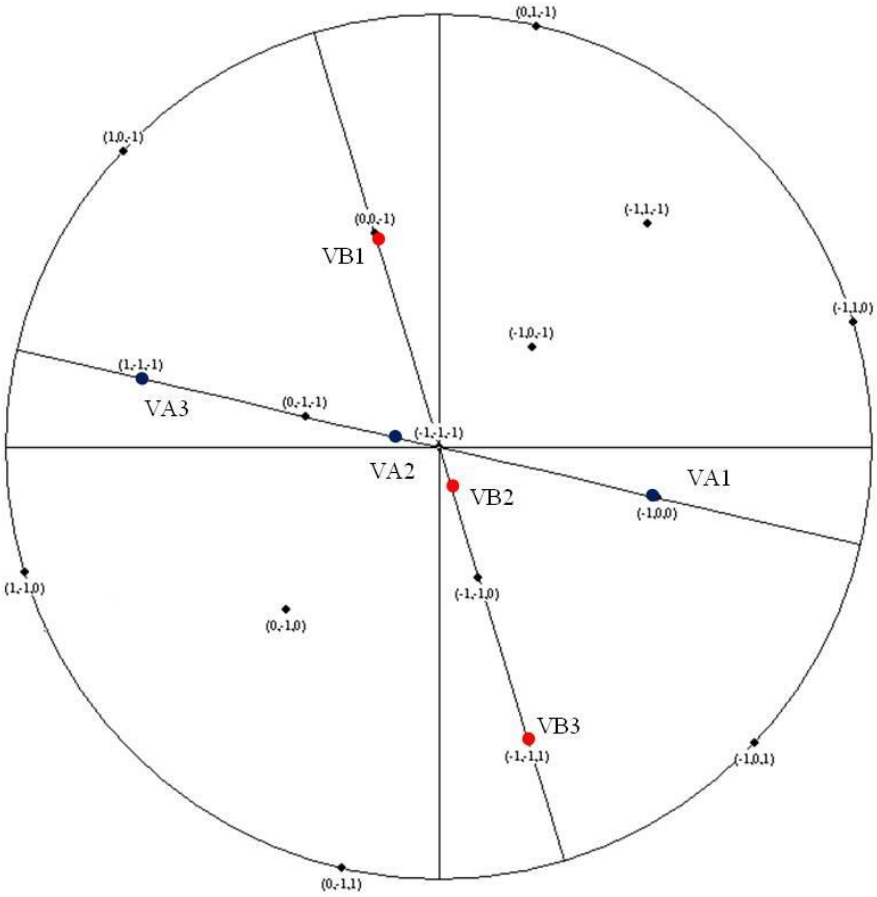

Figure 5 The stereographic projection of bcc structure in $(\bar{1}\,\bar{1}\,\bar{1})$ pole with the $(01\bar{1})$ and $(\bar{1}\,10)$ trace lines and $<11\bar{2}\,0>$ projections in both Burgers α variants. In this situation, one of the $<11\bar{2}\,0>$ in VA is parallel to $(1\bar{1}\,\bar{1})$ and the $<11\bar{2}\,0>$ in VB to $(\bar{1}\,11)$.

60 °_3	VA$<11\bar{2}\,0>$_1	VA$<11\bar{2}\,0>$_2	VA$<11\bar{2}\,0>$_3
VB$<11\bar{2}\,0>$_1	70.6	76.0	54.9
VB$<11\bar{2}\,0>$_2	76.0	18.2	44.9
VB$<11\bar{2}\,0>$_3	54.9	44.9	82.4

Table 4 The third possibility for the angles between $<11\bar{2}\,0>$ in each Burgers α variant when the angle between (0001) in each variant is 60 °.

REFERENCES

1. Westbrook J.H., *Intermetallic Compounds*. 1967, New York: John Wiley & Sons, Inc.
2. Schulze G.E.R., *Metallphysik*. 1967, Berlin: Akademie - Verlag.
3. http://www.kmm-vin.eu, in *Intermetallics*, European Virtual Institute on Knowledge-Based Multifunctional Materials AISBL.
4. Djanarthany S., Viala J.C., and Bouix J., *An overview of monolithic titanium aluminides based on Ti3Al and TiAl.* Materials Chemistry and Physics, 2001. **72**(3): p. 301-319.
5. Zhang W.J., Reddy B.V., and Deevi S.C., *Physical properties of TiAl-base alloys.* Scripta Materialia, 2001. **45**(6): p. 645-651.
6. Mishin Y. and Herzig C., *Diffusion in the Ti-Al system.* Acta Materialia, 2000. **48**(3): p. 589-623.
7. Herzig C., Przeorski T., and Mishin Y., *Self-diffusion in γ-TiAl: an experimental study and atomistic calculations.* Intermetallics, 1999. **7**(3-4): p. 389-404.
8. Sprengel W., Oikawa N., and Nakajima H., *Single-phase interdiffusion in TiAl.* Intermetallics, 1996. **4**(3): p. 185-189.
9. Lapin J., *TiAl based alloys: present status and future perspectives.* Metals, 2009. **19-21**(5): p. 1-12.
10. Christoph Leyens M.P., ed. *Titanium and Titanium Alloys: Fundamentals and Applications*. 2005, Wiley-VCH Verlag GmbH & Co. KGaA: Weinheim.
11. Wu X., *Review of alloy and process development of TiAl alloys.* Intermetallics, 2006. **14**(10-11): p. 1114-1122.
12. Appel F., et al., *Recent progress in the development of gamma titanium aluminide alloys.* Advanced Engineering Materials, 2000. **2**(11): p. 699-720.
13. Jarvis D.J. and Voss D., *IMPRESS Integrated Project--An overview paper.* Materials Science and Engineering: A, 2005. **413-414**: p. 583-591.
14. Yamaguchi M., Inui H., and Ito K., *High-temperature structural intermetallics.* Acta Materialia, 2000. **48**(1): p. 307-322.
15. Inkson B.J., Boothroyd C.B., and Humphreys C.J., *Boride morphology in A (Fe, V, B) Ti-alloy containing B2-phase.* Acta Metallurgica et Materialia, 1995. **43**(4): p. 1429-1438.
16. Kitkamthorn U., Zhang L.C., and Aindow M., *The structure of ribbon borides in a Ti-44Al-4Nb-4Zr-1B alloy.* Intermetallics, 2006. **14**(7): p. 759-769.
17. Cheng T.T., *The mechanism of grain refinement in TiAl alloys by boron addition -- an alternative hypothesis.* Intermetallics, 2000. **8**(1): p. 29-37.
18. De Graef M., Löfvander J.P.A., and Levi C.G., *The structure of complex monoborides in γ-TiAl alloys with Ta and B additions.* Acta Metallurgica et Materialia, 1991. **39**(10): p. 2381-2391.
19. Valencia J.J., et al., *In-situ-grown reinforcements for titanium aluminides.* Materials Science and Engineering: A, 1991. **144**(1-2): p. 25-36.
20. Hu D., *Effect of composition on grain refinement in TiAl-based alloys.* Intermetallics, 2001. **9**(12): p. 1037-1043.

21. De Graef M., et al., *The evolution of metastable B_f borides in a Ti---Al---B alloy.* Acta Metallurgica et Materialia, 1992. **40**(12): p. 3395-3406.
22. Godfrey A.B. and Loretto M.H., *The nature of complex precipitates associated with the addition of boron to a γ-based titanium aluminide.* Intermetallics, 1996. **4**(1): p. 47-53.
23. Chen C.L., et al., *Orientation relationship between TiB precipitate and γ - TiAl phase.* Scripta Materialia, 2007. **56**: p. 441-444.
24. Chen C.L., et al., *Orientation relationships between TiB(B27), B2 and Ti_3Al phases.* Journal of Materials Research, 2009. **24**(5): p. 1688-1692.
25. Murray J.L., *The Al-Ti (Aluminum-Titanium) System*. Phase Diagrams of Binary Titanium Alloys. 1987: ASM.
26. Okamoto H., *Al-Ti (Aluminum-Titanium).* Journal of Phase Equibibria, 1993. **14**(6): p. 764.
27. Okamoto H., *Al-Ti (aluminum-titanium).* Journal of Phase Equilibria, 2000. **21**: p. 311-311.
28. Julius C. Schuster M.P., *Reassessment of binary Aluminium-Titanium phase diagram.* Journal of Phase Equilibria and Diffusion, 2006. **27**(3): p. 255-277.
29. Raghaven V., *Al-Ti (Aluminum-Titanium).* Journal of Phase Equilibria and Diffusion, 2005. **26**(2): p. 171-172.
30. Zhang G., Blenkinsop P.A., and Wise M.L.H., *Phase transformations in HIPped Ti-48Al-2Mn-2Nb powder during heat-treatments.* Intermetallics, 1996. **4**(6): p. 447-455.
31. Hyman M.E., in *University of California*. 1991, University of California: Santa Barbara.
32. Hyman M.E., et al., *Evolution of boride morphologies in TiAl-B alloys.* Metallurgical Transations A, 1991. **22A**: p. 1647-1662.
33. Burgers W.G., Physica, 1934. **1**.
34. Dahmen U., *Orientation relationship in precipitation systems.* Acta Metallurgica, 1982. **30**: p. 63-73.
35. Karthikeyan T., Saroja S., and Vijayalakshmi M., *Evaluation of misorientation angle-axis set between variants during transformation of bcc to hcp phase obeying Burgers orientation relation.* Scripta Materialia, 2006. **55**(9): p. 771-774.
36. Gey N. and Humbert M., *Specific analysis of EBSD data to study the texture inheritance due to the β to α phase transformation* Journal of Materials Science, 2003. **38**: p. 1289-1294.
37. Blackburn M.J., in *The science, technology and applications of titanium*, R. I. Jaffee and Promisel N.E., Editors. 1970, Pergamon Press: Oxford. p. 633.
38. Nishida M., et al., *Electron microscopy studies of Ti - 47 at. % Al powder produced by plasma rotating electrode process.* Scripta Metallurgica et Materialia, 1992. **27**(3): p. 335-340.
39. Valencia J.J., et al., *Solidification microstructure of supercooled Ti-Al alloys containing intermetallic phases.* Acta Metallurgica, 1989. **37**(9): p. 2517-2530.
40. Gouma P.I., Saunders N., and Loretto M.H., *Microstructural evolution and microsegregation of gas atomised powders of a TiAI based alloy.* Materials Science and Technology, 1996. **12**: p. 823-830.
41. Hyman M., et al., *Microstructure evolution in TiAl alloys with B additions: Conventional solidification.* Metallurgical and Materials Transactions A, 1989. **20**(9): p. 1847-1859.

42. Larsen D.E., et al., *Investment-cast processing of XD^{TM} near-γ titanium aluminides.* Materials Science and Engineering: A, 1991. **144**(1-2): p. 45-49.
43. Larson E., *Effect of XD^{TM} TiB_2 Volume Fraction on the Microstructure of a Cast Near-Gamma Titanium Aluminide Alloy.* MRS Symposium R, 1990. **194**(Spring): p. 285-294.
44. Inkson B., J., Boothroyd C., B., and Humphreys C., J., *Boron segregation in a (Fe, V, B) TiAl based alloy.* J. Phys. IV France, 1993. **03**(C7): p. C7-397-C7-402.
45. Godfrey A.B., *Grain Refinement of a Gamma-Based Titanium Aluminide Using Microalloy Additions*, in *The School of Metallurgy and Materials*. 1996, The University of Birmingham: Birmingham, UK.
46. Hu D., *Effect of boron addition on tensile ductility in lamellar TiAl alloys.* Intermetallics, 2002. **10**(9): p. 851-858.
47. Imayev R.M., et al., *Alloy design concepts for refined gamma titanium aluminide based alloys.* Intermetallics, 2007. **15**(4): p. 451-460.
48. Hecht U., et al., *Grain refinement by low boron additions in niobium-rich TiAl-based alloys.* Intermetallics, 2008. **16**(8): p. 969-978.
49. Drevermann A., et al., *Online process control for directional solidification by ultrasonic pulse echo technique.* Ultrasonics, 2004. **42**(1-9): p. 105-108.
50. Yong Won Kim and Dimiduk D.M., *Progress in the understanding of gamma titanium aluminides.* JOM, 1991(August): p. 40-47.
51. Kawabata T., Tamura T., and Izumi O., *Effect of Ti/Al ratio and Cr, Nb, and Hf additions on material factors and mechanical properties in TiAl.* Metallurgical and Materials Transactions A, 1993. **24**(1): p. 141-150.
52. Tokuzou Tsujimoto, Kenki Hashimoto, and Nobuki M., *Alloy design for improvement of ductility and workability of alloys based on intermetallic compound TiAl.* Materials Transactions, JIM, 1992. **33**(11): p. 989-1003.
53. Huang S.-C. and Hall E.L., Materials Research Society Symposium Processings, 1989. **133**: p. 373-383.
54. Morinaga M., et al., *Electronic effect on the ductility of alloyed TiAl compound.* Acta Metallurgica et Materialia, 1990. **38**(1): p. 25-29.
55. Song Y., et al., *Theoretical investigation of ductilizing effects of alloying elements on TiAl.* Intermetallics, 1998. **6**(3): p. 157-165.
56. Kawabata T., Tamura T., and Izumi O., in *High temperature ordered intermetallic alloys III*, C.T.Liu A.I.T., N.S. Stoloff, C.C. Koch, Editor. 1989, MRS: Pittsburpg. p. 329-334.
57. Jinlong Y., et al., *Site preference of ternary additions in gamma -TiAl: A density-functional cluster-model study.* Physical Review B, 1992. **46**(21): p. 13709.
58. Huang S.-C. and Hall E., *The effects of Cr additions to binary TiAl-base alloys.* Metallurgical and Materials Transactions A, 1991. **22**(11): p. 2619-2627.
59. Shida Y. and Anada H., *The influence of ternary element addition on the oxidation behaviour of TiAl intermetallic compound in high temperature air.* Corrosion Science, 1993. **35**(5-8): p. 945-953.
60. Karabi Das P.C., Siddhartha Das, *The Al - O - Ti (Aluminum - Oxygen - Titanium) system.* Journal of Phase Equibibria, 2002. **23**(6): p. 525-536.
61. Park H.S., et al., *Refinement of the lamellar structure in TiAl-BASED intermetallic compound by addition of carbon.* Scripta Materialia, 1999. **41**(11): p. 1197-1203.

62. Loiseau A. and Lasalmonie A., *Influence of the thermal stability of TiAl on its creep behaviour at high temperatures.* Materials Science and Engineering, 1984. **67**(2): p. 163-168.
63. Nishiyama Y., et al., in *HIgh Temperature Aluminides and Intermetallics*, S.H. Whang C.T.L., D.P. Pope, J.O. Stiegler, Editor. 1990, TMS: Warrendale, PA, USA. p. 557.
64. Maki K., et al., *Effect of silicon and niobium on oxidation resistance of TiAl intermetallics.* Materials Science and Engineering: A, 1992. **153**(1-2): p. 591-596.
65. Chen Y.Y., Li B.H., and Kong F.T., *Microstructural refinement and mechanical properties of Y-bearing TiAl alloys.* Journal of Alloys and Compounds, 2008. **457**(1-2): p. 265-269.
66. Appel F., Oehring M., and Wagner R., *Novel design concepts for gamma-base titanium aluminide alloys.* Intermetallics, 2000. **8**(9-11): p. 1283-1312.
67. Wayne E. Voice M.H., Edward F.J. Shelton, Xinhua Wu, *Gamma titanium aluminide, TNB.* Intermetallics, 2005. **13**: p. 959-964.
68. Hu D., Huang A.J., and Wu X., *On the massive phase transformation regime in TiAl alloys: The alloying effect on massive/lamellar competition.* Intermetallics, 2007. **15**(3): p. 327-332.
69. Saage H., et al., *Microstructures and tensile properties of massively transformed and aged Ti46Al8Nb and Ti46Al8Ta alloys.* Intermetallics. **17**(1-2): p. 32-38.
70. Gebauer K., *Performance, tolerance and cost of TiAl passenger car valves.* Intermetallics, 2006. **14**(4): p. 355-360.
71. Noda T., *Application of cast gamma TiAl for automobiles.* Intermetallics, 1998. **6**(7-8): p. 709-713.
72. Karthikeyan S., et al., *Mechanisms and effect of microstructure on creep of TiAl-based alloys.* Materials Science and Engineering A, 2002. **329-331**: p. 621-630.
73. Loria E.A., *Quo vadis gamma titanium aluminide.* Intermetallics, 2001. **9**(12): p. 997-1001.
74. Harding R.A. and Wickins M., *Temperature measurements during induction skull melting of titanium aluminides.* Materials Science and Technology, 2003. **19**(September): p. 1235-1246.
75. Brian James W., *New shaping methods for powder metallurgy components.* Materials & Design. **8**(4): p. 187-197.
76. Jinka A.G.K., *A finite-element prediction of densification kinetics during the hot isostatic pressing of metal powder compacts.* Journal of Materials Processing Technology, 1996. **57**(3-4): p. 382-392.
77. Bocanegra-Bernal M.H., *Hot Isostatic Pressing (HIP) technology and its applications to metals and ceramics.* Journal of Materials Science, 2004. **39**(21): p. 6399-6420.
78. Wang J.N. and Xie K., *Grain size refinement of a TiAl alloy by rapid heat treatment.* Scripta Materialia, 2000. **43**(5): p. 441-446.
79. Wen C.E. and Chen C.Q., *New microstructure-property approach: Quenching/tempering treatment in gamma TiAl alloy.* Scripta Metallurgica et Materialia, 1995. **33**(8): p. 1283-1288.
80. Clemens H., et al., *Grain refinement in [gamma]-TiAl-based alloys by solid state phase transformations.* Intermetallics, 2006. **14**(12): p. 1380-1385.
81. Hu D., Wu X., and Loretto M.H., *Advances in optimisation of mechanical properties in cast TiAl alloys.* Intermetallics, 2005. **13**(9): p. 914-919.

82. Gerling R., Clemens H., and Schimansky F., *Powder Metallurgical Processing of Intermetallic Gamma Titanium Aluminides.* Advanced Engineering Materials, 2004. **6**(1-2): p. 23-38.
83. Thomas M., Raviart J.L., and Popoff F., *Cast and PM processing development in gamma aluminides.* Intermetallics, 2005. **13**(9): p. 944-951.
84. Habel U. and McTiernan B.J., *HIP temperature and properties of a gas-atomized γ-titanium aluminide alloy.* Intermetallics, 2004. **12**(1): p. 63-68.
85. Préauchat B., Popoff F., and Thomas M., *Characterization of HIPed and Extruded Powder Metallurgy Titanium Aluminide.* Advanced Engineering Materials, 2002. **4**(3): p. 133-138.
86. Fuchs G., *The effect of processing on the hot workability of Ti-48Al-2Nb-2Cr alloys.* Metallurgical and Materials Transactions A, 1997. **28**(12): p. 2543-2553.
87. Mashl S., Hebeisen J., and Hjorth C., *Producing large P/M near-net shapes using hot isostatic pressing.* JOM Journal of the Minerals, Metals and Materials Society, 1999. **51**(7): p. 29-31.
88. Seliverstov D., et al., in *Hot isostatic pressing*, Delaey L. and Tas H., Editors. 1994, Elsevier Science BV: Amsterdam. p. 555-560.
89. Raisson G. and Samarov V., in *Hot isostatic pressing*. 1996, Materials Park, OH, ASM International: Andover, MA, USA. p. 133-137.
90. Dellis C., et al., in *Hot isostatic pressing*. 1996, Materials Park, OH, ASM International: Andover, MA, USA. p. 75-78.
91. Davidson A., et al., *Influence of surface layer on properties of hipped Ti-6Al-4V.* Materials Science and Technology, 2006. **22**: p. 553-560.
92. Hsiung L.M. and Nieh T.G., *Microstructures and properties of powder metallurgy TiAl alloys.* Materials Science and Engineering A, 2004. **364**(1-2): p. 1-10.
93. Angelo P.C. and Subramanian R., *Powder Metallurgy: science, technology and applications*. 2008: PHI Learning Pvt. Ltd.
94. Gerling R., et al., *Structural characterization and tensile properties of a high niobium containing gamma TiAl sheet obtained by powder metallurgical processing.* Intermetallics, 2004. **12**(3): p. 275-280.
95. Maziasz P. and Liu C., *Development of ultrafine lamellar structures in two-phase &λτ;ι&γτ;©&λτ;/ι&γτ; -TiAl alloys.* Metallurgical and Materials Transactions A, 1998. **29**(1): p. 105-117.
96. Fuchs G.E., *Effect of W additions to Ti-48Al-2Nb-2Cr alloys.* Materials Science and Engineering A, 1995. **192-193**(Part 2): p. 707-715.
97. Kim Y.-W., *Microstructural evolution and mechanical properties of a forged gamma titanium aluminide alloy.* Acta Metallurgica et Materialia, 1992. **40**(6): p. 1121-1134.
98. Jones S.A. and Kaufman M.J., *Phase equilibria and transformations in intermediate titanium---aluminum alloys.* Acta Metallurgica et Materialia, 1993. **41**(2): p. 387-398.
99. Denquin A. and Naka S., *Phase transformation mechanisms involved in two-phase TiAl-based alloys--I. Lambellar structure formation.* Acta Materialia, 1996. **44**(1): p. 343-352.
100. Denquin A. and Naka S., *Phase transformation mechanisms involved in two-phase TiAl-based alloys--II. Discontinuous coarsening and massive-type transformation.* Acta Materialia, 1996. **44**(1): p. 353-365.

101. Massalski T.B., *Massive transformation revisited.* Metallurgical and Materials Transactions A, 2002. **33A**(August): p. 2277-2283.
102. Hu D. and Botten R.R., *Phase transformations in some TiAl-based alloys.* Intermetallics, 2002. **10**(7): p. 701-715.
103. Chen G.L., et al., *Microsegregation in high Nb containing TiAl alloy ingots beyond laboratory scale.* Intermetallics, 2007. **15**(5-6): p. 625-631.
104. Huang Z.W., *Inhomogeneous microstructure in highly alloyed cast TiAl-based alloys, caused by microsegregation.* Scripta Materialia, 2005. **52**(10): p. 1021-1025.
105. Singh A.K., Muraleedharan K., and Banerjee D., *Solidification structure in a cast γ alloy.* Scripta Materialia, 2003. **48**(6): p. 767-772.
106. Larson D.J., Liu C.T., and Miller M.K., *Boron solubility and boride compositions in α_2 + γ titanium aluminides.* Intermetallics, 1997. **5**(6): p. 411-414.
107. Hu D., et al., *The effect of boron and alpha grain size on the massive transformation in Ti-46Al-8Nb-xB alloys.* Intermetallics, 2006. **14**(7): p. 818-825.
108. Li Z.X. and Cao C.C., *Effect of minor boron addition on phase transformation and properties of Ti-47.5Al-2Cr-2Nb alloy.* Intermetallics, 2005. **13**: p. 251-256.
109. Menand A., Huguet A., and Neac-Partaix A., *Interstitial solubility in γ and α_2 phases of TiAl-based alloys.* Acta Materialia, 1996. **44**(12): p. 4729-4737.
110. Jones C.Y., Luecke W.E., and Copland E., *Neutron diffraction study of oxygen dissolution in α_2-Ti_3Al.* Intermetallics, 2006. **14**(1): p. 54-60.
111. Huang A., et al., *The role of oxygen content and cooling rate on transformations in TiAl-based alloys.* Intermetallics, 2006. **14**(7): p. 838-847.
112. Lefebvre W., et al., *Atom probe study of phase transformations in a Ti-48 at.% Al alloy.* Materials Science and Engineering A, 2002. **327**(1): p. 40-46.
113. Lefebvre W., Menand A., and Loiseau A., *Influence of oxygen on phase transformations in a Ti-48 At. pct Al alloy.* Metallurgical and Materials Transactions A, 2003. **34**(10): p. 2067-2075.
114. Hemker K.J., Viguier B., and Mills M.J., *Dislocation core structures in the ordered intermetallic alloy TiAl.* Materials Science and Engineering: A, 1993. **164**(1-2): p. 391-394.
115. Appel F. and Wagner R., *Microstructure and deformation of two-phase γ-titanium aluminides.* Materials Science and Engineering: R: Reports, 1998. **22**(5): p. 187-268.
116. Chan K.S. and Shih D.S., *Fundamental aspects of figue and fracture in a TiAl sheet alloy.* Metallurgical and Materials Transactions A, 1998. **29A**(January): p. 73-87.
117. Hazzledine P.M., et al., *Internal stress in TiAl based lamellar composites.* MRS 1992. **273**: p. 81.
118. Appel F., Beaven P.A., and Wagner R., *Deformation processes related to interfacial boundaries in two-phase [gamma]-titanium aluminides.* Acta Metallurgica et Materialia, 1993. **41**(6): p. 1721-1732.
119. Yoo M. and Fu C., *Physical constants, deformation twinning, and microcracking of titanium aluminides.* Metallurgical and Materials Transactions A, 1998. **29**(1): p. 49-63.
120. Christian J.W. and Mahajan S., *Deformation twinning.* Progress in Materials Science, 1995. **39**(1-2): p. 1-157.
121. Mecking H., Hartig C., and Kocks U.F., *Deformation modes in γ-TiAl as derived from the single crystal yield surface.* Acta Materialia, 1996. **44**(4): p. 1309-1321.

122. Appel F., et al., *Thermally activated deformation mechanisms in micro-alloyed two-phase titanium amminide alloys.* Materials Science and Engineering A, 1997. **233**(1-2): p. 1-14.
123. Wardle S., Phan I., and Hug G., *Analysis of twin intersections in TiAl.* Philosophical Magazine A, 1993. **67**(2): p. 497 - 514.
124. Farenc S., Coujou A., and Couret A., *An in situ study of twin propagation in TiAl.* Philosophical Magazine A, 1993. **67**(1): p. 127 - 142.
125. Jin Z. and Bieler T.R., *An in-situ observation of mechanical twin nucleation and propagation in TiAl.* Philosophical Magazine A, 1995. **71**(5): p. 925 - 947.
126. Viswanathan G.B., Mills M.J., and Vasudevan V.K., *Microstructual effects on the tensile properties and deformation behavior of a Ti-48Al gamma titanium alunimide.* Metallurgical and Materials Transactions A, 2003. **34A**: p. 2113-2127.
127. Zheng R.T., et al., *The ambient temperature tensile behavior of duplex γ-TiAl-based alloys.* Materials Science and Engineering A, 2003. **362**(1-2): p. 192-199.
128. Kong F.T., Chen Y.Y., and Li B.H., *Influence of yttrium on the high temperature deformability of TiAl alloys.* Materials Science and Engineering: A, 2009. **499**(1-2): p. 53-57.
129. Kim Y.-W., *Effects of microstructure on the deformation and fracture of γ-TiAl alloys.* Materials Science and Engineering A, 1995. **192-193**(Part 2): p. 519-533.
130. Cao G., et al., *The relationships of microstructure and properties of a fully lamellar TiAl alloy.* Intermetallics, 2000. **8**(5-6): p. 647-653.
131. Hu D., Jiang H., and Wu X., *Microstructure and tensile properties of cast Ti-44Al-4Nb-4Hf-0.1Si-0.1B alloy with refined lamellar microstructures.* Intermetallics, 2009. **17**(9): p. 744-748.
132. Moll J.H. and McTiernan B.J., *PM TiAl alloys: the sky's the limit.* Metal Powder Report, 2000. **55**(1): p. 18-22.
133. Liu C.T., et al., *Tensile properties and fracture toughness of TiAl alloys with controlled microstructures.* Intermetallics, 1996. **4**(6): p. 429-440.
134. Zhang G., Blenkinsop P.A., and Wise M.L.H., *Hot-isostatic-pressing/microstructure/property relationships in a powder metallurgy γ TiAl alloy*, in *Titanium '95: Science and Technology*, Blenkinsop P.A., Evans W.J., and Flower H.M., Editors. 1995, The Insititute of Materials: Birmingham, UK. p. 542.
135. Zhang G., *Processing/structure/property relationships in powder and cast γ titanium aluminide*, in *School of Metallurgy and Materials*. 1996, The University of Birmingham: Birmingham.
136. Inui H., et al., *Room-temperature tensile deformation of polysynthetically twinned (PST) crystals of TiAl.* Acta Metallurgica et Materialia, 1992. **40**(11): p. 3095-3104.
137. Cheng T.T., Willis M.R., and Jones I.P., *Effect of major alloying additions on the microstructure and mechanical properties of gamma-TiAl.* Intermetallics, 1999. **7**: p. 89-99.
138. Zhang W.J., Deevi S.C., and Chen G.L., *On the origin of superior high strength of Ti-45Al-10Nb alloys.* Intermetallics, 2002(10): p. 403-406.
139. Botten R.R., *The development of gamma titanium aluminide Ti-44Al-8Nb-1B*, in *IRC in Materials for High Performance Applications*. 2000, The University of Birmingham: Birmingham.
140. Thomas M., et al., *Effects of exposure at 700^{0}C on RT tensile properties in a PM γ-TiAl alloy.* Intermetallics. **14**(10-11): p. 1143-1150.

141. Recina V. and Karlsson B., *Tensile properties and microstructure of Ti-48Al-2W-0.5Si gamma-titanium aluminide at tempertures between room temperature and 800^{0}C.* Materials Science and Technology, 1999. **15**: p. 57-66.
142. Chan K.S. and Davidson D.L. Structural Intermetallics, ed. Darolia R., et al. 1993, Warrendale: TMS. 223.
143. Kim Y.-W., *Strength and ductility in TiAl alloys.* Intermetallics, 1998. **6**(7-8): p. 623-628.
144. Chan K.S. and Kim Y.W., *Effects of lamellae spacing and colony size on the fracture resistance of a fully-lamellar TiAl alloy.* Acta Metallurgica et Materialia, 1995. **43**(2): p. 439-451.
145. Hazzledine P.M. and Kad B.K., *Yield and fracture of lamellar γ/α_2 TiAl alloys.* Materials Science and Engineering A, 1995. **192-193**(Part 1): p. 340-346.
146. Lorenz U., Appel F., and Wagner R., *Dislocation dynamics and fracture processes in two-phase titanium aluminide alloys.* Materials Science and Engineering A, 1997. **234-236**: p. 846-849.
147. Campbell J.P., Venkateswara Rao K.T., and Ritchie R.O., *The effect of microstructure on fracture toughness and fatigure crack growth behavior in gamma-titanium aluminide based intermetallics.* Metallurgical and Materials Transactions A, 1999. **30A**(March): p. 563-577.
148. Gnanamoorthy R., Mutoh Y., and Mizuhara Y., *Fatigue crack growth behavior of equiaxed, duplex and lamellar microstructure γ-base titanium aluminides.* Intermetallics, 1996. **4**(7): p. 525-532.
149. Chan K., *The fatigue resistance of TiAl-based alloys.* JOM Journal of the Minerals, Metals and Materials Society, 1997. **49**(7): p. 53-58.
150. Hénaff G. and Gloanec A.-L., *Fatigue properties of TiAl alloys.* Intermetallics, 2005. **13**(5): p. 543-558.
151. Sastry SML and HA L., *Fatigue deformation of TiAl base alloys.* Metallurgical Transations A, 1977. **8A**: p. 299-308.
152. Bentley S.A., Mantle A.L., and Aspinwall D.K., *The effect of machining on the fatigue strength of a gamma titanium aluminide intertmetallic alloy.* Intermetallics, 1999. **7**(8): p. 967-969.
153. Vaidya W., Schwalbe K.-H., and Wagner R., *Understanding the fatigue resistance of gamma titanium aluminide,* in *International symposium on gamma titanium aluminides*, Y-W Kim R.W., M Yamaguchi, Editor. 1995, The Minerals, Metals and Meterials Society: Warrendale. p. 867.
154. Sharman A.R.C., et al., *The effects of machined workpiece surface integrity on the fatigue life of γ-titanium aluminide.* International Journal of Machine Tools and Manufacture, 2001. **41**(11): p. 1681-1685.
155. Sharman A.R.C., et al., *Workpiece surface integrity considerations when finish turning gamma titanium aluminide.* Wear, 2001. **249**(5-6): p. 473-481.
156. Wu X., et al., *The role of surface condition, residual stress and microstructure on pre-yield cracking in Ti44Al8Nb1B.* Intermetallics, 2004. **12**(3): p. 281-287.
157. Wright P.K., et al., *Defect behavior in gamma titanium aluminides,* in *Structural intermetallics*, al K.H.e., Editor. 2001, The Minerals, Metals and Materials Society: Snow King Resort. p. 315.
158. Recina V. and Karlsson B., *High temperature low cycle fatigue properties of Ti-48Al-2Cr-2Nb gamma titanium aluminides cast in different dimensions.* Scripta Materialia, 2000. **43**(7): p. 609-615.

159. Recina V. and Karlsson B., *High temperature low cycle fatigue properties of Ti-48Al-2W-0.5Si gamma titanium aluminide.* Materials Science and Engineering: A, 1999. **262**(1-2): p. 70-81.
160. Recina V., Lundström D., and Karlsson B., *Tensile, creep, and low-cycle fatigue behavior of a cast <i>γ</i> -TiAl-based alloy for gas turbine applications.* Metallurgical and Materials Transactions A, 2002. **33**(9): p. 2869-2881.
161. Recina V., *High temperature low cycle fatigue properties of two cast gamma titanium aluminide alloys with refined microstructure.* Materials Science and Technology, 2000. **16**: p. 333-340.
162. Gloanec A.L., et al., *Cyclic deformation mechanisms in a gamma titanium aluminide alloy at room temperature.* Scripta Materialia, 2005. **52**(2): p. 107-111.
163. Umakoshi Y., Yasuda H.Y., and Nakano T., *Plastic anisotropy and fatigue of TiAl PST crystals: a review.* Intermetallics, 1996. **4**(Supplement 1): p. S65-S75.
164. Umakoshi Y., Yasuda H.Y., and Nakano T., *Plastic anisotropy and fracture behavior of cyclically deformed TiAl polysynthetically twinned crystals.* Materials Science and Engineering A, 1995. **192-193**(Part 1): p. 511-517.
165. Nakano T., et al., *Anomalous behaviour of cyclic deformation and fatigue properties of TiAl PST crystals under constant applied stress.* Acta Materialia, 1997. **45**(11): p. 4807-4821.
166. Yasuda H.Y., Nakano T., and Umakoshi Y., *Thermal stability of deformation substructure of cyclically deformed TiAl PST crystals.* Intermetallics, 1996. **4**(4): p. 289-298.
167. Chan K. and Shih D., *Fatigue and fracture behavior of a fine-grained lamellar TiAl alloy.* Metallurgical and Materials Transactions A, 1997. **28**(1): p. 79-90.
168. Choi C., Lee Y.T., and Lee C.S., *Microstructural influence on the fatigue crack propagation of a gamma-TiAl alloy.* Scripta Materialia, 1996. **36**(7): p. 821-827.
169. Gloanec A.L., et al., *Fatigue crack growth behaviour of a gamma-titanium-aluminide alloy prepared by casting and powder metallurgy.* Scripta Materialia, 2003. **49**(9): p. 825-830.
170. Gloanec A.L., et al, *Fatigue properties of a Ti-48Al-2Cr-2Nb alloy produced by casting and powder metallurgy* in *International symposium on gamma titanium aluminides* Kim. Y-W R.A., Clemens. H, Editor. 2003, TMS: San Diego CA. p. 485-492.
171. Lang M., *Explanation of an apparent abnormality in fatigue crack growth rate curves in titanium alloys.* Acta Materialia, 1999. **47**(11): p. 3247-3261.
172. Hénaff G., et al., *Fatigue crack propagation resistance of a Ti48Al2Mn2Nb alloy in the as-cast condition.* Materials Science and Engineering A, 1996. **219**(1-2): p. 212-220.
173. Hénaff G, Tonneau A, and C M., *Near-threshold fatigue crack growth mechanism in TiAl alloys*. Structural intermetallics, ed. Hemker KJ. 2001, Snow King Resort, Jackson Hole: The Minerals, Metals & Materials Society.
174. Rosenberger A.H., *Effect of environment on the fatigue crack growth of gamma titanium aluminide alloys at ambient temperatures.* Scripta Materialia, 2001. **44**(11): p. 2653-2659.
175. Rosenberger A.H., Worth B.D., and Larsen J.M., *Effects of microstructure, temperature and environment on fatigue crack growth in Ti-46.5Al-3Nb-2Cr-0.2W,*

in *Structural intermetallics*, Nathal M.V., et al., Editors. 1997, The Minerals, Metals & Materials Society: Seven Springs, PA. p. 555-561.
176. Hénaff G., Tonneau A., and Mabru C., *Near-threshold fatigue crack growth mechanism in TiAl alloys*, in *Structural Intermetallics*, Hemker K., Editor. 2001, The Minerals, Metals and Materials Society: Snow King Resort, Jackson Hole. p. 571-580.
177. Hénaff G., *Environmentally - asisted fatigue crack growth mechanisms in iron and titanium aluminides*, in *Eighth international fatigue congress*, Blom A.F., Editor. 2002, EMAS: Stockholm, Sweden. p. 689-690.
178. Worth B., Jones J., and Allison J., *Creep deformation in near-γ TiAl: II. influence of carbon on creep deformation in Ti-48Al-1V-0.3C.* Metallurgical and Materials Transactions A, 1995. **26**(11): p. 2961-2972.
179. Oikawa H. and Maruyama K. Gamma Titanium Aluminides, ed. Kim Y.W., Wagner R., and Yamaguchi M. 1995, Warrendale: TMS. 919.
180. Beddoes J., Wallace W., and Zhao L., *Current understanding of creep behaviour of near γ-titanium aluminides.* International Materials Reviews, 1995. **40**: p. 197-217.
181. Lapin J. and Nazmy M., *Microstructure and creep properties of a cast intermetallic Ti-46Al-2W-0.5Si alloy for gas turbine applications.* Materials Science and Engineering A, 2004. **380**(1-2): p. 298-307.
182. Jimenez J.A., et al., *The effect of microstructure on the creep behavior of the Ti-46Al-1Mo-0.2Si alloy.* Intermetallics, 2005. **13**(10): p. 1021-1029.
183. Beddoes J., Wallace W., and Zhao L., *Current understanding of creep behavior of near γ-titanium aluminides.* International Materials Reviews, 1995. **40**(5): p. 197-217.
184. Hayes R.W. and London B., *On the creep deformation of a cast near gamma TiAl alloy Ti---48Al---1 Nb.* Acta Metallurgica et Materialia, 1992. **40**(9): p. 2167-2175.
185. Wang J.N., et al., in *Gamma titanium aluminides*. 1995, The Minerals, Metals, and Materials Society: Las Vegas, NV, USA. p. 948-958.
186. Appel F., Christoph U., and Oehring M., *Creep deformation in two-phase titanium aluminide alloys.* Materials Science and Engineering A, 2002. **329-331**: p. 780-787.
187. Appel F., et al., *Creep Behavior of TiAl Alloys with Enhanced High-Temperature Capability.* Metallurgical and Materials Transactions A, 2003. **34A**(October): p. 2149-2164.
188. Appel F., *Diffusion assisted dislocation climb in intermetallic gamma TiAl.* Materials Science and Engineering A, 2001. **317**(1-2): p. 115-127.
189. Zhang W.J., et al., *A preliminary study on the creep behavior of Ti-45Al-10Nb alloy.* Materials Science and Engineering A, 2001. **315**(1-2): p. 250-253.
190. Seo D.Y., Beddoes J., and Zhao L., *Primary creep behavior of Ti-48Al-2W as a function of stress and lamellar morphology.* Metallurgical and Materials Transactions A, 2003. **34A**(October): p. 2177-2190.
191. Zhang W.J., et al., *Deformation mechanisms in a high-Nb containing γ-TiAl alloy at 900^{0}C.* Materials Science and Engineering A, 1999. **271**(1-2): p. 416-423.
192. Maurice V., et al., *XPS study of the initial stages of oxidation of α_2-Ti_3Al and γ-TiAl intermetallic alloys.* Acta Materialia, 2007. **55**(10): p. 3315-3325.
193. Kim B.G., Kim G.M., and Kim C.J., *Oxidation behavior of TiAl-X (X = Cr, V, Si, Mo or Nb) intermetallics at elevated temperature.* Scripta Metallurgica et Materialia, 1995. **33**(7): p. 1117-1125.

194. Möck P., *A Direct Method for Orientation Determination Using TEM (I). Description of the Method.* Crystal Research and Technology, 1991. **26**(5): p. 653-658.
195. Möck P., *A Direct Method for Orientation Determination Using TEM (II). Experimental Example.* Crystal Research and Technology, 1991. **26**(6): p. 797-801.
196. Kofstad P., ed. *Nonstoichiometry, Diffusion, and Electrical Counductivity in Binary Metal Oxides*. 1972, Willy-Interscience
197. He J., et al., *Prediction of high-temperature point defect formation in TiO_2 from combined ab initio and thermodynamic calculations.* Acta Materialia, 2007. **55**(13): p. 4325-4337.
198. Becker S., et al., *Mechanism of Isothermal Oxidation of Intermetallic TiAl and TiAl Alloys.* Oxidation of Metals, 1992. **38**: p. 425-464.
199. Rahmel A., Schütze M., and Quadakkers W.J., *Fundamentals of TiAl oxidation - A critical review.* Materials and Corrosion/Werkstoffe und Korrosion, 1995. **46**(5): p. 271-285.
200. Yang R., et al., *Alloy development and shell mould casting of gamma TiAl.* Journal of Materials Processing Technology, 2003. **135**(2-3): p. 179-188.
201. Rahmel A and J S.P., *Thermodynamic aspects of TiAl and $TiSi_2$ oxidation: The Ti-Al-O and Si-Ti-O phase diagrams.* Oxidation of Metals, 1991. **35**: p. 53-68.
202. http://www.doitpoms.ac.uk/tlplib/ellingham_diagrams/ellingham.php.
203. Meier G.H., Pettit F.S., and Hu S., *Oxidaton behavior of titanium aluminides.* Journal De Physique IV, 1993. **3**: p. 395-402.
204. Rakowski J.M., et al., *The effect of surface preparation on the oxidation behavior of gamma TiAl-base intermetallic alloys.* Scripta Materialia, 1996. **35**(12): p. 1417-1422.
205. Gil A., et al., *The effect of microstructure on the oxidation behaviour of TiAl-based intermetallics.* Corrosion Science, 1993. **34**(4): p. 615-630.
206. Kekare S. and Aswath P., *Oxidation of TiAl based intermetallics.* Journal of Materials Science, 1997. **32**(9): p. 2485-2499.
207. Kelly T.J., et al., *Effect of elevated temperature exposure on cast gamma titanium aluminide (Ti---48Al---2Cr---2Nb).* Scripta Metallurgica et Materialia, 1994. **30**(9): p. 1105-1110.
208. Pather R., et al., *The effect of high temperature exposure on the tensile properties of γ–TiAl alloys.* Intermetallics, 2003. **11**(10): p. 1015-1027.
209. Draper S.L., et al., *Effect of exposure on the mechanical properties of Gamma MET PX.* Intermetallics, 2005. **13**(9): p. 1014-1019.
210. Wu X., et al., *Oxidation-induced embrittlement of TiAl alloys.* Intermetallics, 2009. **17**(7): p. 540-552.
211. Bacos M.P., et al., *The effect of long term exposure in oxidising and corroding environments on the tensile properties of two gamma-TiAl alloys.* Intermetallics, 2006. **14**(1): p. 102-113.
212. Ramanujan R.V., Maziasz P.J., and Liu C.T., *The thermal stability of the microstructure of γ-based titanium aluminides.* Acta Materialia, 1996. **44**(7): p. 2611-2642.
213. Lee W.B., Yang H.S., and Mukherjee A.K., *Mechanical properties and microstructural characterization of a superplastic TiAl alloy.* Materials Science and Engineering A, 1995. **192-193**(Part 2): p. 733-740.

214. Prasad U., et al., *Surface damage of a TiAl-based alloy during high temperature annealing.* Intermetallics, 2000. **8**(2): p. 125-131.
215. Touloukian Y.S., *Thermophysical properties of high temperature solid materials_Volume 1: elements*. 1967: New York ; London : Macmillan (N.Y.) Collier-Macmillan.
216. Xia J., et al., *The structural and mechanical property characterisation of thermal oxidation treated γ-based titanium aluminide.* Thin Solid Films, 2004. **458**(1-2): p. 212-222.
217. Xia J., et al., *Nanoindentation and nanoscratch properties of a thermal oxidation treated γ-TiAl based alloy.* Surface and Coatings Technology, 2006. **200**(16-17): p. 4755-4762.
218. Shemet V., et al., *Synthesis of the cubic Z-phase in the Ti---Al---O system by a powder metallurgical method.* Intermetallics, 1997. **5**(4): p. 271-280.
219. Copland E.H., Gleeson B., and Young D.J., *Formation of Z-Ti50Al30O20 in the sub-oxide zones of γ-TiAl-based alloys during oxidation at 1000^{0}C.* Acta Materialia, 1999. **47**(10): p. 2937-2949.
220. Dettenwanger F., et al., *Microstructural Study of Oxidized γ-TiAl.* Oxidation of Metals, 1998. **50**(3): p. 269-307.
221. Dettenwanger F., et al., *Development and microstructure of the Al-depleted layer of oxidized TiAl.* Materials and Corrosion/Werkstoffe und Korrosion, 1997. **48**(1): p. 23-27.
222. Beye R., et al., *Oxidation subscale of γ-titanium aluminide.* Acta Materialia, 1996. **44**(10): p. 4225-4231.
223. Zheng N., et al., *The significance of sub-surface depletion layer composition for the oxidation behaviour of γ-titanium aluminides.* Scripta Metallurgica et Materialia, 1995. **33**(1): p. 47-53.
224. Li X.L., et al., *Reactions and phase relations in the Ti---Al---O system.* Acta Metallurgica et Materialia, 1992. **40**(11): p. 3149-3157.
225. Lee J., et al., *Corrosion behaviour of Ti_3Al and Ti_3Al-11 at.% Nb intermetallics.* Materials Letters, 2003. **57**(9-10): p. 1528-1538.
226. Lavrenko V.A., Panasyuk A.D., and Firstov S.A., *Corrosion of Titanium-Aluminum Intermetallides. Part 2. Electrolytic Oxidation of γ-TiAl, $TiAl_3$, and α_2-Ti_3Al in Sea Water.* Powder Metallurgy and Metal Ceramics, 2003. **42**(5): p. 291-296.
227. Saffarian H.M.Q., Hadkar G., R. G., and Warren W., *Corrosion behavior of binary titanium aluminide intermetallics.* Corrosion Science, 1996. **52**(8): p. 626-633.
228. Ziomet-Moroz M., Su W., and Covino B.S.J., *Investigation of Passive Films on alpha-2 and gamma Titanium Aluminides by X-Ray Photoelectron Spectroscopy.* Corrosion Science, 1999. **55**(7): p. 635-643.
229. Du H.L., et al., *High temperature corrosion mechanisms of certain new TiAl-based intermetallic alloys in an aggressive $H_2/H_2O/H_2S$ environment at 850^{0}C.* Corrosion Science, 2007. **49**(5): p. 2406-2420.
230. Tang Z., Wang F., and Wu W., *Hot-Corrosion Behavior of TiAl-Base Intermetallics in Molten Salts.* Oxidation of Metals, 1999. **51**(3): p. 235-250.
231. Nicholls J.R., Leggett J., and Andrews P., *Hot Salt Corrosion of titanium aluminides.* Materials and Corrosion, 1997. **48**(1): p. 56-64.
232. Feng C.R., Michel D.J., and Crowe C.R., *Microstructural characteristics of two-phase titanium aluminides.* Materials Science and Engineering: A, 1991. **145**(2): p. 257-264.

233. Voice W., *The future use of gamma titaniium aluminides by Rolls-Royce.* Aircraft Engineering and Aerospace Technology, 1999. **71**(4): p. 337-340.
234. Jeon J.H., et al., *Recrystallization in cast 45-2-2 XD(TM) titanium aluminide during hot isostatic pressing.* Materials Science and Engineering A, 1999. **271**(1-2): p. 128-133.
235. Voice W., *Practical advice on the use of Ti-45-2-2-XD^{TM} gamma titanium aluminide,* in *Titanium Alloy at Elevated Temperature: Structural Development and Service Behavior*, Winstone M.R., Editor. 2001, IOM Communications Ltd: London. p. 237-250.
236. Yoshihara M. and Miura K., *Effects of Nb addition on oxidation behavior of TiAl.* Intermetallics, 1995. **3**(5): p. 357-363.
237. Yoshihara M. and Kim Y.W., *Oxidation behavior of gamma alloys designed for high temperature applications.* Intermetallics, 2005. **13**(9): p. 952-958.
238. Seishi Tsuyama S.M.a.K.-n.M., *Alloy modification of gamma-based titanium aluminide for improved oxidation resistance, creep strength and fracture toughness.* Materials Science and Engineering A, 1992. **153**: p. 451-456.
239. Jiang H., et al., *Effect of Nb on the high temperature oxidation of Ti-(0-50 at.%)Al.* Scripta Materialia, 2002. **46**(9): p. 639-643.
240. Kim Y.W., *Intermetallic Alloys Based on Gamma Titanium Aluminide.* JOM, 1989. **41**(July): p. 24-30.
241. Nakano T. and Umakoshi Y., *Effect of boron addition on the plastic behaviour of polysynthetically twinned crystals of TiAl.* Intermetallics, 1994. **2**(3): p. 185-191.
242. Morris M.A., *Dislocation mobility, ductility and anomalous strengthening of two-phase TiAl alloys: effects of oxygen and composition.* Intermetallics, 1996. **4**(5): p. 417-426.
243. Vasudevan V.K., et al., *The influence of second phase Ti_3Al on the deformation mechanisms in TiAl.* Philosophical Magazine Letters, 1989. **59**(6): p. 299 - 307.
244. Zhu H., et al., *Microstructural stability of fine-grained fully lamellar XD TiAl alloys by step aging.* Metallurgical and Materials Transactions A, 2005. **36**(5): p. 1339-1351.
245. Larsen D.E., Kampe S.L., and Christidoulou L., Materials Research Society Symposium Processings, 1990. **194**: p. 185-290.
246. Seo D.Y., Zhao L., and Beddoes J., *Microstructural evolution during heat treatments in Ti-45 and 47Al-2Nb-2Mn+0.8vol.%TiB_2 XD^{TM} alloys.* Materials Science and Engineering A, 2002. **329-331**: p. 130-140.
247. Mercer C., et al., *Effects of temperature on the fatigue crack growth behavior of cast gamma-based titanium aluminides.* Metallurgical and Materials Transactions A, 2001. **32**(11): p. 2781-2794.
248. McKelvey A., Venkateswara Rao K., and Ritchie R., *High-temperature fracture and fatigue-crack growth behavior of an XD gamma-based titanium aluminide intermetallic alloy.* Metallurgical and Materials Transactions A, 2000. **31**(5): p. 1413-1423.
249. Chaturvedi M.C., Richards N.L., and Xu Q., *Electron beam welding of a Ti-45Al-2Nb-2Mn+0.8 vol.% TiB_2 XD alloy.* Materials Science and Engineering: A, 1997. **239-240**: p. 605-612.
250. Lee D.B., Shim W.S., and Seo D.Y., *High temperature oxidation of Ti-(45,47)%Al-2%Mn-2%Nb-0.8vol%TiB_2 alloys.* Materials Transactions, JIM, 2002. **43**(10): p. 2527-2530.

251. Jones I.P., *Chemical Microanalysis Using Electron Beams*. 1992, London: The Institute of Materials.
252. Hu D., et al., *Grain refinement in beta-solidifying Ti44Al8Nb1B.* In the process of clearance by Rolls-Royce plc.
253. Larson D.J., Liu C.T., and Miller M.K., *The alloying effects of tantalum on the microstructure of an $\alpha_2+\gamma$ titanium aluminide.* Materials Science and Engineering A, 1999. **270**(1): p. 1-8.